Ultrafast Spectroscopic Studies of Solution-Processing Organic Photovoltaic Materials and Devices

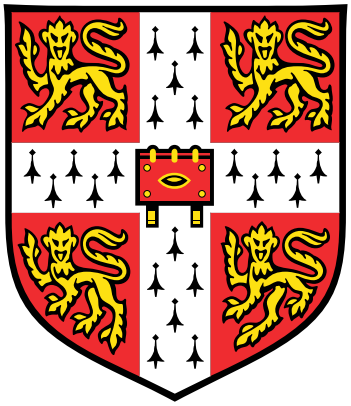

Jiangbin Zhang

Supervisor: Prof. Sir Richard H. Friend
Dr. Artem A. Bakulin

Cavendish Laboratory
University of Cambridge

This thesis is submitted for the degree of
Doctor of Philosophy

Homerton College

September 2019

This thesis is dedicated to my family.

Declaration

The research described in this thesis was carried out by the author between October 2015 and September 2019 and includes nothing which is the outcome of work done in collaboration, except where specifically indicated in the text. This dissertation has not been submitted in whole or in part for the award of a degree at this, or any other university and does not exceed 60,000 words in length.

Jiangbin Zhang

September 2019

Ultrafast Spectroscopic Studies of Solution-Processing Organic Photovoltaic Materials and Devices

Jiangbin Zhang

Organic solar cells (OSCs) have potential applications in wearable electronics as well as in-door and building-integrated photovoltaics, owing to features such as low-temperature processing, light weight and flexibility, and synthetic versatility. Due to the development of new materials systems with unique optoelectronic properties, a breakthrough in the OSC performance has been achieved. However, knowledge of the underlying mechanism still lags behind. Such understanding is essential for further development of organic photovoltaics. The needed comprehensive investigation mainly comes from studying the carrier dynamics on promising OSC systems. To this aim, the used tool kits, ultrafast spectroscopic methods, are the subject of this thesis.

First three chapters of the thesis present the general paradigm of photoconversion in OSCs and outlines the key models used to describe their photovoltaic performance. The ability of OSCs to generate electrical current in response to absorbing sunlight greatly differs, depending on materials and the following device fabrication methods. In the device operation, the performance is related to the conversion efficiency from molecular excited states into charge carriers. Chapter 2 presents a historical review of different material combination, device architecture and key processes relevant for solar cell performance. This leads to the key questions that this thesis addresses: which molecular properties are most important for photoconversion in OSCs? How much energy is required to convert from molecular excited states to free charges? What are the optimal preparation procedure and microstructure of OSC devices? Chapter 3 gives an overview of spectroscopic tools used to address these questions.

Chapters 4 to 8 target above questions in application to different material systems, from the 'classical' broadly studied polythiophene-fullerene blends to the high-performance OSC devices based on non-fullerene acceptors (NFAs). Firstly, the rate of exciton dissociation is studied in state-of-the-art organic blends with NFAs. The charge generation is found to be slow (ps), in sharp contrast with the ultrafast timescales in traditional blends based on fullerene acceptors. Secondly, a new technique is developed, namely temperature-dependent pump-push photocurrent spectroscopy, which is able to measure the strength of interaction between charges in working OSCs. This technique is applied to research which factors govern the dissociation of molecular excited states in fullerene-based blends. Thirdly, recombination processes are studied using a set of ultrafast techniques, focusing on their effect on device performance, and the dependence on processing conditions and used materials. Finally, a new method 'via sequential deposition' is demonstrated for fabrication of efficient NFA-based devices. We discuss the properties of OSCs fabricated by this method and the potential for its commercialisation.

Acknowledgements

To start with, I thank Dr. Artem Bakulin for kindly accepting me into the fabulous OE family, and for his consistent support for research and much care for life. I also thank Prof. Sir Richard Friend to take me over from Artem in my first year after Artem moved to Imperial College, and for his readily available support and guidance. I thank them for leading me into this quickly evolving research frontier and for the freedom to explore research questions.

Secondly, I feel grateful to work with many excellent colleagues in Cambridge and Imperial. I am lucky to stay in the glorious Fastlab to know so many smart spectroscopists till its unofficial disappearance. I thank Andrew for interviewing me and showing me how to decompose spectroscopic signals from the physical instinct; Andy, a hard-core fastlabber, who welcomed me on my first day and knows how to encourage people around; Hannah, who sets a good example of work-life balance and research focus; Florian for organising formal dinners - the roast duck from Pembroke is my favourite till now; Johannes and Jasmine for sharing perovskite amazings; Vincent, Alex and David for taking care of the laser setup. I thank Prof. Feng Li and Dr. Emrys Evans for kindly taking me to the doublet world and teaching me OLED fabrication without reservation - I learned from you how to cope with failure from the time when struggling to improve substrate cleaning, measurement reliability, and device layout; in particular, I appreciate Feng's frankness as a friend and colleague, and his research guidance as a teacher. I thank Dawei for encouraging me on the scientific journey; Sanyang for giving me chance to explore the photophysics of lanthanide-organic complex system, and sharing his life experience which always triggers my thinking. In Imperial, I feel much indebted to my best lab mate Tom who also acts as my English teacher - you always become the first guy to ask for proofreading my publications; you also show us by action how to be organised and devoted; I thank Yifan for building the cryostat system and Mike for taking care of the fsTAS setup.

It is always a great pleasure to collaborate with many groups in the world. I thank Dr. Akshay Rao and Dr. Andreas Jakowetz for involving me in their project which led to my first co-authored and first-authored papers; Prof. Yongsheng Chen, Prof. Xiangjian Wan and Dr. Bin Kan from Nankai University, for providing newly developed high-performance materials for the photophysics study and for always making me feel at home when visiting their lab;

Prof. Jianhui Hou and Dr. Huifeng Yao from Institute of Chemistry, Chinese Academy of Science, for hosting my visit and sharing their enthusiasm for recent photovoltaic developments; Prof. Feng Gao from Linköping University, for supporting me in the Gordon conference and for his insightful discussion; Prof. Donatas Zigmantas and Eglé from Lund University for allowing me to use their advanced two-dimensional electronic spectroscopy; Prof. Yana Vaynzof from Heidelberg University for sharing the new characterisation technique and much support for my scientific journey. Help from other collaborators is also indispensable and greatly appreciated: Prof. Christopher McNeill (Monash University), Prof. Bruno Ehrler (AMOLF), Prof. Prashant Sonor (Queesland University of Technology), Dr. Josh Cooper (Rutherford Appleton Laboratory), Prof. Zhixiang Wei and Dr. Dan Deng (National Center for Nanoscience and Technology), and Prof. Weiwei Li (Beijing University of Chemical Technology).

Thank you to friends in the research lab, whose accompany makes the lab time interesting: Qifei, Lang, Dawei, Xiaoke, Emrys, Le, Emily, Linsong, Nana, Ligang, Ziyue, Matt, Florian, Alex, Guoming, Yuanhui, Yutian, Ren, Jiaming, Alessio, Robin, Renren, Sanyang, Zhilong, Mengxia, Linjie, Arya, David, Xinyu, Qinying, Jiale, Kuangyu, Arfa, Patrick, Guangru. I also have a lot of fun with friends from Department of Chemistry: Ji, Yang, Chuan, Zhijun, Ziyi, Zhenpin and Yuewen. I like the very friendly and positive environment with Imperial colleagues: Andrei, Ernest, Tom, Yifan, Neath, Rhea, Polly, Zhu, Jiaxin, Shawn, Chloe, Lin and Ahhyun as well as people in Durrant Group, Mike, Jiaying, Weidong, Hyojung and Jinho. I also thank my friends Danyang, James and Junlin who make Homerton College a home to stay at.

The research is not possibe without the technical and administrative support from Richard, Roger, Alison, Jennie, William and Egle in OE Group, Barry and Hwu in Electronic Workshop, and Matt in Mechanics Workshop. Xiaoe and Pabitra in Imperial offer much help to teach me to use Imperial facilities.

I extend my gratitude to Dr. Sarah Bohndiek and Ms Emily Challis for supporting my brave idea of establishing the SPIE Cambridge Student Chapter in Cavendish Laboratory. I feel so grateful to have enormous support from the committee members Arfa, Qifei and Dale, carrying out networking and career events that benefit local graduate students. I am so proud of the successor Arfa, who has lead the chapter to a new level. I hope this chapter will continue its glory in the years to come.

Most traditional Chinese festivals in Cambridge were filled with joy with friends from NUDT. I feel grateful to NUDT for offering the study-abroad program which guides me to Cambridge, and China Scholarship Council for fully funding my four-year PhD study. I

also thank my supervisor Prof. Jinbao Chen (NUDT) who gives me much guidance and life wisdom.

Last but not the least, the gratitude towards my parents, whose unconditional support makes my life abroad more settled. My sincere thanks go to my wife Zhongyang for encouraging and supporting me along the way. The last bit goes to our lovely daughter Jane, who successfully challenges her parents' ability and is staying happily with her grandparents temporarily.

List of publications

Published journal articles

1. **Jiangbin Zhang**, Andreas C. Jakowetz, Guangru Li, Dawei Di, S. Matthew Menke, Akshay Rao, Richard H. Friend and Artem A. Bakulin*, "On the Energetics of Bound Charge-Transfer States in Organic Photovoltaics", *Journal of Materials Chemistry A*, **5**, 11949-11959, 2017.

2. **Jiangbin Zhang***, Qinying Gu, Thu Trang Do, Kira Rundel, Prashant Sonor, Richard H. Friend, Christopher R. McNeill and Artem A. Bakulin*, "Control of Geminate Recombination by the Material Composition and Processing Conditions in Novel Polymer:Nonfullerene Acceptor Photovoltaic Devices", *Journal of Physical Chemistry A*, 122(**5**), 1253–1260, 2018.

3. Bin Kan†, **Jiangbin Zhang**†, Feng Liu, Xiangjian Wan, Chenxi Li, Xin Ke, Yunchuang Wang, Huanran Feng, Yamin Zhang, Guankai Long, Richard H. Friend, Artem A. Bakulin* and Yongsheng Chen*, "Fine-Tuning the Energy Levels of a Nonfullerene Small-Molecule Acceptor to Achieve a High Short-Circuit Current and a Power Conversion Efficiency over 12% in Organic Solar Cells", *Advanced Materials*, 30(**3**), 1704904, 2018.

4. **Jiangbin Zhang**†, Bin Kan†, Andrew J. Pearson, Andrew J. Parnell, Joshaniel F. K. Cooper, Xiao-Ke Liu, Patrick J. Conaghan, Thomas R. Hopper, Yutian Wu, Xiangjian Wan, Feng Gao, Neil C. Greenham, Artem A. Bakulin, Yongsheng Chen*, Richard H. Friend*, "Efficient Non-fullerene Organic Solar Cells Employing Sequentially Deposited Donor-Acceptor Layers", *Journal of Materials Chemistry A*, 37(**6**), 18225-18233, 2018.

5. **Jiangbin Zhang**, Moritz H. Futscher, Vincent Lami, Felix U. Kosasih, Changsong Cho, Qinying Gu, Aditya Sadhanala, Andrew J. Pearson, Bin Kan, Giorgio Divitini,

Xiangjian Wan, Daniel Credgington, Neil. C. Greenham, Yongsheng Chen, Caterina Ducati, Bruno Ehrler, Yana Vaynzof*, Richard H. Friend, Artem. A. Bakulin*, "Sequentially Deposited and Conventional Nonfullerene Organic Solar Cells: Interfacial Trap States, Vertical Stratification and Exciton Dissociation", *Advanced Energy Materials*, 9(**47**), 1902145, 2019.

6. Andreas C. Jakowetz, Marcus L. Böhm, **Jiangbin Zhang**, Aditya Sadhanala, Sven Huettner, Artem A. Bakulin, Akshay Rao*, and Richard H. Friend*, "What Controls the Rate of Ultrafast Charge Transfer and Charge Separation Efficiency in Organic Photovoltaic Blends." *Journal of the American Chemical Society*, 138(**36**), 11672-11679, 2016.

7. Deping Qian, Zilong Zheng, Huifeng Yao, Wolfgang Tress, Thomas R. Hopper, Shula Chen, Sunsun Li, Jing Liu, Shangshang Chen, **Jiangbin Zhang**, Xiao-Ke Liu, Bowei Gao, Liangqi Ouyang, Yingzhi Jin, Galia Pozina, Irina A. Buyanova, Weimin M. Chen, Olle Inganäs, Veaceslav Coropceanu*, Jean-Luc Bredas, He Yan, Jianhui Hou, Fengling Zhang, Artem A Bakulin*, Feng Gao*, "Design Rules for Minimizing Voltage Losses in High-efficiency Organic Solar Cells", *Nature Materials*, 17(**8**), 703-709, 2018.

8. Baodan Zhao, Sai Bai, Vincent Kim, Robin Lamboll, Ravichandran Shivanna, Florian Auras, Johannes M. Richter, Le Yang, Linjie Dai, Mejd Alsari, Xiao-Jian She, Lusheng Liang, **Jiangbin Zhang**, Samuele Lilliu, Peng Gao, Henry J. Snaith, Jianpu Wang, Neil C. Greenham, Richard H. Friend*, Dawei Di*," High-Efficiency Perovskite-Polymer Bulk Heterostructure Light-Emitting Diodes", *Nature Photonics*, (12)**12**, 783-789, 2018.

9. Hongling Yu, Heyong Wang, **Jiangbin Zhang**, Jun Lu, Zhongcheng Yuan, Weidong Xu, Lars Hultman, Artem A. Bakulin, Richard H. Friend, Jianpu Wang, Xiao-Ke Liu* and Feng Gao*, "Efficient and Tunable Electroluminescence from In-Situ Perovskite Quantum Dots", *Small*, 15(**8**), 201804947, 2019.

10. Yifan Dong, Hyojung Cha, **Jiangbin Zhang**, Ernest Pastor, Pabitra S. Tuladhar, Iain McCulloch, James R. Durrant, Artem A. Bakulin*, "The Binding Energy and Dynamics of Charge-Transfer States in Organic Photovoltaics with Low Driving Force for Charge Separation", *The Journal of Chemical Physics*, 150(**10**), 104704, 2019.

11. Vincent Lami, Andreas Weu, **Jiangbin Zhang**, Yongsheng Chen, Zhuping Fei, Martin Heeney, Richard H. Friend, and Yana Vaynzof*, "Visualising the Vertical Energetic Landscape in Organic Photovoltaics", *Joule*, 3(**10**),2513-2534, 2019.

Conference papers

1. **Jiangbin Zhang**, Aleksei V. Emelianov, Artem A. Bakulin* and Ivan I Bobrinetskiy, "Molecular Doping of Single-Walled Carbon Nanotube Transistors: Optoelectronic Study", *Physical Chemistry of Interfaces and Nanomaterials XV*, SPIE Optics+Photonics, San Diego, California, 2016.

2. Vasily A. Trukhanov, Daniil S. Anisimov, Vladimir V. Bruevich, Elena V. Agina, Oleg V. Borshchev, Sergei Ponomarenko, **Jiangbin Zhang**, Artem A. Bakulin*, Dmitri Y. Paraschuk, "Monolayer Organic Field Effect Phototransistors: Photophysical Characterization and Modelling", *Organic Photovoltaics XVII*, SPIE Optics+Photonics, San Diego, California, 2016.

Table of contents

List of figures

List of tables

Chapter 1

Introduction

Renewable energy is needed now more than ever. Traditional ways to generate energy like burning fossil fuels have caused global problems, like climate change. To address these global challenges, turning to renewable energy has become the world consensus. For example, the percentage of renewable energy in all energy sources produced in UK hit a record high at 33% in 2018.[2]

Among many renewable energy technologies, sunlight is the most abundant, safe and clean energy source.[3] Therefore, photovoltaic technologies have been heavily researched in academia and industry. To evaluate the photovoltaic performance, an important figure of merit is called the power conversion efficiency (PCE), the ability to convert incident solar photon energy into the output electric energy. The certified values are maintained and published by National Renewable Energy Laboratory (NREL).[4] From the table, sophisticated multi-junction solar cells have reached a record efficiency of 46%. However, these devices are too expensive to be broadly adopted. Instead, the polycrystalline silicon solar cells with a reasonable efficiency around 20% are most popular, and become a workhorse for the photovoltaic-based electric generation.

During the last four decades, the price of silicon solar cells has significantly dropped by over three hundred times, reaching below 30 US cents per watt. The reduction in solar price has greatly increased its adoption, which conquers approximately 90% of the total photovoltaic market. Currently, photovoltaic energy accounts for a record-high, yet small fraction of the total consumption. For instance, 3.9% of total energy consumption in the UK in 2018 comes from the photovoltaic energy.[5] Worldwide, the deployment of solar energy experiences an exponential growth. Going forward, there is a bright future for photovoltaic technologies as an important means to generate renewable energy.

Complementary to silicon solar cells, organic solar cells have niche applications in wearable electronics, in-door and building-integrated photovoltaics, owing to features such

as low-temperature processing, light weight, flexibility and synthetic versatility.[6] These devices use organic semiconductors as light-absorbing materials, which have been widely applied in lighting and displays in the form of organic light-emitting diodes (OLEDs).[7] In the past five years, new breakthroughs in material systems have nearly doubled the PCE to the level of 17%, with potential to reach even 20%.[8] Even though some challenges in device stability and large-scale fabrication still await solutions, organic solar cells hold the promise for commercialisation in the near future.

Despite the fast development of device performance, the mechanism of new-generation organic solar cells is still poorly understood. In organic materials, photon-to-charge conversion is mediated through excitonic states. These states arise from a large Coulomb attractive force between electron and hole due to the low dielectric constant. By contrast, inorganic materials with a large dielectric constant effectively screens the Coulomb interaction and free charges are spontaneously generated. From the fundamental point of view, the Coulomb interaction distinguishes organic and inorganic materials and brings about the physics of electron-hole interactions which lie at the heart of this thesis.

Under light exposure, in organic electronic materials, excitons, bound electron-hole pairs, are generated but cannot be easily separated before their recombination. The widely adopted solution to this involves a heterostructure between two electronically dissimilar materials, providing a driving force for exciton dissociation. This separation process occurs at a fs-ps timescale. To observe such fast events, we utilise femtosecond laser pulses to take snapshots of the studied system, and identify the representative features of excited-state species, like excitons and charges. Understanding how charges are generated and recombined provides deep physical insight into the functionality of organic photovoltaic cells.

After almost three decades of research, organic solar cells can reach close-to-unity charge generation and collection efficiency under external bias. The main limitation is a relatively large voltage loss in organic devices, defined as the difference between the semiconductor bandgap and the device voltage output. This voltage loss for polymer:fullerene solar cells (typically 0.7 eV) is much higher than inorganic counterparts at around 0.4 eV.[9] Between organic and inorganic cells, the difference in the voltage loss is mainly ascribed to the driving force (the energy offset between donor and acceptor), a requirement at the heterostructure to separate excitonic states in organics. In emerging non-fullerene acceptor (NFA) systems, a general observation is that a large driving force is not required to achieve high device efficiencies.[10] Together, the non-radiative recombination loss is significantly reduced. Till now, answers to these observations are, however, still unclear.

This thesis intends to understand charge generation mechanism in organic solar cells, with the focus on the excitonic state at the heterojunction, charge-transfer states (CTSs). This state

is the most important state for device operation, because the separation and recombination of CTSs determines the device performance. We probe this state in a range of material systems, including fullerene- and NFA- based blends via ultrafast optical spectroscopies.

Chapter 2 introduces the physical background of organic electronics. We also explain the working principle of organic solar cells, and review the history of organic solar cells, with the emphasis on the recent developments in NFA-based devices. Chapter 3 describes experimental setups, mainly the spectroscopic methods. Other methods are attached into respective chapters when certain measurements are performed.

Chapter 4 describes a new experimental method to determine the binding energy of CTSs from temperature-dependent pump-push photocurrent spectroscopy. Using this technique, we study the effect of driving energy and fullerene aggregation by changing the fullerene derivatives and fullerene loadings. Chapter 5 combines two ultrafast spectroscopic methods - pump-push photocurrent spectroscopy and pump-probe spectroscopy to probe the geminate recombination of CTSs. The relationship between geminate recombination and device photocurrent is related by varying parameters, such as solvent, thermal annealing and NFA type.

Chapter 6 researches the charge dynamics in high-efficiency NFA-based blends. The broadband pump-probe spectroscopy is analysed first by selectively exciting donor and acceptor components. The possible energy and charge transfer processes are analysed. Due to the overlapping spectra of exictons and charges, global analysis enables the decomposition of different excited species and their interconversion. Models with and without triplet states are analysed.

Chapter 7 presents a new method to prepare the active layer in NFA-based solar cells. We systematically analyse the photovoltaic performance and additionally measure the exciton diffusion length of a benchmark polymer. Chapter 8 conducts a more comprehensive study to understand the photophysics in devices fabricated from two methods, from the perspective of trap states, vertical heterogeneity and exciton dissociation.

Chapter 9 concludes the whole thesis by providing a bigger picture in charge generation mechanism in NFA-based organic solar cells. Some directions for future studies are also discussed.

Chapter 2

Theory and Background

Of the two million compounds known, approximately 90% are organic, customarily carbon containing compounds.[11] To understand these compounds, human develop chemistry and learn to synthesise millions of new materials. Plastics (or polymers), is one important application in life due to their tailored properties, such as lightweight, water and shock resistant, and thermally and electrically insulating. The discovery of electronically conductive polymers, such as halogen-doped polyacetylene, not existing in nature, enables them electronic functionality, and thus bring together interdisciplinary fields of chemistry and physics.[12] The second generation of conducting polymers, initiated by the discovery of polymer electroluminescence (EL) [13], extends these materials into organic semiconductors, and generates huge interest in developing optoelectronic devices, such as organic light-emitting diodes (OLEDs), organic solar cells (OSCs) and organic thin-film transistors. The third generation of polymers, containing electron donating and accepting units, are currently being used in high-performance optoelectronic devices.[14]

In this chapter, the electronic structure of organic semiconductors is briefly introduced followed by the definition of electronic states and their transitions. Following these concepts, we will review the development of OSCs from material evolvement and photophysics understanding. Finally, we will emphasise opportunities and challenges in understanding new low-offset cells based on non-fullerene acceptors (NFAs).

2.1 The Electronic Structure of π-Conjugated Systems

2.1.1 Atomic Orbital and Bonding

Organic semiconductors are carbon-based materials, thus the electronic structure of carbon needs to be understood before we dig into the optoelectronic properties of organic molecules. Of the ground state of the carbon atom, the electronic configuration is $1s^2 2s^2 2p^2$. Four electrons reside in the outer shell: two electrons are paired in the s orbital, and two unpaired electrons are in separate p orbitals. When a carbon tends to bond with another atom, multiple atomic orbitals can be hybridised, forming new degenerate orbitals with certain symmetry and preferential bonding directions. For instance, by promoting one electron from an s orbital into an empty p orbital, one configuration combines the remaining s orbital and three singly-occupied p orbitals to form four equivalent sp^3 *hybrid orbitals* in a tetrahedral arrangement, available to bond four atoms nearby. Methane and diamond are examples based on this configuration.

Another type of configuration is to mix one $2s^2$ and two $2p^2$ orbitals, forming three sp^2 *hybrid orbitals*. These bonds are equally separated apart at 120° and lie in the same plane that is perpendicular to the remaining atomic p orbital, the p_z orbital. Similarly, one $2s^2$ orbital and one $2p^2$ orbital can also hybridise and thus generate two *sp hybrid orbitals* which are co-linear. The bonding between these hybridised orbitals forms σ-bonds. The unchanged p_z orbitals on neighbouring carbon atoms can interact and form bonding and anti-bonding orbitals, which form π-bonds. Depending on the number of π-bonds, double-bonded and triplet-bonded carbons appear in addition to one σ-bond already formed. Ethylene and acetylene illustrate these two cases, respectively.

The above discussion is visualised in Fig.2.1. The electron, depending on which orbital it occupies, can be classified as a π *electron* or σ *electron*. It is notable that separation of π-orbital and σ-orbital is only valid in perfectly planar molecules (such as polymer chains); as long as this planarity is broken, mixing between σ-orbital and π-orbital occurs.

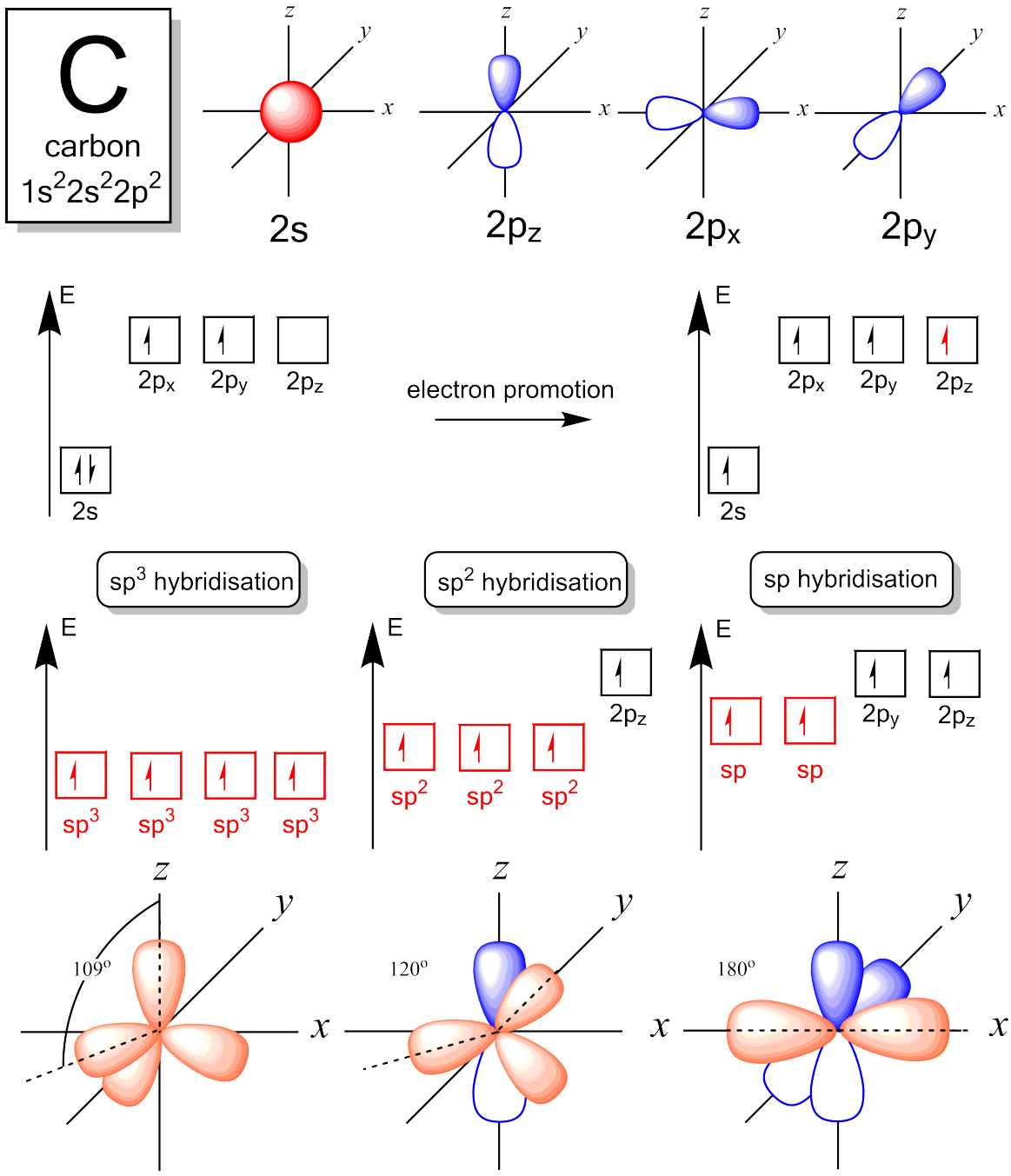

Fig. 2.1 Carbon is the key element in organic electronics. The electron configuration of carbon is $1s^2 2s^2 sp^2$, and the electron distribution in 2s, $2p_x$, $2p_y$ and $2p_z$ atomic orbitals; the formation of hybridised orbitals of sp^3, sp^2 and sp hybrid orbitals; electron distribution in hybrid orbitals and remaining p orbital in space. The angles of neighbouring electron lobes for sp^3, sp^2 and sp hybrid orbitals are 109 degrees, 120 degrees and 180 degrees, respectively.

2.1.2 Molecular Brbital: Hückel Model

Out of a range of complex theories that explain the formation of molecular orbitals, the simplest is probably the Hückel model. The key concept behind this model is that the molecular orbitals are constructed from a *linear combination of atomic orbital* (LCAO). The Hückel model does not have a specific basis set (a basis set is a collection of well-defined functions to approximate the molecular orbitals). We consider all atomic orbitals (that form π-molecular orbitals) as the basis set. Here we only discuss the perturbation and formation of π-orbitals to give intuitive physical insight and to help understand basic concepts, although the method is also applicable to understand σ-orbitals.

At this stage, it would be convenient to introduce some basic formulae from quantum mechanics along the introduction of some key concepts. To describe a time-independent quantum system, the Schrödinger equation is given as

$$\hat{H}\Psi = E\Psi \tag{2.1}$$

where $\hat{H}$ is the Hamiltonian operator of the quantum system, Ψ is the orbital wavefunction that fully describes the system and E is the energy of a stationary system.

A full description of the Hamiltonian describes the energy of a system as a function of all physical properties, including electronic, nuclear and spin coordinates. The spin and orbital motion of an electron gives it a magnetic field. Their interaction, i.e. spin-orbital coupling, causes a split in the energy levels of molecular orbitals. A more detailed description of spin-orbital coupling is presented in Section 2.2.5. With this effect neglected at the moment, the molecular Hamiltonian is represented as the interaction of electron and nuclei,

$$\hat{H}_{\text{mol}} = \hat{H}_{\text{el-el}} + \hat{H}_{\text{nuc-nuc}} + \hat{H}_{\text{el-nuc}} \tag{2.2}$$

A more detailed description is presented below. The electron-only Hamiltonian contains its kinetic energy and potential energy,

$$\hat{H}_{\text{el-el}} = \hat{T}_{\text{el-el}} + \hat{V}_{\text{el-el}} = -\sum_i \frac{\hbar^2}{2m_e}\nabla_i^2 + \frac{1}{2}\frac{1}{4\pi\varepsilon_0}\sum_{i\neq j}\frac{e^2}{\left|r_i - r_j\right|} \tag{2.3}$$

where $\hat{T}_{\text{el-el}}$ is the electron kinetic energy, $\hat{V}_{\text{el-el}}$ the Coulombic potential energy, $\hbar$ the reduced Planck's constant, m_e the mass of electron, ∇_i^2 the Laplacian operator on electron i, ε_0 the permittivity of free space, and $\left|r_i - r_j\right|$ the absolute distance between electron i and j.

In the same vein, the nuclei-only Hamiltonian can be expressed below

$$\hat{H}_{\text{nuc-nuc}} = \hat{T}_{\text{nuc-nuc}} + \hat{V}_{\text{nuc-nuc}} = -\sum_{\alpha} \frac{\hbar^2}{2M_\alpha} \nabla_\alpha^2 + \frac{1}{2} \frac{1}{4\pi\varepsilon_0} \sum_{\alpha \neq \beta} \frac{Z_\alpha Z_\beta e^2}{|R_\alpha - R_\beta|} \tag{2.4}$$

where $\hat{T}_{\text{nuc-nuc}}$ is the nuclei kinetic energy, $\hat{V}_{\text{nuc-nuc}}$ the Coulombic potential energy, M_α the mass of nucleus α, ∇_α^2 the Laplacian operator on nucleus α, $Z_\alpha(Z_\beta)$ the proton number of the nucleus α (β) and $|R_\alpha - R_\beta|$ the absolute distance between nucleus α and β.

Between the electrons and nuclei, their Coulombic interaction is

$$\hat{H}_{\text{el-nuc}} = -\frac{1}{4\pi\varepsilon_0} \sum_{\alpha,i} Z_\alpha \frac{e^2}{|R_\alpha - r_i|} \tag{2.5}$$

A system composed of many electrons and nuclei is indeed a many-body system, and their analytic as well as numerical solution is very complex to solve. More assumptions are needed to simplify this equation as follows:

1. **Many-body reduction** In Hückel model, there is no electron-electron interaction, except for the nearest neighbour. Electrons far away are independent on each other and their interaction is ignored. Electron-nuclear interaction is simplified to interact with its own nucleus. Nuclear-nuclear interaction is set to constant. The molecular Hamiltonian can thus be reduced to a sum of independent single electron items,

$$\hat{H}_{mol} \simeq \sum_i \hat{H}_{eff}(i) = -\frac{\hbar^2}{2m_e} \sum_i \nabla_i^2 + \sum_i v(i) \equiv \hat{H}_{huc} \tag{2.6}$$

   where $\hat{H}_{eff}$ is the effective Hamiltonian, v the electron's potential expressed as its own coordinates, and $\hat{H}_{huc}$ is the derived Hückel Hamiltonian. $\sum_i v(i)$ can be approximated by an average potential V_{el} as an effect of other electrons and the Coulombic potential with its own nucleus.

$$\sum_i v(i) = V_{el} - \frac{1}{4\pi\varepsilon_0} \sum_i Z_i \frac{e^2}{|R_i - r_i|} \tag{2.7}$$

2. **π-electron models.** The energy of σ-orbitals is lower as on average they are closer to the nuclei. The σ-electrons are therefore more stable due to stronger Coulomb attraction with the positively charged nuclei. Due to the large gap between the energy of occupied π-orbital and σ-orbital, the occupied π-orbital and unoccupied π^*-orbital define the frontier molecular orbitals. The contribution of σ-electrons, if necessary,

can be collected in the form of a static dielectric constant that considers the screening effect between the nucleus and the electron. Rigorous calculation of the effect of the σ-electrons is theoretically feasible but computationally costly, and therefore this effect is either neglected or approximated as a static constant.

The lowest energy transition of π-π^* gives the definition of the transport gap of conjugated polymers.[15] Due to the large energy gap in σ-σ^*, the modification on these orbitals is negligible on the electronic properties compared to the easily perturbed π-π^* transition. These π-orbitals determine the main electronic properties of conjugated polymers, which gives chemists much freedom to tailor their molecular properties by manipulating the frontier π orbitals.

The following calculation expands the molecular orbitals as a linear combination of the p_z atomic orbitals, $|\varphi_i\rangle$. The molecular wavefunction for a molecular orbital, $|\psi\rangle$, can be expressed as,

$$|\psi\rangle = \sum_j c_j |\varphi_j\rangle \tag{2.8}$$

The parameter c_j is the coefficient for the atomic orbital $|\varphi_j\rangle$. The magnitude of this coefficient describes how much this atomic orbital contributes to the overall molecular orbital.

This equation is substituted into the Schrödinger equation,

$$\hat{H}|\psi\rangle = E|\psi\rangle \tag{2.9}$$

with $\hat{H}$ the Hamiltonian and E the energy of the corresponding molecular orbital to give:

$$\sum_j c_j \hat{H}|\varphi_j\rangle = \sum_j E c_j |\varphi_j\rangle \tag{2.10}$$

This equation is multiplied by $\langle\varphi_i|$ and we have

$$\sum_j c_j (H_{ij} - E S_{ij}) = 0 \tag{2.11}$$

where H_{ij} is the element in the Hamiltonian matrix,

$$H_{ij} = \langle\varphi_i|\hat{H}|\varphi_j\rangle = \int \varphi_i H \varphi_j \, d\upsilon \tag{2.12}$$

and S_{ij} is the overlap integral,

$$S_{ij} = \langle \varphi_i | \varphi_j \rangle = \int \varphi_i \varphi_j \, d\upsilon \tag{2.13}$$

For j varying from 1 to N, the equations can be presented,

$$\begin{bmatrix} c_1(H_{11} - E\,S_{11}) + c_2(H_{12} - E\,S_{12}) + \cdots + c_N(H_{1N} - E\,S_{1N}) \\ c_1(H_{21} - E\,S_{21}) + c_2(H_{22} - E\,S_{22}) + \cdots + c_N(H_{2N} - E\,S_{2N}) \\ \cdots\cdots\cdots \\ c_1(H_{N1} - E\,S_{N1}) + c_2(H_{N2} - E\,S_{N2}) + \cdots + c_N(H_{NN} - E\,S_{NN}) \end{bmatrix} = 0 \tag{2.14}$$

c_i can be rearranged into a vector and this equation can be formulated into a matrix,

$$\begin{bmatrix} H_{11} - E\,S_{11} & H_{12} - E\,S_{12} & \ldots & H_{1N} - E\,S_{1N} \\ H_{21} - E\,S_{21} & H_{22} - E\,S_{22} & \ldots & H_{2N} - E\,S_{2N} \\ \ldots & \ldots & \ldots & \ldots \\ H_{N1} - E\,S_{N1} & H_{N2} - E\,S_{N2} & \ldots & H_{NN} - E\,S_{NN} \end{bmatrix} \begin{bmatrix} c_1 \\ c_2 \\ \ldots \\ c_N \end{bmatrix} = 0 \tag{2.15}$$

This equation is called *Hückel secular equation*. To have a non-zero solution c_i, the *secular determinant* must be zero,

$$\det | H_{i,j} - E\,S_{i,j} | = 0 \tag{2.16}$$

The full description of this equation is,

$$\begin{vmatrix} H_{11} - E\,S_{11} & H_{12} - E\,S_{12} & \ldots & H_{1N} - E\,S_{1N} \\ H_{21} - E\,S_{21} & H_{22} - E\,S_{22} & \ldots & H_{2N} - E\,S_{2N} \\ \ldots\ldots\ldots\ldots & & & \\ H_{N1} - E\,S_{N1} & H_{N2} - E\,S_{N2} & \ldots & H_{NN} - E\,S_{NN} \end{vmatrix} = 0 \tag{2.17}$$

To further simplify this equation, we make the following assumptions,

1. **Orthogonality of the overlap integral.** $|\varphi_i\rangle$ is chosen as the basis set for the construction of molecular orbitals. $S_{i,j}$ describes the overlap between the basis orbitals. LCAO theory assumes that the atomic orbitals are orthogonal,

$$S_{i,j} = \langle \varphi_i | \varphi_j \rangle = \begin{cases} 1, & \text{if } i = j \\ 0, & \text{if } i \neq j \end{cases} \tag{2.18}$$

This is not true for adjacent atoms that undergo bonding, the overlap integrals of which are on the order of 0.2-0.4. Such treatment can introduce acceptable error for ground state calculation, but is a poor approximation for excited state properties such as orbital energies and their relative arrangement. Some advanced theories, not under discussion here, will take this error into account at different degrees.

2. **Coulomb integral.** The matrix element $H_{i,j}$ is a constant value for all identical orbitals ($i = j$). We define

$$\alpha = \langle \varphi_i | \hat{H} | \varphi_i \rangle = \int \varphi_i H \varphi_i \, d\upsilon \tag{2.19}$$

which is referred to as the *Coulomb integral* or *site energy*. This quantity describes the energy of a bound electron in its orbital. This assumption is valid when a) all the energies of atomic orbitals are the same; b) the system is neutral, i.e. not ionic.

3. **Exchange Integral** When $i \neq j$ in $H_{i,j}$, we define

$$\beta = \langle \varphi_i | \hat{H} | \varphi_j \rangle = \int \varphi_i H \varphi_j \, d\upsilon \tag{2.20}$$

which is referred to as either the *exchange* or *resonance integral*, describing the energy gain arising from the interacting atoms next to each other in a bond.

These assumptions greatly simplify the secular equation to

$$\begin{vmatrix} \alpha - E & \beta & \dots & \dots & 0 \\ \beta & \alpha - E & \beta & \dots & 0 \\ \dots & \dots & \dots & \dots & \dots \\ \dots & \dots & \dots & \dots & \beta \\ 0 & \dots & \dots & \beta & \alpha - E \end{vmatrix} = 0 \tag{2.21}$$

If we define a variable $x = (\alpha - E)/\beta$, the formula is reformatted into

$$\begin{vmatrix} x & 1 & \dots & \dots & 0 \\ 1 & x & 1 & \dots & 0 \\ \dots & \dots & \dots & \dots & \dots \\ \dots & \dots & \dots & \dots & 1 \\ 0 & \dots & \dots & 1 & x \end{vmatrix} = 0 \tag{2.22}$$

This equation will give us N solutions with x values, from which we can obtain the energy of the molecular orbitals as $E_i = \alpha - x_i * \beta$.

For the simplest case, we take ethylene as an example when $N = 2$, shown in Fig.2.2. This gives a solution of $x = \pm 1$, thus $E = \alpha \mp \beta$. The gap between the states is 2β. We use the above notation $|\varphi_1\rangle$ and $|\varphi_2\rangle$ as the p_z of carbon atoms, and $|\psi_1\rangle$ and $|\psi_2\rangle$ as the molecular π-orbitals. The obtained normalised wavefunction is

$$|\psi_1\rangle = \frac{1}{\sqrt{2}}(|\varphi_1\rangle + |\varphi_2\rangle) \text{ and } |\psi_2\rangle = \frac{1}{\sqrt{2}}(|\varphi_1\rangle - |\varphi_2\rangle) \tag{2.23}$$

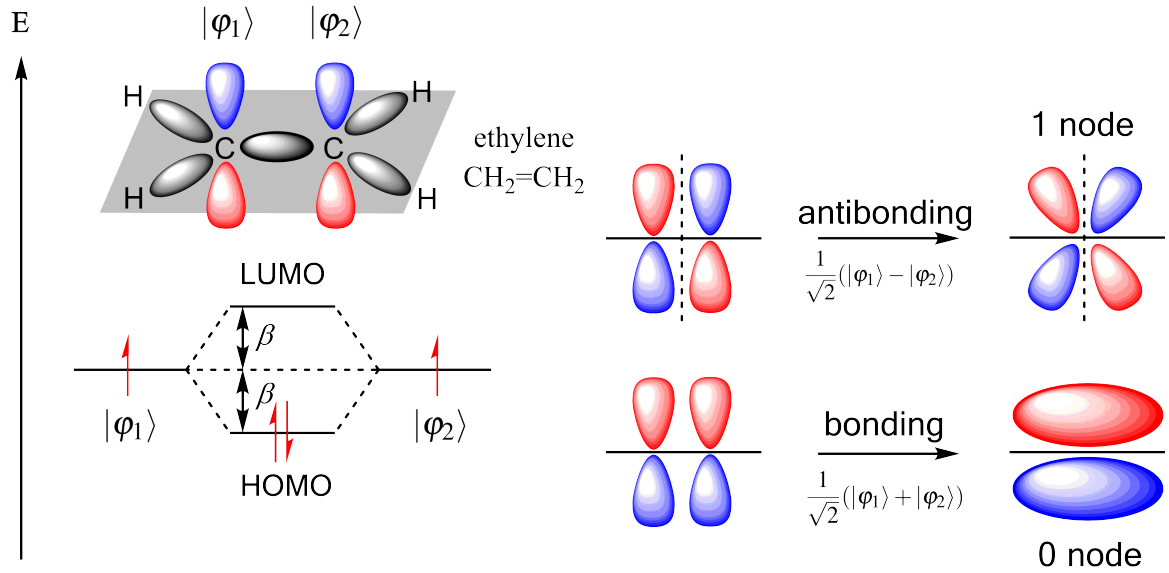

Fig. 2.2 Bonding and antibonding molecular orbitals of ethylene, obtained by linear (in-phase and out-of-phase) combinations of the p_z orbitals on the carbon atoms. Left panel: Carbon and hydrogen atoms are in the same plane. The remaining p_z orbitals ($|\varphi_1\rangle$ and $|\varphi_2\rangle$) are perpendicular to the plane formed by carbon and hydrogen atoms. The interaction between $|\varphi_1\rangle$ and $|\varphi_2\rangle$ give rise to HOMO and LUMO orbitals, separated by the interaction energy 2β. Right panel: electron distribution of anti-bonding orbitals where 1 node line exists, and bonding orbitals where zero node exists. Adapted from [16].

2.1.3 Molecular Orbital: Polyene

The Hückel model presents a semi-qualitative description of the formation of molecular orbitals constructed from atomic orbitals. To develop a deeper physical insight, we take probably the most classical example through the evolution of electronic properties of polyene following an increasing bonding length along the polymer backbone, and guide the final discussion briefly to the Bloch theory in the condensed matter context.

Ethylene only has two carbon atoms which are both sp^2-hybridised. There are 12 valence electrons, ten out of which are σ-electrons. Strong σ-bonds between the neighbouring carbons and their adjacent hydrogen atoms form the σ-plane. In this plane, σ-electrons exhibit a finite amplitude of electron density, while the two remaining π-electrons have zero density with its π-atomic orbital perpendicular to the σ-plane.

As discussed in the Hückel model, the in-phase combination $\frac{1}{\sqrt{2}}(|\varphi_1\rangle + |\varphi_2\rangle)$ gives the *highest occupied molecular orbital* (HOMO) of the ethylene. This doubly occupied π-molecular orbital is referred to as a *bonding* orbital due to an increase in the π electron density between the nuclei. Higher electron density pulls the two nuclei closer to each other, lowering the orbital energy. In the other case, the out-of-phase combination $\frac{1}{\sqrt{2}}(|\varphi_1\rangle - |\varphi_2\rangle)$ generates the *lowest unoccupied molecular orbital* (LUMO). This π^*-molecular orbital is *antibonding*, meaning reduced electron density between the nuclei so that the orbital energy is raised. This interaction results in a split of an energy that is twice the exchange integral β, as shown in Figure 2.2.

Now we can extend this method to a longer version of polyene. As shown in Figure 2.3, the bottom of the occupied states reaches a lower energy while the top of the occupied states arrives at a lower energy. The resultant gap between HOMO and LUMO is narrower, reaching 0 when $N = \infty$, and the bandwidth of the whole band becomes 4β. The occupied states make the π-band while the unoccupied states make the π^*-band. The molecular orbital of the lowest energy has the interaction between neighbouring atomic orbital as bonding, while the molecular orbital of the highest energy as antibonding. The HOMO is a state that bonding and antibonding interaction happen on double and single bonds, where LUMO corresponds to the interaction in which the bonding and antibonding happen on single and double bonds, respectively. If the bond length between neighbouring carbon atoms is the same, HOMO and LUMO has the exactly same situation thus their energy level is the same. There is a clear discrepancy with the fact that the infinite polymer (polyacetylene) has a bandgap.

Without putting in the π-electron in the molecular orbital, the σ-bond length between sp^2 carbon orbitals is nearly equal, on the order of 1.51 Å. When π-electrons are considered, electron distribution on the C-C bond is not uniform due to the electron-nucleus interaction.

The bonding orbital will pull together the nuclei. In HOMO, this effect appears as the alternation of double-like and single-like bonds - *bond-length alternation*, originating from the alternation of π-electron bond densities - *bond-order alternation*.

We show that the essence of double and single bond is the electron density between the bonding nuclei, and the bond length of double-like bond is $\sim$ 1.36Å and single-like bonds of $\sim$1.44 Å. This gives rise to a different exchange integral β of the bonding on double bond and single bond, in contrast to the assumption in Hückel model where we assume all bonds are of the same length, resulting in a single β for neighbouring atoms. HOMO has all the bonding orbitals on double bond and the antibonding orbitals on the single bond.

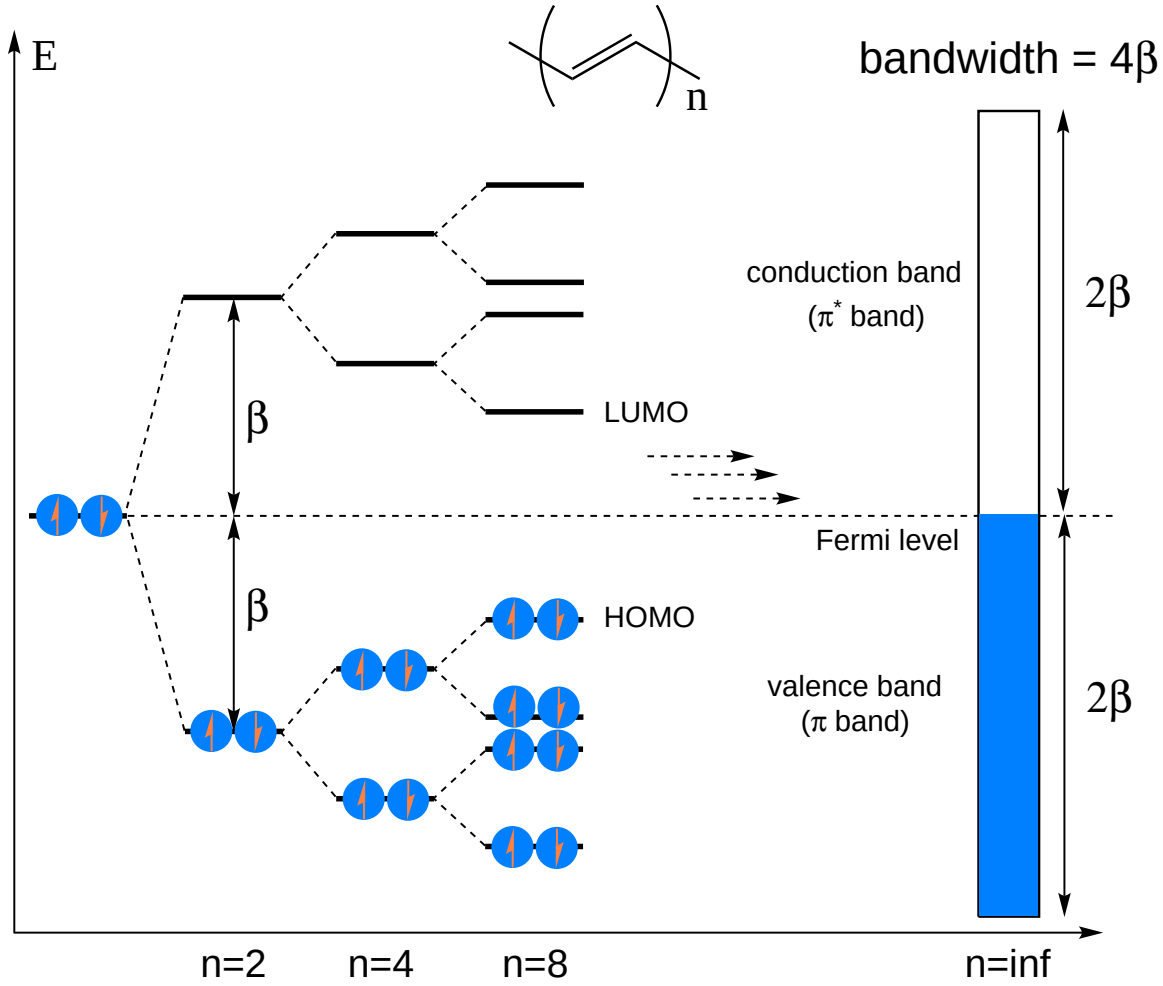

Fig. 2.3 Bonding and antibonding molecular orbitals of ethylene, butadiene and the conjugated polymer obtained by linear (in-phase and out-of-phase) combinations of the π-orbitals on the carbon atoms. The gap between HOMO and LUMO narrows when the chain length (N) increases. When N = ∞, the π band from the occupied states forms the valence band and the π^* band from the unoccupied band forms the conduction band. The bandwidth is four times the exchange energy β. Adapted from [16]

These discrete states changes into a band with a continuum energy spectrum. We thus can name the occupied band as the valence band and the unoccupied as the conduction band. The *Fermi level*, defined by the energy level at which 50% of the levels are occupied, sits at where these two bands cross.

Alternation of double and single bond benefits from the combination of co-planarity and the p_z of π-bond, the structure of which is termed *conjugation*. The much extended conjugation leads to the well-known polymer, polyacetylene. The pure form is not very electrically conductive, but the unintentionally iodine-doped polyacetylene was found to be conductive like metals. The discovery of conductive polymers was later awarded Nobel Prize in Chemistry at the right at the beginning of the new century.[12]

An important classification of organics is called conjugated aromatic compound; *aromatic* comes from the odour of these materials, as exemplified by its simplest example, benzene. Historically, the structure of benzene was discovered by a German chemist, Friedrich August Kekulé, whose intuition actually stemmed from in his dream in which a snake eating its own tail. Such understanding was formed in late nineteenth century, nearly half a century before the subject of quantum chemistry even existed. Now we understand that the overlapping neighbouring p_z orbitals result in a delocalised electron density distribution over the entire ring. This delocalised π-bond appears to be more stable than the case in which double and single bond alternate. Stacked benzene forms naphthalene, anthracene, tetracene, pentacene and hexane and so forth, named polyacenes or acenes. This series of materials have been researched for decades as molecular crystals, and still under heavy study in their amorphous state as semiconducting materials for optoelectronic devices.

The electronic properties of conjugated polymers is mainly determined by the properties of π electrons. The HOMO and LUMO are π- and π^*- orbitals, respectively, and therefore the transition from the filled to the unfilled orbital is named as $\pi \rightarrow \pi^*$ transitions, and is usually the lowest energy transition for the molecule. This energy in many materials lies in the energy range of visible light and can be optically accessed, and therefore it is also known as the *optical gap*.

2.1.4 Spin States: Singlet and Triplet

In the progression of atomic orbitals to molecular orbitals, we work out where a single electron can occupy a single molecular orbital. The next step is to describe the behaviour of a collection of electrons, as the electronic *states*. The *ground state* is a configuration where the arrangement of electrons possess the lowest energy. In closed-shell organic molecules, the orbitals are filled, and fully occupied orbital with the highest energy is termed as HOMO; LUMO is defined in the same vein. Excitation from HOMO to LUMO intially forms an exciton.

Excitons. Optical excitation, with energy larger than the bandgap, promotes one electron into the LUMO, thereby leaving a 'hole', i.e. a missing electron, on the HOMO. A similar excited state can be formed by electrically injecting an electron into the LUMO while extracting one from the HOMO in the device configuration where the active layer is sandwiched between electrodes. As electron and hole are oppositely charged, they experience an attractive force, forming a state of a bound electron-hole pair with a lower overall energy. Such one-quasi-particle state is termed as 'exciton' due to its neutral nature to its surroundings. The low dielectric constant of the organic materials ($\varepsilon_r \approx 3.5$) gives a high exciton binding energy between 0.2-0.5 eV.[17] This type of exciton is named as *Frenkel exciton*. In contrast, the dielectric constant in inorganic semiconductors is much higher ($\varepsilon_r \approx 10-20$), so that the Coulomb attraction is effectively screened. Excitation from valence band to conduction band results in immediate generation of free charges at room temperature. The so-called *Wannier-Mott excitons* are usually observed at low temperatures of a few Kelvin.

Identical particles. Identical particle, an important concept in quantum mechanics, represents indistinguishable particles in a quantum system. Here, we start from a system of two electrons. The electron wavefunction is defined as $\phi(q)$, where q includes spatial and spin coordinates, thus a time-independent system can be fully described as $\psi(q_1,q_2)$. These two electrons are *identical*, meaning that the probability of finding electron 1 at q_1 and electron 2 at q_2 must be the same as the probability density for finding electron 1 at q_2 and electron 2 at q_1. This can be expressed by

$$|\psi(q_1,q_2)|^2 = |\psi(q_2,q_1)|^2 \tag{2.24}$$

These two functions at most differ by a phase factor, and it is easy to get their relationship,

$$\begin{aligned} \psi(q_1,q_2) &= \psi(q_2,q_1) \text{ symmetric} \\ \psi(q_1,q_2) &= -\psi(q_2,q_1) \text{ antisymmetric} \end{aligned} \tag{2.25}$$

This relationship represents *definite exchange symmetry*, a property that ensures that identical particles cannot be distinguished. The exchange symmetry of a system of identical particles is closely related to the spin of particles. The wavefunction of a system composed of particles (such as photons and phonons) with integer spin is symmetric while for electrons with spin of 1/2 the wavefunction is antisymmetric.

Pauli exclusion principle. Without the consideration of electron-electron interaction, let us assume the electron 1 is in state k_1 and the electron 2 in state k_2. We need to construct a wavefunction of the system being antisymmetric (labelled as the superscript A).

$$\begin{aligned}\psi^A_{k_1k_2}(q_1,q_2) &= \frac{1}{\sqrt{2}}[\phi_{k_1}(q_1)\phi_{k_2}(q_2)-\phi_{k_1}(q_2)\phi_{k_2}(q_1)] \\ &= \frac{1}{\sqrt{2}}\begin{vmatrix}\phi_{k_1}(q_1) & \phi_{k_1}(q_2)\\ \phi_{k_2}(q_1) & \phi_{k_2}(q_2)\end{vmatrix}\end{aligned} \tag{2.26}$$

If $k_1 = k_2$, $\psi^A_{k_1k_2}(q_1,q_2) = 0$, meaning that this state does not exist. This leads to the famous *Pauli exclusion principle*, stating that two identical fermions cannot occupy the same state. We note that this does not exclude the possibility that two states are in degeneracy where two states are singly occupied by two electrons, which is the case for molecular oxygen.

Without consideration of spin-orbital coupling, the wavefunction should be separable into space wavefunction and spin wavefunction.

Spin of two correlated electrons. The spin angular momentum for q-th electron is $\hat{S}_q (q = 1 \text{ and } 2)$. The total spin angular momentum of the two-electron system is

$$\hat{S} = \hat{S}_1 + \hat{S}_2 = \sum_i \hat{S}_i = \sum_i \hat{S}_{1i} + \hat{S}_{2i}, i = x, y, and\, z \tag{2.27}$$

We also define

$$\hat{S}^2 = \sum_{i=1}^{3} \hat{S}_i^{\,2}, i = x, y, and\, z \tag{2.28}$$

In one-electron case, the spin eigenfunction for $\hat{S_{qz}}$ is $|\uparrow_q\rangle$ and $|\downarrow_q\rangle$. In the two-electron system, the eigenfunctions for $(\hat{S_{1z}}, \hat{S_{2z}})$ can be $|\uparrow_1\uparrow_2\rangle$, $|\uparrow_1\downarrow_2\rangle$, $|\downarrow_1\uparrow_2\rangle$, and $|\downarrow_1\downarrow_2\rangle$. Among them, $|\uparrow_1\downarrow_2\rangle$ and $|\downarrow_1\uparrow_2\rangle$ are not exchange symmetric, but their linear combination generate wavefunction that has certain exchange symmetry, $\frac{1}{\sqrt{2}}(|\uparrow_1\downarrow_2\rangle + |\downarrow_1\uparrow_2\rangle)$ and $\frac{1}{\sqrt{2}}(|\uparrow_1\downarrow_2\rangle - |\downarrow_1\uparrow_2\rangle)$. However, these two wavefunctions are not eigenfunctions of $\hat{S_{1z}}$ because

$$\hat{S_{1z}}\frac{1}{\sqrt{2}}(|\uparrow_1\downarrow_2\rangle \pm |\downarrow_1\uparrow_2\rangle) = \frac{\hbar}{2\sqrt{2}}(|\uparrow_1\downarrow_2\rangle \mp |\downarrow_1\uparrow_2\rangle) \tag{2.29}$$

This superposition state is called *quantum entanglement* as it cannot be expressed as a product of individual electron spin wavefunction.

We find these four wavefunctions are eigenfunctions of $\hat{S}_z$

$$\begin{aligned}
\hat{S}_z|\uparrow_1\uparrow_2\rangle &= \frac{\hbar}{2}|\uparrow_1\uparrow_2\rangle \\
\hat{S}_z|\downarrow_1\downarrow_2\rangle &= -\frac{\hbar}{2}|\downarrow_1\downarrow_2\rangle \\
\hat{S}_z\frac{1}{\sqrt{2}}(|\uparrow_1\downarrow_2\rangle + |\downarrow_1\uparrow_2\rangle) &= 0 \\
\hat{S}_z\frac{1}{\sqrt{2}}(|\uparrow_1\downarrow_2\rangle - |\downarrow_1\uparrow_2\rangle) &= 0
\end{aligned} \tag{2.30}$$

Also, we can verify that they are eigenfunction of $\hat{S}^2$

$$\begin{aligned}
\hat{S}^2|\uparrow_1\uparrow_2\rangle &= 2\hbar^2|\uparrow_1\uparrow_2\rangle \\
\hat{S}^2|\downarrow_1\downarrow_2\rangle &= 2\hbar^2|\downarrow_1\downarrow_2\rangle \\
\hat{S}^2\frac{1}{\sqrt{2}}(|\uparrow_1\downarrow_2\rangle + |\downarrow_1\uparrow_2\rangle &= 2\hbar^2\frac{1}{\sqrt{2}}(|\uparrow_1\downarrow_2\rangle + |\downarrow_1\uparrow_2\rangle \\
\hat{S}^2\frac{1}{\sqrt{2}}(|\uparrow_1\downarrow_2\rangle - |\downarrow_1\uparrow_2\rangle &= 0
\end{aligned} \tag{2.31}$$

Therefore we can use $(\hat{S}^2, \hat{S}_z)$ as a complete set to describe the total spin wavefunction.

Singlet and triplet state. From the complete set, we can use the a set of quantum numbers $|S, M_s\rangle$ (S for $\hat{S}^2$ and M_s for $\hat{S}_z$) to represent the eigenfunctions,

$$\begin{aligned}
\textbf{Singlet}(S=0): &\quad |0,0\rangle = \tfrac{1}{\sqrt{2}}(|\uparrow_1\downarrow_2\rangle - |\downarrow_1\uparrow_2\rangle) \\
\\
&\quad |1,+1\rangle = |\uparrow_1\uparrow_2\rangle \\
\textbf{Triplet}(S=1): &\quad |1,0\rangle = \tfrac{1}{\sqrt{2}}(|\uparrow_1\downarrow_2\rangle + |\downarrow_1\uparrow_2\rangle) \\
&\quad |1,-1\rangle = |\downarrow_1\downarrow_2\rangle
\end{aligned} \tag{2.32}$$

The anti-symmetric spin wavefunction has one state and the symmetric spin wavefunction has three states. As Hamiltonian only depends on spatial coordinates and not spin, we immediately conclude that these three states are degenerate - even when taking into account of the electron-electron interaction. From spectroscopic parlance, the three degenerate states are termed a *triplet*, and the unique state is called a *singlet*.

Spatial wavefunction. As the total wavefunction, a product of spatial wavefunction and spin wavefunction, must be antisymmetric, the spatial wavefunction of singlet is symmetric

and that of triplet is antisymmetric. The spatial wavefunction can be written as

$$\begin{aligned}\psi_S = \psi^S_{k_1,k_2}(r_1,r_2) = \frac{1}{\sqrt{2}}(\phi_{k_1}(r_1)\phi_{k_2}(r_2) + \phi_{k_2}(r_1)\phi_{k_1}(r_2)) \\ \psi_T = \psi^A_{k_1,k_2}(r_1,r_2) = \frac{1}{\sqrt{2}}(\phi_{k_1}(r_1)\phi_{k_2}(r_2) - \phi_{k_2}(r_1)\phi_{k_1}(r_2))\end{aligned} \tag{2.33}$$

It is important to note that the influence of the spin is indirect which constrains the symmetry of the spatial wavefunction.

Energy of singlet and triplet states. Once electron-electron interaction is taken into account, singlet and triplet states have different energies. In a simple way to understand their energetics, for the same position, $r_1 = r_2$,

$$\begin{aligned}\psi_S(r_1,r_1) = \sqrt{2}\phi_{k_1}(r_1)\phi_{k_2}(r_1) \neq 0 \\ \psi_T(r_1,r_1) = 0\end{aligned} \tag{2.34}$$

Because electrons repel each other more when they are closer, we expect the singlet to have more electron-electron repulsion with a higher energy. One of *Hund's rules* says that, for degenerate non-interacting states, the configuration with highest spin multiplicity lies lowest in energy.

We will give a more strict understanding of their energetics below. The Hamiltonian does not contain spin coordinate thus the energy of the system is not relevant to the spin state, and only depends on its spatial wavefunction. To consider the electron-electron interaction, the Coulomb interaction is added into the system energy. We create the following notation,

$$\begin{aligned}\psi_S = \frac{1}{\sqrt{2}}(\phi_{k_1}(r_1)\phi_{k_2}(r_2) + \phi_{k_2}(r_1)\phi_{k_1}(r_2)) \equiv \frac{1}{\sqrt{2}}(k_1k_2 + k_2k_1) \\ \psi_T = \frac{1}{\sqrt{2}}(\phi_{k_1}(r_1)\phi_{k_2}(r_2) - \phi_{k_2}(r_1)\phi_{k_1}(r_2)) \equiv \frac{1}{\sqrt{2}}(k_1k_2 - k_2k_1)\end{aligned} \tag{2.35}$$

The related energy is

$$\begin{aligned}\text{Singlet} \quad \Delta E = \langle k_1k_2 + k_2k_1|V|k_1k_2 + k_2k_1\rangle = \\ \langle k_1k_2|V|k_1k_2\rangle + \langle k_2k_1|V|k_1k_2\rangle + \langle k_1k_2|V|k_2k_1\rangle + \langle k_2k_1|V|k_2k_1\rangle \\ \text{Triplet} \quad \Delta E = \langle k_1k_2 - k_2k_1|V|k_1k_2 - k_2k_1\rangle = \\ \langle k_1k_2|V|k_1k_2\rangle - \langle k_2k_1|V|k_1k_2\rangle - \langle k_1k_2|V|k_2k_1\rangle + \langle k_2k_1|V|k_2k_1\rangle\end{aligned} \tag{2.36}$$

We define $J_{12} = \langle k_1 k_2 | V | k_1 k_2 \rangle$ as *Coulomb integral* and $K_{12} = \langle k_1 k_2 | V | k_2 k_1 \rangle$ as *exchange integral*. As $V(|r_1 - r_2|)$ is exchange symmetric, we can obtain that $J_{12} = J_{21}$ and $K_{12} = K_{21}$. Both J_{12} and K_{12} are positive as they arise from electron-electron repulsion. We thus get

$$\begin{aligned} \text{Singlet} \quad & \Delta E = J_{12} + K_{12} \\ \text{Triplet} \quad & \Delta E = J_{12} - K_{12} \end{aligned} \tag{2.37}$$

We can see that singlet state is higher in energy than the triplet sate. The energy difference, defined as the exchange energy is ΔE_{ST}, is equal to $2K_{12}$. To the first order approximation, this exchange energy scales with the overlap of HOMO and LUMO. In organic polymers, the HOMO-LUMO overlap is usually significant, leading to typical exchange energies of 0.6-1.0 eV,[18] while it can be quite small for molecules with a certain symmetry, e.g. close to 0.3 eV in C_{60} fullerenes.

Singlet fission, a process that converts one singlet exciton into two triplet excitons, has the potential to break the Shockley-Queisser limit in the photovoltaic technology.[19] The energetic consideration requires the energy of the triplet state is near half of the singlet state. The mechanism of singlet fission is gradually being elucidated.[19, 20] In another perspective, such process can be regarded as a black box and further innovation of utilizing these triplet states in the device is also challenging. Recently, Baldo et al. demonstrated triplet harvesting in silicon solar cell at an efficiency of 133%, bringing this concept into real-world application.[21]

In OLEDs, harvesting 75% of the formed excited states, triplet states, is the key to improve the device efficiency. A new class of materials with a 0.1 eV ΔE_{ST} pioneered by Chihaya Adachi, used in OLEDs, have the ability to efficiently convert triplet into singlet states, a process called *thermally activated delayed fluorescence* (TADF).[22] This mechanism has its unique strength to address the efficient and narrowband blue emitters.[23] Singlet fission is also introduced in OLED and has a promise to increase the quantum efficiency to 125% by directly converting singlets to triplets, and even to 200% in a complex system which combines TADF as singlet fission sensitiser.[24]

2.1.5 Spin States: Doublet

For closed-shell molecules, the molecular orbitals are doubly occupied by electrons with opposite spin, resulting in the ground state of singlet. Open-shell molecules have unpaired electrons in the ground state. The molecular orbital with an unpaired electron forms a radical centre. For two degenerate molecular orbitals, they can be individually filled by one electron, forming diradical. Diradicals are usually a triplet state with a lower energy than its singlet form, like O_2. For the system with an unpaired electron, the electron spin can be either up or down, resulting in a spin multiplicity of two, termed *doublet*. The frontier orbital is called singly occupied molecular orbital, or the degenerate state, singly unoccupied molecular orbital. The unpaired electron usually causes the instability of molecules and thus radicals are usually used as intermediate products in chemistry synthesis, not as active materials in organic electronics.

Recently, radical-based material has seen breakthrough both in stability and optoelectronic applications. A relatively stable carbon radical, called tris(2,4,6-trichlorophenyl)methyl (TTM), was synthesised in 1987, but the application of this type of materials into light emission was missing for a long time.[25] The idea of applying radicals into emission is pioneered by Prof. Feng Li from Jilin University, who demonstrated the first radical-based OLED in 2015.[26] A milestone was the demonstration of a record efficiency above 25% at 710 nm by adopting the donor-acceptor strategy, much higher than other infrared lighting technologies.[27] The emission mechanism is the transistion from a doublet excited state (D_1) to the doublet ground state (D_0), shown in Figure.2.4. To form D_1 under electrical injection, the electrons need to be injected into singly occupied molecular orbital and holes injected into HOMO, forming the electron distribution in Figure.2.4. The stability of these D-A type materials is much better than the TTM itself, which was partly due to the SOMO level lying below the HOMO level.[28]

In addition to the heavily researched single and triplet states, the doublet state has important implications for the photophysics of organic materials, and open up new possibilities for studying the fundamental science of excitons.

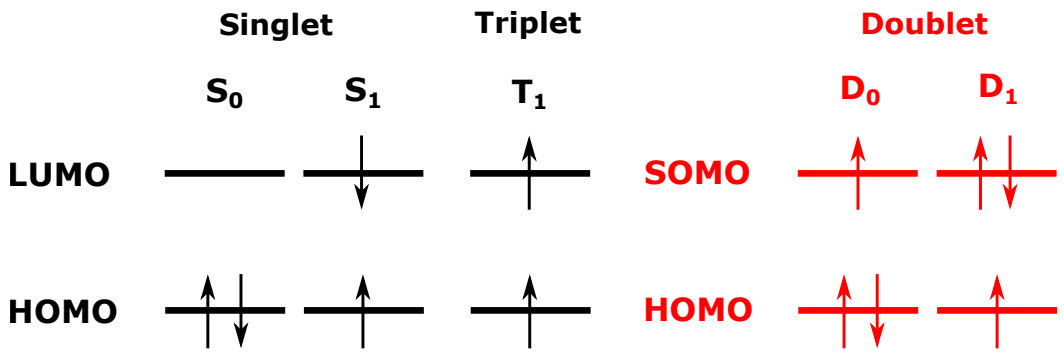

Fig. 2.4 Electron distribution in frontier energy levels of singlet, doublet and triplet states. Singlet ground state (S_0) has two electrons with opposite spin in HOMO; singlet and triplet excited states (S_1 and T_1) with two electrons in HOMO and LUMO have a total spin of 0 and 1 respectively. The doublet ground state (D_0) and excited state (D_1) have only one electron with a spin of 1/2. The lowest-energy transition is from HOMO to SOMO.

2.1.6 Charge

Following photo-excitation and exciton dissociation, the electron or hole on the molecule (polaron) is the precursor for photocurrent generation in OSCs. The ability of charges to move in the film is mainly governed via a hopping mechanism between adjacent molecules, in contrast to band transport in silicon. Therefore the charge mobility in organic films is several orders of magnitude lower than inorganic counterparts, which intrinsically limits the active layer thickness to several hundred nm, much thinner than Si or perovskite films.

In organic molecules, the ground state of a molecule is usually neutral without positive or negative charges. Additional electrons or holes can be introduced to the LUMO or the HOMO, respectively, either from injection from an electrode, charge transfer from another material, or chemical doping of the material. A free charge on the organic molecule or polymer can polarise its surroundings, distorting the molecular arrangement and lowering the overall energy. This interaction is treated as a quasi particle called a 'polaron'. Polarons also exist in inorganic semiconductors where the crystal lattice gets deformed by a localised charge.[29]

A single carrier added onto the polymer chain generates a spin - 1/2 polaron. Due to polaronic relaxation, two localised transitions in the bandgap form, donated as P_1 and P_2, shown in Figure.2.5.The P_1 and P_2 transitions are observable in the transient absorption spectra. Another way to delocalise these charge carriers is to optically induce this transition, resulting in vibrationally hot states[30]. Such extra energy may help couple certain electronic transitions, and is the basis of the pump-push photocurrent spectroscopy. We also note that bipolaron (two polarons in one molecule), electron paramagnetic resonance (EPR) inactive

species, is also reported by electrochemical doping in P3HT.[31] To determine if a certain transition is singlet, doublet or triplet, the g factor from EPR measurements can be used.[32]

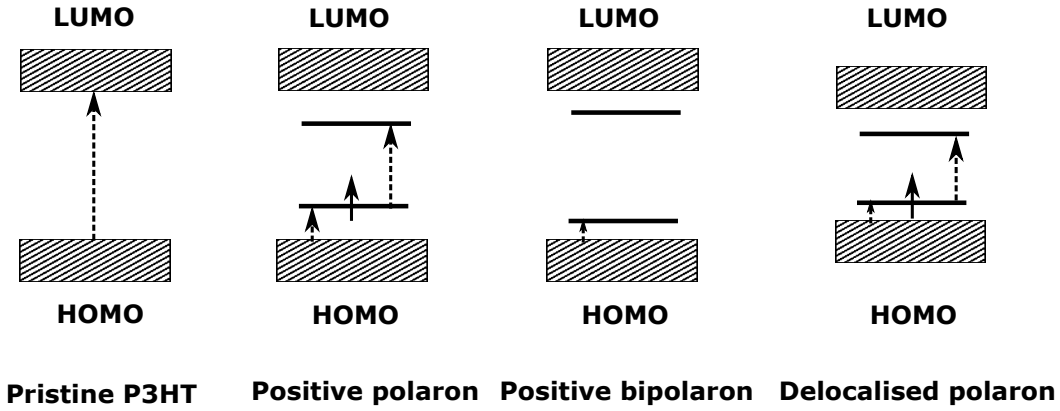

Fig. 2.5 The optical transition in P3HT as an example: the HOMO to LUMO transition in pristine material; positive polaron related transition; positive bipolaron; delocalised polaron from the ordered lamellar packing. Adapted from [31].

2.2 Optical Transitions between Molecular States

Having established how atomic orbitals combine to form molecular orbitals, ad how molecular orbitals are filled to form molecular states, we will now focus on how transitions occur between molecular states, starting from the absorption of light.

2.2.1 Born-Oppenheimer Approximation

The adiabatic Born-Oppenheimer approximation uses the great disparity between electron and nuclear mass, meaning that electrons respond spontaneously to a change in nuclear motion while the nucleus takes time to adjust following electronic excitation. A *adiabatic* process happens without exchange of heat or mass of substances between a thermodynamic system and its surroundings. The change in the nucleus position is reflected on the work being done on the molecular shape, without an abrupt change in electronic configuration. Electrons experience a static potential created from the nuclear configuration, which can be described as a potential energy surface (PES). The consequence of adiabatic Born-Oppenheimer approximation is that two energy surfaces can never cross, meaning that electrons cannot change their states just through nuclear motion. There are cases when this approximation does not hold, namely, when there is coupling between nuclear and electronic coordinates, also known as vibronic coupling.[33] As a result, the electronic wavefunction is worked out using static nuclear coordinates and the nuclei are regarded as moving in PES of an electronic state as a function of nuclear coordinates. The overall wavefunction can be separated into an electronic and a nuclear part as well as the electron spin:

$$\psi_{total} = \psi_{el}\psi_{vib}\psi_{spin} \tag{2.38}$$

2.2.2 Fermi's Golden rule

Paul Dirac developed a framework to calculate transition probabilities from an initial state to a continuum of states under the perturbation of Hamiltonian $\hat{H}_I$. The main result is known as *Fermi's Golden Rule*,

$$k_{i\to f} = \frac{2\pi}{\hbar}\rho|\langle\psi_f|\hat{H}_I|\psi_i\rangle|^2 \tag{2.39}$$

where ρ is the density of the final states, ψ_i and ψ_f the wavefunction of the initial and final states, respectively. This transition probability depends on the overlap between wavefunctions of initial and final wavefunctions after perturbation by an electric field. The incident electromagnetic wave only causes the electrons to move in resonance. The nuclei are too slow to respond on the time scale of the oscillations. Spins are not influenced by the changing

electric field but are affected by the changing magnetic field, which is too small to have any effect. This leads to an expression into different categories,

$$k_{i\to f} = \frac{2\pi}{\hbar}\rho |\langle \psi_{el,f}|\hat{H}_I|\psi_{el,i}\rangle|^2 |\langle \psi_{vib,f}|\psi_{vib,i}\rangle|^2 |\langle \psi_{spin,f}|\psi_{spin,i}\rangle|^2 \tag{2.40}$$

For an allowed transition all three items must be non-zero. The rate of an optical transition therefore depends on three factors: the electronic factor, the vibrational factor, and the spin factor. We will discuss each in turn.

2.2.3 The Electronic Factor: Conservation of Symmetry

The interaction Hamiltonian is equal to

$$\hat{H}_I = -q\sum_i \hat{r}_i \cdot E\cos(\omega t) = \hat{\mu}\cdot E\cos(\omega t) \tag{2.41}$$

where $\hat{\mu}$ is the dipole moment operator. By definition, $\hat{\mu} = e\hat{r}$, thus it changes its sign with respect to spatial inversion. To zero order approximation, the rate of an electronic transition depends on the spatial overlap between initial and final state wavefunctions and the transition dipole moment. The transition dipole moment is the oscillating electric dipole moment for a given transition. The initial and final states must be of opposite symmetry under spatial inversion if the total transition rate is to be non-zero. The symmetry of a state is determined from how it responds to certain symmetry operations in group theory. Here, we only concern about the inversion symmetry, or parity. The molecules for photovoltaic applications in this thesis are not so related to symmetrical issue, but some project (not shown here) needs to consider the symmetry effect, thus some discussion about symmetry is still included. As *Laporte selection rule* states, for centrosymmetric molecules with an inversion centre, the allowed transition must involve a change in parity, either from *g* (*gerade* = even (German)) to *u* (*ungerade* = odd), or vice versa.

For example, in a system with an even number of π-electrons, the ground state can be symmetric under symmetry operation, and is defined as $^1\mathrm{A_g}$. A or B specify the symmetry or asymmetry of the states under certain transformations in group theory; the subscript *g* or *u* defines the parity of the state; the superscript 1 or 3 designates that the state is a singlet state with spin 0, or a triplet state with spin 1. Therefore, only *u*-excited states appear in the absorption spectrum. $g \to g$ transition can occur via an intermediate or virtual state in the case of two photon absorption. Further we can see the integral also scales with the transition dipole momentum along the molecular axis, which could result in stronger absorption and emission in oligomers with longer chains.

However, we note that forbidden transitions are allowed if the centre of symmetry is disrupted. The symmetry breaking can be due to Jahn-Teller effect, describing the geometrical distortion of molecules with a spatially degenerate electronic ground state. This effect removes the degeneracy and lowers the overall energy, and is often observed in transition-metal complexes and also the novel organic-inorganic perovskites Another possible mechanism is vibronic coupling that induces asymmetric vibrations of a molecule so that some forbidden transitions are weakly allowed.

The transitions between orbitals, which are centred on the same part of the molecule (eg. $\pi \rightarrow \pi^*$), are more intense than those transitions between orbitals that occupy different spaces (eg. charge-transfer transition, $n \rightarrow \pi^*$ transitions or metal-to-ligand charge-transfer transitions) due to the wavefunction overlap.

2.2.4 The Vibrational Factor: Phonon Coupling

The electronic transitions control the overall transition intensity (allowed, forbidden or somewhere between), while the spectral shape of absorption and emission is controlled by the vibrational term $|\langle \psi_{vib,f} | \psi_{vib,i} \rangle|^2$, the so-called Franck-Condon factor.

Following the same assumption as the Born-Oppenheimer approximation, the *Franck-Condon principle* states that all optical transitions between molecular states occur without change in nuclear coordinate $\mathbf{Q}$. As optical absorption happens within 1 fs, the nuclear arrangement is not fast enough to respond. The generated 'hot' (energetically higher) excited states relax via the vibrational manifold at sub-ps to a new equilibrium of the excited state, termed as internal conversion.

From the Born-Oppenheimer approximation, we know that the electronic states can be represented in a two-dimensional diagram of nuclear coordinate $\mathbf{Q}$ and energy E. Figure.2.6 also illustrates that each electronic state is composed of many vibrational levels that are equally separated by the vibrational energy. The optical transition can be viewed as a vertical line in the PES diagram. From this diagram, the energy minima of ground state and excited states are separated by $\Delta\mathbf{Q}$. This change of nuclear coordinate is due to change in bond orders and electron density, which can shift the wavefunction of vibrational states that have a significant effect on the vibrational wavefunction overlap integral, *Franck-Condon factor*. In the case of $\Delta\mathbf{Q} = 0$ for highly rigid molecules, the transition between the lowest vibrational levels $S_{0,0} \rightarrow S_{1,0}$ would dominate. When $\Delta\mathbf{Q}$ increases, the integral maximum will shift to higher vibrational level for absorption and for emission.

The nuclear reorganisation leads to dissipation of heat as phonon emission (quanta of lattice vibrations), relaxing to the lowest vibrational level before the emission occurs. The emission spectra can be viewed as a mirror image of the absorption spectrum, constructed

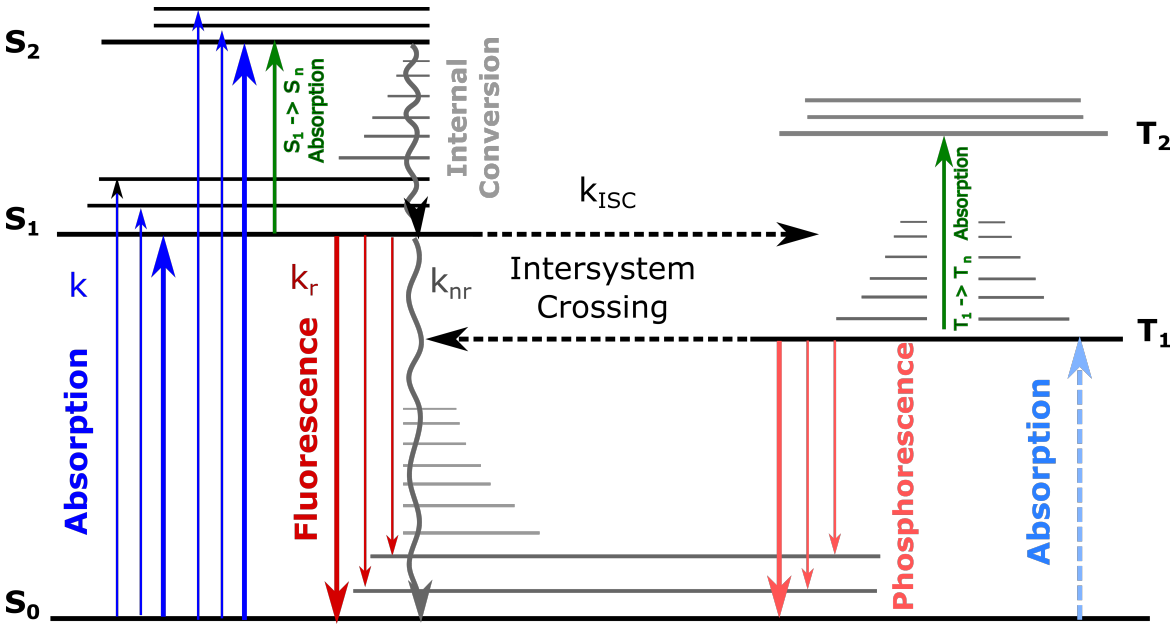

Fig. 2.6 Electronic energy levels of singlets and triplets and related optical transitions in a conjugated organic molecule. Absorption from the ground state S_0 (blue arrow) gives rise to a higher-lying singlet state S_n, which relaxes via ultrafast non-radiative relaxation, termed as internal conversion (grey arrows), to the lowest vibrational level of S_1. Intersystem crossing between the spin singlets and spin triplets is expressed by dashed grey arrows and can generate triplet population on the molecules, as the triplet state T_1 is lower in energy than S_1. Emission (red arrows) can occur from lowest energy level within each spin-manifold. Emission from S_1 and T_1 are called fluorescence and phosphorescence, respectively. Additional absorption from excited states (green arrows) within the corresponding spin manifold are called photo-induced absorption, if originating from an optical absorption. Figure adapted from Andreas Jakowetz.[34].

similarly from the transitions from the lowest excited vibrational state $S_{1,0}$ to the manifold of the ground electronic state $S_{0,m}$. The energy dissipation from the dominant transitions following absorption and emission is known as *reorganisation energy* λ.

Even though multiple modes usually exist in the molecular motion, we only consider one vibrational mode at frequency of ω here to simply the expression. The intensities of the individual optical transitions can be calculated as

$$\begin{aligned} I_{PL}(\hbar\omega) &= [k(\hbar\omega)\cdot\hbar\omega]^3 \cdot \sum_n \frac{S^n}{n!} e^{-S} \cdot \Gamma \cdot \delta(\hbar\omega - (\hbar\omega_0 - m\hbar\omega_n)) \\ I_{abs}(\hbar\omega) &= [k(\hbar\omega)\cdot\hbar\omega] \cdot \sum_m \frac{S^m}{m!} e^{-S} \cdot \Gamma \cdot \delta(\hbar\omega - (\hbar\omega_0 + n\hbar\omega_m)) \end{aligned} \tag{2.42}$$

where $n, m = 0, 1, 2, \cdots$ define the vibrational quanta of the excited state and ground state, respectively; $k(\hbar\omega)$ the refractive index of the transition energy; $\hbar\omega$ energy of the electronic

transition; $\hbar\omega_0$ energy of the $S_{1,0} \leftarrow S_{0,0}$ transition; S the Huang-Rhys factor for mode ω; Γ the lineshape function either a Gaussian, a Lorentzian or a linear combination of both.

This expression can easily explain the mirror image between absorption and emission, and S can be obtained from the ratio intensities between $S_{1,1} \leftarrow S_{0,0}$ and $S_{1,0} \leftarrow S_{0,0}$. From the experiment, we use this equation to approximate S. The energy spacing between the $S_{1,0} \leftarrow S_{0,0}$ absorption and $S_{1,0} \rightarrow S_{0,0}$ emission is defined as the *Stokes Shift*.

The central term is the Huang-Rhys factor S, related to change of nuclear coordinate $\Delta\mathbf{Q}$

$$S = \frac{M\omega}{2\hbar}(\Delta\mathbf{Q})^2 \tag{2.43}$$

where M is the reduced mass of the vibrating system; $\Delta\mathbf{Q}$ the movement of nuclear coordinate in relaxation. *Huang-Rhys factor* expresses the strength of the electron-vibrational coupling interaction, and has a link with the dominant vibrational level of all vibronic transitions,

$$\lambda = S\hbar\omega = n\hbar\omega \tag{2.44}$$

n corresponds to the most possible transition.

2.2.5 The Spin Factor: Conservation of Spin

For pure states with a spin multiplicity, the spin integral $|\langle\psi_{spin,f}|\psi_{spin,i}\rangle|^2$ is 1 if the initial and final spin states are equal, and 0 if they are not. This spin selection rule tells that transitions between singlet states or triplet states are spin-allowed, such as $S_1 \leftarrow S_0$, $S_n \leftarrow S_1$ and $T_n \leftarrow T_1$; transitions between singlet and triplet states are spin-forbidden, such as $T_1 \rightarrow S_0$. Nevertheless, weak luminescence from triplet states is observed and termed *phosphorescence* ($T_1 \rightarrow S_0$). Phosphorescence happens at a much slower rate than $S_1 \rightarrow S_0$ transition, the *fluorescence*. Such apparent violation of the spin selection rule is due to a ubiquitous phenomenon that allows the triplet state to gain certain character from the singlet state.

The single-triplet mixture can be formed when the system is perturbed by a mechanism, *spin-orbital coupling* (SOC). This mechanism is based on the principle of the conservation of momentum, saying that a change in the spin angular momentum s can be compensated by a change in an opposite change in the orbital angular momentum l, if the total angular momentum does not change, $j = l + s$. If the energy associated with SOC is small compared to the total energy of the system, the effect of SOC on the state wavefunction can be described in the framework of perturbation theory. For example, the triplet state can be mixed with

multiple singlet states,

$$|T_1^{'}\rangle = |T_1\rangle + \sum_k \frac{\langle S_k|\hat{H}_{SO}|T_1\rangle}{E(T_1) - E(S_k)} |S_k\rangle \tag{2.45}$$

where $|T_1^{'}\rangle$, $|T_1\rangle$ and $|S_k\rangle$ are the perturbed triplet excited state, the pure triplet excited state and k-th pure singlet excited state, respectively. Similarly, ground singlet state can be perturbed by multiple higher-lying triplet states,

$$|S_0^{'}\rangle = |S_0\rangle + \sum_k \frac{\langle T_k|\hat{H}_{SO}|S_0\rangle}{E(S_0) - E(T_k)} |T_k\rangle \tag{2.46}$$

where $|S_0^{'}\rangle$, $|S_0\rangle$ and $|T_k\rangle$ are the perturbed singlet ground state, the pure singlet ground state and k-th pure triplet excited state, respectively. The energy separation between the singlet ground state and high-lying triplet states are large that the triplet mixing in the singlet ground state is very small. However, this small mixing of singlet character into the triplet state is enough to make the $T_1^{'} \rightarrow S_0$ weakly allowed. In organic molecules, the slow radiative transition rate makes the triplet really long-lived in the absence of strong non-radiative recombination.

From the above equations, the admixture of singlet to the triplet state depends not only on the energy separation, but also depends on the magnitude of SOC. For organometallic complexes, such as iridium-complexes for phosphor OLEDs, the inclusion of heavy metals greatly enhance the SOC. This *heavy metal effect* facilitates the mixed triplet state with singlet states, thus accelerates the ISC rate, finally enabling larger radiative recombination rate to compete with its non-radiative channel. It is encouraging to see that for many materials this non-radiative transition can be minimal, and we will understand such non-radiative channels in the next section.

2.2.6 Interconversion of Excited States

In the previous section, we have discussed the absorption and radiative decay transitions between the ground state and excited states. Excited states can also interconvert, for example between S_n and S_1, and between S_1 and T_1, through isoenergetic non-radiative transition. *Internal conversion* connects two electronic states of the same spin via the isoenergetic point, and is usually followed by a fast dissipation of heat in the electronic state via vibrational relaxation. For example, conversion from the zeroth vibrational level of a high-lying singlet state S_n to the k-th vibrational level of S_1. A similar non-radiative recombination mechanism is called *intersystem crossing* (ISC). This process is much slower than internal conversion as it requires a spin flip. A typical example is $S_1 \rightarrow T_1$ transition. ISC can also occurs in

the reverse direction, ie. $S_1 \leftarrow T_1$. When the energy separation of S_1 and T_1 is small, the thermal activation of T_1 to a vibrational level that has the same energy of S_1 efficiently drive the emission from S_1, known as TADF process.

The competition between the non-radiative transitions and radiative transitions determines the *photoluminescence quantum yield* (PLQY),

$$\text{PLQY} = \frac{k_{rad}}{k_{rad} + k_{non-rad}} \tag{2.47}$$

To calculate the non-radiative transitions, we have to go beyond the Born-Oppenheimer approximation. We can obtain a similar expression but spin and electronic term cannot be separated,

$$k_{i\to f} = \frac{2\pi}{\hbar}\rho |\langle \psi_{el,f}\psi_{spin,f}|\hat{H}'|\psi_{spin,i}\psi_{el,i}\rangle|^2 |\langle \psi_{vib,f}|\psi_{vib,i}\rangle|^2 \tag{2.48}$$

where $\hat{H}'$ is the perturbing Hamiltonian that induces the radiationless transition. We can define the electronic coupling between the two states J,

$$J = |\langle \psi_{el,f}\psi_{spin,f}|\hat{H}'|\psi_{spin,i}\psi_{el,i}\rangle|^2 \tag{2.49}$$

It also has a Franck-Condon factor $|\langle \psi_{vib,f}|\psi_{vib,i}\rangle|^2$, but has a different consequence for the non-radiative transitions. We define ΔE as the energy gap between 0-0 energies of initial and final states, which can be the triplet energy level in $T_1 \leftarrow S_0$ transition. This leads to an exponential dependence of the non-radiative transition rate on the energy gap, known as *energy gap law*,

$$k_{i\to f} \propto exp(-\gamma \frac{\Delta E}{\hbar\omega_M}) \tag{2.50}$$

where $\hbar\omega_M$ is the vibrational quanta of the highest frequency mode, and γ can be expressed through molecular parameters. Multiple modes can be involved, but the exponential dependence on the vibrational frequency supports that considering the highest-energy frequency is sufficient for most situations. To test whether a specific mode dominates the non-radiative rate, one can measure the change in recombination rate through atom substitution (ie. hydrogen to deuterium) that changes the effective mass in the vibration and the vibrating frequency.

Energy gap law has several implications which are useful in understanding various phenomenons

- **Kasha's rule.** The internal conversion from S_2 to S_1 and from T_2 to T_1 ($\sim 10^{12}$ s^{-1}) is usually faster than its recombination rate from S_2 to S_0 and from T_2 to S_0, respectively. Thus the emission usually occurs from the lowest excited states of a spin manifold, and

this empirical rule is known as *Kasha's rule*. A natural consequence is the *Vavilov rule*, stating that PLQY is independent of the excitation wavelength above the bandgap.

- **PLQY of S_1 and T_1.** The radiative and non-radiative transition rate for T_1 is slower than S_1. This absolute contrast does not influence PLQY as only the ratio of k_{nr} and k_r matters. However, energy gap law speeds up the non-radiative transition rate at a lower bandgap. The large exchange energy in common organic molecules generally results in generally lower PLQY for triplet states.

- **Energy and rate.** When T_1 gets energetically closer to S_1, the non-radiative recombination rate of T_1 is smaller, while the transition rate from T_1 to S_1, although endothermic, can be larger than its recombination to the energetically favourable ground state S_0. This seems to be relevant in many other situations, such as separation of charge-transfer states into charge-separated states, and endothermic singlet fission such as in tetracene.

2.2.7 Charge Transfer

To generate electricity, excitons must be separated into charges. The self-dissociation rate of excitons is quite small, not able to compete with its recombination. Therefore, the invention of bulk-heterojunction enables the use of electronically dissimilar materials to separate the tightly bound excitons.

Charge transfer is a very important process for ultrafast spectroscopic studies. CT can be classified into electron transfer and hole transfer, depending on their relative energy levels. Traditionally, the focus is on electron transfer in fullerene-based solar cells as the main absorbing material is the polymer donor. The recent research efforts have been shifted to non-fullerene acceptors, which absorb light well, thus requiring equal emphasis on hole transfer process. The most common framework to understand charge transfer is the Marcus theory developed in 1950s by Rudolph A. Marcus who was awarded Nobel Prize in Chemistry in 1992.[35, 36]

The *Marcus theory* regards excited singlet and charge-transfer states as individual potential energy surfaces with a parabolic shape, harmonic oscillator. Electron transfer occurs at the intersection point between the two parabolic curves where the nuclear configuration does not change.

There is an activation energy barrier $\Delta G^{\dagger}$ which has to be overcome for charge transfer and can be calculated as,

$$\Delta G^{\dagger} = \frac{(\lambda + \Delta G)^2}{4\lambda} \tag{2.51}$$

where λ is the reorganisation energy, ΔG the Gibbs free energy (often referred as driving energy). The rate of charge transfer can be formulated following Fermi's Golden Rule as

$$k_{\mathrm{ET}} = \frac{2\pi}{\hbar} V^2 \, FC = \frac{2\pi}{\hbar\sqrt{4\pi\lambda kT}} V^2 \exp\left(-\frac{(\lambda + \Delta G)^2}{4\lambda kT}\right) \tag{2.52}$$

where kT is the thermal energy, FC the Franck-Condon factor, V the matrix element of

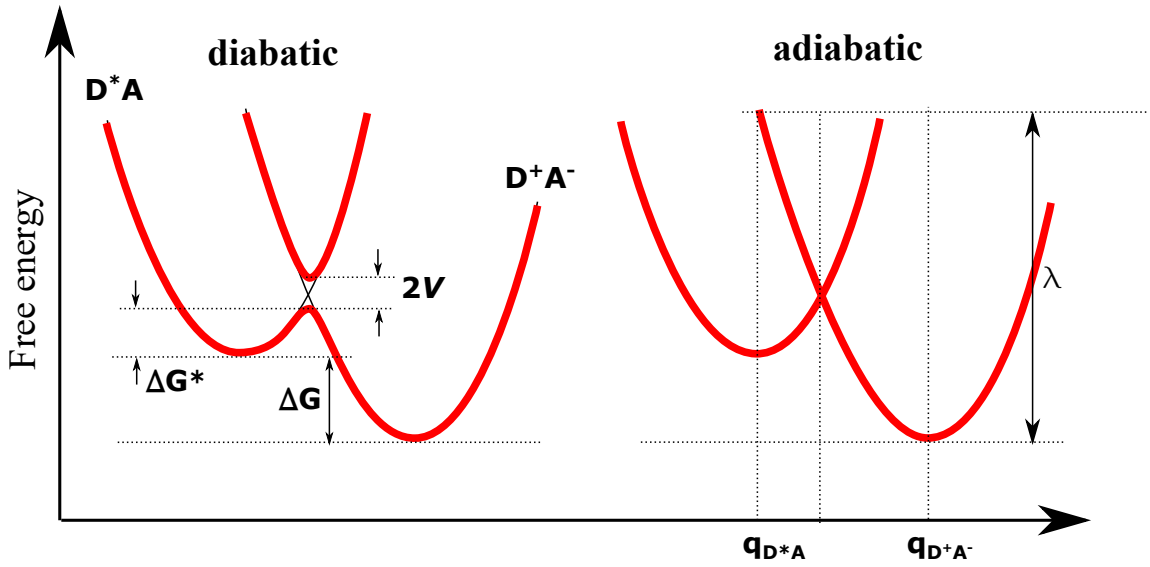

Fig. 2.7 Diabatic and adiabatic diagram in Marcus theory. The weak coupling between donor and acceptor gives the electronic coupling term V; the energy barrier for electron transfer is ΔG and the driving force is ΔG; the reorganisation energy is λ. In the adiabatic case, the reaction happens via the intersection point between the initial and final state.

.

electronic coupling between S_1 and CTS. Depending on the coupling strength between donor and acceptor materials, diabatic process (shown below), which allows exchange of heat, can lower the barrier for charge transfer.

From this relationship, two regions can be identified, the Marcus normal region and the inverted region. In the Marcus *normal region*, k_{ET} increases with an increase in the driving energy $-\Delta G$ together with a decreased $\Delta G^{\dagger}$. The maximal rate is reached when $-\Delta G = \lambda$. Further increasing the driving energy leads to a declining k_{ET}, known as the *inverted region*. This region proceeds without the need of an activation energy and forwarded electron transfer is highly favourable, but the rate is lower.

In fullerene-based OSCs, ultrafast electron transfer was observed to occur of order 100 fs which depends on electronic structure and morphology.[37] However, Marcus theory and its extension Marcus-Levich-Jortner theory cannot explain this ultrafast timescale. The

mechanism of resonant coupling between singlet state and a high-energy manifold from fullerene electronic states was shown to drive such fast process, bypassing the localised CT states.[38] Recently, a reduction in driving energy for charge transfer in NFA-based OSCs raises the interest to understand such process from Marcus theory.[39] We will discuss more in the section later.

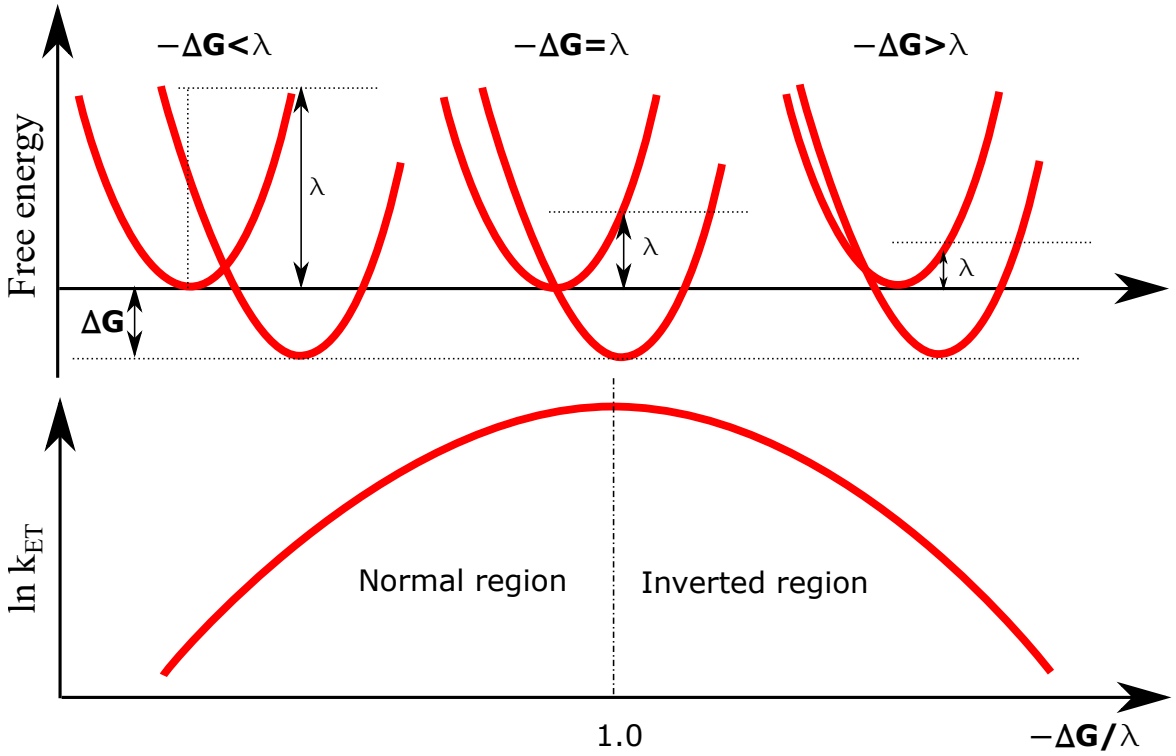

Fig. 2.8 The relationship between the driving energy $-\Delta G$ and the reorganisation energy λ. Variation of the rate constant in the logarithm of electron transfer with the driving force for the reaction. In normal region, the electron transfer rate increases with the driving force, while in the inverted region, the electron transfer rate decreases.

.

2.2.8 Energy Transfer and Exciton Annihilation

In a well-aligned molecular crystal, exciton transports in a wave-like, coherent manner as the energy variation between neighbouring sites is small. In amorphous films, energetic disorder is significant and breaks the exciton band, leading to localised exciton and incoherent transport. To describe such transport, there are two mechanisms, *Förster resonance energy transfer* (FRET) and *Dexter energy transfer*. FRET results from dipole-dipole interaction and thus the interaction range can be quite long. As FRET is via virtual photons, there is no

actual emission or absorption. The relationship is described as

$$k_{\mathrm{ET}} \propto \frac{|\mu_D|^2 |\mu_A|^2}{R^6} J \tag{2.53}$$

where μ_D and μ_A are the transition dipole moments of energy donor and acceptor ($\mu = \langle \psi^* | \hat{\mu} | \psi \rangle$), respectively; R the donor-acceptor distance; J the overlap integral, which can be expressed as,

$$J = \int I_D(\lambda) \varepsilon_A(\lambda) \lambda^4 d\lambda \tag{2.54}$$

where $I_D(\lambda)$ is the donor emission; $\varepsilon_A(\lambda)$ the acceptor absorption. The proportionality of the FRET rate to the oscillator strengths of the donor and acceptor transitions means that triplet states do not undergo FRET efficiently. Instead, Dexter energy transfer based on exchange interaction dominates over short distances,

$$k_{\mathrm{ET}} \propto \exp^{-2R/L} J \tag{2.55}$$

Förster and Dexter energy transfer have a different relationship with the donor-acceptor separation distance. We define Förster radius (R_0) as the separation distance at which energy transfer from donor to acceptor is equally probable as the spontaneous decay of the excited donor ($1/\tau_D$),

$$k_{\mathrm{ET}} = \frac{1}{\tau_D} (\frac{R_0}{R})^6 \tag{2.56}$$

For conjugated polymers, the exciton diffusion length is small that limits the domain size in binary OSCs as charge transfer at donor/acceptor interface must occur before exciton recombination for photocurrent generation. Triplet exciton, important for singlet fission, also needs to diffuse to the interface for energy transfer or separation.

The fate of an exciton after diffusion in the same material, other than recombination, is to encounter another exciton and annihilate. This can be thought of another type of energy transfer mechanism between two excited-state chromophores. In an organic system with singlet excitons, triplet excitons and polarons, there are a number of interactions that can occur.

$$\begin{aligned}
S_1 + S_1 &\rightarrow S_0 + S_n \rightarrow S_0 + S_1 + \mathit{phonons} \\
S_1 + T_1 &\rightarrow S_0 + T_n \rightarrow S_0 + T_1 + \mathit{phonons} \\
T_1 + T_1 &\rightarrow S_0 + T_n \rightarrow S_0 + T_1 + \mathit{phonons} \\
T_1 + T_1 &\rightarrow S_0 + S_n \rightarrow S_0 + S_1 + \mathit{phonons}
\end{aligned} \tag{2.57}$$

Charges can also interact with excitons and dissipate energy.

$$\begin{aligned} S_1 + polaron &\rightarrow S_0 + polaron + phonons \\ T_1 + polaron &\rightarrow S_0 + polaron + phonons \\ polaron + polaron &\rightarrow S_0 + polaron + phonons \end{aligned} \tag{2.58}$$

The exciton annihilation, specific to excitonic materials, occurs more often at high excitation densities, and is relevant to performance of excitonic optoelectronic devices. The annihilation related to singlet is prevalent in optical excitation such as OSCs. Recently, the diffusion of excitons in NFA OSCs has shown to be efficient so that annihilation is present at very low excitation densities.[40] In OLED devices, the annihilation of triplet states is of critical importance in electrical injection. A common phenomenon under high electric injection is the efficiency roll-off, that is a lower efficiency at higher injection current.[41] Triplet-triplet annihilation can also generate singlet emission, a mechanism of some commercialised OLEDs.[42] Now annihilation or excited state interaction becomes more related to the device performance, but the physical understanding of these processes is not complete and requires further study.

2.2.9 Coupling between Identical Molecular States

Intermolecular interactions in disorder films and solutions influence the electronic structure of the system. To describe these different intermolecular electronic states, we will first consider the interactions between two identical molecules before considering the interactions between different molecules.

Here we take a *physical* dimer between weakly interacting identical molecules. This is different from a *chemical* dimer where the molecules are covalently bonded. In the physical dimer, the adjacent molecules experience weak van-der-Waals force (electron-electron interaction, Coulomb interaction in essence) so that the energy of the ground state as well as the excited state tends to be lower, as described by the polarisation energies, D and D', respectively. This interaction depends on the dipole orientation and their intermolecular distance. Both D and D' are negative as they are attractive interaction that stablises the system, and further we can obtain $|D'| > |D|$, meaning that the gap after Coulomb interaction is smaller in the dimer. The coupling of identical molecules, on the other hand, splits the degenerate electronic levels into two levels, both in the occupied orbital and unoccupied orbitals, from the single electron picture. The split in the unoccupied orbitals leads to two distinct states, whose energies are donated as E^+ and E^-, respectively. These two states are separated by the resonance interaction energy 2β.

Based on the magnitude of the resonance interaction, we discuss three situations below.

1. **Small interaction.** Large intermolecular distance, for instance in a dilute solution, leads to a negligible resonance interaction ($\beta \approx 0$). This is also true for *solid solution* for OLED devices where guest material is immersed in a host matrix with a low doping concentration of several percent. In the solid state where the molecules are closely stacked, this interaction can be neglected when the mean splitting from resonance interaction is much smaller than its inhomogeneous broadening ($\beta \ll \sigma(\Delta D)$). Based on the above ideas, a small intermolecular interaction can also be manipulated and achieved via synthetic modification or solution processing, for example, by attaching steric side groups to the chromophores, or by using a low-boiling solvent in spin-coating to freeze the structural disorder from solution.

2. **Modest interaction, H- and J- aggregates.** In planar and linear π-conjugated molecules, such as naphthalene and anthracene, the resonance interaction is moderate and not negligible, typically on the order of 100 meV. A sandwich arrangement where one molecule lies flat on top of the other molecule favours the formation of a dimer. This moderate interaction does not lead to significant changes in the intermolecular distance or reorientation (represented as a small change in coordinate of the dimer). The theory

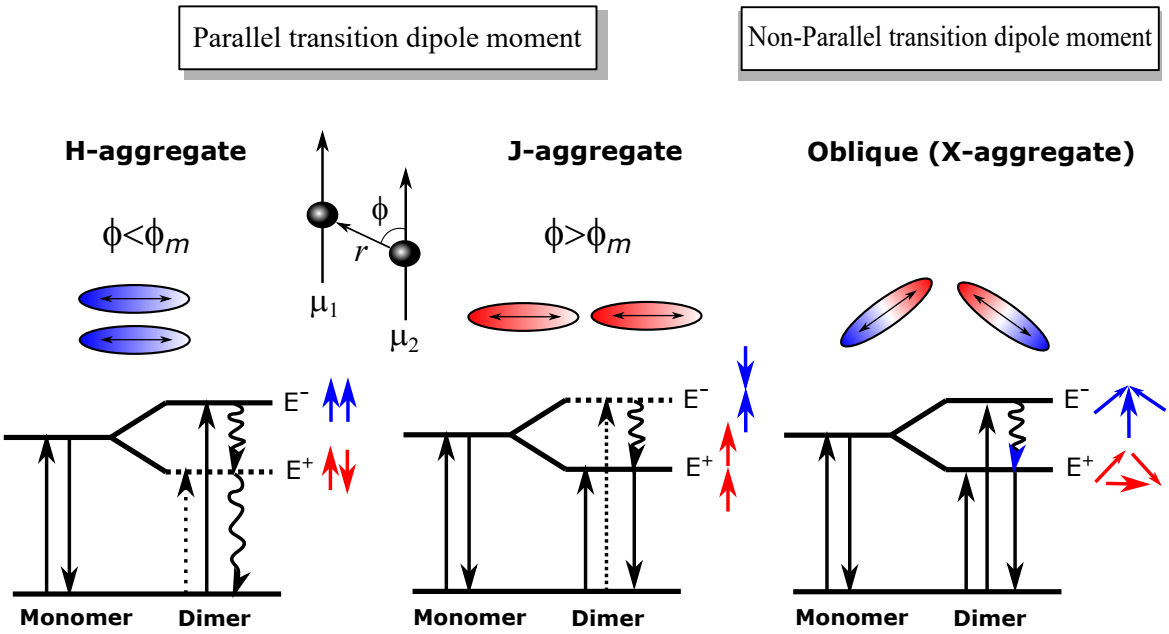

Fig. 2.9 Dimer interaction and their related electronic structure. In H aggregates (side by side), the transition from antiparallel dipole moment alignment is lower in energy and forbidden while the parallel alignment is optically allowed and energetically higher. In J aggregate (head to tail), the lower energy state is optically allowed from where the photoluminescence also strongly occurs. In oblique dipole alignment, both transitions have oscillator strength. The angle between the parallel dipole moments and the displaced vector determines the interaction type to be H or J.

to define the selection rule for dimer was initiated by Kasha based on Frenkel exciton theory. The transition dipole moment of the dimer is determined to be the vector sum of the transition dipole moments of its individual molecules, depending on their relative orientation. We first consider two extreme cases, when the transition dipole moment is side-by-side or head-to-tail. The former one is termed as *H-aggregate* and the latter one is known as *J-aggregate*.

In H-aggregate, antiparallel arrangement leads to a decrease of the energy level but cancels out the transition dipole moment. Thus the absorption of the lowest excited state is forbidden, behaving as a *dark* state. In contrast, the parallel arrangement raises the energy level and enhances the transition dipole moment, so that this high-energy transition gives the dominative absorption. The luminescent efficiency of H-aggregate is usually poor as the emission occurs from the dark excited state. Some misorientation or vibronic coupling in the excited state can induce a weak oscillator strength, leading to a weak, long-lived emission from H-aggregate. This weak coupling to the ground state may facilitate the intersystem crossing to triplet state and gives phosphorescence.

On the other hand, J-aggregates exhibit a large transition dipole moment for the low energy level E^+ and thus are usually quite luminescent; the transition to the high energy level is forbidden.

It should be noted that multiple terms are used to describe the transition strength in atoms and molecules, such as Einstein A and B coefficient, oscillator strength and transition dipole moments. Oscillator strength (f), originating from a classical picture, describes the ratio of stength of the absorption to the (hypothetical) strength of a single electron using a harmonic oscillator model. f can be quantified from the absorption coefficient $\varepsilon(\nu)$ where ν is the light frequency

$$f = 4.319 \times 10^{-9} \int_{band} \varepsilon(\nu) d\nu \tag{2.59}$$

Transition dipole moment (μ) is to determine if transitions are allowed under the electric dipole interaction. The relationship between μ and f is

$$\mu^2 = \frac{3e^2\hbar}{4\pi m_e \nu} \times f \tag{2.60}$$

where m_e is the mass, and e is the charge of the electron. For reference, $f = 1$ at 800 nm corresponds to a μ of 13 Debye.

Between the extreme cases shown above for the parallel transition dipole moments, we consider the general case of the Coulomb interaction, using the model of dipole-dipole interaction under the point dipole approximation

$$J_C = \frac{\mu \cdot \mu - 3(\mu \cdot \hat{r})(\mu \cdot \hat{r})}{4\pi\varepsilon R^3} = \frac{\mu^2(1 - 3\cos^2(\phi))}{4\pi\varepsilon R^3} \tag{2.61}$$

where μ is the transition dipole moment, $\vec{R} = R\hat{r}$ is the displacement vector between the dipoles, ϕ is the angle between the displacement vector and the transition dipole moment. The angle at $J_C = 0$ is called *magic angle* (ϕ_m= 54.7 degrees). For $J_C > 0$ ($\phi < \phi_m$), it is the H-aggregate region; for $J_C < 0$ ($\phi > \phi_m$), it is the J-aggregate region. For simplicity, the resonant interaction is the same in the illustration (Figure 2.9). In reality, β is related to the angle ϕ.

When the transient dipole moments are not parallel, both transitions are allowed, seen as two peaks from E^+ and E^- in the absorption spectrum. From the absorption gap between these two states, we can experimentally determine the resonance interaction.

The intermolecular interaction provides a simple way to self-assemble the molecules both in solid state and in solution. The aggregation behaviour not only exists in small molecules, but also in polymers. With the emergence of new materials, the theory evolved from Kasha's original work to explain the molecular aggregate is still under development. For a comprehensive picture, readers are referred to recent reviews by Frank Spano and Frank Würthner.[43, 44]

3. **Strong interaction - Excimer.** When the resonance interaction is strong, two interacting molecules need to reorient and optimise their interaction that forms the excited dimer, *excimer*. There is no splitting of the excited state so that the absorption spectrum is not distinguishable from isolated molecules. In the solution phase, such as pyrene, one excited molecule needs to collide with another ground-state molecule to form excimer. In the excimer state, the emission occurs from the equilibrium position at a smaller **Q**. This means that excimer emission is usually strongly red-shifted from the emission of isolated molecules and the spectral shape is structureless without vibronic progression. After emission, the ground state relaxes to its equilibrium position. As excimer formation in solution is a collision-based event, its formation rate depends on temperature, viscosity, and concentration. Molecules in the solid state are not as mobile as that in the solution phase. Therefore, the excited state interaction is greatly restricted by the molecular arrangement. Figure.2.10 is the energetic level of states comparison of excimer and dimer.

It is important to note the classification of dimer and excimer is not fundamentally exclusive but depends on the strength of the resonance interaction and the geometric relaxation of two molecules. Both can exist to some extent in one material. For example, in amorphous materials like tetracene, there are more than one type of intermolecular arrangements. In general, a herringbone arrangement favours the dimer formation as the face-to-edge orientation prevents molecules from approaching each other. Meanwhile, molecules that are π-stacked have more space to rearrange after excitation can form excimers. However, even showing the signature of excimer emission (structureless, and strongly redshifted emission), some weak dimer absorption might be observed under certain arrangements.

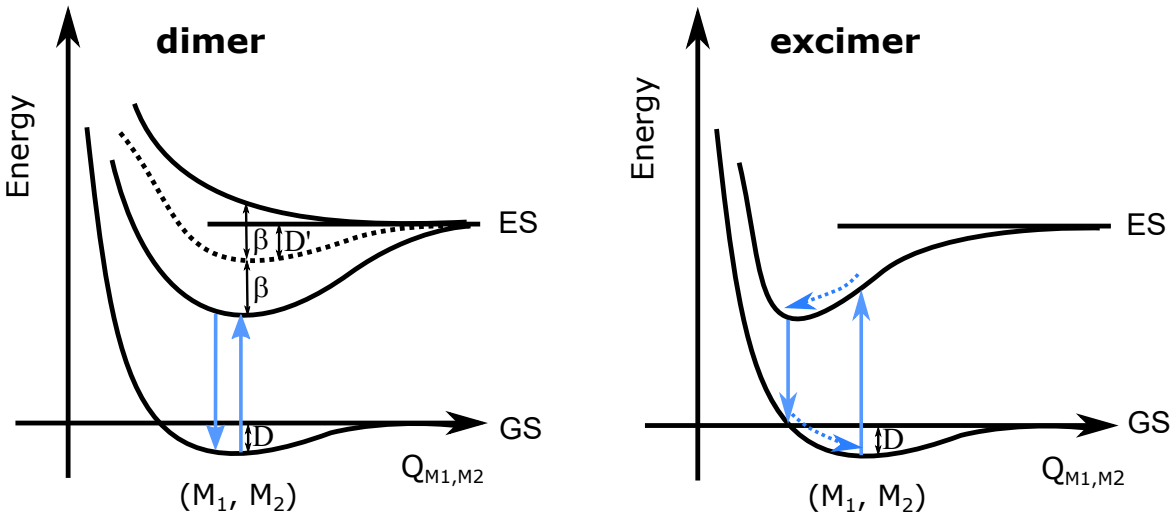

Fig. 2.10 PES of dimer and excimer formation. In dimer formation, the intermolecular interaction is not large enough to cause the change in coordination. In the excimer, molecules reorientate themselves to find the minimal in potential energy surface, and the emission is significantly red-shifted. β is the resonance interaction energy, D and D' are the lowered energy of the ground state and excited state due to the van-der-Waals force in the dimer interaction.

2.2.10 Coupling between Dissimilar Molecular States

The concept of dimers and excimers can also be extended to the coupling between different molecules. Between dissimilar molecules, charge transfer can occur from a molecule which is excited to a different, coupled molecule, forming electron donor and acceptor radicals. From its definition, an exciplex state should not have its own absorption band while CT state does. Geometrical relaxation actually exists in both CT exciton and exciplex state. From experiment, it is difficult to distinguish these two excited states, due to two main reasons: (1) separated electron and hole density: the absorption of CT state is weak, usually three orders of magnitude smaller than the individual compound; (2) the emission spectra of CT and exciplex are both red-shifted and structureless. Sometimes, people do not distinguish them when using the CT exciton or exciplex, but generally refer to intermolecular states at the donor-acceptor interface.

The intermolecular CT complexes are central to optoelectronic devices. In OSCs, the CT state acts as the precursor for free charges. The weak absorption also indicates the small oscillation strength for emission, which is likely to have a low PLQY of CT state if the non-radiative decay dominates as the case in OSCs. This quantity is important as it determines the device voltage output. If this CT state does not funnel into a singlet state or local triplet state, we can measure PLQY of CT states under electrical injection regime, termed as *EL efficiency*. EL efficiency determines the overall OLED performance, in which the intermolecular state is

often termed exciplex rather than CT state, probably because (1) the absorption profile does not matter for light emission and (2) the initial photo-excitation process of OLED materials is less understood compared to the process of its electrical excitation. This careless treatment has resulted in confusion and even mistakes. Several reports have directly measured sub-bandgap absorption in traditionally believed "exciplexes", such as m-MTDATA:POT2T[45] and BF-DPB:B4PYMPM[46]. The use of the term "exciplexes" therefore needs to used more carefully.

2.3 Organic Solar Cells

Organic solar cells are a type of optoelectronic devices which convert light into electricity. Since the price of silicon solar cells is already cheaper than fossil fuels, OSCs are unlikely to compete in the power-generation photovoltaic market. However, their light weight, flexible, and low-cost means that OSCs could have niche applications for wearable electronics and building-integrated photovoltaics. Design of new organic materials and better understanding of device physics has enabled the device efficiency reaching over 17%. The trend in efficiency and improvements in stability may lead to the commercialisation of OSCs.

Organi chromophores are strong absorbers of light. As early as 1975, chlorophyll from green plants was integrated into the photovoltaic devices which achieved 0.01% power conversion efficiency.[47] In 1977, conjugated polymes were discovered to have metallic charge transport, and thus the semiconductor form was expected to have photovoltaic effects.[48] By adopting the p-n junction from silicon solar cells , C. W. Tang was able to demonstrate a 1% device made from a bilayer of electron donating and accepting small molecules.[49] This work started to raise interest in this field. This planar heterojunction (PHJ) structure was limited by the exciton diffusion length of 10-20 nm, so that the active layer was not thick enough to absorb a substantial amount of sunlight. Ultrafast electron transfer between two electronically dissimilar materials was observed to separate the strongly bound exciton in 1992.[50] Later on, in 1995, a novel bulk-heterojunction (BHJ) structure made from solvent deposition was invented by Heeger and Friend research group.[51, 52] This structure overcomes the exciton bottleneck for dissociation in PHJ by creating a large interfacial area for exciton dissociation, after forming nano-structured penetrating donor-acceptor networks. Until now, this BHJ structure is still the standard geometry for high-efficiency devices. [53]

In years before 2015, for material blends in BHJ, the most important acceptor material is fullerene or its derivatives. C_{60} was modified to increase the solubility in solvent which forms [6,6]-phenyl-C61-butyric acid methyl ester, hereafter referred to as $PC_{61}BM$. In solution processing, the morphology optimisation is to ensure formation of enough interfaces for charge generation, while maintaining appropriate charge transport properties for charge collection. This stage is mainly focusing on optimising the performance of poly(3-hexylthiophene-2,5-diyl) (P3HT):$PC_{61}BM$ blends. However, the electronic property such as the energy level is not tunable and $PC_{61}BM$ does not well absorb light. Later, [6,6]-Phenyl C71 butyric acid methyl ester ($PC_{71}BM$) was developed which has a deeper LUMO and absorbs light in the greenish region, together with a higher oscillation strength due to symmetry breaking, contributing to a higher photocurrent in the device. The main effort in the following stage is to develop narrow-bandgap polymers working together with $PC_{71}BM$ to achieve higher device efficiency. Fullerene cannot be the destination, considering the predicted maximal

efficiency to be around 10%. To overcome this efficiency threshold, alternative materials must be developed to replace fullerene. A novel molecule, ITIC, developed by Xiaowei Zhan, triggered the storm of non-fullerene acceptor research.[54] The device efficiency has easily surpassed 10%, arriving at 17% now.[8] A higher efficiency towards 18%-20% is achievable for the following years.[10]

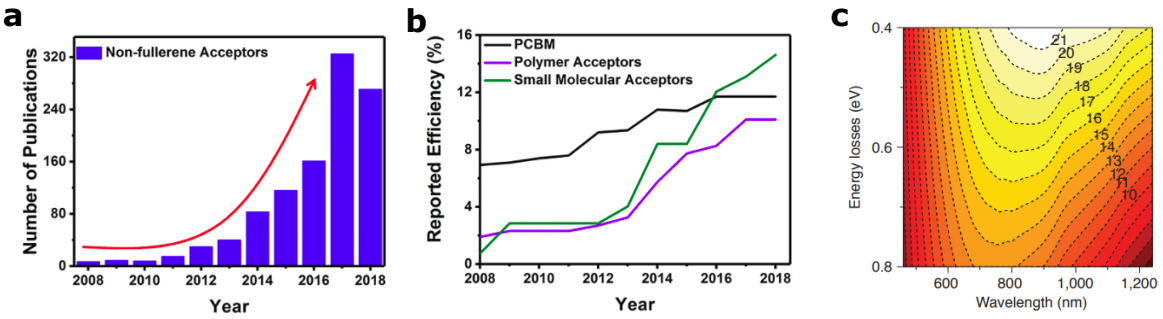

Fig. 2.11 Development of NFA-based OSCs. (a) The number of publication on NFA-based OSCs from Web of Science until July 2018. (b) The efficiency chart in the last decade including fullerene-based OSCs, NFA-based OSCs, and polymer acceptor based OSCs.[55] (c) Prediction of power conversion efficiency related to the absorption onset and energy loss.[10].

2.3.1 Basic Operation of Organic Solar Cells

The maximum theoretical efficiency of OSCs is defined by the Shockley-Queisser limit.[56, 57] The thermodynamic balance predicts the best performance of $\sim$31% at a bandgap of $\sim$1.4 eV for a single-junction solar cell under AM 1.5G 1 sun illumination. A good solar cell must have strong luminescence efficiency. Following this design rule, a remarkably high power conversion efficiency (PCE) of 28.8% is realised in single-junction GaAs. This high efficiency is attributed to the photon recycling effect, in which the emitted photons have a high chance of being reabsorbed in the active layer.[58]

The organic solar cell is usually composed of the active layer to absorb light, the charge transport layer and the extraction electrodes. The charge transport layers help form the Ohmic contact, and maintain the voltage potential. Two device configurations are developed, the conventional and inverted layouts. The conventional device takes the layout of ITO/PEDOT:PSS/active layer/electron transport layer/Al, where the electron transport layer can be Ca, LiF or PDINO, PFN-Br.[59] Both PEDOS:PSS and low work function metals can cause stability issues related to oxygen and moisture. To solve this problem, the inverted device (ITO/ZnO/active layer/MoO_3/Ag) with high work function metal usually achieves a better device stability.[60] The main drive for efficiency improvement is the active layer material. In the following session, an introduction is given on the material development through three stages.

2.3.2 Stage 1: Amorphous Polymer:$PC_{61}BM$

For conjugated polymers, the absorption coefficient (ε) can be on the order of 10^5 cm^{-1}, one order of magnitude higher than the inorganic counterparts. This high absorptivity enables a thinner active layer thickness to harvest the equivalent light. To strongly absorb sunlight, organic layers with 300 nm are enough as opposed to several microns in silicon solar cells. However, due to low charge carrier mobility and internal light field distribution, the optimised thickness for the organic active layer is usually around 100 nm.

To increase the polymer solubility, small functional groups, such as alkyl, alkoxy, acid, ester and phenyl groups, are linked at the side chain position. Phenylene vinylene (PPV) and its derivatives are representative polymers in this stage. Poly(2-methoxy-5-(3',7'-dimethyloctyloxy)-1,4-phenylene vinylene (MDMO-PPV) and $PC_{61}BM$ was the most successful material combination. MDMO-PPV is quite amorphous thus the packing is not influenced by the fullerene loading. Following this property, MDMO-PPV is used in Chapter 4 to combine with different fullerene acceptors.

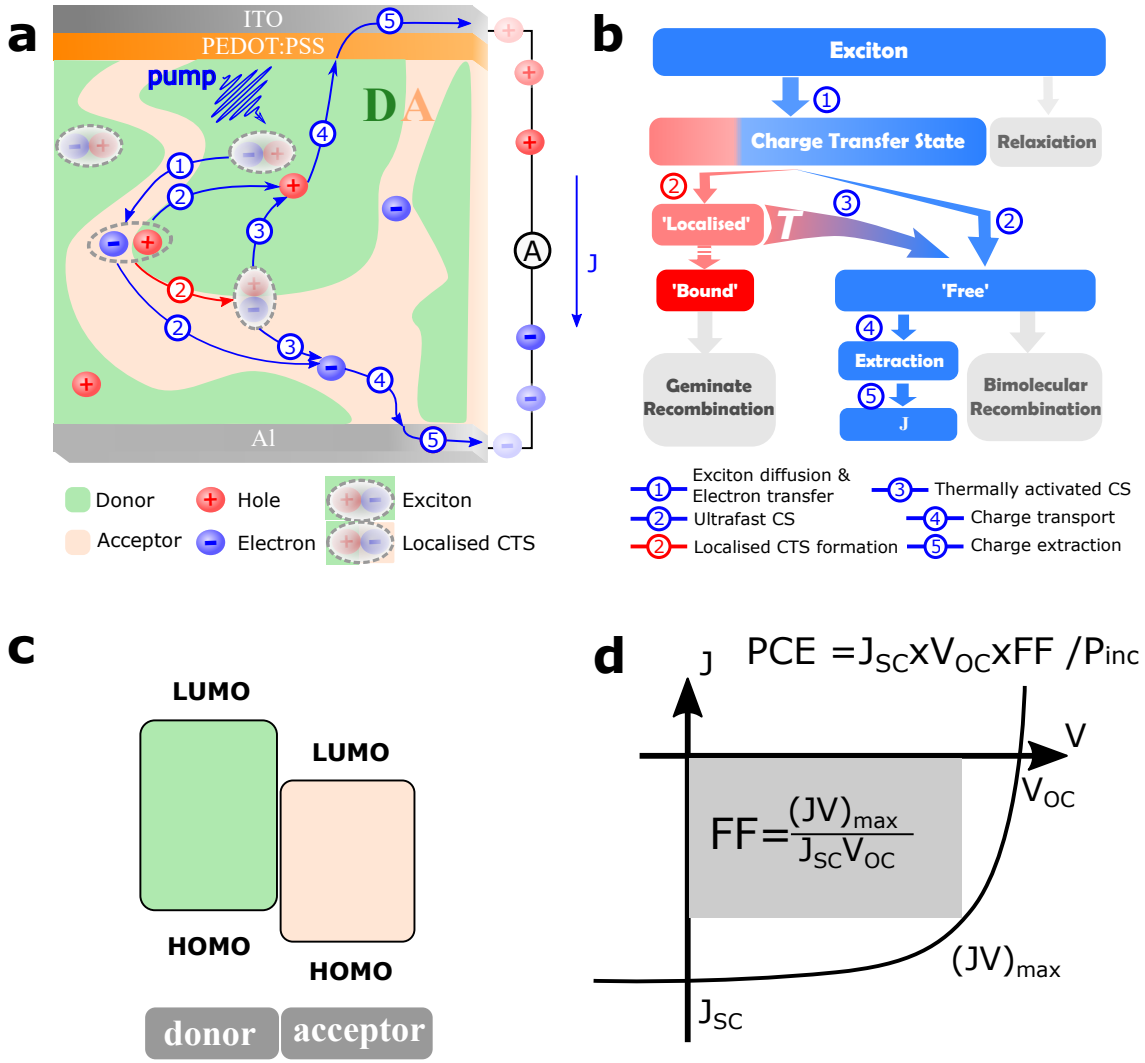

Fig. 2.12 Basic operation of organic solar cells. (a-b) In the device, the active layout is sandwiched between electrodes. The active layer is composed of electron donor and electron acceptor with a proper phase separation. (1) exciton diffusion and electron transfer; (2) after ultrafast charge separation, both long-range charge separation to generate charge carrier, and localised charge-transfer states form; (3) the thermal activation of local charge-transfer states to generate free charges; (4) after charge separation, electron and hole transport in the corresponding phase; (5) charge extraction to the electrodes. (c) the energetic alignment of type II heterostructure. (d) the related device parameters to characterise a solar cell.

2.3.3 Stage 2: Regioregular P3HT:$PC_{61}BM$

The most studied conjugated polymer is P3HT. The optical bandgap is 1.9 eV with a broad absorption between 450 nm and 650 nm in the solid state. The hole mobility is also high. Polythiophene was successfully synthesised first in 1980, but the solubility is poor. The soluble derivatives was poly(3-alkylthiophene), first synthesised in 1986. Depending on

the position of the side chains, it has different coupling between adjacent thiophene units, leading to a certain degree of randomness. Further efforts to synthesise highly regioregular P3HT was obtained by McCullough in 1993 with 99% head-to-tail regioregularity.[61] After continuous efforts for a decade, P3HT:$PC_{61}BM$ is probably the most well researched blend around the world. Between 2002 and 2010, there are more than 1033 publications focusing on BHJ based on P3HT:$PC_{61}BM$.[62] However, the device efficiency distribution is quite broad, for example, some papers with less than 0.5% efficiency when the top efficiency is already around 5% in 2010. Further development in these years has pushed this efficiency to around 7%.[63]

This broad distribution is probably due to the sensitivity of device performance to many fabrication conditions. The most efficient weight ratio for P3HT:$PC_{61}BM$ is around 1:0.8 to 1:1 with a small excess of P3HT. The solvent is usually chlorobenzene or o-dichlorobenzene. These high boiling point solvents allow for moderate crystallisation of P3HT without further annealing. Spin-coating recipe can be optimised by tuning spin-speed, spin-time, and spin-acceleration together with some solvent additives. Gelation behaviour due to liquid-state aggregation during the ageing of solutions is present in many material solutions. As a result, the stirring, storage and heating parameters of P3HT:$PC_{61}BM$ solution are the important conditions before spin-coating. Thermal annealing after spin-coating is usually needed to achieve proper phase separation as the initially formed blend is too intermixed. The temperature and duration of thermal annealing should be carefully controlled to achieve domain sizes comparable to the exciton diffusion length, and the resulting optimal parameters depend on P3HT properties (molecular weight, polydispersity index, and regioregularity), blend ratio and solvent. To tune the electronic properties, various fullerene derivatives were developed, such as bis-PCBM and indene-C60 bisadduct (ICBA). However, the tunability is still limited. The difficulty to repeat published results in part hinders the development of this field. These problems are mitigated in NFA-based blends where device performance is more reproducible mainly due to the controlled aggregation property of donor and acceptor molecules.

During this period, the research interest is more in academic merit, and there is little hope to commercialise organic photovoltaics. However, the developed understanding of the structure-function -relationship properties and various processing methods to optimise the blend morphology provides a rich knowledge base for accelerating future optimisation of novel blends. A large number of techniques to characterise organic materials and optoelectronic devices were also developed. P3HT thus acts as the model material to study novel concepts bringing together different fields.

2.3.4 Stage 3: Low-Bandgap Polymer:$PC_{71}BM$

After huge efforts in the community, the PCE of P3HT:$PC_{61}BM$ devices can achieve around 5%. The main limitation comes from the bandgap of P3HT polymer around 2 eV, which defines the onset absorption of around 650 nm. The ability to tune the bandgap, and therefore the absorption onset of materials can open the possibility to absorb more photons and to achieve higher photocurrent. On the other hand, the device voltage output, strongly correlated with the frontier orbital alignment, also needs to be optimised. More light absorbing molecules with various energy levels are obviously in need. The next rise of efficiency benefits from the design of polymer donor materials, which have driven the efficiency over 10% threshold, long believed as a milestone for photovoltaic technology.

Potentially, one can decrease the bandgap by further increasing the conjugation length. In reality, the bandgap does not narrow further after a repeating unit of $\sim$10. To tune the bandgap and energy levels, a new concept of donor-acceptor interaction is introduced. These low-bandgap polymers with E_g below 1.6 eV are usually push-pull type, seemed as third-generation semiconducting polymers.[14] The mechanism behind bandgap tuning in donor-acceptor copolymer is 1) delocalisation of electrons along the polymer backbone and 2) hybridisation of of frontier orbitals.[64, 65] The electron-rich unit and electron-deficient unit alternate in the polymer chain. Due to an intra-chain electron transfer from the donor to the acceptor unit, the rearrangement of the electrons, thus the frontier orbitals gives a higher HOMO than the D unit and a lower LUMO than the A unit, resulting in an narrowed HOMO-LUMO gap for the copolymer. The rule of designing a polymer donor is to downshift the HOMO level while keeping the LUMO energy level above that of the acceptor material. The planarity along the aromatic backbone creates a high degree of delocalisation of π-electrons. Similar as polyacetylene, a longer conjugation length can further lower the bandgap, and the bandgap increases when the torsion of the polymer backbone disrupt this conjugation. The push-pull polymer bandgap can be tuned to mid-IR below 0.5 eV[66]. These infrared absorbing polymers have wide application in spectral management such as in tandem and ternary organic solar cells.

Knowing some electron-rich and electron-deficient groups is beneficial to better understand device performance and choose some materials for spectroscopic studies. Some widely used electron-deficient groups include benzothiadiazole, thieno[3,4-b]thiophene, and diketopyrrolopyrrole, isoindigo units. Other electron-rich groups are benzodithiophene, thiophene. For other low-bandgap polymers, such as perylene diimide or naphthalene diimide have been used as electron acceptors. A typical example is the copolymer of naphthalene diimide-bithiophene, also known as N2200. The method of energy level tuning can also be introduced in organic small molecules.

Recently, He Yan has demonstrated multiple cases for high-efficiency (>10%) fullerene-based organic solar cells.[67] The morphology is controlled by the temperature-dependent aggregation (TDA) behaviour of the donor polymer and not sensitive to the used fullerene derivatives. These TDA polymers are mostly disaggregated and can be dissolved in solution at high temperature, but aggregate when the solution is at room temperature.[68] This transition between order and disorder tuned by temperature allows better control of phase separation.

The development of low-bandgap polymer is successful, reaching the internal quantum efficiency close to unity[69] and PCE above 11%[70]. These cells can generate charge perfectly but still suffer from a high recombination loss, leaving a large gap in the device voltage output compared to inorganic photovoltaic technologies. The imbalance of donor and acceptor function is obvious where donor is mainly responsible for absorbing light while the acceptor is mainly helping dissociate the excitons. Such function asymmetry is solved in the next-generation NFA-based solar cells.

2.3.5 Stage 4: Polymer:Nonfullerene Acceptor

During the past five years, the emergence of non-fullerene acceptors has revolutionised the field of organic solar cells. The efficiency has kept on growing around at a steady pace. The state-of-the-art single junction and tandem solar cells have achieved PCE of over 16% and 17%, respectively. For a detailed overview, readers are suggested to go through reviews published recently.[10, 71–76]

In 2015, Xiaowei Zhan from Peking University reported a promising non-fullerene acceptor called ITIC, which gave a PCE of 6.8% blended with PTB7-Th, setting the record at that time.[54] Next year, Jianhui Hou combined ITIC with a polymer PBDB-T, which surprisingly giv a high PCE of 11%, comparable to top fullerene-based devices.[77] In 2016, Henry Yan reported another type of high-efficiency NFA based on PDI derivatives.[78] Following these pioneering works and using knowledge from designing polymer donors, molecular engineering of non-fullerene acceptors by different research groups has pushed the efficiency up quickly and provides a large pool of high-performance materials. In 2018, Yongsheng Chen achieved over 17% device efficiency adopting the tandem structure.[8] In 2019, Yingping Zou invented a new NFA named as Y6 which gave 15% efficiency in a single junction.[79] In the same year, a derivative of Y6 achieved PCE over 16%.[80] This race is still ongoing and 18%-20% is expected to be achieved in the following years. To aim for commercialisation, another important area is to improve the device stability. Fullerene derivatives are generally not stable under light and heat. Improved device stability was observed in PBDB-T:ITIC and P3HT:O-IDTBR compared to fullerene-based counterparts, which indicates the potential of NFA to achieve stable devices.[81, 77, 82]. Such stability is

shown to be influenced by molecular conformation such as twist [83] and chemical structure such as the end group [84]. It is encouraging to see that 10-year device lifetime was achieved in such a short time research.[84] Recently, a major breakthrough from Forrest et al. has demonstrated that fullerene-based blends made from the thermal evaporation can reach superior stability, as good as in OLEDs. Such stability, together with recent high efficiency developments, presents that OPV technology is very close to its commercialisation.[85]

The development of high-efficiency single junction solar cells also spurs other directions. Ternary blends where the active layer consists of three components offer an easy way to extend light absorption. The third component can be a fullerene-based acceptor[86], a polymer or small molecule donor[87], or a NFA (either polymer or small molecule)[88]. In addition to better absorption, the morphology is optimised and an alloy-like structure[89] seems to form (under debate [90]), which probably leads to much stable devices.[91] Despite the great progress in ternary blends, there is still a gap in understanding its device photophysics. Semi-transparent and flexible solar cells are gaining increasing attention due to their application in real-world applications.[92] Just by absorbing the UV and NIR light and letting the visible light transmit, the device efficiency can approach 11% assisted with high-throughout optical screening.[93] Another attractive feature is the colour tunability simply by using different bandgap materials.

The success of non-fullerene acceptors is mainly due to 1) light absorption: wide absorption range enabled by both donor and acceptor materials; 2) charge generation: efficient charge generation under a reduced driving force; 3) charge recombination: decreased non-radiative recombination loss. We will discuss 2) in the next session, and now focus on the the voltage loss part first.

The voltage loss, defined as the difference between the bandgap (the smaller in the blend) and V_{OC}, can be decomposed into three components[78],

$$q\Delta V = E_{\mathrm{gap}} - qV_{\mathrm{OC}} = (E_{\mathrm{gap}} - qV_{\mathrm{OC}}^{\mathrm{SQ}}) + (qV_{\mathrm{OC}}^{\mathrm{SQ}} - qV_{\mathrm{OC}}^{\mathrm{rad}}) + (qV_{\mathrm{OC}}^{\mathrm{rad}} - qV_{\mathrm{OC}}) = \Delta E_1 + \Delta E_2 + \Delta E_3 \tag{2.62}$$

where q is the elementary charge, ΔV is the voltage loss, E_{gap} is the bandgap of the smaller compound, $V_{\mathrm{OC}}^{\mathrm{SQ}}$ is the maximum voltage based on the Shockley-Queisser limit, in which the EQE is step-wise (1 above the bandgap and 0 below the bandgap)[56], $V_{\mathrm{OC}}^{\mathrm{rad}}$ is the open-circuit voltage when the radiative recombination is unity.

The first term ΔE_1 is mainly due to the mismatch between radiation from a narrow solid angle from the sun, and omnidirectional radiative recombination from absorption above the bandgap. Such loss is usually 0.25 and 0.30 eV and is unavoidable for any type of solar cells. The second term ΔE_2 is due to additional radiative recombination from the absorption

below the bandgap. The absorption of sub-bandgap states, CT states in fullerene-based solar cells, is the main contributor. The voltage loss related to the driving energy is included in this term. In NFA blends, it is widely reported that the absorption of CT states is negligible and CT energy is very close to the singlet, but the detailed mechanism is not fully understood. The voltage loss related to the energy level of CT states is minimised and mainly comes from non-ideal absorption. The third term ΔE_3 comes from non-radiative recombination, where EQE_{EL} is the electroluminescence efficiency under LED working regime under dark condition. The relationship between the electroluminescence efficiency and the non-radiative voltage loss is

$$qV_{\mathrm{OC}}^{\text{non-rad}} = -kT\ln(EQE_{\mathrm{EL}}) \tag{2.63}$$

This equation supports the argument that a good solar cell needs to be a good LED.

A reduction in the energetic offset between singlet and CT states was measured to increase the electroluminescence efficiency.[78] Recent high-efficiency devices show quite overlapping EL emission in the blend with the spectrum taken from the pristine material.[78] This was also observed in low-offset fullerene-based OSCs[94], then this observation is not inherent to NFA-based blends. From such observation, improving the PLQY of individual component, for the first time, becomes important for organic solar cells.[39] In fullerene-based blends, the reason for non-radiative recombination is related to the rich intramolecular vibrations at carbon-carbon frequency of organic semiconductors.[95] However, the situation in NFA-based blends is still unclear.

2.3.6 Single Component Organic Solar Cells

The adoption of BHJ structure has been quite successful, dominating the top-efficiency device performance of organic solar cells. The single-component organic solar cell (SCOSC) has its intrinsic advantage of being stable and resistant to change in phase separation in BHJ. For photophysics study, it offers a unique platform to study the structure-function relationship in organic solar cells.

The concept of BHJ is also introduced in SCOSC where the electron donor and acceptor is linked by a covalent bond or a chain as the linker. Depending on the linker position, these molecules can be divided into diblock conjugated polymers (on the backbone) and double-cable conjugated polymers (on the side chain). Double-cable conjugated polymers are easier to synthesise and the optoelectronic properties can be tuned as well. The central aim for morphology optimisation is to separate the strongly bound exciton, and collect the free charges to the electrode before recombination, similar to the BHJ layout. Molecular packing

and crystallisation are important to form the channel for charge transport and suppress charge recombination.

This field is not as much studied as the BHJ, and the device efficiency is still relatively low at 6.3%.[96] Currently, both donor and acceptor components need to crystalline to form proper phase separation and the selection of moiety is quite limited. Future advances in molecular synthesis will probably lead to higher efficiency devices, and understanding the photocurrent and photovoltage loss is necessary.

2.4 Photophysics of Organic Solar Cells

For BHJ OSCs, the photocurrent generation is a multiple step process, which usually involves the light absorption, exciton generation and diffusion, charge transfer and charge generation, charge recombination and charge collection. The voltage loss, as discussed earlier, is mainly related to the driving force to generate CTSs, and charge recombination loss via the CTSs. In fullerene-based blends, a certain driving energy is necessary otherwise the charge generation efficiency significantly drops[97–99, 94] with one exception reported.[100] Therefore, there is usually a trade-off between high photocurrent and high photovoltage in fullerene-based OSCs. However, efficient charge generation under a small (even negligible) driving force has been easily observed in many NFA-based blends.[78, 101–106] The community is still not clear whether the tolerance to the driving energy is specific to some properties of NFAs, or just benefiting from their energy level alignments.

In the following sections, we will briefly introduce each photophysical process and discuss their potential opportunities and challenges, particularly for emerging NFA blends. For a detailed review on the photophysics of fullerene-based OSCs, readers are directed to recent reviews from different perspectives, such as interfacial states[107–109], theoretical models[110, 111], as well as some comprehensive discussion.[112, 113] Reviews on NFA-based OPVs are quite limited and more experiment data is still needed.[114, 115]

2.4.1 Exciton Diffusion

Exciton can hop from one molecule to another via non-radiative energy transfer with a typical lifetime of nanosecond, and a diffusion length of 5-20 nm in amorphous and polycrystalline organic semiconductors.[116, 117] Such short diffusion lengths intrinsically limit the direct use of these strongly bound electron-hole pairs in photovoltaic applications. If the exciton diffuses to the interface before its recombination to ground state, it has chance to be dissociated to generate free charges. Otherwise, it will decay to the ground state via radiative

or non-radiative recombination. Some other unlikely competing channels include singlet fission and intersystem crossing. This initial competition between exciton recombination, and exciton diffusion and dissociation determines the initial efficiency for charge generation.

Morphology plays an important role in determining the fate of excitons. There are usually three phases in the polymer:fullerene BHJ: mixed phase, D phase and A phase. When donor and acceptor forms intermixed phase, there is no need for long exciton diffusion to find the interface where ultrafast generation of charge carriers occurs. For excitons generated in the pure phase, slow exciton diffusion may result in slow charge generation.

For NFAs, the exciton diffusion length can be higher, between 20 nm and 50 nm [40], with the exciton diffusion coefficient higher than 2×10^{-2} $cm^2 s^{-1}$ and being activationless. This is due to enhanced long-range energy transfer, rising from planar molecular structure, aligned molecular packing and higher chromophore density.[40] This results in exciton-exciton annihilation at very low excitation density. The lifetime of the single molecule can be obtained from a polysterene:molecule matrix where intermolecular interaction is minimised. The single exponential fitting can give lifetime longer than 100 ps. In the blend, donor and acceptor tend to aggregate and the formation of the intermixed phase is less seen from the sub-bandgap absorption spectrum. particularly for the low-offset blends, whether a CT absorption band exists or not is still an open question.

We measured the exciton diffusion length of PBDB-T to be 10 ± 3 nm using photon action spectra. Details can be found in Section 7.10. For other methods to determine the exciton diffusion length, please refer to the recent review papers. [116, 117].

2.4.2 Energy Transfer

Energy transfer is an important mechanism to direct the energy flow, for example, in natural photosynthesis. In organic solar cells, energy transfer happens from a high-bandgap material to a low-bandgap material. In fullerene-based blends, charge transfer is quite often observed but some reports also argue that ultrafast energy transfer between P3HT and PCBM occurs before the hole transfer process[118]. In state-of-the-art NFA-based BHJs, where the donor and acceptor absorb light in different regions, ultrafast energy transfer is also observed.[1] The following charge separation is more important to determine the overall device efficiency.[119] In particular in ternary blends when multiple interfaces exist, the control of exciton and charge flow is more complex.[120–123]

2.4.3 Charge Transfer and Charge Separation

Charge transfer is the key process to break the bound excitons to form extractable free carriers. Charge separation process is widely believed to consist of the initial dissociation of excitons (charge transfer, CT) at the D-A interface or near the interface[124] forming an intermediate CTS (electron-hole pair at the interface), and the following separation into free charges (charge separation, CS). The former process (electron transfer[50] or hole transfer[125]) is closely related to energy levels of blend materials and happens in less than 100 fs while the time scale of CS process is within 1 ps both in BHJ[126, 127, 30] or bilayer[128] devices with a critical separation distance of $\sim$4 nm[127, 129].

To investigate charge separation mechanism, morphology, electric-field and temperature dependent studies are performed with various electrical and optical characterization techniques. However, there is still no single model capable of reconciling all these observations. In the following content, several models are discussed including their strengths, weaknesses and related experimental evidence.

When considering CT states manifold, the lowest-energy or relaxed CT state is so-called a "cold" CT state. This cold CT state can be formed directly through sub-bandgap excitation or thermalisation after electron or hole transfer.

In the widely used Onsager-Braun model[130–133], this CT state is the only precursor of the free charges and dissociates when undergoing a diffusive walk. The dissociation yield $\phi(F,T)$ of CT states into free charges critically depends on the trade-off between temperature and field-dependent dissociation rate $k_d(F,T)$ as well as the decay rate $k_f = 1/\tau$, where τ is the lifetime of CT state,

$$\phi(F,T) = \frac{k_d(F,T)}{k_d(F,T) + k_f} \tag{2.64}$$

where F is the electric field and T the temperature.

This theory can fit the current-voltage response[134–136] in organic solar cells. The inconsistencies sometimes arise from the fitting parameter, for example in mobility-lifetime product (not shown here), is extremely large. In the context of physics, the assumption of thermal equilibrium between CTSs and free charges is incompatible with the observation of charge separation on the ultrafast timescale. The dissociation field formula is in sharp contrast with the reported electric field and temperature-independent charge generation observations[38] in time-resolved experiments.

Rather than consider one state in Onsager-Braun model, the manifold CT states should be included in the dissociation model. The excess energy depends on the energy difference between electron affinities of the acceptor and ionization potentials of the donor and is usually

defined as below or between LUMO levels.

$$\Delta G_{\mathrm{CS}} = E_g - (IP_D - EA_A) \text{ or } \Delta G_{\mathrm{CS}} = LUMO(D) - LUMO(A) \tag{2.65}$$

In the context of cold dissociation, this excess energy would dissipate and does not influence charge separation at all. Strong supporting evidence comes from the similar internal quantum efficiency of sub-bandgap photon with high-energy excitation[137] and from efficient charge generation from sub-bandgap excitation in both steady-state measurement[138] and time-resolved measurement[139, 140].

Different from dissociation from relaxed CT states, vibrationally hot CT states can also dissociate into free charges, termed as "hot dissociation". Even though the excess energy dissipated in the initial CT process hardly influences charge transfer[141, 142], it might facilitate the charge separation process[143]. The timescale for hot CT relaxation was reported within 1 ps by recent photocurrent measurements[144, 30] and terahertz spectroscopy[141], setting the competition time for efficient charge separation from hot CT states[142, 145, 146].

There are various ways to explain how this excess energy influences the dissociation of the interfacial CTS. For example, excess photon energy, inheriting[142, 145, 147] from ultrafast CT into hot CTSs by surpassing exciton relaxation, is supported by internal quantum efficiency measurements [142, 148, 149], Transient Absorption Spectroscopy (TAS)[144], fast PL[145], two-dimentional electronic spectroscopy (2DES) [147] and PPP [97], leading to faster electron transfer rate and higher charge generation. On the other hand, time-delayed collection field (TDCF) on a 10 ns time resolution also suggests that excess photon energy does not increase current density in BHJ devices, although the time scale is too slow to make relevant observations on exciton relaxation and ultrafast charge transfer.[150] The general conclusion is that large excess energy is not necessarily needed for efficient charge generation in some systems. In this way, the reduction of energy offset by rational material design could potentially increase the open-circuit voltage (V_{OC}) and the device performance.

In parallel, a number of quantum mechanical models have been proposed, where the electronic dynamics is determined by delocalisation and vibronic effects[30, 151, 152]. There are various forms of delocalisation, including intramolecular[30] and intermolecular[38, 153] delocalisation as well as exciton delocalisation[128, 145, 154]

In the delocalisation regime, excess energy helps the charges to sample a larger portion of the density of states (DOS)[155]. Some hot CTSs are delocalised, which allows long-range electron-hole separation, lowering the binding energy of CTSs[152]. The cold CTSs are still present[129, 156] and are proposed to act as trap states[153, 157], which geminately recombine into ground states without contribution to charge generation yield at early time[142].

Intermolecular delocalisation consists of hole delocalisation and electron delocalisation.[111, 153] Several recent studies focus on electron delocalisation from fullerene clusters and its influence on CTS energies[127, 38, 146, 156, 158, 159]. One important step is the model by Savoie et al. proposing the direct coupling between excitation and fullerene acceptor[38]. Fullerene aggregation changes the availability of CS states, thus energy level alignment is possible. The direct branching between the $S_1 \rightarrow$ CT and $S_1 \rightarrow$ CS channels[129, 142, 153] rules out the CTSs as the free charge precursor. Another possible explanation could be the hybridisation of absorption of donor component and hot CTSs[156, 160, 161]. However, some evidence opposes the direct coupling model.[136]

Recently, long-range charge separation has been explored by various spectroscopic techniques. By tracking the time-resolved electro-absorption signal composed from TAS, Gelinas et al.[127] observed ultrafast long-range charge separation within 40 fs. This "ballistic" charge generation could be explained by their simulation based on delocalised or fully coherent dynamics. In another study, by monitoring molecular conformation dynamics by time-resolved resonance-Raman spectroscopy, the structural evolution of the polarons was not seen between first 300 fs and the following 50 ps[126], suggesting long-range charge separation within 300 fs. However, long-range charge separation was not observed in electric field-induced second harmonic experiment[162], which might be due to the nature of the microscopic probe.

The role of entropy in charge separation has received increased investigation.[163–165] With time-resolved two-photon photoemission spectroscopy, Monahan et al.[165] observed e-h pairs climbing up the Coulomb potential within 100 fs. The increase in entropy came from larger DOS, which compensated the increase in enthalpy. Feng et al.[163] investigated the entropy by considering the temperature-dependent nature of entropy in a free energy diagram.

In the NFA-based blends, the striking feature is the efficient charge generation under low driving energy.[10] Energy level alignment brings the energy of CTS closer to the local exciton (LE) state. As the electronic coupling between CTS and ground states changes the radiative and non-radiative rate to the same degree, the overall EL efficiency does not change. To explain the EL efficiency, another state, LE state, and its associated coupling with CTS must be included.[166] Hybridisation of CT and LE states rationalises the improved EL efficiency of CTSs by intensity borrowing mechanism from more luminescent LE state.[39, 167, 168]

Charge generation is a convolution of exciton diffusion and charge transfer. Exciton diffusion does not seem to become a limiting factor, and the observed slow charge generation is assigned to slow charge transfer.[39] Experimental evidence in the literature mainly comes

from a slow rise of the donor GSB when exciting the low-bandgap NFA. This donor GSB rise in some papers is shown to correlate with the decay of the acceptor GSB.[169] However, we note that hole transfer from A to D should not give a decay in acceptor GSB. A more reasonable explanation should consider the overlapping features in that region, where acceptor polaron possibly also contributes.

To further increase the device voltage output, there is interest to understand where is the limit for the energetic offset and non-radiative recombination loss. Blends with zero HOMO offset has shown efficiency over 10% with a hole transfer rate of several ps.[169] Even a negative HOMO offset still shows a slow hole transfer at 400 ps (offset = -50 meV)[169] and device efficiency of 6.6% (offset = -30 meV)[170]. A recent study blending a polymer with various ITIC derivatives gives decent device efficiency (>10%) with a HOMO offset greater than 150 meV, while the device efficiency with IEICO derivatives only gives 2.76% and 0.25% at a HOMO offset of -100 meV and -20 meV, respectively.[171] Non-radiative recombination loss is linked with the low-offset from the hybridisation picture[167, 168]. However, in high-offset blends, small voltage loss below 0.6 eV can also be achieved[172]. Currently, non-radiative recombination loss as low as around 100 meV can be achieved when the energy of CT state is high ($\sim$2.5 eV).[46] It is still a challenge to achieve low non-radiative recombination loss ($\sim$100 meV) at low energy level of CT states ($\sim$1.5 eV).

Charge generation mechanism remains the central topic to understand the operation of organic solar cells. Many questions remains open in NFA-based OSCs, and future temperature-dependent and field-dependent will probably undercover more underlying physics.

2.4.4 Geminate Recombination

After charge transfer, the electron and hole on different materials are still Coulombically bound to each other. The transition from this CT state to the ground state before its separation is defined as *geminate recombination*. In many BHJ blends, geminate recombination represents an important loss mechanism, in particular at short-circuit condition where the non-ideal EQE arises primarily from geminate recombination[173–175] as the nongeminate recombination at solar illumination is very low[176].

From spectroscopic measurements, geminate recombination, a monomolecular event, is identified from the fluence independence of charge population. The dissociation of geminate charge pairs is often assumed to be a diffusive event, described by Onsager theory as mentioned earlier. The decay curve can be a single exponential[174], or non-exponential if this geminate pair diffuses along the interface. In fullerene-based solar cells, geminate recombination is usually not significant as long-range charge separation leads to free carriers

directly. In NFA-based OSCs, geminate recombination represents an important loss channel. This loss is also related to which component is initially excited.[177]

2.4.5 Nongeminate Recombination

In addition to geminate recombination, another important loss mechanism is nongeminate recombination mainly from the recombination of charge carriers from different excitons in BHJ.[178] This process is also called *bimolecular recombination*, referring to a reaction involving two distinct species. At open-circuit condition, the total field imposed by the electrodes and the external field tends towards zero, resulting in a slow charge collection time and thus a higher charge-carrier density in the active layer. Nongeminate recombination are more likely to occur and all the carriers finally recombine to the ground state. These slow events can be measured with transient absorption[179], TDCF[150], and transient photovoltage[180]. Nongeminate recombination is very complex, and may relate to the domain purity, vibration, morphology and so on.[181, 95]

An equilibrium between free carriers and CT states determines the open-circuit voltage.[182] From another perspective, multiple separation and recombination events happen within the lifetime of these excited states[183]. Such equilibrium can be changed upon temperature and is used to probe the binding energy of CT states.[184, 46]

Nongeminate recombination can generate multiple excited species, in particular triplet CT states, and the following local triplet states. As the lowest excited states, triplet states can be an important loss channel in some fullerene-based blends[185, 179]. There is one report on triplets in NFA-based blends, but assignment of local triplet and CT states is ill defined[186, 187]. Long-lived PL, matching the EL spectra of OSC blend, has been observed and interpreted from radiative recombination of reformed CT states.[188] This concept has not been heavily explored and merits future efforts.

Chapter 3

Experimental Methods

3.1 Steady-State Spectroscopy

3.1.1 UV-Vis Absorption Spectroscopy

Spectroscopic studies often start with the measurement of steady-state absorption. UV-Vis absorption spectroscopy is a standard technique to probe optical transitions in the ultraviolet and visible region of the spectroscopic spectrum, where semiconductors absorb light. The absorption of samples, such as solutions and films, is measured on a UV-Vis Spectrometer (HP 8453, Figure 3.1), covering the spectral range between 190 nm and 1100 nm. To correct the background signal, the absorption of pure solvent (or spectrosil quartz for the solid-state sample) is also needed to be measured.

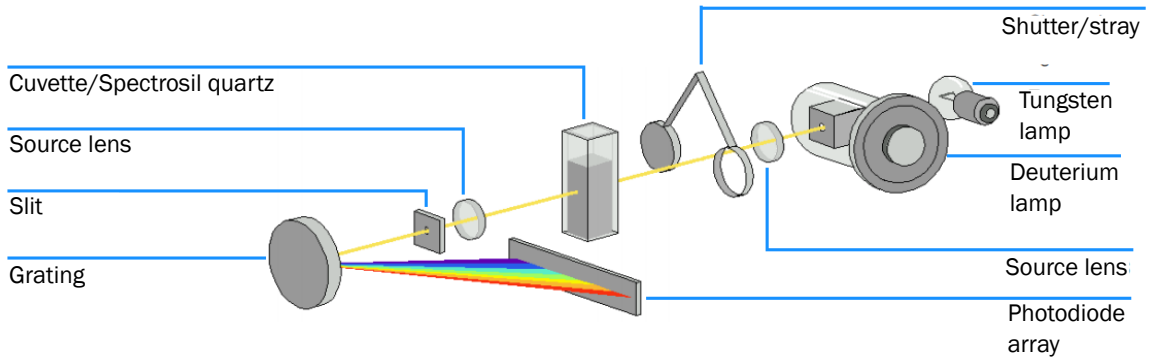

Fig. 3.1 Schematic diagram of the Agilent HP 8453 UV-Vis absorption spectrometer, adapted from the user manual.

For solution samples, the relationship between the measured absorbance (A) and the molar extinction coefficient is the *Beer-Lambert law*,

$$A = \varepsilon cl \tag{3.1}$$

where ε is the molar extinction coefficient (L $mol^{-1}cm^{-1}$), c is the sample concentration (mol L^{-1}) and l is the light path. The thickness of the used cuvette is usually 1 mm (110 QS, Hellma). For solid film measurements, the film is spin-coated on top of an optically transparent quartz spectrosil. The absorbance together with the film thickness can be used to calculate the excitation density (cm^{-3}).

From the absorption spectrum, one important message we can determine is the absorption onset, ie. the bandgap. We take NCBDT as an example, a small molecule that will appear often in later chapters. Figure 3.2 shows its absorption spectra taken from the solution and the solid state. The absorption onset in the solid-state film is determined to be around 845 nm (1.46 eV), seen as the red line. It is clear that this fitting is not perfect, mainly due to disorder in organic semiconductors. The spectrum of film absorption is shifted from the spectrum of solution, possibly due to the energy stabilisation from the polarisation effect in dimer or formed aggregate in the solid state. The spectral shape is modulated by the vibronic coupling. We convert the absorbance from wavelength (nm) to energy (eV) in Figure 3.2 (b). It should be noted that *Jacobian correction* should be applied as the signal after grating is taken per wavelength.[189] The decomposition of the whole spectrum into multiple Gaussian peaks works very well, but the peaks are not equally spaced probably due to multiple vibration modes, such as C-C (150 meV) and C=C (200 meV) stretching modes. From the amplitude of Gaussian peaks for 0-0 and 1-0 transitions, the estimated Huang-Rhys factor is $S = 0.27$, signifying a small relaxation energy λ as $S = \lambda/\hbar\omega$.

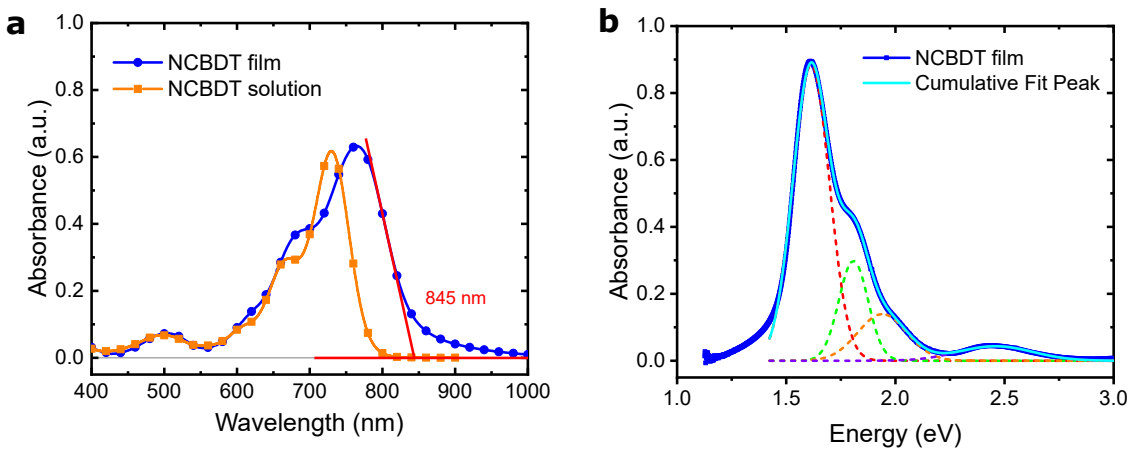

Fig. 3.2 Absorption of NCBDT in wavelength and energy scale. (a) The absorbance spectrum of NCBDT film and solution using nm units; the bandgap is determined to be at around 845 nm. (b) The absorbance spectrum of NCBDT film in eV unit; the spectrum is well fitted with multiple Gaussian peaks.

3.1.2 Photothermal Deflection Spectroscopy

UV-Vis absorption is not capable of measuring samples suffering from scattering, interference or low absorbance. Scattering is an issue when the roughness of material is comparable to the light wavelength, in particular in nanoparticle systems, or uneven surfaces. Low absorbance, due to a small transition dipole moment, is often seen in sub-bandgap transitions, forbidden transitions or some trap states.

To complement the limitation of UV-Vis absorption, a more advanced technique called photothermal deflection spectroscopy (PDS) developed around 1980[190], uses the heat emission from non-radiative relaxation processes to detect the absorbed light. More explanation is in the next paragraph. PDS is not only immune to optical effects such as interference and scattering, but also capable of measuring absorbance down to 10^{-5}.

Figure 3.3 illustrates the principle of PDS measurements. Films spun on quartz substrates immersed in an inert liquid FC-72 Fluorinert® (3M Company) are used for the measurements. A modulated monochromatic beam as pump light shines on the sample, which after absorption produces a thermal gradient near the sample surface through nonradiative relaxation induced heating. This results in a refractive index gradient in the area surrounding the sample surface. Another fixed wavelength CW laser, acting as the probe beam, passed through this refractive index gradient, causing a deflection detected by a photo-diode and lock-in amplifier, which is proportional to the absorbed light at that particular wavelength. Scanning through different excitation wavelengths with a grating generates the complete absorption spectrum.

The sharpness of absorption tail is quantified as the Urbach energy, which is correlated with the materials' aligned morphology, representing the degree of disorder. Conjugated polymers are naturally disordered semiconductors with a high Urbach energy, but some exceptions exist, for example one high mobility polymer was shown to havea low Urbach energy.[191]

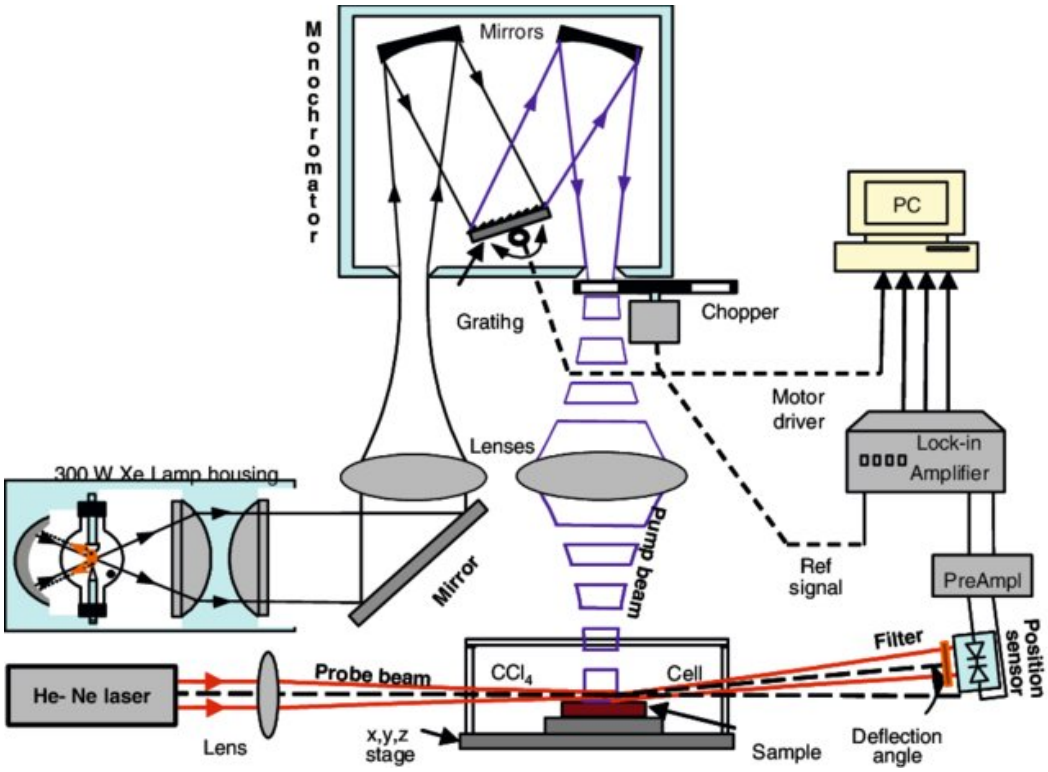

Fig. 3.3 Illustration of PDS measurements. Broadband light from xenon light was dispersed through a monochromator into a narrow-band beam. The beam is modulated by a chopper and then sent onto the sample area. The probe light from He-Ne laser transmits through the area near the sample surface, and the refractive index gradient deflects the light, which is measured by a photodetector. The electronic signal is amplified and red out through a lock-in amplifier at the chopper frequency. Figure from [192].

In organic solar cells, PDS is capable of measuring low-absorbing CT states at the D-A interface. This peak can be quite obvious as a shoulder when CT state is well separated in energy from the singlet state, for example, in fullerene-based OSCs.[193] However, in recent NFA-based OSCs where CT state are almost energetically in resonance with singlet state, the detection of CT absorption becomes difficult and the assignment of species is tricky. The hybridisation effect which introduces electronic coupling between singlet state and CT state [167] seems to suggest that the absorption may look like a single state.

3.1.3 Photoluminescence

After the absorption of photons, the excited states can return to the ground state by emitting a photon at a lower energy. Photoluminescence spectroscopy enables us to probe the nature of these emissive transitions. The high spectral resolution (down to 1 nm), a wide detection window (<1 ps to ms) and a high dynamic range can observe subtle spectral shift in the emission lineshape over time, enabling assigning different emission species and understanding the photophysics of the studied system.

In organic systems, emission generally occurs from the lowest vibrational level of the excited state (for example, fluorescence from the singlet state or phosphorescence from the triplet state). This state usually undergoes radiative transition to the vibrational levels of the ground state, resulting in a 'mirror image' of the absorption spectrum. There are two main set-ups for PL measurements. A commercial FLS 980 spectrometer (Edingburgh Instruments) with excitation mode and emission mode, covering 200-870 nm (R928P PMT detector) and NIR region up to 1.65 μm (InGaAs detector). The other set-up is home-built with a grating spectrometer (Shamrock SR-303i, Andor) equipped with visible and NIR detectors, and is mainly used for measuring PL quantum efficiency as well as temperature-dependent and magnetic-dependent PL.

Photoluminescence quantum yield (PLQY) quantifies the luminescent efficiency of a material, the ability of turning absorbed photons into emissive photons. A method developed by deMello et al. in our group two decades ago was widely used in the community.[194, 195] This method uses the integrating sphere coated with a diffusely reflecting material that can measure the amount of light in the sphere, irrespective of its angular distribution. As shown in Figure 3.4, three measurements are performed: one with the laser hitting the sample inside the sphere, a second one where the laser is not directed onto the sample, and a third one when the sample is absent in the sphere. By comparing the laser and emission spectra from each of these three measurements, the number of photons absorbed and emitted by the sample can be determined.

From the above procedure, PLQY measurement does not seem to be difficult, but to get reliable data is not easy. There are several issues that need to be considered.

1. **Stability.** Our calculation assumes that the laser intensity does not fluctuate in the measurement period. For three sub-measurements, it can take roughly one minute. A small variation can cause some uncertainty in the final value, in particular, for samples with close-to-unity PLQY, sometimes leading to PLQY values of >100%. The stability is also important for fluence-dependent measurement, which takes a longer time to finish. The laser performance degrades during usage and greatly influences its stability and the accuracy of the measured data. One easy way to minimise this

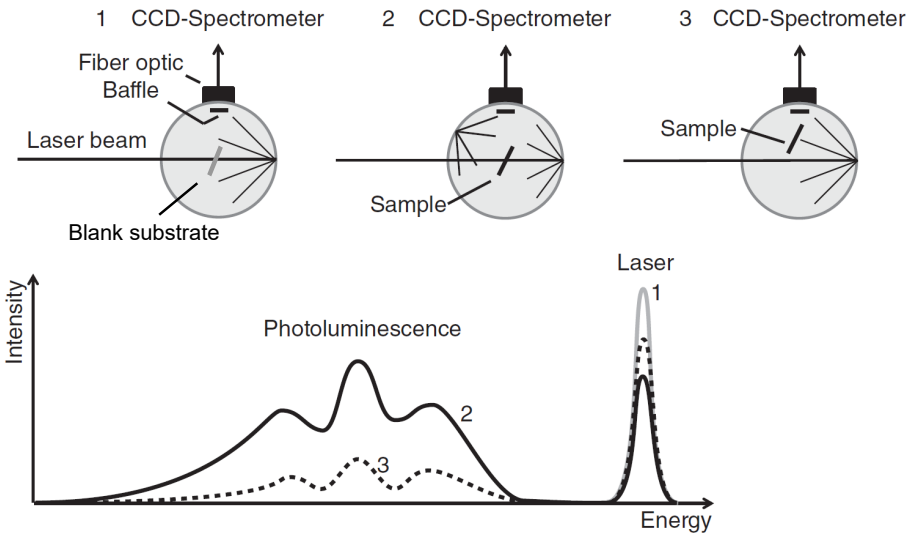

Fig. 3.4 Illustration of deMello method to measure PLQY. 1. The laser beam directly hits the blank substrate. 2. The laser directly hits the sample. 3. The sample is indirectly excited by the diffused light. Adapted from [196].

effect is to couple some light out to a detector and monitor the power stability; to remeasure the data is the simplest solution, when there is a sudden change in power during measurements,

2. **Calibration.** The measured spectra is usually calibrated by a broadband light source, (SLS201L, ThorLabs). The calibration file will change if anyone touches the connection fibre, the grating setting, or used filters. This becomes more serious when different configurations are used, such as low-temperature measurements. One can fix these settings and update the calibration file at a certain period. The best practise is to record the calibration file in the measurements every time.

3. **Contamination.** The integrating sphere can be easily contaminated, in particular by solution samples. Careful background check should be performed before any actual measurement. Magnet is a good way to fix the solid-state film sample onto the holder. The holder should be wrapped with non-luminescent materials, such as PTFE. Repainting the integrating sphere is not cheap and takes time.

The uncertainty of deMello method depends on the PLQY itself. For efficient emitters (PLQY > 90%), the way that it calculates the absorption puts a large uncertainty on the measured value. Recently, Salleo et al. has developed a new method capable of measuring PLQY of quantum dots at 99.6±0.2%.[197]

High PLQY is an important quantity to screen organic materials for light emission application. Top performing organic materials have reached close to 100% PLQY through rational design of molecular structure. In contrast, materials for donor:acceptor photovoltaic blends generally have a PLQY around 1-5%. This low value is believed not to be a problem as long as the eventual charge generation is efficient. However, this paradigm has been changing when the CT state can be brightened via intensity borrowing from the singlet state. A rational strategy is still absent to obtain both strong light absorption and efficient light emission of organic materials.

3.2 Time-Resolved Spectroscopy

3.2.1 Time-Resolved Photoluminescence Spectroscopy

Time-resolved photoluminescence (TR-PL) spectroscopy provides information about the radiative recombination lifetime from excited states and shows dynamics that is averaged out in the steady-state measurement. The steady-state PLQY can be expressed as the ratio of radiative recombination rate (k_{rad}) and non-radiative recombination rate ($k_{\text{non-rad}}$),

$$\text{PLQY} = \frac{k_{\text{rad}}}{k_{\text{rad}} + k_{\text{non-rad}}} \tag{3.2}$$

TR-PL gives the total decay rate $k_{\text{rad}} + k_{\text{non-rad}}$. Together with the measured PLQY, the intrinsic k_{rad} can be calculated.

In our lab, we have three different time-resolved set-ups to cover different time windows. For the very early time (<100 ps), we used transient grating photoluminescence spectroscopy developed by Justin Hodgkiss et al. [198] with a time resolution of ∼100 fs. Time-correlated single photon counting (TCSPC) is a widely used technique that can cover 300 ps-200 ns and intensified charge-coupled device (iCCD) can record until 1 ms.

TCSPC is a very robust technique to measure the decay curve of light emission. It counts the timing of single-photon emission starting from periodic pulse excitation. The random single photon emission by virtue of quantum mechanism is detected by a photomultiplier tube. Micro channel plate then amplifies the weak signal of single photon emission. The probability of receiving two photons per cycle needs to be low otherwise pile-up effects will distort the decay curve. This condition is met simply by reducing the light illumination on the sample. In practice, the ratio of detected emitted rate should be at most 1 to 5% of the excitation rate. The time resolution is influenced by the laser pulse, detector timing error, and associated electronic and optical components, characterised by instrument response function. In our setup, the resolution is $\sim$ 100 ps. The data noise comes from Poisson noise statistics which is square-root of the data point so that the noise on each data point is different. This has big consequences for the numerical analysis as each data point needs to be properly weighted. This also gives a high dynamic range typically at $10^4 : 1$. Three laser heads at 371 nm, 407 nm, and 470 nm (PicoQuant) are available to be used as the excitation source.

In contrast to TCSPC, iCCD is a 2-dimensional detector array that measures the whole spectrum at once. The detection range depends on the photodetector type. For the enhanced visible one, it can easily cover 350 nm to 900 nm, even to around 1100 nm. Although the time resolution (∼2 ns) is poorer than that with TCSPC, this set-up can measure up to 1 ms over a dynamic time range of 6-8 magnitudes, making it the preferred technique

for measuring long-lived PL. Due to the gated amplification of the signal, iCCD is able to selectively enhance PL signals at a given time delay, signals that TCSPC would not be able to resolve. The excitation light comes from a NOPA seeded with a Ti:Sapphire ultrafast laser. The pump light pulses from the NOPA, at a 1 kHz repetition rate. The collected PL is focussed onto the slits of the spectrograph (Shamrock 303i, Andor) coupled to an iCCD (iStar DH740, Andor).

3.2.2 Transient Absorption Spectroscopy

TR-PL is only sensitive to bright or emissive states. For non-emissive species, like triplet states or polarons, we can also find ways to detect them by monitoring them in the excited state. The UV-Vis spectrum gives the optically allowed absorption from the ground state (S_0) to higher-lying state (S_n). Excited states, such as singlets, triplets or polarons, can be optically excited to even higher energy states. This type of absorption has different spectrum from the ground-state absorption. In consequence, every electronic state has its own distinct and characteristic spectrum of absorption and emission, depending on the nature of the state and the DOS. This excited-state absorption measurements are called *transient absorption spectroscopy* (TAS).

The commonly observed features include ground state bleach (GSB), stimulated emission (SE), and photo-induced absorption (PIA). As shown in the bottom figure in Figure 3.5, all these individual spectra contribute to the overall measured signal. By comparing and analysing the temporal evolution and spectral features, the whole spectra can be decomposed into these individual absorption features and further related to the corresponding electronic states. Due to the principle of TAS measurements, i.e. by comparing the transmission spectra of excited and unexcited sample, the fraction of states being monitored typically ranges between 10^{-2} and 10^{-5}. Depending on the absorption cross-section, the ratio of real population can be worked out.

Using a broadband probe light, its transmission through the sample is recorded with (T_{on}) and without (T_{off}) the pump pulse. The difference in transmission (ΔT) after normalization by T_{off} generates the relative pump-induced change, originating from the creation of excited states and depopulation of the ground state.

$$\frac{\Delta T}{T} = \frac{T_{on} - T_{off}}{T_{off}} \tag{3.3}$$

The delay between the pump and probe light is either mechanical (typically between ps and ns) or electronic (typically between ns and ms).

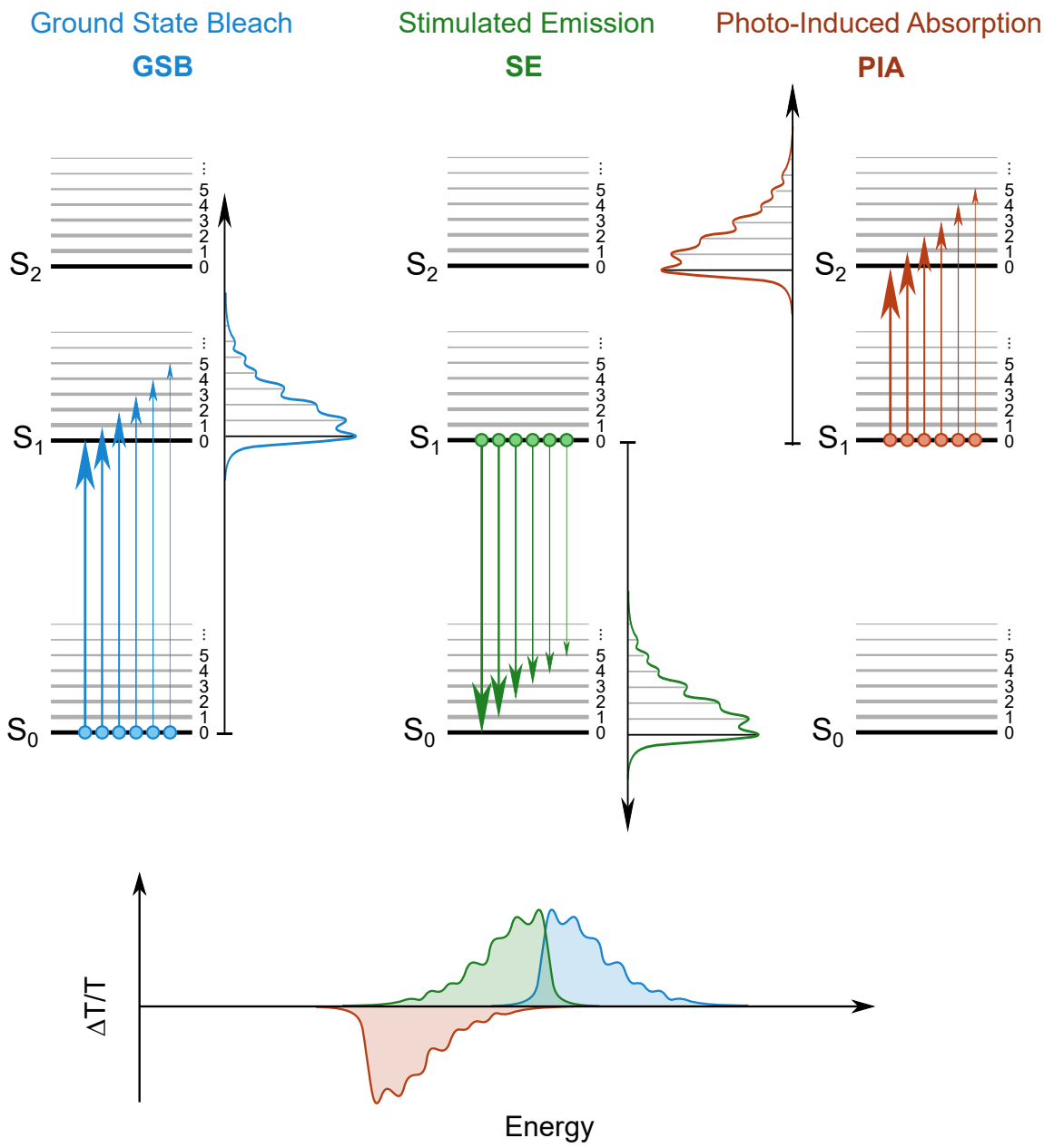

Fig. 3.5 Spectral signatures of optically allowed transitions of a singlet exciton, including ground state S_0 and excited state S_1 and S_2 as well as their vibrational levels. The GSB (blue) originates from $S_0 \rightarrow S_n$ transition, and the inverse process $S_0 \leftarrow S_1$ contributes to SE (green). The PIA signal results from $S_1 \rightarrow S_n$ transitions, usually in the lower energy. Due to their origin, GSB and SE is positive in $\Delta T/T$ and PIA is negative. Figure from Dr. Andreas Jakowetz, used with permission.

The main features, like GSB, SE and PIA, have different origins. GSB comes from a change in ground-state population. After excitation, i.e. depopulation of the ground state, the transmitted probe light is less absorbed and the transmission difference gives a positive

signal and is similar to the ground-state absorption spectrum. GSB disappears only these excited state recombine to the ground state, thus GSB cannot differentiate singlets, triplets and polarons. SE appears only after the formation of excited state. The SE spectrum is similar to the PL spectrum and is usually related to the first excited singlet state S_1, giving a negative signal on the transmission. It is notable that SE can also be observed from CT states, which may have singlet character.[199] PIA signature, usually in the red to IR region, is not present when the molecules are in the ground state, thus gives a negative signal after transmission. Like GSB, all excited states can contribute to the PIA signal. However, they are likely energetically separated and have different decay kinetics, providing a convenient way to assign excited-state species.

Stark effect is a type of signal that does not arise from certain states, but from the shift in absorption in the presence of the electric field. This field is in nature electron-electron interaction from the Coulomb interaction of separating electrons and holes, influencing the surrounding medium. The most significant signal is $S_0 \rightarrow S_1$ transition, giving the shape of the first derivative of the steady-state absorption spectrum. This effect recently has received much attention as a sensitive probe to visualise the charge separation in organic solar cells.[127, 200]

Pump-probe spectroscopy in this thesis is performed in two labs, Friend Lab in Cambridge and Durrant Lab in Imperial College. For the Imperial setup, ultrafast pulses at $\sim$800 nm from a regenerative Ti:Sapphire amplifier system (Spectra Physics, Solstice) were sent into TOPAS-Prime (Light Conversion) to generate tunable pump pulses ($\sim$355-2600 nm). Another portion was sent into a delay stage. Both beams are then sent into a commercial compact transient absorption spectrometer (HELIOS, Ultrafast Systems). The delayed 800 nm light generates broadband probe pulses ($\sim$800-1500 nm) using a substrate made of yttrium aluminum garnet. Part of the probe light was split and used as the reference to reduce pulse amplitude fluctuation. Both probe and reference beams are sent into their corresponding fibres and measured with spectrometers. The beam size of pump and probe pulses were estimated to be $\sim$0.5 mm^2 and the time resolution of pulses to be $\sim$200 fs.

The setup in Cambridge is more complex. After white light generation, the probe light needs to transmit via a long distance before arriving at the sample. This transmission attenuates the light significantly thus the low intensity on the detector cannot fully use its dynamic range. We amplify the white light using the home-built broadband non-linear optical parametric amplifiers (NOPAs).[201] Part of the fundamental light at 800 nm between 5 to 10% is tightly focused into a c-cut sapphire crystal, generating the broadband white light (as seed) via self-phase modulation. The majority of the 800 nm light is doubled in frequency, via transmitting through a β-barium borate (BBO) crystal (θ=29.2°). This intense 400 nm

is used as the pump light. Both pump and seed light are focused into another BBO crystal, separated by a shallow angles depending on the desired spectral range. To amplify the visible region, BBO with θ=31.3° is used; for NIR region, we use BBO with θ=29.2°, depending on the crystal phase-matching curves. The probe spectrum is at best to overlap with the sample absorption so that similar light intensity on the detector can give a good signal-to-noise ratio in a broad spectral range. The probe light from NOPA outputs are equally separated into two parts, one of which serves as the actual probe light and the other being a reference light to calibrate the shot-to-shot fluctuation of the setup.

Narrow-band pump pulses are generated from a TOPAS (Light Conversion) via co-linear combination of optical pulses using non-linear mixing crystals. The light can be tuned between 190 and 2600 nm, maintaining the time resolution of around 100 fs. For shorter light duration, a broadband visible NOPA is first applied to generate a broadband spectrum. The following compression via a pair of dielectric chirped mirror (Layertec 109811) can achieve sub-40 fs time resolution. To further reduce the duration, a combination of chirped mirror and a spatial light modulator can achieve sub-20 fs.[202]

The time resolution needs to be compatible with the precision of delay stage. For ps-ns time delay range, a linear servo motor stage (M-IMS300CCHA, Newport) with 0.7 fs step resolution is used; a piezo driven stage with < 0.2 fs step resolution (SLC-2490-S, SmartAct) can be used for better step resolution. Longer time delay (>2 ns) is realised using an electronic delay generation (DG 535, Stanford Research Systems) to trigger a Q-switched Nd:YVO_4 laser (AOT-YVO-25QSPX, Advanced Optical Technology) as the pump source. This slow ns laser gives the fundamental of 1064 nm, and higher harmonic wavelength (532 nm or 355 nm). To create pump-on and pump-off pulse sequence, a mechanic chopper (MC2000, Thorlabs) modulates the light at 500 Hz, half of the laser frequency. After overlapping at the sample position, the pump and probe pulses are dispersed with a grating spectrograph (Shamrock SR-303i, Andor) and measured on separate visible-enhanced InGaAs detector arrays (Entwicklüngsburo Stresing).

Pump-probe spectroscopy and its multidimensional extensions are well-developed methods to study electronic and structural dynamics of optoelectronic material systems, like solution and solid-state thin films. However, this approach also has several potential shortcomings, such as linear response to optical pump intensity (limited resolvable signal), overlapping spectroscopic signatures, limited spatial resolution and certain requirement on thin film quality.[203] This situation is more severe for optoelectronic devices, such as solar cells at working condition, and functional material at nanoscale. For organic solar cells, the various photophysical processes span over a wide time window, for example, charge generation to be sub-ps and charge recombination to be ns-us. However, an important intermediate

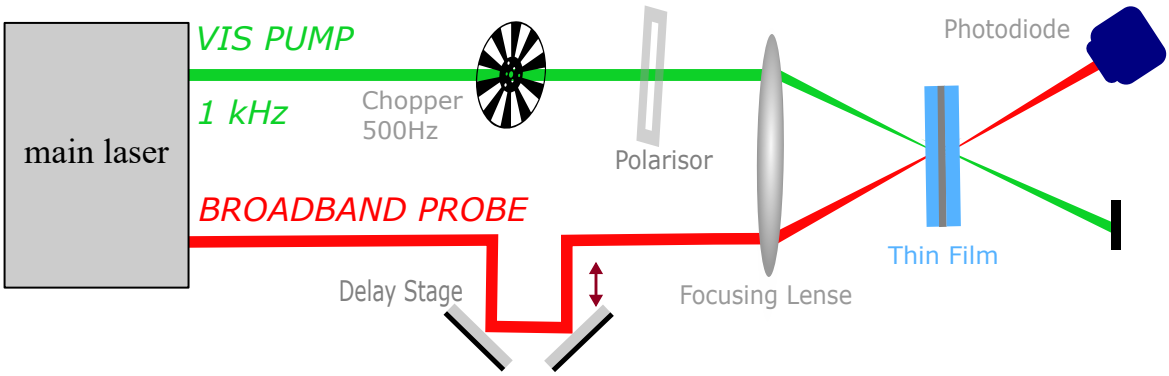

Fig. 3.6 Schematic arrangement of the transient absorption setup. The main laser seeds two amplifier units (either OPA or NOPA) to generate pump and probe lights at 1 kHz. The pump pulses are chopped at 500 Hz, and the probe light is delayed. Both pump and probe light are spatially overlapped on the sample and the transmitted probe light is later dispersed and measured with a detector array.

state, charge-transfer state, has the same spectroscopic signature as charge-separated states. Electro-absorption, arising from the separation of CT states, is difficult to decompose. In next section, we will introduce another spectroscopic technique that is sensitive to the bound interfacial CT states.

3.2.3 Pump-Push Photocurrent Spectroscopy

For optoelectronic devices, one promising alternative to all-optical methods is the hybrid spectroscopic method with electrical detection. The simplest and the most widely used technique is photon action spectra (commonly known as external quantum efficiency (EQE) spectra). Due to the absorption-sensitive nature, photocurrent spectroscopy does not suffer from scattering and reflection artifacts. The main limitation is that the steady-state technique is not capable of time-resolving the dynamics of excited states.

Using photocurrent detection, the first work to resolve excited-state electronic dynamics was reported by Lukin and co-workers in 1981.[204] This steady-state technique was limited to the system where the intermediate excited states are long-lived. To observe the dynamics of intermediate states with a shorter lifetimes, a two-pulse pump-push modification was developed which combines the sensitivity and device relevance of electronic methods with the excitation selectivity, and ultrafast time resolution of optical techniques.[205] Combining the development in solid-state ultrafast lasers, a pioneering work by Frankevich et al. reached sub-ps time resolution and observed the precursor states for charge generation in organic solar cell.[206] This triggers a more detailed study comparing various techniques.[207] Despite the initial success, the visible push realisations does not lead to wide application. The main reason can be two-fold: (1) the high photon energy of visible push lights is sufficient to

generate generate charge carriers through sub-bandgap and above-bandgap states; (2) these strong visible light strongly perturbs the excited-state dynamics.[203]

The limitation of using high-energy push light was overcome using an IR push pulse that is non-resonant with the absorption in the ground state.[30] This IR light can excite the intermediate state into higher-lying states that can couple with other electronic states via a phenomenon, called *vibronic coupling*. Here, we formally name it as *pump-push photocurrent* (PPP) spectroscopy. This technique measures the change in photocurrent as a result of device interaction with IR light pulse. First, the visible 'pump' pulse excites the molecular system and triggers the current flow in the device. Then, an IR 'push' pulse induces the change in the material system that may modulate the current flow. PPP watches the formation and dissociation of bound interfacial CT states, providing a simple quantity to quantify the charge-separation efficiency. This technique is later applied into quantum dot solar cells[208], and oragnic-inorganic hybrid systems[209, 210]. Further applications include use of a pulse pair to generate a broadband excitation of vibrational mode and see their influence on charge transport.[211]

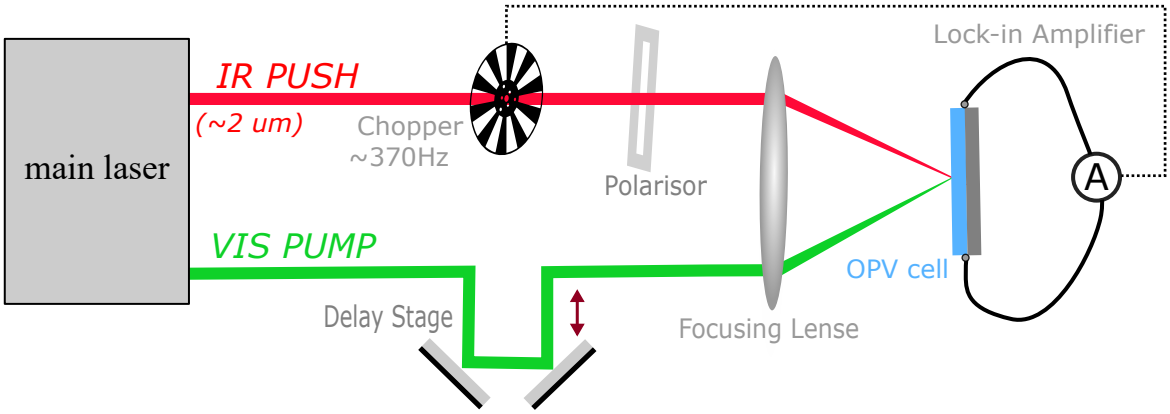

Fig. 3.7 Schematic arrangement of the pump-push photocurrent setup. The main laser seeds two amplifier units (either optical parametric amplifier or NOPA) to generate pump and push pulses at 1 kHz. The push pulses are chopped at ~370 Hz, and the pump light is delayed. Both pump and push light are spatially overlapped on the sample and the push effect on the device is measured with a lock-in amplifier synced with the chopper. In organic solar cells, for example, the pump light excites the material system and exciton forms in the organic materials. After the formation of charge-transfer (CT) states at the donor-acceptor interface, the infra-red light can push relaxed CT states into vibrationally hot CT states which couple with charge separated states. Some of these states that would recombine will contribute additional photocurrent to the external circuit in the device operation. Such total effect as photocurrent is detected, which is related to the number of bound CT states at the interface.

Measurements in Chapter 4 and 5 were performed in Cambridge. Ti:Sapphire amplifier system (Spectra Physics, Solstice) generated ultrafast 100 fs pulses at ~800 nm from a

regenerative 1 kHz. A portion of this power was taken to produce visible pump pulses (with the energy of $\sim$1 μJ per pulse) at $\sim$540 nm through a NOPA, while another portion was used to pump a TOPAS, generating the near-infrared push light at $\sim$2 μm. Pump and push pulses were focused onto the same spot ($\sim$1 mm^2) on the short-circuited device. The reference photocurrent (J), generated with the pump pulses, was recorded by a lock-in amplifier (SRS 830, Stanford Research System). The push pulses were modulated by a mechanical chopper (MC2000, Thorlabs) at $\sim$370 Hz. This push-induced effect was detected by the synchronised lock-in amplifier and was recorded as dJ.

The data in Chapter 7 was taken in Bakulin Group in Imperial College London. A 4 kHz Ti:sapphire regenerative amplifier (Astrella, Coherent) generated $\sim$35 fs pulses at $\sim$800 nm with a total power of 7 W. A portion of this was fed into an optical parametric amplifier (TOPAS-Prime, Coherent) to generate 1140 nm which was converted into 570 nm pump pulses by second harmonic generation in a BBO crystal. Another portion was fed into a separate optical parameter amplifier (TOPAS-Prime, Coherent) to generate the $\sim$2 μm push pulses. Both pump (1.05 μJ cm^{-2}) and push pulses were focused onto the same spot ($\sim$0.5 mm) on the short-circuited devices. The reference photocurrent (J), generated by the pump pulses, was recorded by a lock-in amplifier (SRS 830, Stanford Research System) at 4 kHz. The push pulses were modulated by a mechanical chopper (MC2000B, Thorlabs) at $\sim$1165 Hz, and the push-induced photocurrent (dJ) was detected by the same lock-in amplifier.

3.3 Data Analysis - Genetic Algorithm

Genetic algorithm is a global fitting method to decompose the overlapping spectral signatures of various spectral species and obtain their relevant kinetics. The measured data is a 2D data matrix M. In our model, following the principle of minimize the difference between M another matrix M' can be constructed from the product of *species*, for example, exciton, polaron, or triplet states, represented as vectors ($S = [s_1, s_2, s_3 ...]$), and the *kinetics*, basically their evolution over time, also represented as vectors ($t = [t_1, t_2, t_3 ...]$),

With a certain solution of the species, the relevant kinetics can be obtained

$$t = M^{-1} \times S^T \tag{3.4}$$

The 2D matrix can be constructed from the obtained kinetics t and S,

$$M' = S^T \times t \tag{3.5}$$

The fitness of a certain solution is expressed as the inverse of the difference and the optimisation goal is to maximise the fitness level,

$$\max \frac{1}{||M - M'||} \tag{3.6}$$

To obtain the initial spectra S, if some prior information is known about the spectra, the initial spectra can be assigned. Otherwise, random numbers will be generated to get the initial guess. The second step, *clone* is to generate a larger population $S_1, S_2, S_3, ...$ by copying the original spectra and adding some noises onto each of them. As you can tell from the algorithm, we define a *mutate* operation, to randomly exchange digits of two possible solutions, which forms new species $S'_1, S'_2, S'_3, ...$ Certain noises are added again onto each possible solutions $S_1, S_2, S_3, ..., S'_1, S'_2, S'_3, ...$ All these solutions are then sorted according to their fitness levels. From these solutions, we only keep a certain number of solutions and enter into another iteration of *mutation*. After a certain number of mutations, this loop is over and we again select a certain number of best solutions, and save them into the *clone* operation loop. Some additional penalty can be added for non-physical results in the fitness evaluation equation. The noise level is reduced after each *clone* iteration, so that the solutions can approach the convergence.

Genetic algorithm can help decompose the signal which gives a direct impression of how species interconvert. However, it is notable that results from this algorithm should be carefully analysed and compared to the photophysical model. In particular, when the signal

amplitude varies by several orders of magnitude, more attention should be paid to check the physical meaning of the spectra and kinetics.

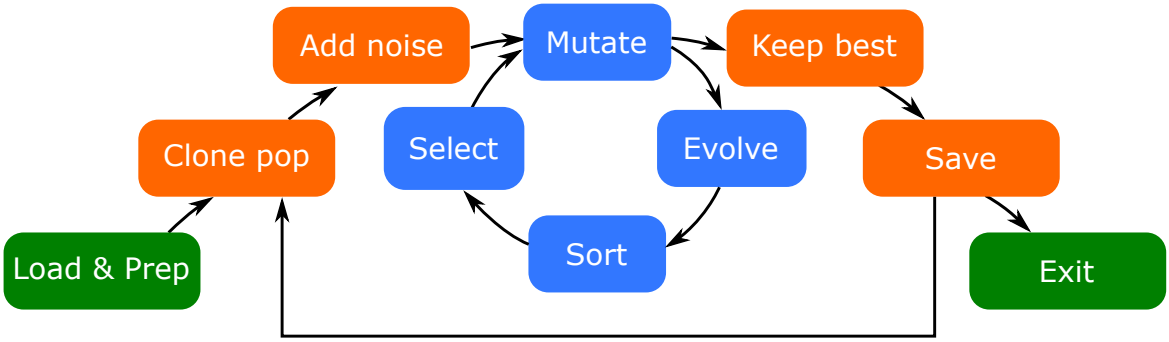

Fig. 3.8 A schematic of the processing procedures of genetic algorithm. *Load and Prep*: load the data and prepare the initial solutions and relevant parameters; *Clone pop*: clone a number of the remaining solutions; *Add noise*: add some random noises to the existing solutions according to the set parameter; *Mutate*: randomly exchange digits of certain solutions; *Evolve*: add some random noise again in this loop; *Sort*: sort the fitness of all solutions according to their fitness level; *Select*: keep a number of solutions for the next iteration and delete others; *keep best*: keep a number of best solutions for the *clone* loop; *Save*: save data; *Exit*: exit the program.

Chapter 4

Binding Energy of Localised Charge-Transfer States

Note: This chapter is closely adapted from the publication: J. Zhang, A. C. Jakowetz, G. Li, D. Di, S. M. Menke, A. Rao, R. H. Friend, A. A. Bakulin*. "On the Energetics of Bound Charge-Transfer States in Organic Photovoltaics" *J. Mater. Chem. A*, **2017**, 5, 11949-11959. (Reproduced from Ref. [184] with permission from the Royal Society of Chemistry.)

Device fabrication and characterisation, and temperature-dependent pump-push photocurrent spectroscopy were carried out in the University of Cambridge by J. Zhang. The paper was written by J. Zhang supervised by R. H. Friend and A. A. Bakulin.

4.1 Introduction

Organic photovoltaic cells (OPVs) can efficiently harvest solar energy using two electronically dissimilar organic semiconductor materials – namely electron donor and acceptor. Among the best devices, mainly achieved by morphology optimisation, these materials may partially segregate to form an interpenetrating molecular network architecture known as bulk heterojunction (BHJ).[51, 52] In BHJ devices, generation of free carriers begins with the absorption of a photon by the donor, usually a polymer, or the acceptor, often a fullerene. This light absorption generates a strongly bound intramolecular electron-hole (e-h) pair, called a singlet exciton. The energetic difference between the molecular orbitals of the donor and the acceptor provides the driving force for the dissociation of the singlet exciton into a pair of charge carriers - a hole on the donor and an electron on the acceptor. This initial process is usually addressed as charge transfer (CT) (electron transfer [212] or hole transfer [125]) and the resultant states are often called charge transfer states (CTSs) – an

electron-hole pair separated across the donor-acceptor (D-A) heterojunction. In general, the electron and the hole in the CTS are expected to be strongly bound together by a relatively large Coulomb interaction of up to 350 meV.[112] However, in efficient OPV devices, most CTSs subsequently go through a long-range (∼4 nm) charge separation (CS) process to form free mobile carriers (separated-charge states, SC states), while some stay bound at the interface and subsequently recombine before collection at the electrodes.

While this phenomenological picture of OPV operation is broadly accepted, the particular molecular-level mechanism of CT, long-range CS and recombination in BHJs of organic semiconductor materials are still subjects of discussion.[112, 213, 113, 109, 107, 108, 214–217] Apart from the simple electrostatic attraction between carriers discussed above, the effects of excess carrier energy, delocalisation [38, 158, 156, 127, 146, 159, 30, 142, 200, 218], and entropy contribution [163–165, 162, 219] are proposed to control the CS process both in fullerene-based and non-fullerene systems. The interplay between these contributions is at the core of the ongoing debate. For example, even though close-to-unity internal quantum efficiency (IQE) is achieved in some material systems with a high driving energy [69] (roughly the offset between the lowest unoccupied molecular orbitals (LUMO) for electron transfer), it is still unclear where is the fundamental limitation for IQE in material systems with low driving energy.[171] Another aspect is the importance of hot CTSs (possessing excess energy above the lowest CTS) versus the relaxed 'cold' CTSs. Critical evidence for supporting the importance of cold CTSs is the similar IQE performances in OPV devices under above-bandgap and sub-bandgap excitations.[138, 137] At the same time, ultrafast spectroscopy experiments indicate clear effects of hot or delocalised CTSs on long- and short-range CS.[30, 142, 141, 145] Still, the direct evidence to support the importance of hot CTSs in efficient operating devices is lacking.

To build a unified model of charge generation, many groups have focused on the fundamental properties of CTSs and addressed different aspects of photophysics of CTSs, including energetic structures, relaxation rates and coupling to excitonic and SC states.[38, 220–223, 110, 224, 225, 183, 226, 227] Probably the most fundamental parameter characterising the localised (bound) CTSs is their binding energy, which can be defined as the energy difference between the SC state and the localised CTS.[127, 228, 229] For this reason, many different, mostly steady-state, approaches have been applied to determine the binding energy of localised CTSs.[220, 230, 157, 231] However, these studies are difficult to compare: (i) They use quite different photovoltaic blends; (ii) Different methods probe the binding energy from different angles and are difficult to directly compare. Many processes are entangled together, which increases its complexity, such as accurately measuring the energy levels of

SC states, the fast relaxation time of bound CTSs, the influence of internal electric-field and the dispersion of energy levels in the blends with inhomogeneous nanomorphology.

Temperature-dependent (T-dependent) measurements provide a robust tool to probe material energetics and to achieve further insight into the charge generation mechanism, inspiring numerous studies on the influence of temperature on CS process in various material systems.[145, 135, 232–237, 97] The majority of these studies aim to relate the T-dependent variation of device parameters, including mainly short-circuit current (J_{SC}) and open-circuit voltage (V_{OC}) [163, 222, 238–240] with the charge generation process. The results from these measurements have been mainly rationalised in the framework of the Onsager-Braun model and its modifications. We note that Onsager model (which regards CTSs as precursor states for charge generation) has many limitations and it fails to explain, for example, energetic disorder and BHJ morphology dependence. Temperature, together with the external electric field, is considered to be a most critical parameter in the dissociation efficiency of CTSs (precursors for free charges).[134] Though Onsager-Braun models are able to reproduce some experimental results, the fitting parameters in the dissociation efficiency formula are not always consistent with other measurements or sometimes not physically reasonable.[107] The reason for this, as some authors have pointed out, is that the steady-state photocurrent arises from multiple T-dependent processes including exciton dissociation, charge transport, and bimolecular recombination.[163, 134] This prevents steady-state measurements from selectively addressing the energetics of CTSs and the early-time non-equilibrium carrier dynamics. The issue of T-dependent extraction and bimolecular recombination (BR) can potentially be sorted out by considering that all photogenerated e-h pairs recombine in the open-circuit condition. In such a case, V_{OC} might be less affected by the charge transport process, allowing for the exclusive focus on the charge separation process at the D-A interface. Recently, Gao et al.[113] explained the deviation from linear $V_{OC} - T$ relationship at low T due to ineffective geminate dissociation. To summarise, steady-state measurements, in and by itself, have two fundamental weaknesses: (i) The effects of CT exciton dissociation, charge recombination and charge extraction all contribute to device performance but may have different dependence on temperature.[138, 97] (ii) Geminate recombination (GR) and BR cannot be easily disentangled when the integrated photocurrent is solely measured.

The above issues can be solved by looking at early-time charge dynamics, or using techniques that are selective to bound CTSs. Previous time-resolved studies on CTSs mostly addressed CTS emission. For example, time-resolved photoluminescence (TR-PL) using transient grating [198] or streak camera [241] can measure radiative recombination of CTSs. The recent T-dependent TR-PL measurements revealed quite different dynamics of CTSs in two benchmark material systems (PTB7:PC_{71}BM and P3HT:PC_{61}BM)[233, 234, 242]

supposedly coming from the differences in non-radiative CTS recombination. Using transient absorption spectroscopy, Barker et al. observed tunneling recombination by freezing carrier movement at cryogenic temperature and measured the e-h separation distance by fitting the decay kinetics. [129] Overall, previous works provide many insightful case studies of CT relaxation and report a large range of binding energies of CTSs (0 meV to 350 meV) [112, 157, 129, 243], with the highest values close to the binding energies of the singlet excitons. However, a systematic and selective investigation of the CTS photophysics in a working device, which correlates the device performance with the binding energy of localised CTSs, is still missing.

In this work, we perform temperature-dependent ultrafast pump-push photocurrent (PPP) spectroscopy on a range of material systems based on a benchmark polymer poly[2-methoxy-5-(3,7-dimethyloctyloxy)-1,4-phenylen]-alt-(vinylene) (MDMO-PPV) and a range of fullerene derivatives. PPP is a device-based technique which selectively monitors the formation and recombination of bound CTSs on the ultrafast (sub-ps) time-scale. T-dependent PPP offers a possibility of overcoming the drawbacks of other methods by specifically targeting the long-range CS of bound CTSs at the interface. With three different fullerene derivatives, the role of the driving energy as well as material morphology is investigated. We first compare the device performance, then we introduce the PPP technique by elucidating the dynamics of bound CTSs at room temperature. Using the Arrhenius model, we extract a single activation energy for the CTS dissociation which comes from the energetic difference of CT states and charge-separated states, exactly the binding energy of CT states. A simple picture with the direct branching from initially exicted excitons into bound CTSs and free charges can qualitatively explain the observed trend. The average activation energy of 90 ± 50 meV for the charge separation process indicates the energetic similarities of bound CTSs regardless of driving energy for charge separation (as provided by donor-acceptor energetic offset) and material composition, in sharp contrast with the obvious trend in device efficiencies. We emphasise that it is not the energy of CTSs that matters; it is the population density of the cold charge-transfer states that controls early charge separation and recombination. In devices with a favourable morphology for charge generation and transport, most CT states are delocalised and very few bound CTSs form at the interface, leading to a better device performance. Our result points to the importance of minimising the number of localised states by morphological control rather than by lowering the dissociation energy of bound CTSs.

4.2 Temperature-Dependent PPP Spectroscopy

In the PPP experiment, a regenerative 1 kHz Ti:Sapphire amplifier system (Spectra Physics, Solstice) generated ultrafast 100 fs laser pulses at 800 nm with the energy of 3.5 mJ per pulse, which was split into two parts. One part was used to pump a broadband non-linear optical amplifier (NOPA) to produce visible pump pulses with the photon energy of 2.30 eV (540 nm. The other part was used to generate mid-infrared (IR) push pulses ($\sim$2 μm, $\sim$0.62 eV) by pumping an optical parametric amplifier (TOPAS, Light Conversion). The device (connected to the external circuit outside the cryostat) was situated in a low-temperature cryostat (Optistat CF™, Oxford Instruments). Temperature inside the cryostat was detected by a sensor of a temperature controller (ITC 503, Oxford Instruments) and controlled by the balance between its heat generation and the flow of helium gas adjusted by a gas-flow controller (VC41, Oxford Instruments). This operation temperature range is between 3.2 K and 500 K.

During the experiment, the devices were measured at the short-circuit condition under different temperatures. Pump pulses (with energy $\sim$1 nJ per pulse) and push pulses (with energy $\sim$1 μJ per pulse) were focused onto a $\sim$1 mm^2 spot on the device. The reference photocurrent, J, induced by the pump pulse was detected at the laser frequency of 1 kHz by a lock-in amplifier (SRS830, Stanford Research System). The repetition rate of the push pulses was modulated by a mechanical chopper (MC2000, Thorlabs) at 370 Hz which was synchronised with the lock-in amplifier to detect the push-induced photocurrent, dJ. We note that the photophysics in the pulse mode excitation may be different from steady-state illumination, or under different fluences. Previously, Marsh et al.[244] performed detailed analysis on the fluence-dependence of external quantum efficiency (EQE) in P3HT:PCBM (poly(3-hexylthiophene-2,5-diyl, P3HT) devices. In our measurements, very low fluence ($\sim$100 nJcm^{-2}) and low photocurrent (<100 nA) ensure the device to work in a similar condition as under a standard one-sun illumination.

Of course, PPP has its limitations. The most severe limitation is that this technique does not work well for efficient photovoltaic blends, as the population of lossy states is tiny in high-efficiency photovoltaic cells. The next difficulty is that the wavelength of the push light is difficult to choose, partly because the photo-induced absorption of polarons in the IR region are difficult to measure. Lastly, the signal-to-noise ratio is limited by the detection precision of the lock-in amplifier.

4.3 In Fullerene-based Organic Solar Cells

4.3.1 Materials and Devices

Fig 4.1(a) and (b) present the chemical structures and energy levels of the used materials, respectively.[37] MDMO-PPV was used as the donor material which was purchased from Merck (lisicon PDO-121). Three fullerene derivatives were chosen as acceptors: Phenyl-C61-butyric acid methyl esters mono-PC61BM (mPCBM), bis-PC61BM (bPCBM), tris-PC61BM (tPCBM) from Solenne BV. The bandgaps of three fullerene derivatives are similar ($\sim$1.7 eV), but the HOMO and the LUMO energy levels are different. This allows for the investigation of the influence of driving energy on charge separation process. The film absorption spectra of these materials are shown in Fig 4.1(c) and the blend film absorption data are shown in Fig 4.1(d)-(f). The advantage of MDMO-PPV is that its electronic energy levels have negligible change when the fullerene weight ratio changes [37]. It is well mixed with fullerenes and forms different morphologies of intercalating polymer/fullerene network in the studied blending ratios (1:1, 1:2 and 1:4). In 1:1 D-A blend, there is not enough fullerene to form aggregates, but in 1:4 D-A blend, fullerene aggregates form.

Table 4.1 Key device parameters of MDMO-PPV as the donor and three fullerene derivatives (mPCBM, bPCBM and tPCBM) as the acceptors with blend ratios of 1:1, 1:2 and 1:4.

Acceptor	Device parameters	Blend ratio		
		1:1	1:2	1:4
mPCBM	V_{OC}(V)	0.91	0.87	0.84
	J_{SC}(mA cm^{-2})	1.61	3.62	4.82
	FF	35%	44%	51%
	PCE	0.51%	1.39%	2.10%
bPCBM	V_{OC}	1.00	0.98	0.98
	J_{SC}	1.01	1.54	2.36
	FF	29%	32%	36%
	PCE	0.29%	0.49%	0.83%
tPCBM	V_{OC}	1.01		1.01
	J_{SC}	0.33		0.76
	FF	25%		29%
	PCE	0.08%		0.22%

Even though the tPCBM(1:2) data is absent because this device was broken in the measurement. From the trend of the data, we can still estimate $V_{OC} \sim 1.01$ V, $J_{SC} \sim 0.5$ mA cm^{-2}, $FF \sim 27\%$, $PCE \sim 0.15\%$.

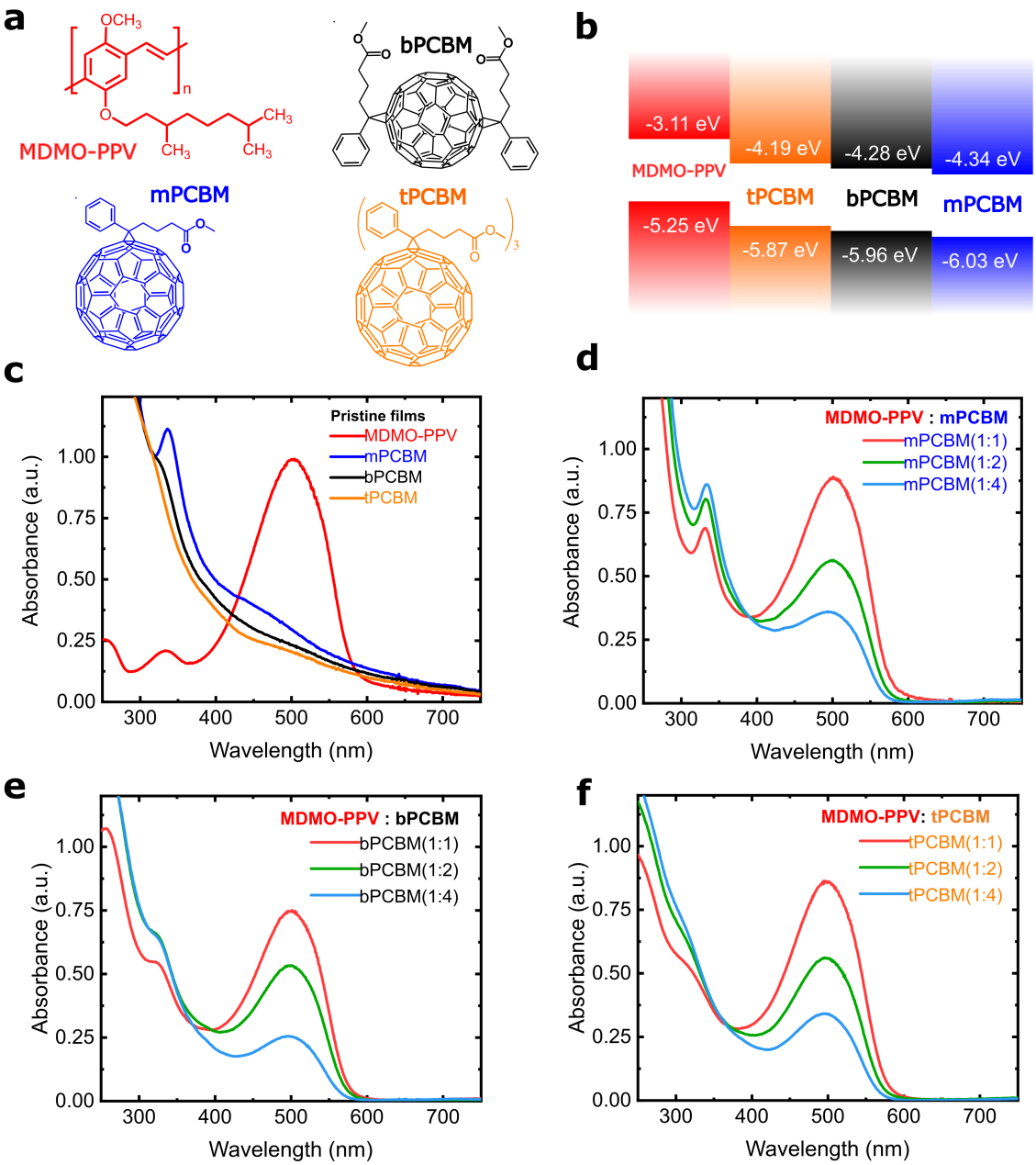

Fig. 4.1 The absorption and energy level of studied materials.(a) Chemical structures of the donor polymer MDMO-PPV and three fullerene acceptor derivatives: mPCBM, bPCBM and tPCBM. (b) HOMO and LUMO energy levels and (c) normalised absorbance for the materials. (d)-(f) Normalised absorbance of MDMO-PPV:fullerene derivatives with blend ratios of 1:1, 1:2 and 1:4.

Substrates were cleaned followed by the deposition of PEDOT:PSS layer. Solution with different blend ratios (wt, 1:1, 1:2 and 1:4) of MDMO-PPV:fullerene derivatives were prepared in certain concentrations in ortho-dichlorobenzene (10 mg ml^{-1}, 12.5 mg ml^{-1} and 15 mg ml^{-1} respectively) by stirring at 50 °C overnght. The solution was then spin-coated

onto the PEDOT:PSS layer at 1500 RPM for 40 s followed by 2000 RPM for 20 seconds. [245] An 80 nm layer of aluminium was deposited on top of the active layer by thermal evaporation under high vacuum ($\sim 10^{-6}$ mbar).

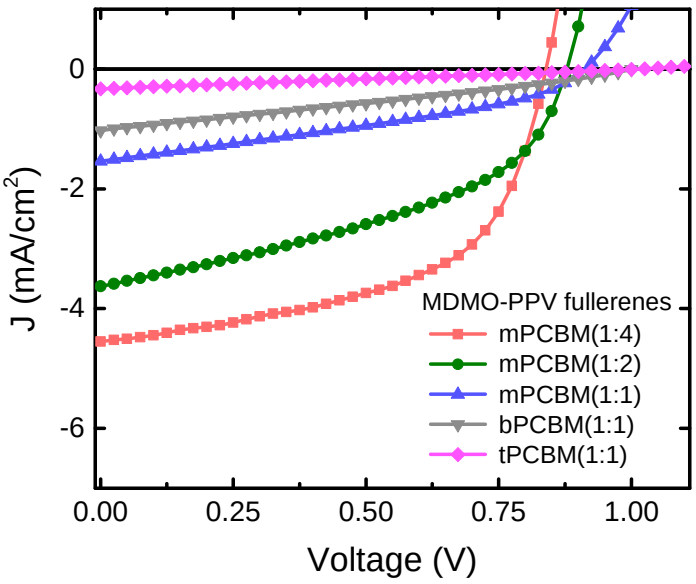

Fig. 4.2 Current-density voltage of MDMO-PPV:fullerene derivatives devices under AM 1.5G illumination.

Typical $J-V$ curves are shown in Fig 4.2 and the full set of device parameters are summarised in Table 4.1. We typically measure 3 pixels to ensure that the device performance is reproducible. Two devices for each combination was made and data were chosen from those working devices. When both devices worked, the device performance was close and reproducible. From the $J-V$ data, increasing the fullerene loading or decreasing the number of side chains in the fullerene improve the device PCE through improved J_{SC} and fill factor (FF). This trend is in good agreement with the fullerene packing and aggregate size measured by small-/wide-angle X-ray scattering [37]. In 1:4 blend, a better photovoltaic performance is accompanied with the presence of fullerene aggregation. Such observation supports the importance of wave-function delocalisation induced by fullerene aggregation.[38] Previously, transient absorption techniques indicated that the electron transfer time from polymer (MDMO-PPV) to fullerene derivatives ranges from 37 fs to 100 fs, and a high driving energy is not needed to facilitate this ultrafast CT. Combined with our device data, it is logical to assume that the great differences in J_{SC} and PCE do not originate from the ultrafast CT, but rather from the differences in the subsequent long-range CS, charge transport and extraction processes.

4.3.2 Room-Temperature PPP experiments

To study the influence of film morphology and driving energy on charge separation efficiency, it is necessary to separate GR and BR processes which dominate the dynamics on different time scales. To compare specifically the difference in the early-time charge dynamics, we perform pump IR-push photocurrent spectroscopy on these working devices.[30]

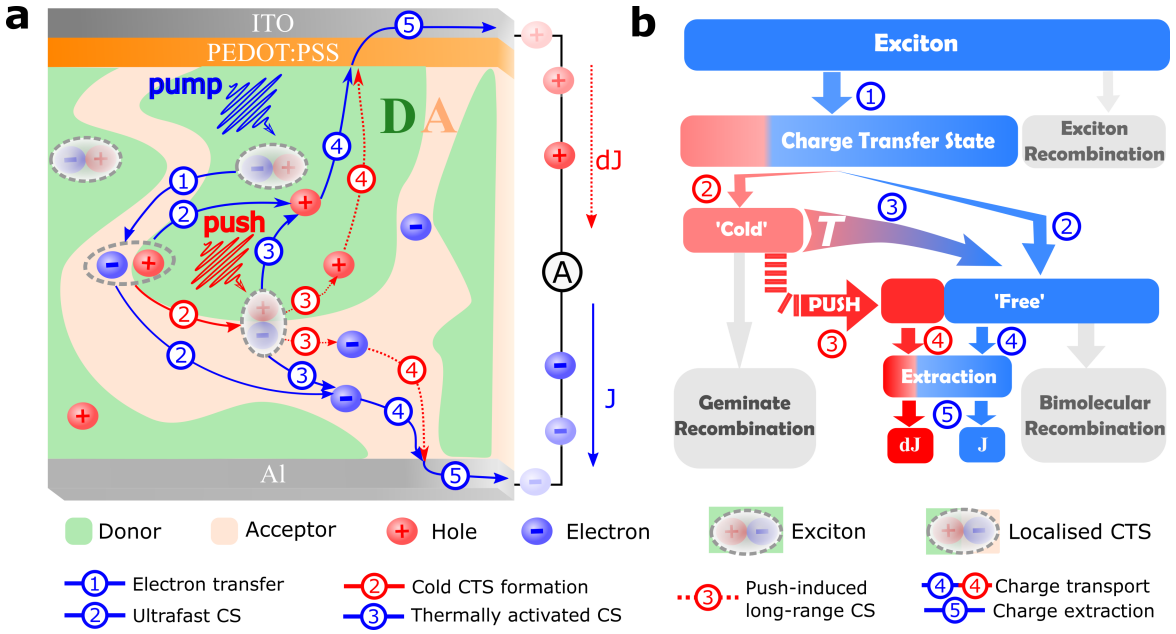

Fig. 4.3 Model of photogeneration processes involved in the PPP experiment in organic solar cells. Without electron acceptors, excitons generated by the pump pulses in the polymer phase recombine into the ground state. In the presence of a good acceptor, the ultrafast CT processes quench singlet excitons before recombination and form initial CTSs at the D-A interface (process 1). These initial CTSs ('hot') subsequently branch between 'cold' CTSs and 'free' charges (process 2) usually on sub-ps time scale. 'Cold' CTSs either geminately recombine to the ground state, or separate into free charges without external perturbation . With the IR-push pulses, 'cold' CTSs are re-excited into 'hot' CTSs, accessing delocalised states capable of spontaneously separating into 'free' charges from another channel (process 3). These additional 'free' charges (from process 3, red) and previous 'free' charges (from process 2 and 3, blue) then interact through bimolecular recombination or flow to the electrodes through charge transport in the separated phases (process 4) before being extracted as dJ and J by external circuits (process 5), respectively. Note that triplet states are not considered in this model.

Fig.4.3 illustrates the relevant electronic processes in the PPP method. The PPP experiment directly measures the formation and recombination of cold CTSs at the interface in real time by detecting the additional photocurrent due to the push pulses which provide additional energy to dissociate these cold CTSs at the D-A interface. The pump pulse, for example, at around 550 nm first generates excitons in the MDMO-PPV donor. With the

acceptor, the fullerene efficiently quenches the excitons at the D-A interface by ultrafast electron transfer and form some intermediate 'hot' CTSs. These 'hot' CTSs then branch into either 'cold' CTSs or undergo long-range CS to form free charges. The separated free charges are collected as photocurrent, J. 'Cold' CTSs also undergo GR or separate into free charges, unless the push pulses arrive and excite the relaxed CTSs to the delocalised band-like states to give them another chance to dissociate. This re-excitation effect is observed as an additional photocurrent $\mathrm{d}J$ detected by a lock-in amplifier. The maximal amplitude $\mathrm{d}J_{\max}/J$ of the normalised dynamics, $\mathrm{d}J/J$, is used to quantify the charge separation efficiency, and is discussed in detail in the next section.

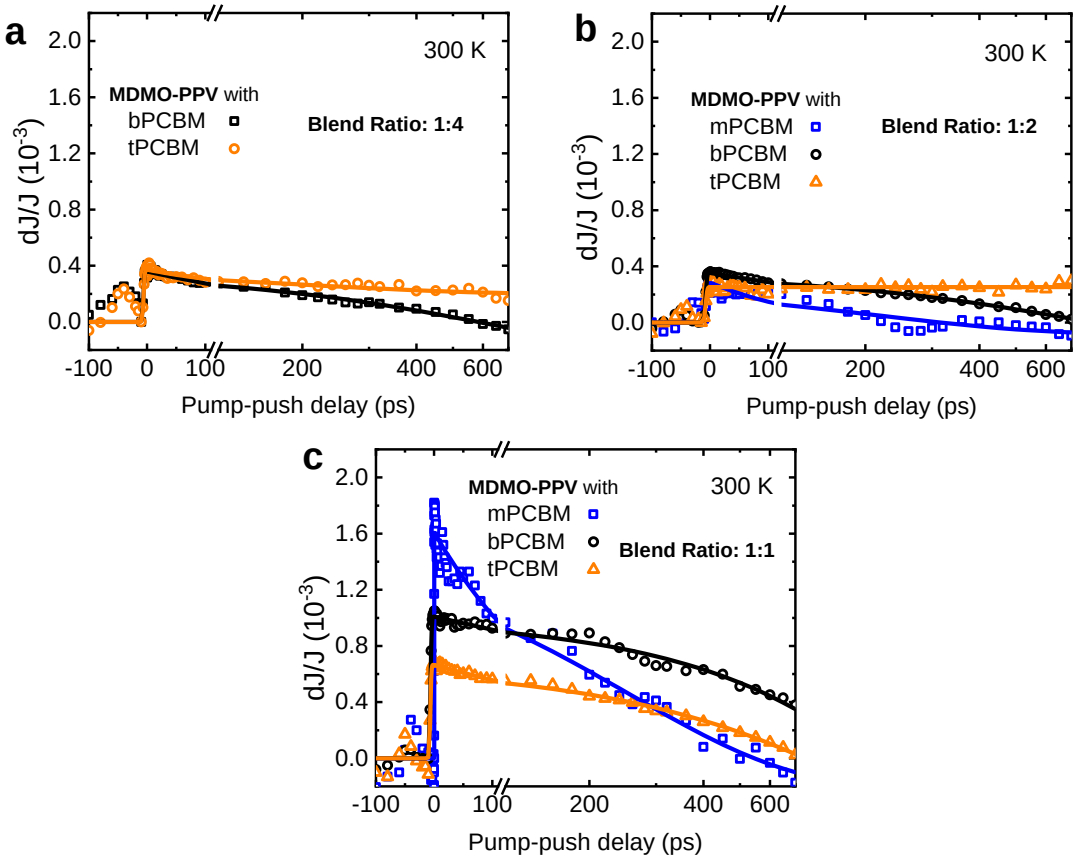

Fig. 4.4 PPP dynamics at room temperature (300 K) of devices with MDMO-PPV:mPCBM(bPCBM, tPCBM) and blends ratios of (a) 1:4, (b) 1:2 and (c) 1:1. Solid lines are guides for the eye. In (a), MDMO-PPV:mPCBM(1:4) data is missing as the signal is too small to be measured.

Fig 4.4 shows the PPP response at room temperature (300 K) with MDMO-PPV:fullerenes of blend ratios (a) 1:4, (b) 1:2 and (c) 1:1. The background signal observed at negative delays is corrected using the signal before time zero, as this background is usually associated with long-lived shallow trapped charges, which can be freed by the IR light, but is not a

subject of the current study. As trapped charges and states take much longer time ($\gg$ 1 ps) to be observed, the significant increase at time zero must be due to the onset presence of CTSs. The devices with higher fullerene loadings consistently have higher CS efficiency (smaller $\mathrm{d}J_{\max}/J$) in all three fullerene devices, which agrees well with the consideration that the morphology is more important for charge generation than the driving force for charge separation provided by donor-acceptor band alignments.

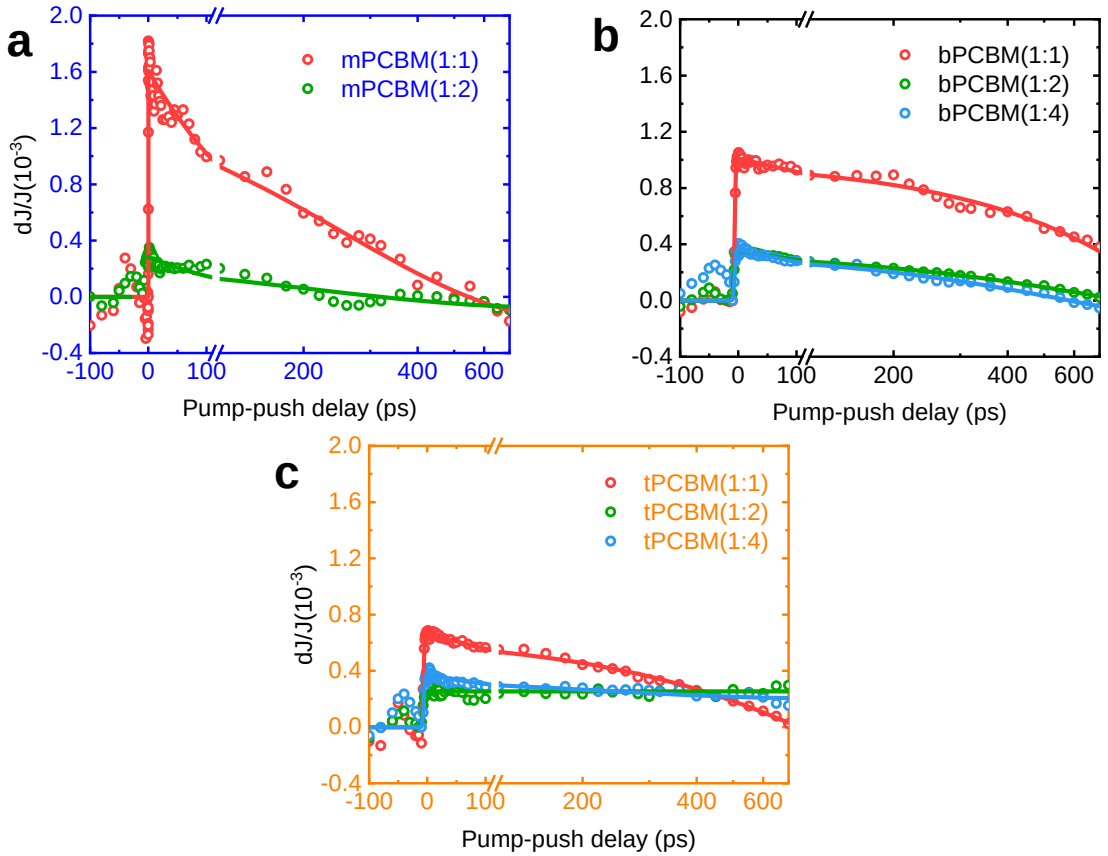

Fig. 4.5 PPP dynamics at room temperature (300 K) of devices with the blends ratios of 1:4, 1:2 and 1:1 with the donor MDMO-PPV and the acceptor (a) mPCBM (b) bPCBM (c) tPCBM. Solid lines are guides for the eye. In (a), MDMO-PPV:mPCBM(1:4) data is missing as the signal is too small to be measured.

Fig 4.5 compares the influence of blend ratios in each D-A blends. For (a) mPCBM and (b) bPCBM blends, the influence on the kinetics is not so significant across different blend ratios. However, for tPCBM, 1:2 and 1:4 blends do not decay as other curves, but show a flat line. This may indicate that the loss channel from geminate recombination is decreased, probably due to the aggregation effect.

4.3.3 Temperature-Dependent PPP: MDMO-PPV:bPCBM 1:1

In Fig.4.3, we assume that there is an early branching between bound CTSs and free charges. Direct evidence comes from ultrafast experiments where free charges can be generated just after charge transfer [107, 127, 142, 129, 37, 126, 246], and other experiments [234, 241] also support this assumption in both BHJ [214, 216, 217] and bilayer devices [128]. After CT, the initial hot CTSs form. As fast as in 1 ps[30], either the formation of bound CTSs or long-range CS may take place. [144] The properties of material system define how many of these hot CTSs form bound CTSs, $N_{\text{bound}}(T)$ and how many separate into free charges, $N_{\text{free}}(T)$. Some of these free charges can escape from BR and generate photocurrent $J(T)$, thus

$$J(T) \propto N_{\text{free}}(T) \times \eta_{\text{extract}}(T) \tag{4.1}$$

where $\eta_{\text{extract}}(T)$ is the extraction efficiency of free charges to the electrode from charge separation. The bound CTSs $N_{\text{bound}}(T)$ mostly decay through GR and only slightly contribute to the photocurrent through the temperature activation measured below. By absorbing IR push photons, bound CT excitons are excited into higher-lying band-like delocalised states, after which being dissociated into free charges[30]. The additional 'push'-induced photocurrent is extracted and measured with the lock-in amplifier as $\mathrm{d}J(T)$. By changing the time delay between the pump and push pulses, we get

$$\mathrm{d}J(T,t) \propto N_{\text{bound}}(T,t) \times P_{\text{activation}}(T) \times \eta_{\text{extract}}(T) \tag{4.2}$$

Here $N_{\text{bound}}(T,t)$ is the number of bound CTSs when the push pulse arrives at time t after the pump pulse, and $P_{\text{activation}}(T)$ is the probability of the bound CTSs to absorb the infrared photons and dissociate into free carriers. The decay of $\mathrm{d}J(T,t)$ is assigned to the decay of bound CTSs at the interface with time due to GR. We point out that free charges also absorb the infrared light but they thermalise very quickly. As they contribute to the photocurrent even without the push pulses, there is no net contribution of free carriers to the modulated photocurrent. Both the generations of J and $\mathrm{d}J$ are mediated by the similar charge transport and extraction processes after CS. Therefore, we use the same charge extraction efficiency $\eta_{\text{extract}}(T)$ (including charge transport process) for Equation 4.1 and 4.2.

Considering that the push-induced re-excitation of charges brings the system into a highly non-equilibrium state, we assume $P_{\text{activation}}(T)$ is a constant at different temperature, and thus we have

$$\frac{\mathrm{d}J(T,t)}{J(T)} \propto \frac{N_{\text{bound}}(T,t)}{N_{\text{free}}(T)} \tag{4.3}$$

The PPP transients sometimes show additional fast component within the pump and push overlap ($t < 200$ fs). This can be caused by multiphoton non-resonant effects like sum-frequency generation and are irrelevant to the process of CS. If this effect is pronounced, we can quantify $\mathrm{d}J_{\max}(T)$ after a few picosecond delay rather than the maximal amplitude,

$$\frac{J(T)}{\mathrm{d}J_{\max}(T)} \propto \frac{N_{\mathrm{free}}}{N_{\mathrm{bound}}}(T) \propto \eta_{\mathrm{CS}}(T) \tag{4.4}$$

where $\eta_{\mathrm{CS}}(T)$ is the charge separation efficiency at temperature T. $\frac{J(T)}{\mathrm{d}J_{\max}(T)}$ measured from PPP experiment is proportional to the initial branching between bound CTSs and free charges $\frac{N_{\mathrm{free}}}{N_{\mathrm{bound}}}(T)$, which quantifies the CS efficiency ($\eta_{\mathrm{CS}}(T)$) at the interface. Since the temperature dependence of the extraction process is cancelled out, we can more clearly monitor the effect of temperature on long-range CS process, and directly observe the dynamics and yield of the bound carriers.

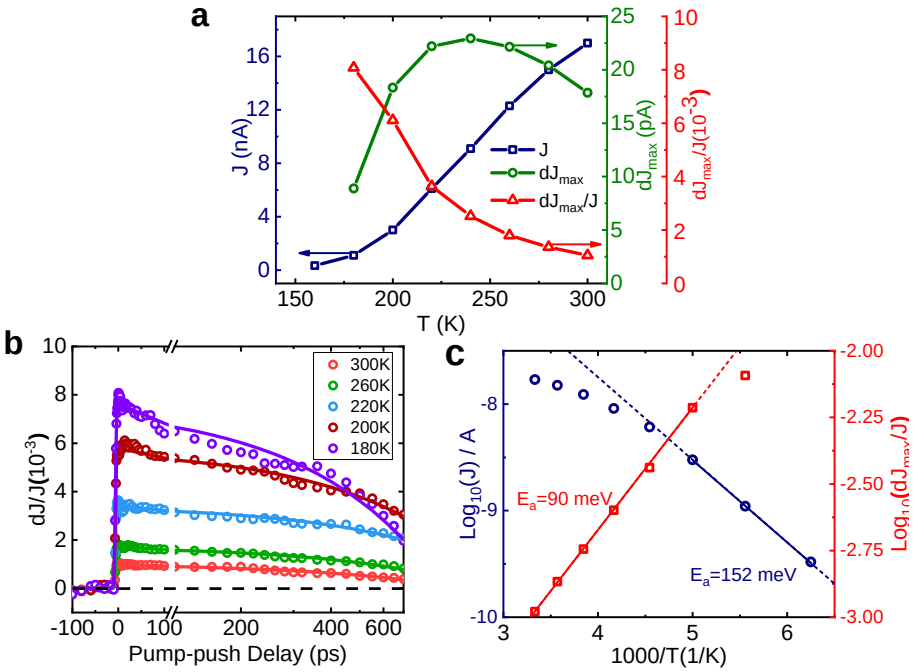

Fig. 4.6 Summary of temperature-dependent PPP of MDMO-PPV:bPCBM(1:1) device and the extracted activation energy from the Arrhenius plot. (a) Temperature-dependent PPP response of MDMO-PPV:bPCBM (1:1) from 180K to 300K. PPP dynamics on the sub-ns time scale with a guideline at $\mathrm{d}J/J = 0$ for comparison. Solid lines are multiexponential fitting for guidance. (b) Photocurrent (J, blue), push-induced photocurrent change ($\mathrm{d}J_{\max}$, green) and $1/\eta_{\mathrm{CS}}$ ($\mathrm{d}J_{\max}/J$, red) at different temperatures. (c) Arrhenius plots for J (blue) and $1/\eta_{\mathrm{CS}}$ (red); $\eta_{\mathrm{CS}}(T)$ showed an activation energy of 90 meV from 200 K to 300 K while the activation energy for J was 152 meV below 200 K. Solid segments show respective linear fits and dashed lines illustrates the extrapolation of the solid lines.

Here, we take a MDMO-PPV:bPCBM device with 1:1 blend ratio as an example and will discuss other dataset together in later sections. Fig.4.6 shows the result of temperature-dependent steady-state photocurrent $J(T)$ and PPP spectroscopy at temperatures from 160 K to 300 K. Fig.4.6(a) (blue line) shows the change of photocurrent measured at different temperatures. The constant decrease of photocurrent J at lower temperatures agrees with previous results [134] and might be caused by the variation of $N_{\text{free}}(T)$ or $\eta_{\text{extract}}(T)$ from Equation 4.1.

The not normalised quantity $\mathrm{d}J_{\text{max}}$ is also shown in Fig.4.6 (a) (green line). Such data is extracted from the PPP kinetics in Fig.4.6(b). Some curves of PPP kinetics without background removal can be found in Fig.4.7. At all temperatures, the maximal amplitude is obtained within 1 ps, which indicates that exciton diffusion is not a limiting factor for exciton dissociation.[144]. The peak at 240 K in $\mathrm{d}J_{\text{max}}$ curve can be rationalised as an interplay between a decrease in the number of bound carriers and an increase in $\eta_{\text{extract}}(T)$ at higher temperatures, according to 4.2. At lower temperatures, the charge mobility determines $\mathrm{d}J_{\text{max}}$ and it steadily decreases in the range from 240 K to 160 K. Together, the normalised photocurrent ($\mathrm{d}J_{\text{max}}/J$, red curve) in Fig.4.6 (a) effectively provides a correction for the extraction efficiency and shows a drastic increase in the yield of bound carriers at low temperatures.

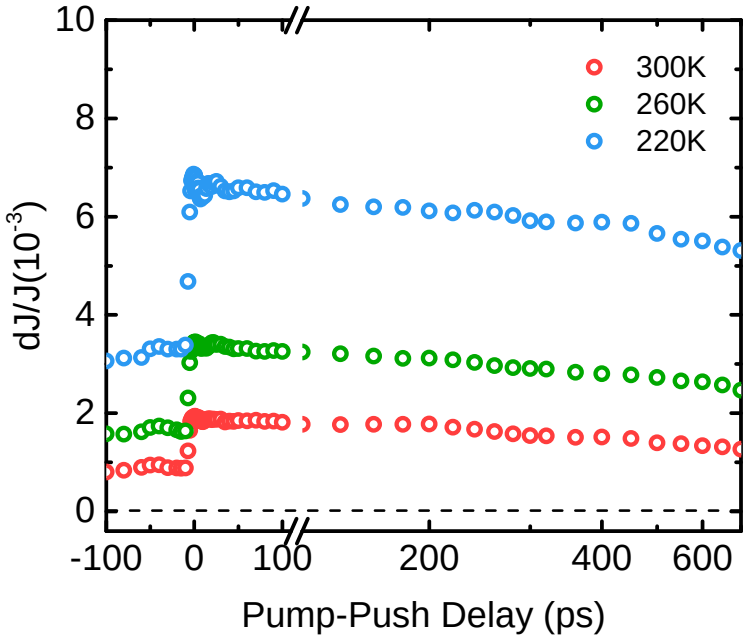

Fig. 4.7 Typical raw PPP kinetics without background removal in MDMO-PPV:bPCBM(1:1) device. The background signal is assigned to long-lived trapped states and multi-photon excitations.

To measure the activation energy, temperature-dependent measurements are usually performed to construct Arrhenius plots. In such plots, the rate of some chemical or electronic processes is plotted against the inverse of the temperature. The slope of this line is linked to the activation energy, see the equation below. The activation energy corresponds to the energy difference between two energy levels. To analyse the temperature-dependent behaviour, the simplest case is the existence of one activation energy, seen as a straight line in the Arrhenius plot. However, in real measurements, the data points may not be well fitted into a line. The Arrhenius plot of the photocurrent J in Fig.4.6 (c) (blue curve) does not show a single activation energy from 300 K to lower temperatures, as the a single line is not a good fit for the data. Such behaviour confirms that a direct photocurrent response represents a convolution of multiple T-dependent processes. In Fig.4.6 (c), we obtain a single activation energy of 90 meV for $1/\eta_{\mathrm{CS}}(T)$ in the range from 200 K to 300 K. 90 meV is around three times larger than the thermal energy (26 meV) at room temperature, representing a barrier for charge separation from CTSs into free carriers. The deviation from the linearity in (b) at low temperature may come from some other temperature-dependent processes, such as change of transient charge mobility, or the breakdown of the constant cross-section of CTSs of the IR light. Further studies may look into this behaviour. We emphasise again that this single activation energy is absent in either J or $\mathrm{d}J_{\mathrm{max}}$ at around 300 K due to an interplay between the number of bound CTSs and temperature-dependent charge extraction. Thus, this single activation energy strongly demonstrates the significance of the $\eta_{\mathrm{CS}}(T)$ defined in this paper. From this simple picture, we have

$$\eta_{\mathrm{CS}}(T) \propto \frac{N_{\mathrm{free}}}{N_{\mathrm{bound}}}(T) \propto e^{-\frac{E_{\mathrm{a}}}{k_{\mathrm{B}}T}} \tag{4.5}$$

where E_{a} is the activation energy of bound CTSs, T is the temperature and k_{B} is the Boltzmann constant.

To have a better idea of how the kinetics (shown in Fig.4.6 (b)) changes with temperature, Fig.4.8 shows the normalised kinetics shown in Fig.4.8. In Fig.4.8 (a), it is quite clear that the lifetime is not constant. In order to compare them easily, we choose 20 ps (dashed line) as the reference starting time point, and define the period decreasing to half of its amplitude at 20 ps as the lifetime we mention here. The relationship between lifetime and temperature is drawn in Fig.4.8 (b), where it first increases until around 220 K before decreasing when lowering the temperature. More efforts are needed to systematically understand the relationship between lifetime and temperature, which is part of future research.

We also make it clear that the reason of using early time $\mathrm{d}J/J$ (such as 1 ps) rather than late (such as 700 ps, shown below) is that it can exclude the interference from temperature-

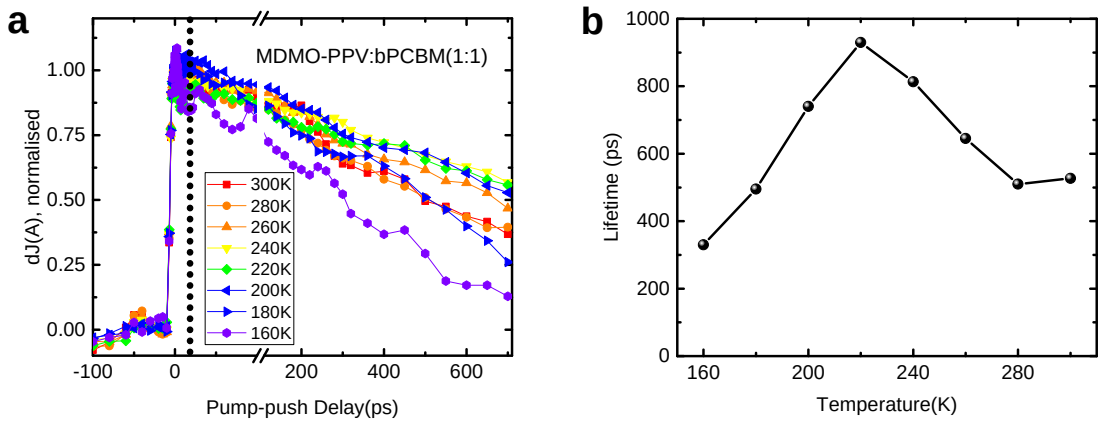

Fig. 4.8 PPP kinetics of MDMO-PPV:bPCBM with the blend ratio of 1:1. (a) Normalised kinetics. (b) Half-amplitude lifetime starting from 20 ps. The lifetime here is defined as the time period from the amplitude at 20 ps to half its amplitude.

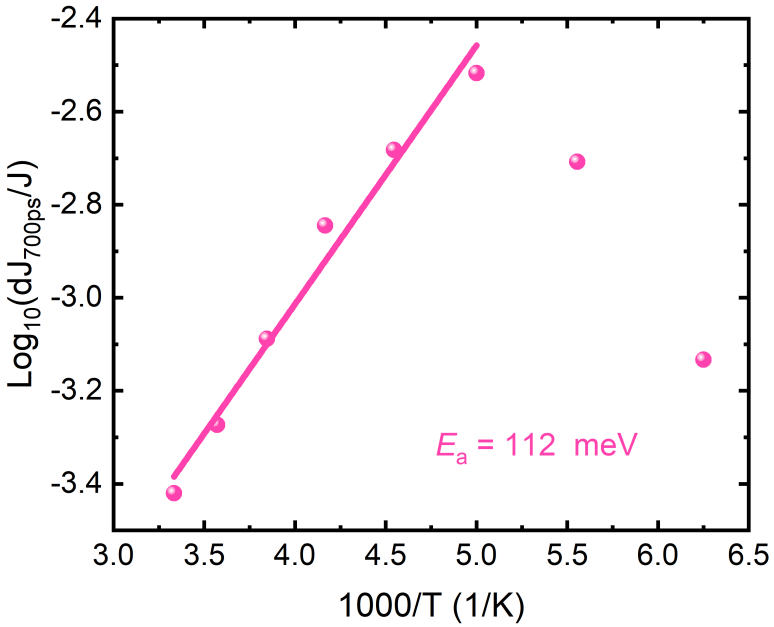

Fig. 4.9 Activation energy of MDMO-PPV:bPCBM with the blend ratio of 1:1 taken at $\mathrm{d}J/J$ at 700 ps.

dependent non-radiative recombination process, which can greatly influence the results. Fig.4.9 shows the Arrhenius plot by taking $\mathrm{d}J/J$ at 700 ps. The fitting is not as good as in Fig.4.6(c), due to the complex dynamics in later times. However, the activation energy is still quite close. The further investigation of combining temperature-dependent time-resolved

PL and PPP offers the possibility to achieve new insights into the ongoing debate on charge generation mechanism.

4.3.4 Temperature-Dependent PPP: All Devices

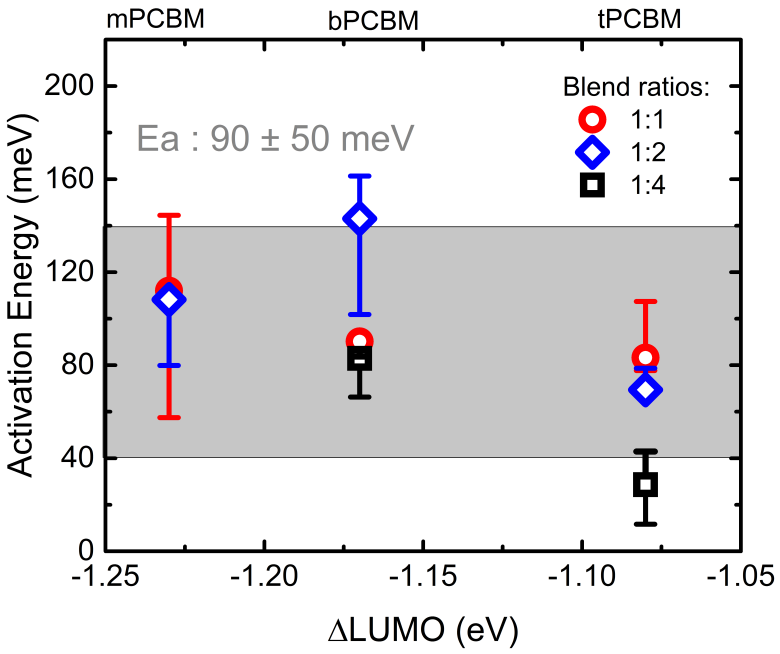

Fig. 4.10 Activation energy as a function of driving energy in the studied blends with different donor:acceptor blend ratios (1:1, 1:2 and 1:4). Driving energy is taken roughly as the energy difference between the LUMO energy levels of MDMO-PPV and the respective fullerene derivatives. The uncertainty of the activation energy is obtained from the linear fit of the Arrhenius plot. MDMO-PPV:mPCBM 1:4 data is not measured as the amplitude is too small.

Fig.4.11 and Fig.4.12 shows all the pump-push data of the measured devices as well as the Arrhenius graphs with the fitted lines for the activation energy (E_a). The activation energy is summarised in Fig.4.10. We find that Ea does not change much across the whole range of samples – E_a is neither a function of LUMO offset, nor is a function of D-A ratio. The average value of all these activation energies is 90 meV and the horizontal dark grey line shows the energy level in the graph. To our surprise, there is no obvious correlation between the material composition or driving energy with the change of activation energy. We assume an uncertainty of 50 meV higher or lower than the 90 meV "median value" to include all of our data ranging from 40 meV to 140 meV, shown as grey area in Fig.4.10. We note that 150 meV is a narrow range to tune the driving energy. However, a number of works have

shown that even modest variations in the driving energy can lead to a substantial change in photophysics. [112, 135]

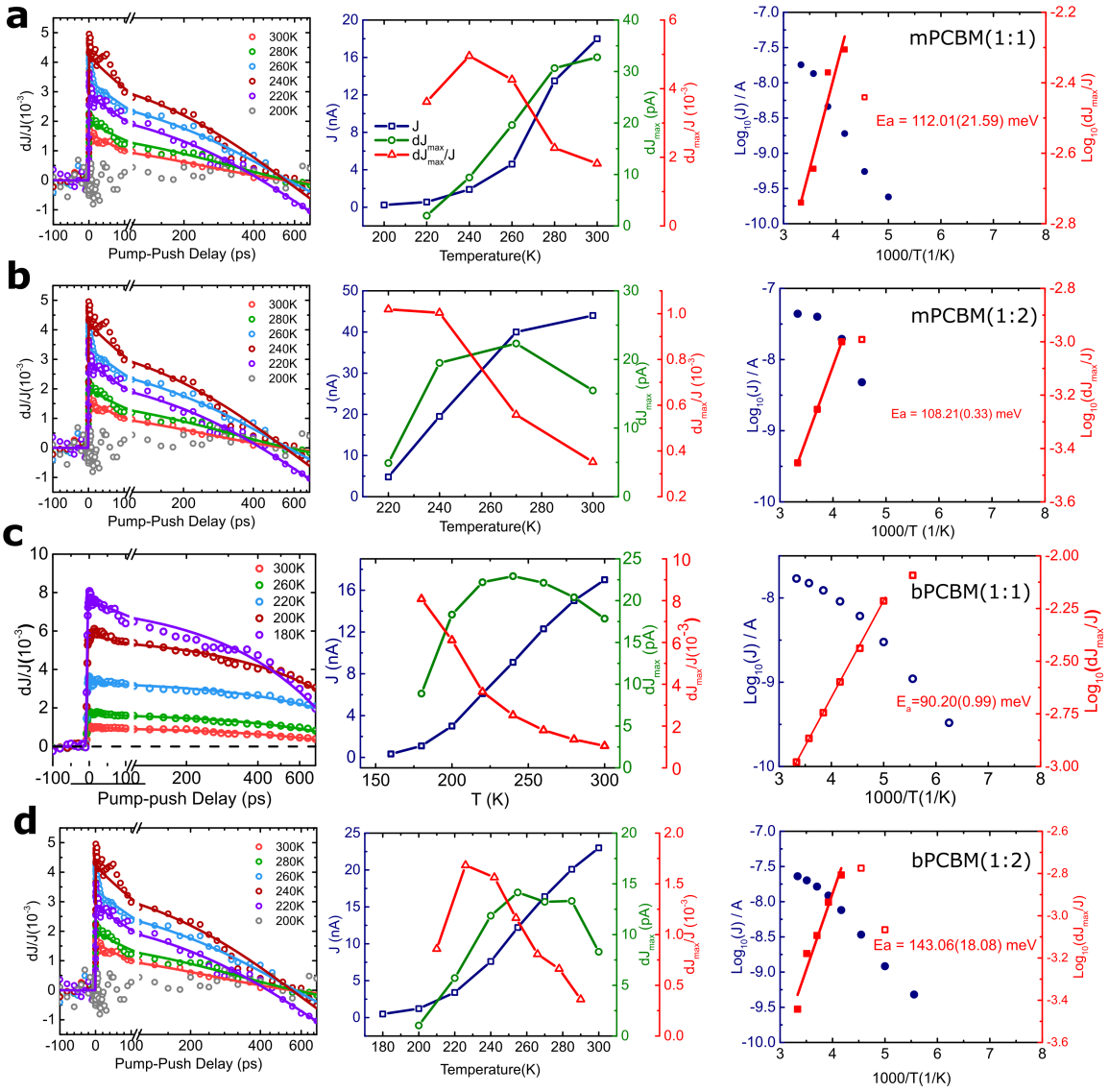

Fig. 4.11 Full dataset of (i) the PPP dynamics in different devices, (ii) temperature dependence of J, $\mathrm{d}J_{\max}$ and $\mathrm{d}J_{\max}/J$, and (iii) Arrhenius plots of J and $\mathrm{d}J_{\max}/J$. (a) mPCBM with D-A ratio of 1:1 (b) mPCBM with D-A ratio of 1:2 (d) bPCBM with D-A ratio of 1:2

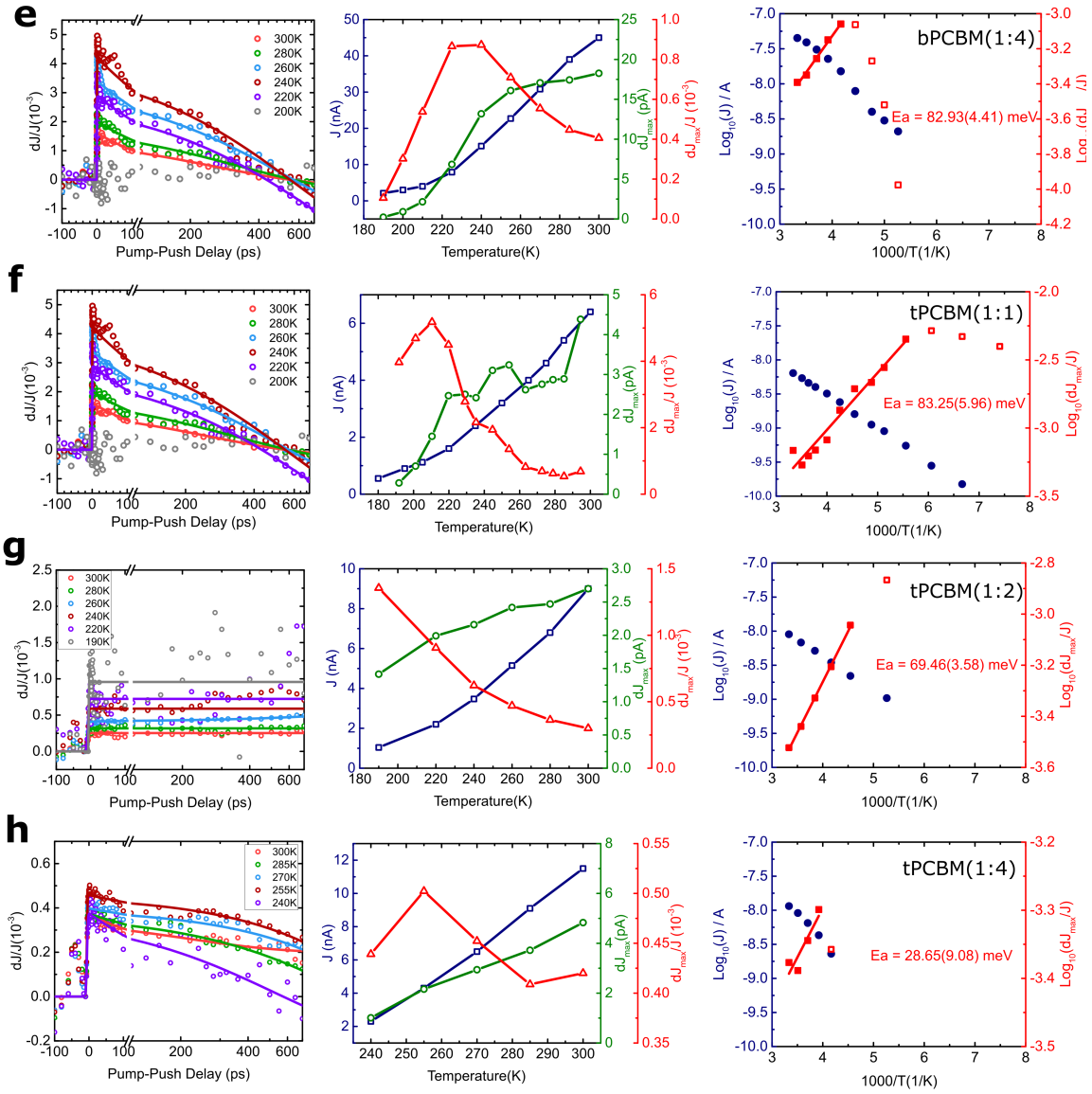

Fig. 4.12 Full dataset of PPP data. (i) the PPP dynamics in different devices, (ii) temperature dependence of J, d$J_{\max}$ and d$J_{\max}/J$, and (iii) Arrhenius plots of J and d$J_{\max}/J$. (e) bPCBM with D-A ratio of 1:4 (f) tPCBM with D-A ratio of 1:1 (g) tPCBM with D-A ratio of 1:2 (h) tPCBM with D-A ratio of 1:4

From the Arrhenius plot in Fig.4.6 (c), there is a transition temperature in $\eta_{CS}(T)$, at which the Arrhenius model does not apply any more, to be around 190±10 K. This transition temperature is quite different across devices, as summarised in Table.4.2. The deviation from linearity might come from many reasons. We exclude the possibility that the absorption cross section of CTSs changes dramatically within this temperature range. The transition temperature correlates nicely with the device efficiency data: a higher device efficiency corresponds to a higher transition temperature. At higher temperatures, the push pulses might better separate the bound CTSs and contribute more to the photocurrent, while at lower temperatures, even though the CTSs may already be separated at the first place, the separated charges may experience a higher level of local disorder which reduces the mobility, leading to more severe recombination.

Table 4.2 Transition temperature in the Arrhenius plot for $\mathrm{d}J_{\max}/J$ in different devices

Acceptor	1:1	1:2	1:4
mPCBM	240 ± 10 K	230 ± 10 K	
bPCBM	190 ± 10 K	230 ± 10 K	230 ± 10 K
tPCBM	172.5 ± 7.5 K	205 ± 15 K	247.5 ± 7.5 K

4.3.5 Discussion

Our results demonstrate that the dissociation of localised CTSs is a temperature-dependent process in the material systems studied. The extracted activation energy is one of the fundamental parameters describing bound geminate pair formation and recombination immediately after photoexcitation, as it is important for charge separation and device performance. Energetically, a large binding energy restricts the charge separation efficiency from CTSs. The observed single activation energy value supports the assumptions which we have made during the analyses, including (i) the exciton dissociation in our study is not a temperature-dependent process [163], (ii) the activation of the CTSs by a push pulse is not temperature-dependent, and (iii) branching between localised CTSs and those contributing to free carriers occurs on the sub-ps timescale.

Here, we note that the push pulses acting on the free charges, followed by the fast thermalisation, might enhance local charge mobility. However, this does not influence the measureable quantities ($\mathrm{d}J$ and J) in PPP for two reasons: (i) As the free charge is excited to a higher state only once and for just ∼0.1 ps [30], the gain in diffusion is probably no more than 5 nm considering the disordered electronic structure away from the interface [200].

Therefore the effect caused by enhanced mobility should be negligible. (ii) As the following charge collection process is very slow (∼1 ms for 1 kHz experimental setup we use), the enhanced mobility would just slightly change the total time of charge collection (<1 ms), but not the total number of extractable free carriers.

Surprisingly, the binding energy of bound CTSs does not show a clear correlation with material composition or driving energy despite the huge difference in device performance (See Table.4.1) on page 82. The device performance of mPCBM blend is higher than bPCBM and tPCBM blends. This might be due to a reduced density of side chains that reduces the level of disorder and increases the electron mobility, which can greatly influence the BR process, affecting FF and J_{SC}. Table.4.1 shows that the higher fullerene loading increases the device performance, which is probably related with the charge separation efficiency. This points to the importance of fullerene aggregation in efficient charge generation. Excess fullerene loading enables the delocalisation of the CTSs which decreases the number of bound carriers at the interface, while the energetic difference between the bound CTSs and the SC states is similar, see Fig.4.10. For fullerene derivatives with different driving energies at the interface, the energy levels of the bound CTSs probably change as there is a linear relationship between V_{OC} and the energy levels of the CTSs. However, the binding energies of bound CTSs are still similar. We point out that this 90 meV binding energy of the localised CTSs measured in benchmark polymer:fullerene systems with a range of driving energies and film morphologies should be quite typical for the studied blends, and it indicates the unexpected similarities of the energetics between bound CTSs in OPVs.

Apart from η_{CS}, the kinetics of dJ/J gives information about GR and other processes involved in the early time window (around 1 ns in our data). We notice that the dynamics of bound CTSs is quite different for MDMO-PPV:tPCBM 1:2 devices in Fig.4.12 when compared with other devices in Fig.4.11 and Fig.4.12, showing a much longer lifetime. This may be connected with the higher LUMO energy level of tPCBM. The lifetime of bound CTSs and the transition temperature in the Arrhenius plot need further investigation in the future.

Our results agree well with the current design rules of efficient OPVs. Improved material systems are expected to have reduced LUMO offsets (for smaller voltage loss), charge delocalisation (for efficient charge separation) and higher charge mobilities (for better charge collection) to achieve efficient solar cell operation. This improvement is a challenge for fullerene-based solar cells due to the limited choice of acceptor properties. Non-fullerene acceptors offer more synthetic flexibility, providing the possibility to simultaneously fulfil these design criteria, leading to OPVs with low voltage loss, high photocurrent and high fill

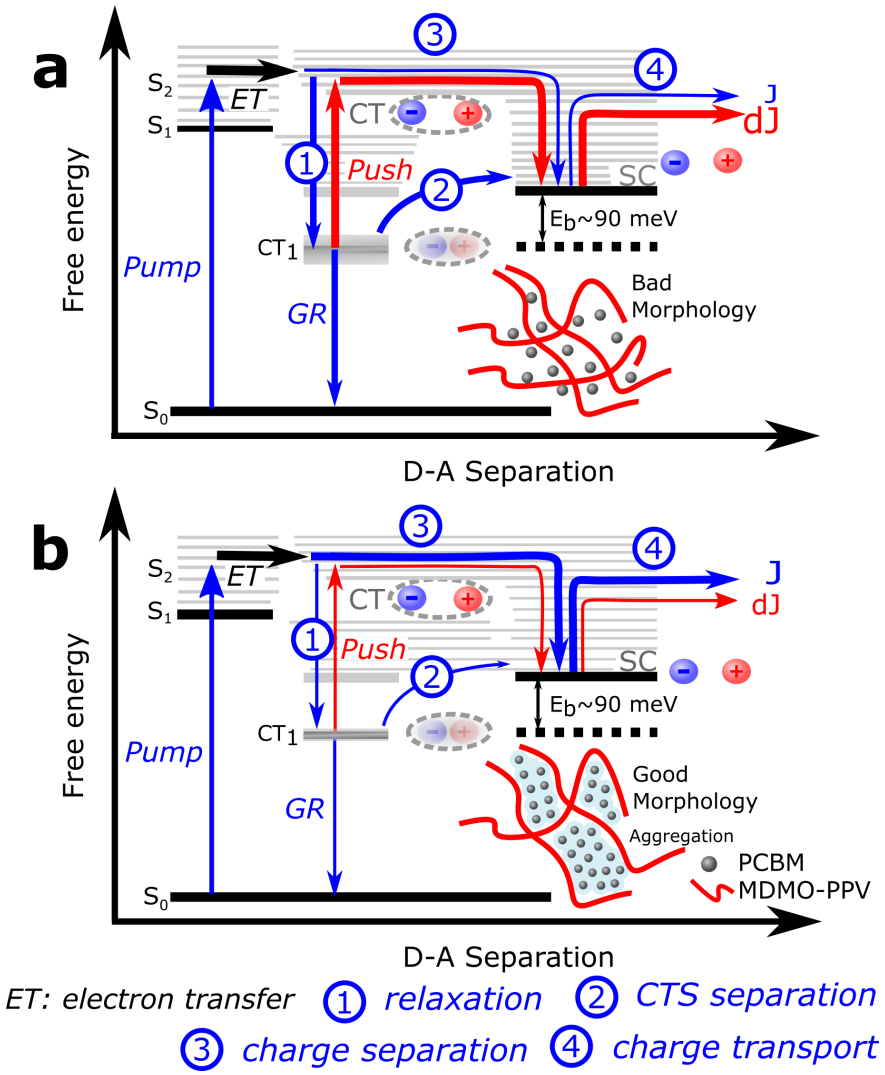

Fig. 4.13 State energy diagram describing the effect of fullerene aggregation on free charge generation. (a) bad morphology without excess fullerene aggregates; (b) good morphology with excess fullerene aggregates. The pump light forms the exciton in pristine materials and forms hot CTSs after electron transfer. There is competition between cold CT states via relaxation, and free charges via long-range charge separation. The push pulse promotes the bound CTSs to delocalised states which can then separate into free charges spontaneously. Pump-push photocurrent spectroscopy measures the charge separation efficiency. From the temperature-dependent pump-push photocurrent spectroscopy, the activation energy for CTS separation is measured. The binding energy of ~90 meV, the energy difference between CT state charge-separated states, is not so strongly correlated with the morphology. The presence of fullerene aggregation in (b) promotes delocalised CTSs and fewer bound CTSs are formed, compared with relatively bad morphology in (a).

factor. Recent research has shown some promising development of non-fullerene organic solar cells which satisfy our design considerations.[247, 248, 77, 78, 249, 250]

4.4 Conclusion

In conclusion, using ultrafast PPP spectroscopy in organic solar cells, we observe a temperature-dependent dissociation of localised CTSs. By applying the Arrhenius equation, we are able to extract a single activation energy for this behaviour which can be associated with the binding energy for localised CTSs. We rationalise our findings using a simple model in which the initially formed CTSs can evolve through one of the two separate pathways on the sub-ps timescale: (i) formation of localised (bound) CTSs followed by efficient GR or (ii) formation of delocalised CTSs eventually dissociating into free charge carriers. We did not observe major differences in the activation energy (90 ± 50 meV) across different material systems, despite varying both the driving energy for charge separation and the D-A blend ratio. As the binding energy of localised CTSs is well above the thermal energy under working conditions, we speculate that it is not the activation barrier for CTSs but the number of available localised states at the interface which is important for the device performance. Our results support the current view about the design rules for the next-generation solar cells that include a better donor-acceptor energetic alignment, a higher degree of charge delocalisation, and a reduced density of low-energy recombination centres in order to achieve high performance OPVs with low voltage loss, high photocurrent and high fill factor.

Chapter 5

Geminate Recombination in Novel NFA-based Solar Cells

Note: This chapter is closely adapted from the publication[174]. Reprinted (adapted) with permission from (J. Zhang*, Q. Gu, T. T. Do, K. Rundel, P. Sonar, R. H. Friend, C. R. McNeill, A. A. Bakulin*. "Control of Geminate Recombination by the Material Composition and Processing Conditions in Novel Polymer:Non-Fullerene Acceptor Photovoltaic Devices" *J. Phys. Chem. A*, **2018**, 122, 1253-1260.). Copyright (2019) American Chemical Society.

Material was synthesised by T. T. Do supervised by P. Sonar. Solar cells were fabricated and characterised by Q. Gu and K. Rundel supervised by C. R. McNeill. Pump-probe experiment was performed by Q. Gu and pump-push photocurrent experiment was conducted by J. Zhang. The paper was written by J. Zhang supervised by R. H. Friend and A. A. Bakulin.

5.1 Introduction

The past several years have witnessed a rapid improvement to the power conversion efficiency (PCE) of single-junction organic solar cells (OSCs), with current record efficiencies in excess of 16%.[80] Much of this progress is due to the continuing development of small-molecule non-fullerene acceptors (NFA). Compared with the fullerene-based solar cells, NFA-based OSCs exhibit superior thermo- and photo- stability, more tunable energy levels, higher electron mobility, and stronger absorption cross sections. The impressive progress in the single-junction efficiencies has also motivated research on more complex materials systems, such as ternary blends or semi-transparent and efficient devices for tandem applications. This progress is accompanied by the overall improvement of the efficiency-stability-cost combined

value.[91] All these advances might allow flexible and tunable OSCs to be competitive with silicon and perovskite solar cells for future commercialization.

We have introduced the photophysics in Chapter 4. Without special notice, CTSs mentioned below refer to localized/cold CTSs. From this localized state, the electron-hole pair experiences relaxation to the ground state, usually by geminate recombination (GR). Another loss channel comes from bimolecular recombination (BR). In most polymer:fullerene blends, the large share of long-range charge separation is shown to occur directly after exciton dissociation at the ultrafast timescale. This is probably facilitated by the strong coupling between the exciton and charge-separated states and by the strong coupling with different fullerene molecules.[38, 127] This coupling and electron delocalization due to fullerene aggregation was suggested to play a critical role in promoting photocurrent generation.[37, 179]

For efficient NFAs, the most popular materials seem to be based on A-D-A ladder-type structures. For instance, A-D-A molecules employing indacenodithiophene[251] as the central building block, with 2-(3-oxo-2,3-dihydroinden-1-ylidene)-malononitrile as the capping groups, has effectively pushed the efficiency of NFA-based OSCs well above 10% and kept the highest efficiency above 14%. Some other central units, such as benzodi(cyclopentadithiophene)[250], previously quite popular in donor design,[252] and thiophene-thieno[3,2-b]thiophene-thiophene[253], were shown to be excellent candidates with above 10% efficiency. There is broad interest within the community to explore further building blocks for A-D-A molecules. In particular, low-bandgap NF molecules (E_g < 1.5 eV) with extended absorption into the near-infrared (NIR) region give better device performance and are receiving increased interest.[87, 253] In the published paper by our collaborator, two new NFAs were synthesised.[254] Both molecules contain a ketone-based central building block, 9-fluorenone (FN) or 9,10-anthraquinone (ANQ), and are both capped with diketopyrrolopyrrole (DPP) groups. However, unexpectedly, devices based on these new molecules gave a low PCE of $\sim$ 1%. Understanding which step in the charge generation processes limits the device efficiency might offer new insight into the photophysics of NFA OSCs, and help to further the device optimisation.

In this chapter, we studied the charge dynamics of two A-D-A type NFAs with P3HT as the donor. By using ultrafast NIR spectroscopy methods, namely pump-push photocurrent (PPP) spectroscopy, we identified GR as the main loss channel in a batch of devices made with different processing (varying solvent and annealing) conditions. We also performed transient absorption spectroscopy (TAS) and global data analysis to build a comprehensive photophysical picture for the dynamics of excitons, CTSs and free carriers. Combining with the morphological analysis, we are able to rationalize our results and discuss the implications for the optimisation of emerging NFA OSCs.

5.2 Device Performance

5.2.1 Materials, Preparation and Characterisation of Thin Films

P3HT (Mw = 60,000 Da) was purchased from Rieke Metals, and 9-fluorenone and 9,10-anthraquinone end-capped with diketopyrrolopyrrole (DPP-ANQ-DPP and DPP-FN-DPP) were synthesised according to methods described before.[254] Fig.5.1(a) shows the chemical structures of the novel NF-SMAs, DPP-FN-DPP and DPP-ANQ-DPP, respectively. The energy levels of highest occupied molecular orbit (HOMO), measured by photoelectron spectroscopy in air and lowest unoccupied molecular orbit (LUMO), calculated by HOMO and the optical gap, taken from our previous study [254], are shown in Fig.5.1(b).

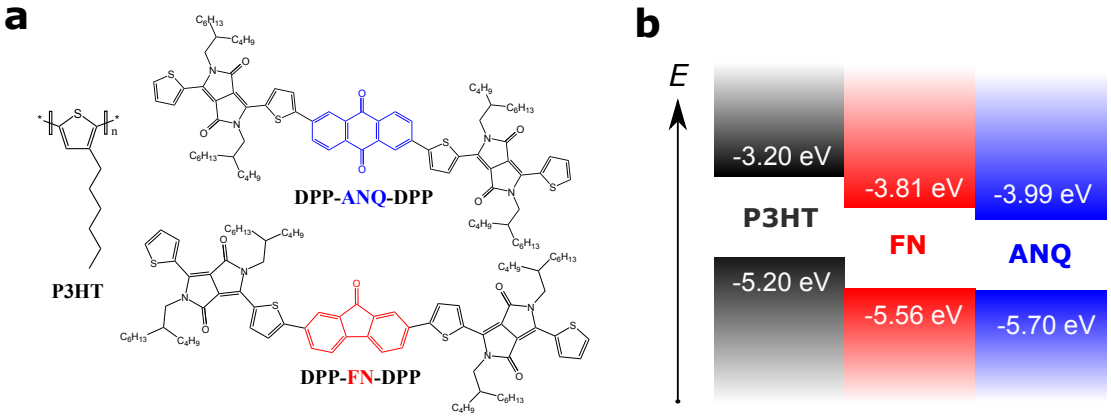

Fig. 5.1 Molecular structure and energy levels. (a) Chemical structures and (b) energy levels of the donor material (P3HT) and two novel non-fullerene acceptor molecules, DPP-ANQ-DPP and DPP-FN-DPP.

Thin films were prepared from 1 cm × 1 cm glass substrates, which were sequentially cleaned by sonication in acetone and 2-propanol for 10 min each followed by another 10-min UV-ozone treatment. The substrates were then moved into a glovebox under nitrogen atmosphere for deposition of the active layer. For the most efficient device, the optimum blend weight ratio was 2:1 for P3HT:DPP-FN-DPP with spin speed of 3000 revolutions per minute (RPM) and 1:2 for P3HT:DPP-ANQ-DPP with spin speed of 1000 RPM, respectively. Immediately after deposition, half of these samples were annealed at 120 °C for 5 min.

Fig.5.2 presents the absorption spectra of the pure films. In the blend films (P3HT:DPP-ANQ-DPP and P3HT:DPP-FN-DPP), the small peak at around 680 nm probably comes from π-π stacking of the small molecules, which were also seen in the pristine films (dashed lines). Because the absorption spectra of these molecules are different to that of P3HT, the NFA can be selectively excited. In our experiment, the excitation wavelength is $\sim$ 700 nm, except

where specifically stated. Selective excitation of P3HT is not easy but still possible, for example, at 500 nm where P3HT strongly absorbs and NFA weakly absorbs.

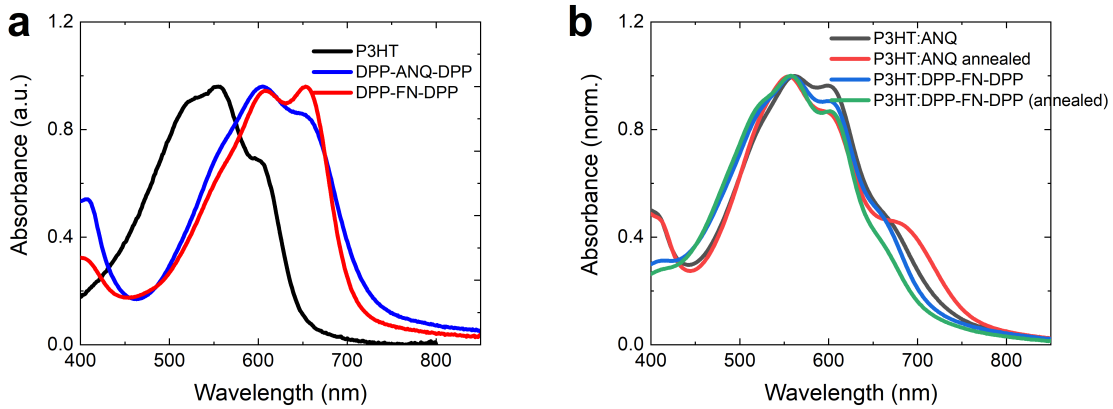

Fig. 5.2 (a) Absorption spectra of P3HT and the pristine non-fullerene acceptors (DPP-FN-DPP and DPP-ANQ-DPP); (b) absorption spectra of the as-cast and annealed blends, P3HT:DPP-FN-DPP and P3HT:DPP-ANQ-DPP.

5.2.2 Device Fabrication

Devices were made with a ITO/ZnO/PEIE/active layer/MoO_x/Ag structure. The glass slides with indium tin oxide (ITO) were subsequently cleaned using detergent and deionized water, acetone and isopropanol for 10 min each. A 0.1M zinc oxide (ZnO) solution was prepared by dissolving zinc acetate dihydrate (220 mg) in 10 ml 2-methoxyethanol, with ethanolamine (61 mg) as a stabilizer. The solution was then stirred at 60 °C for 12 hours under ambient conditions. The 0.4% poly(ethylenimine) ethoxylated (PEIE) precursor was prepared by dissolving 40 mg PEIE in 10 ml of 2-methoxyethanol. Both solutions were filtered before use. A ZnO film was first spin coated on top of the ITO glass substrate at a speed of 4000 RPM, followed by film annealing on the hot plate in ambient conditions at 200 °C for 30 min. A PEIE film was then deposited by spin coating at 5000 RPM. After baking the PEIE film at 120 °C for 20 min, the substrates were transferred to a glovebox under nitrogen atmosphere for deposition of active layers, MoO_x and Ag. The deposition and post-annealing of the BHJ layers were the same as that in the film described in the main text. Samples were then loaded into a vacuum deposition chamber to evaporate a 12-nm molybdenum oxide (MoO_x) and 100 nm silver cathode on top of the active layer subsequently. A mask was used during vacuum evaporation to generate eight individual pixels in each substrate with the active device area of 4.5 mm^2. Finally, these devices were fitted with edge clips, encapsulated by

epoxy and glass, and placed inside the glovebox overnight, enabling the epoxy to be dried before further testing or characterization.

To better control the experimental conditions, we measured 8 different devices by varying acceptors (DPP-FN-DPP and DPP-ANQ-DPP), processing conditions (as cast and annealing) and solvent types (dichlorobenzene, DCB and chloroform, CF).

5.2.3 Device Characterisation

Current density-voltage curves of the solar cells were recorded by a Keithley 2635 source meter under illumination of a solar simulator (SS50AAA, Photo Emission Tech). The intensity of the simulated sunlight (100 $\mathrm{mW\,cm^{-2}}$) was calibrated with a standard silicon reference cell and a KG3 filter. The external quantum efficiency (EQE) spectrum was measured by an Oriel Cornerstone 130 monochromator.

The device characteristics are summarised in Table.5.1. We believe dissimilar optimal concentrations (2:1 for P3HT:DPP-FN-DPP and 1:2 for P3HT:DPP-FN-DPP) might be related to the morphological difference between fluorenone and anthraquinone units in the acceptor when forming solid-state stacking in the film. In our previous work, device efficiency was doubled after thermal annealing processing for P3HT:DPP-FN-DPP (from 0.58% to 1.2%) and P3HT:DPP-ANQ-DPP (from 0.46% to 0.7%) devices.[254] As shown by previous morphological study,[254] these enhancements in efficiency are due to the improved crystallinity of both P3HT and NF-SMA phases, increasing the electron and hole mobilities. However, the detailed photophysics behind these changes in efficiency, and more importantly, the identity of the efficiency-limiting photophysical process, are still not completely clear.

5.3 Pump-Push Photocurrent Spectroscopy

In order to further understand the difference in charge dynamics in these two novel NF-SMAs, we perform ultrafast pump-push photocurrent spectroscopy and pump-probe spectroscopy on the relevant films and devices.

Fig.5.3 illustrates the kinetics from PPP spectroscopy with excitation wavelength at 540 nm. The pump energy per pulse is around 1 μJ, and the push light is at 2 μm. The focused spot size is around 1 $\mathrm{mm^2}$. A detailed description can be found in Chapter 3. All eight curves are divided into two panels (a) and (b), considering the large variation in amplitude. The maximal response is around 0.4 while the minimal is only around 0.002. For this reason, logarithm scale is adopted in panel (a). This amplitude variation is correlated with the solvent type used for sample preparation, CF and DCB. In PPP, $\mathrm{d}J/J$ does not depend on charge

Table 5.1 Solar Cell Performance of DPP-FN-DPP and DPP-ANQ-DPP based Blends in DCB.

Material blend (solvent,processing)	Thickness (nm)	V_{OC} (V)	J_{SC} (mA cm^{-2})	FF (%)	PCE (%)	EQE J_{SC} (mA cm^{-2})	Max EQE
P3HT:DPP-FN-DPP (DCB, As cast)	39 ± 2	0.98	1.96	30.4	0.58	1.82	12.0
P3HT:DPP-FN-DPP (DCB, Anneal)	39 ± 2	0.97	3.20	37.2	1.20	3.00	22.8
P3HT:DPP-ANQ-DPP (DCB, As cast)	75 ± 7	0.85	1.32	41.1	0.46	1.25	7.3
P3HT:DPP-ANQ-DPP (DCB, Anneal)	75 ± 7	0.85	2.00	38.7	0.70	2.20	13.7
P3HT:DPP-FN-DPP (CF, Anneal)	/	0.93	0.72	30.61	0.21	0.94	8.24
P3HT:DPP-FN-DPP (CF, Anneal)	/	0.98	1.02	30.94	0.35	1.90	12.15
P3HT:DPP-ANQ-DPP (CF, As cast)	/	0.85	0.79	24.17	0.16	1.05	8.40
P3HT:DPP-ANQ-DPP (CF, Anneal)	/	0.85	1.37	27.23	0.32	1.37	9.89

The thicknesses of the bottom four blends were not measured, and marked as absent (/).

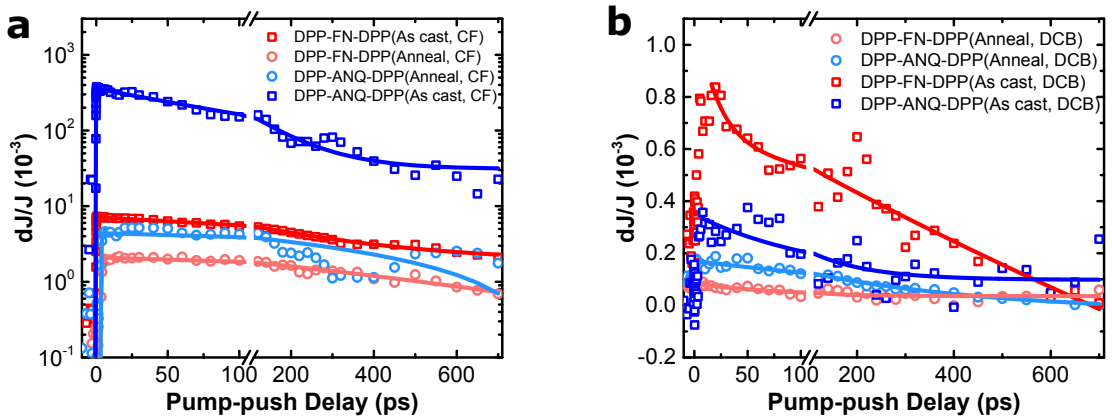

Fig. 5.3 PPP responses for devices with CF (a) and DCB (b) as the solvent.Solid fitting lines in (a) and (b) are multi-exponential guides to the eye. The excitation wavelength is 540 nm which mainly excites P3HT. The fluence is 100 $\mu J\,cm^{-2}$

collection efficiency or bimolecular recombination. As the number of free (collected) carriers does not change at ns time scale, the evolution of dJ/J in time is proportional to the number of bound carriers and reflects their GR to the ground state.[30] The maximal amplitude, dJ_{max}/J, therefore characterizes the overall efficiency of long-range charge separation; less GR means better charge separation, and hence a smaller dJ_{max}/J value is observed.

In Fig.5.4, a larger photocurrent (J) in x-axis correlates with an exponentially smaller dJ_{max}/J in y-axis. As photocurrent is a product of GR-related CT state dissociation efficiency and BR-related collection efficiency. This inverse correlation suggests that the device performance is mainly limited by GR. Even though GR in some devices is small (seen by a small dJ_{max}/J, around 10^{-3}), there are still other processes limiting the device efficiency, mainly bimolecular recombination. This is seen as a low FF in Table.5.1, and does not change much when varying processing methods. However, to further study BR is out of current work's scope. We note that due to the non-zero background signal, we take the signal change just after time zero and before zero as $\Delta J/J$ for further comparison.

Table.5.2 lists J and $\Delta J/J$ of the eight devices under study. In general, thermal annealing reduces $\Delta J/J$ by increasing the aggregation of polymer or NFA and reducing the recombination interface. This supports that GR can be suppressed by optimizing the morphology. However, this processing does not necessarily result in a higher photocurrent, for example, between Sample 5 and 7. This suggests that even though GR is suppressed, the following charge collection and overall device performance might be hindered due to morphological issues, for instance degradation of the bicontinuous D-A network. Another observation is that the solvent used for device fabrication has a major effect on GR. When DCB is used as the solvent (Samples 1-4), the photocurrent is above 40 nA and $\Delta J/J$ is less than 10^{-3}, implying

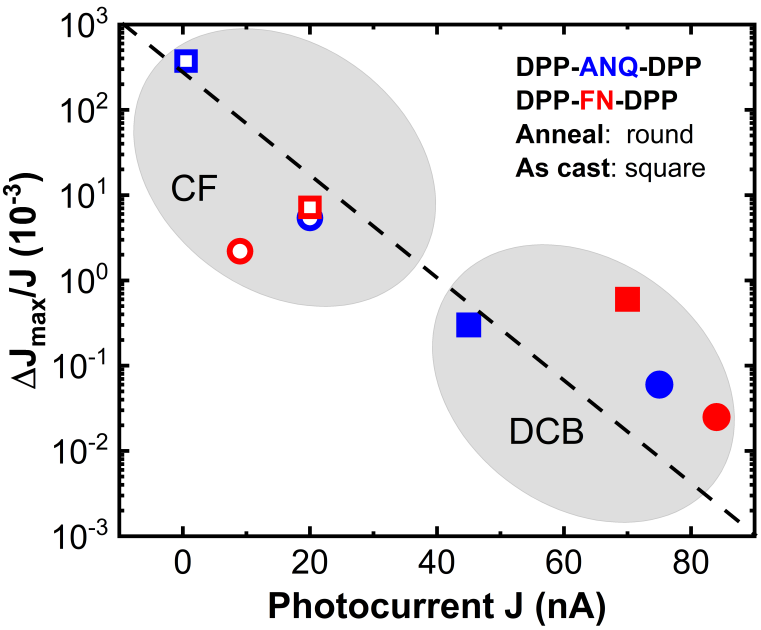

Fig. 5.4 Scatter map showing the inverse relationship between $\Delta J_{\max}/J$ and photocurrent J for devices with different processing conditions. The straight dash line is guide to the eye.

Table 5.2 Summary of Pump-Push Responses of the Studied Material Blends with Different Processing Conditions.

Sample	Acceptor	Processing	Solvent	PCE (%)	J (nA)	$\Delta J/J$ (10^{-3})
1	DPP-FN-DPP	Anneal	DCB	1.2	84	<0.025
2	DPP-ANQ-DPP	Anneal	DCB	0.7	75	0.06
3	DPP-FN-DPP	As cast	DCB	0.58	70	0.6
4	DPP-ANQ-DPP	As cast	DCB	0.46	45	0.3
5	DPP-FN-DPP	Anneal	CF	0.35	9	2.2
6	DPP-ANQ-DPP	Anneal	CF	0.32	20	5.4
7	DPP-FN-DPP	As cast	CF	0.21	20	7.2
8	DPP-ANQ-DPP	As cast	CF	0.16	0.5	373

that GR is not so severe. When CF is used as the solvent (Sample 5-8), the photocurrent is smaller than 20 nA and $\Delta J/J$ is larger than 2×10^{-3}, implying that GR is more severe than the DCB-processed samples. The solvent is known to be critical for the formation of a favorable blend morphology. Further work towards optimizing the annealing conditions in order to maintain a bicontinuous network [255] might further improve the device efficiency of DPP-FN-DPP and DPP-ANQ-DPP devices.

To compare these three conditions more clearly, we constructed Table.5.3 which shows how GR is sensitive to each variable by fixing the other two conditions. From this table, it is quite clear that the solvent type is the most influential parameter, which agrees with our earlier analysis. Interestingly, it seems that there is no fundamental difference in the level of GR between the two NFAs.

Although the type of NFA is not as influential as other two parameters, the analysis reveals that the FN and ANQ moieties behave differently. In the as-cast film, DPP-ANQ-DPP hinders P3HT crystallization while DPP-FN-DPP does not.[254] This results in a very low photocurrent (0.5 nA) and extremely high $\Delta J/J$ for Sample 8 in Table.5.2. The $\Delta J/J$ as large as 0.37 is the maximal number we have measured, which shows a tremendous amount of bound CTSs at the interface failing to escape GR.

Table 5.3 Sensitivity Comparison of $\Delta J/J$ in Devices with Different Processing Conditions.

Variant	Value 1	Value 2	Value 3	Value 4
Annealing As cast	$\frac{Sample1}{Sample3} = \frac{0.6}{0.025} = 24$	$\frac{S2}{S4} = \frac{0.3}{0.06} = 5$	$\frac{S5}{S7} = \frac{7.2}{2.2} = 3.27$	$\frac{S6}{S8} = \frac{373}{5.4} = 69$
FN ANQ	$\frac{Sample1}{Sample2} = \frac{0.06}{0.025} = 2.4$	$\frac{S3}{S4} = \frac{0.3}{0.6} = 0.5$	$\frac{S5}{S6} = \frac{5.4}{2.2} = 2.45$	$\frac{S7}{S8} = \frac{373}{7.2} = 51.8$
DCB CF	$\frac{Sample1}{Sample5} = \frac{2.2}{0.025} = 88$	$\frac{S2}{S6} = \frac{5.4}{0.06} = 90$	$\frac{S3}{S7} = \frac{7.2}{0.6} = 12$	$\frac{S4}{S8} = \frac{373}{0.3} = 1243$

5.4 Pump-Probe Spectroscopy

To further understand the early charge generation and recombination dynamics, we performed pump-probe experiments on P3HT:DPP-ANQ-DPP films.

The transient absorption experiment was performed with a commercial transient absorption spectrometer (HELIOS, Ultrafast Systems). Ultrafast pulses at $\sim$ 800 nm from a regenerative Ti:Sapphire amplifier system (Spectra Physics, Solstice) were sent into TOPAS-Prime (Light Conversion) to generate tunable pump pulses ($\sim 355-2600$ nm), while another portion was sent into a delay stage, followed by generation of broadband probe pulses ($\sim 800-1400$ nm) using a substrate made of yttrium aluminum garnet. Part of the probe light was split and used as the reference to reduce pulse amplitude fluctuation. Both probe and reference beams were sent into their corresponding fibres and measured with spectrometers. The beam size of pump and probe pulses were estimated to be ~ 0.5 mm^2 and the time resolution of pulses to be ~ 200 fs.

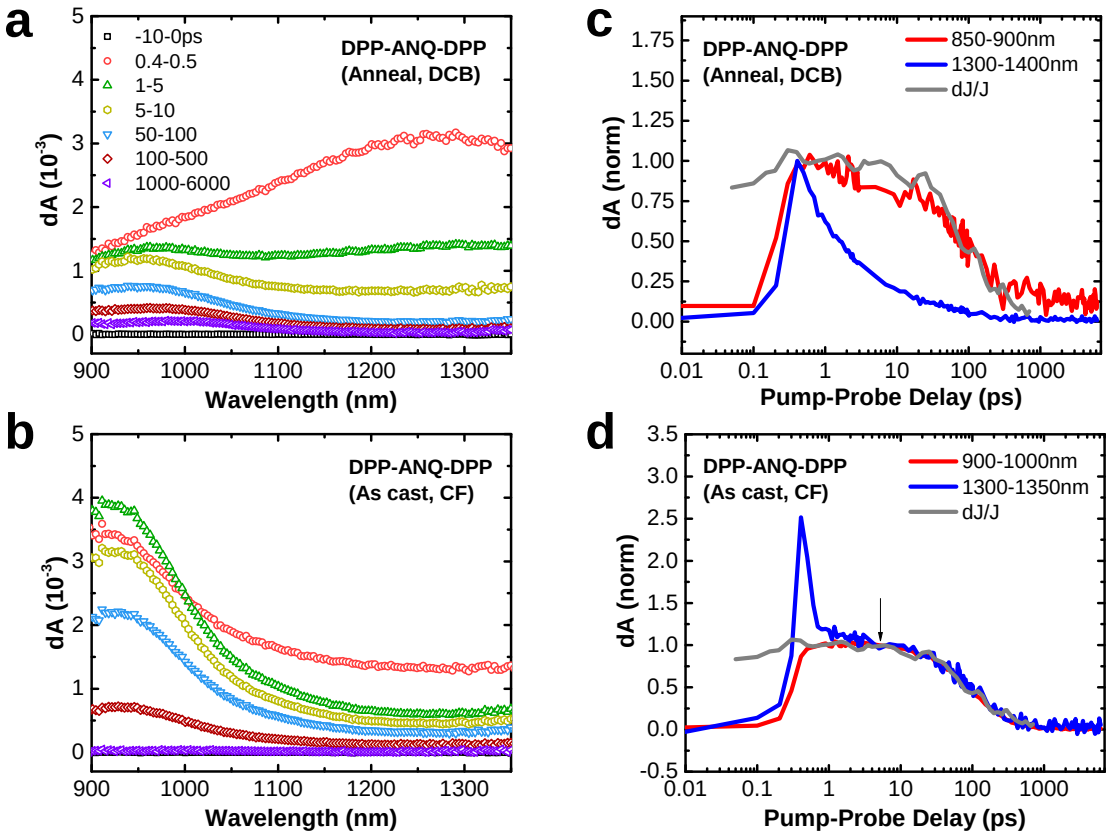

Fig. 5.5 Broadband transient absorption spectroscopy for P3HT:DPP-ANQ-DPP films. (a,b) Spectral slices spanning from 900 nm to 1350 nm using two processing methods (a) DCB as the solvent, being annealed; (b) CF as the solvent, as-cast films; (c,d) Selected kinetics showing the decay of mainly excitonic and polaronic contributions. The grey reference line shows the dynamics of recombination of bound CT states in the as-cast film. The arrow in (d) indicates that curves are normalized at 5 ps. The pump wavelength is 690 nm for selective acceptor excitation, and the pump pulse energy is 50 nJ.

Fig.5.5 shows the spectra and kinetics obtained from broadband pump-probe spectroscopy comparing the same material blend (P3HT:DPP-ANQ-DPP) with different processing conditions. The broadband probe (900-1350 nm) can result in the photo-induced absorption (PIA) of different species, which gives a comprehensive knowledge of the studied material system. To understand the complex spectra with overlapping PIA responses, we first assigned different spectral contributions to the relevant species. In Fig.5.5(a) at very early time (within 500 fs), we assigned a Gaussian-like peak around 1250 nm to the acceptor exciton PIA, as the pump light (690 nm) mainly excites the acceptor exciton. This exciton signal decays and the spectrum evolves into another peak at 950 nm after $\sim$ 10 ps, which we assigned to the exciton dissociation and formation of CTSs. Later (around 5 ns), a different spectrum (purple line in Fig.5.5(a)) is seen with a peak at $\sim$ 1020 nm which we assign to free charges.

In Fig.5.5(b), the exciton signature even at 0.5 ps is much weaker compared with the same line in Fig.5.5(a), which suggests an ultrafast exciton dissociation within several hundred fs. Accompanied with the decrease of exciton signal, there is an obvious appearance of CTS signature. Due to morphological effect, free charges are more likely to be located in crystalline region where energy is lower than amorphous region. In contrast, bound charges in CT states near the interface is more likely located in the amorphous region. Assuming the same absorption coefficient of polarons in both films, from the amplitude of CTS signal, under the same excitation density, the amplitude of charges (900-1000 nm) in annealed film at early times (around 5 ps) is only 25% of that in as-cast film, indicating direct charge generation is enhanced in annealed films through bypassing CTS formation. This is similar to previous studies on P3HT:fullerene blends.[153]

In Fig.5.5(c) and (d), we selected two representative wavelengths at around 900 nm and 1300 nm regions to retrieve the kinetics of excited states. In Fig.5.5(d), an ultrafast decay (several hundred femtoseconds) of the exciton signal is observed, while after several picoseconds, the signal is dominated by CTS signal across the whole spectrum. The decay of pump-probe signal associated with CTSs matches very well the decay of pump-push response measured in the same devices (grey line). This strongly supports that this species identified in pump-probe are related with local (bound) CTSs. We emphasise that PPP spectroscopy only measures the bound CTSs that do not contribute to the photocurrent, while pump-probe measures all the localized CTSs. The good match between both techniques suggests that the thermal activation of localized CTSs to free charges, sometimes called 'cold' charge separation pathway, is minimal. These CTSs are generated after the exciton dissociation and decay through GR to ground states, which is a dominant loss channel. However, in Fig.5.5(c), the grey reference line does not fully overlap with the kinetics around 900 nm. This probably comes from the comparable population of multiple species and spectral overlap.

5.5 Global Analysis of Pump-Probe Data

Genetic algorithm is a global fitting method to decompose the overlapping spectral signatures of various spectral species and obtain their relevant kinetics. The detailed description can be found elsewhere.[157] In short, a large number of random spectra are generated and selected to form later generations according to their fitness compared to the original spectra. For a certain solution, the fitness is evaluated as the inverse sum of squared residual and an additional penalty is added for non-physical results. The selected spectra are then modified by mutating with each other to avoid local minima, similar to the natural evolution process. This flexible method allows for avoiding pure mathematical solutions to a large extent and

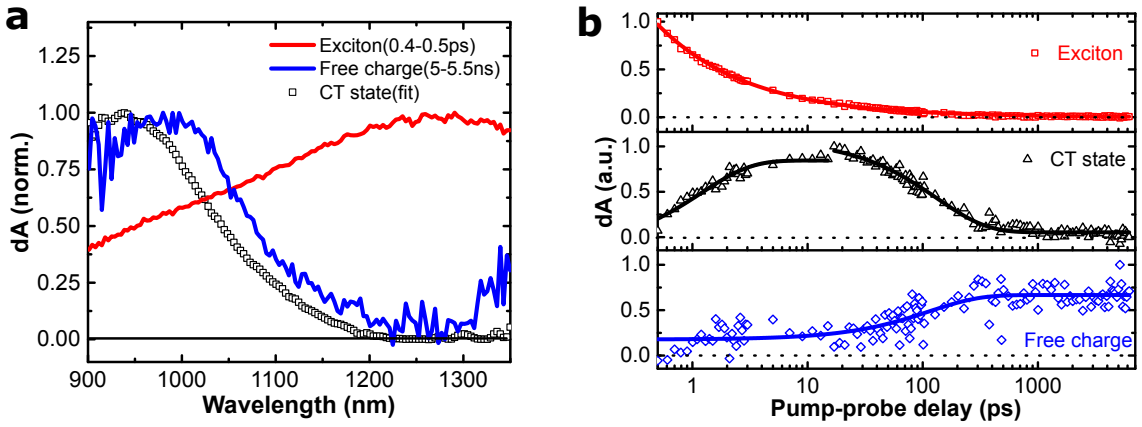

Fig. 5.6 GA decomposition of the broadband pump probe spectra of P3HT:DPP-ANQ-DPP (Anneal, DCB). (a) Spectra of excitons and free charges are fixed and extracted from $0.4-0.5$ ps and $5-5.5$ ns, and the spectra of CTSs is obtained from GA algorithm. (b) The respective kinetics. The red line is the power law fit for the exciton decay, due to exciton diffusion before charge generation. The blue and black lines are the exponential fitting for CT states and free charges, respectively. The decay rate of CTS is fitted to be around 133 ± 6 ps.

obtains physically reasonable solutions, which usually performs better than singular value decomposition.

In Fig.5.7, we also measured the fluence dependent TA spectra of P3HT:DPP-ANQ-DPP films and observed the charge feature at 960 nm. For the annealed film fabricated with DCB, the excitation energy varies from 10 μJ to 200 μJ. Below 20 μJ, there is no fluence dependence, and should be only geminate recombination. Above 50 μJ, there is clear fluence-dependent kinetics, in particular at early time before 10 ps, which probably due to exciton-exciton annihilation and exciton-charge annihilation. In contrast, for the as-cast film fabricated with CF, we do not see dependence until 200 μJ. Such late dependence is probably related with ultrafast exciton dissociation.

To separate the overlapping PIA signals measured in Fig.5.5(a), we used a global analysis technique based on a genetic algorithm (GA) which imitates the natural selection process to select the best fitting solution. Fig.5.6 shows the deconvoluted spectra and kinetics. The spectrum at $0.4-0.5$ ps was fixed as the 'pure' exciton signal, and the long-lived signal at $5-5.5$ ns was fixed for free charges; CTSs should have negligible contribution at these timescales. The absorption by CTSs peaks around 940 nm, while free charges absorb mostly at $\sim$ 1000 nm. This supports our previous observation that two species except excitons are present in the spectra, and that CTSs and free charges might exhibit different absorption signatures. The difference might be caused by the local D-A morphology. Near the D-A interface, it is more likely to form amorphous region, while away from the interface, more

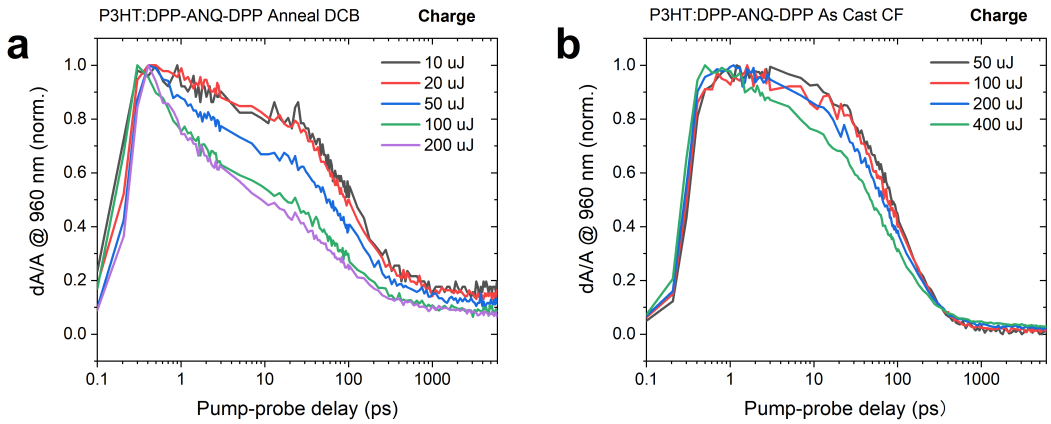

Fig. 5.7 Fluence dependence of P3HT:DPP-ANQ-DPP films. (a) The kinetics of the annealed films processed with the solvent DCB at 960 nm at various fluence from 10 uJ/pulse to 200/pulse; (b) The kinetics of as-cast films processed with the solvent CF at 960 nm at various fluence from 50 uJ/pulse to 400/pulse;

crystalline regions form. Energetically, crystalline regions have lower energy, providing some driving force. However, if charge moves from the interface, the entrpy will increase. Thus, there is a balance of entropy and driving energy for separation of CT states. The decay of excitons in Fig.5.6(b) follows a power-law trend, which might be related to large domains for exciton diffusion before reaching the interface for charge transfer.[256] The rising rate for CTSs $\sim$ 2 ps correlates with the decay of excitons. The decay rate of CTSs after 20 ps is 133 $\pm$ 6 ps, which agrees well the decay rate of 125 $\pm$ 1 ps obtained from the red line in Fig.5.5(d). The component presented in the bottom panel shows very slow increase, which we assign to the generation of free charges. This signal does not change much after 500 ps, probably as BR does not happen yet due to a low concentration and/or mobility of free carriers.

5.6 Photophysical Model

Fig.5.8 presents the photophysical model summarizing the observation from both PPP and pump-probe spectroscopy. In the as-cast film, donor and acceptor phases were well intermixed leading to an ultrafast decay of exciton signal. From the energetic view, this ultrafast fast decay might result from the large driving force (LUMO difference: 0.79eV) at the heterojunction for charge generation, and agrees with observations in fullerene-based systems. With morphology optimisation by solvent type and post annealing treatment in ANQ-based molecules, the domain purity probably increases and phase segregation improves,[257, 258] supported by previous morphological observations.[254] The exciton

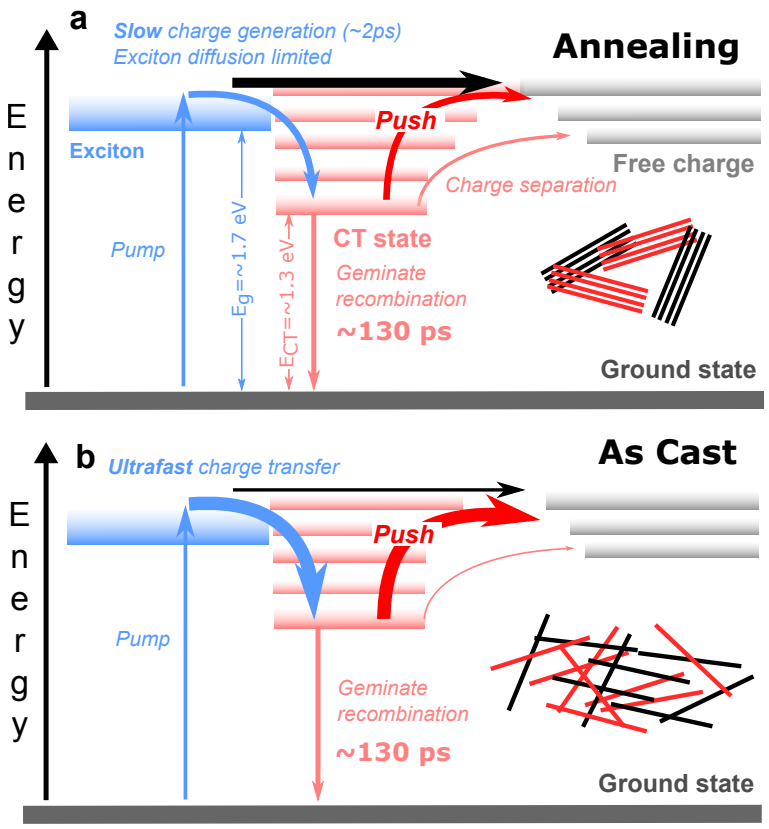

Fig. 5.8 Diagram of the relevant charge dynamics of the P3HT:DPP-ANQ-DPP blends. After annealing processing together with solvent change, slower charge generation rate and more efficient charge separation result in better device performance. The energy level of singlet state was estimated from HOMO-LUMO gap for the acceptor ($\sim$ 1.7 eV) and CT state from the diagonal gap between acceptor and donor ($\sim$ 1.3 eV).

population obeys a power-law decay, suggesting dispersive exciton diffusion and/or a time-dependent diffusion coefficient[256]. The exact charge transfer rate is not clear, but the charge generation is probably limited by exciton diffusion. In the annealed film, this slower exciton dissociation (compared to as-cast films) also correlates with slower CTS formation (shown in Fig.5.6 (b)). The efficiency of direct charge generation almost doubled in more ordered film phases, similar to fullerene aggregation case.[38] A rather big difference in charge separation efficiency suggests substantial improvement of interfaces for charge separation. In all materials CTSs decay at a similar rate ($\sim$ 130 ps, shown in Fig.5.5 (d)) as observed in PPP and pump-probe experiments. This indicates that this time scale is inherent independent of the morphology, which is also seen at polymer-polymer interface.[259] The invariance of decay to the material composition and processing suggests that states are strongly bound and 'cold' charge generation pathway cannot compete with GR even after morphology optimisation. The dominance of fast GR over slow hopping-mediated charge separation mainly limits its

charge generation efficiency, agreeing with its low efficiency. This fast GR time scale might come from strong non-radiative recombination of CTSs. The same recombination rate of CTSs regardless of its morphology obtained here may not be applicable to other material blends. We note that the recombination rate of CTSs may also vary with its electron-hole separating distance. However, for excited CTS, either strongly coupled to charge-separated states, or quickly relaxing to its localized CTSs, its lifetime is not easy to measure. The extreme case is the realisation of long-lived luminescence from the charge-separated states in exciplexes.[260]

5.7 Conclusion

In this work, two ultrafast techniques, pump-push photocurrent spectroscopy and near-infrared transient absorption spectroscopy, were used to elucidate the charge dynamics in photovoltaic devices based on two novel non-fullerene small-molecule acceptors. By changing the solvent type and the thermal treatment, we observed a large variation in charge separation efficiency. The strong correlation between geminate recombination and device efficiency suggests that geminate recombination is the main limiting process for efficient device operation. This correlation demonstrates the useful nature of the photocurrent-detection technique for guiding device optimisation. In-depth investigation by pump-probe experiments allowed us to identify specific spectral signatures for CTSs and charges and confirmed the observed CTSs generation and recombination rates. This agreement suggests charge separation is not favorable for localized CTSs. The geminate recombination rate is coherent and independent of the morphology. Further optimisation of the studied materials should probably focus on facilitating long-range charge separation and avoid the formation of localized charge transfer states. Our investigation of charge dynamics offers new insight into geminate recombination in a family of non-fullerene acceptor materials, and should be of great relevance to the broad community.

Chapter 6

Charge Dynamics in High-Efficiency NFA-based Blends

Note: Part of this chapter is adapted from the publication[1]. Copyright(2019) Wiley. Used with permission from (B. Kan†, J. Zhang†, F. Liu, X. Wan, C. Li, X. Ke, Y. Wang, H. Feng, Y. Zhang, G. Long, R. H. Friend, A. A. Bakulin* and Y. Chen*, Fine-Tuning the Energy Levels of a Nonfullerene Small-Molecule Acceptor to Achieve a High Short-Circuit Current and a Power Conversion Efficiency over 12% in Organic Solar Cells, Advanced Materials and Wiley Online Library).

Material synthesis and device fabrication were performed by B. Kan under the supervision of X. Wan and Y. Chen. Pump-probe experiment was performed by J. Zhang supervised by A. Bakulin and R. Friend. The paper was co-written by B. Kin and J. Zhang.

6.1 Materials

Since the pioneering work from Jianhui Hou Group reporting a NFA-based blend PBDB-T:ITIC with PCE over 11% in 2016, molecular engineering based on these two molecules has quickly pushed the device efficiency to over 16% for binary OSCs. [77, 79] Using heptacyclic benzodi(cyclopentadithiophene) as the D unit and INCN as the A unit, Yongsheng Chen in Nankai University reported a A-D-A ladder-type NFA, NFBDT with over a PCE over 10%.[250] Later, a weak electron-donating alkyl group (octyl) was introduced to 4,8-positons of the central BDT unit to increase the HOMO energy level. Meanwhile, a strong electron-withdrawing fluorine atom (F) was introduced to the INCN unit to decrease the LUMO energy level. Finaly, NCBDT exhibits a low optical bandgap of 1.45 eV which is 0.11 eV smaller than NFBDT. NCBDT film afforded efficient absorption range covered from 600 to 850 nm,

which is obviously red-shifted to NFBDT. The optimised device based on PBDB-T:NCBDT blend gave a remarkable PCE over 12% with a moderate V_{OC} of 0.839 V, a high FF of 71%, and an outstanding J_{SC} over 20 mA cm^{-2} which is much higher than that for NFBDT-based device. This result was one of the best performance for NFA-based OSC devices with such a low bandgap NFA.

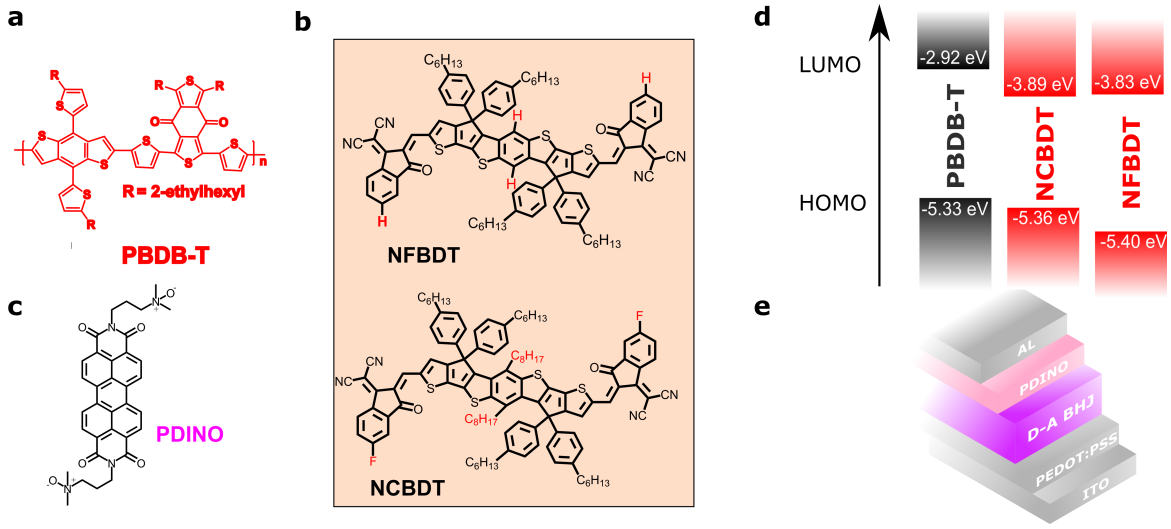

Fig. 6.1 Molecular properties of PBDB-T, NCBDT, NFBDT and PDINO. (a) The molecular structure of donor PBDB-T, (b) two acceptors (NFBDT and NCBDT), and (c) the interlayer PDINO; (d) the frontier energy levels of PBDBT, NFBDT and NCBDT; (e) The device structure: the hole transport layer PEDOT:PSS, the D-A bulk heterojunction, the electron transport layer PDINO, and the electrode Al. The HOMO level was determined in the solution using cyclic voltammetry, and LUMO is determined from the HOMO and the optical bandgap.

Here, we perform pump-probe spectroscopy on PBDB-T:NCBDT by selectively exciting the donor and acceptor materials. The energy/charge transfer process is observed at different time scales. Finally, genetic algorithm help decompose the overlapping signals in the NIR to give the timescale for charge generation. We also discuss the spectroscopic data in the visible region.

6.2 Transition Absorption Spectroscopy in NIR region

6.2.1 Pristine Donor and Acceptor Films

We started our measurements by characterising the steady-state absorption spectra of the pristine solid films, prepared from spin-coating. As shown in Fig.6.2, PBDB-T mainly absorbs the visible light, and two acceptors (NCBDT and NFBDT) mainly absorbs in the near-IR region.

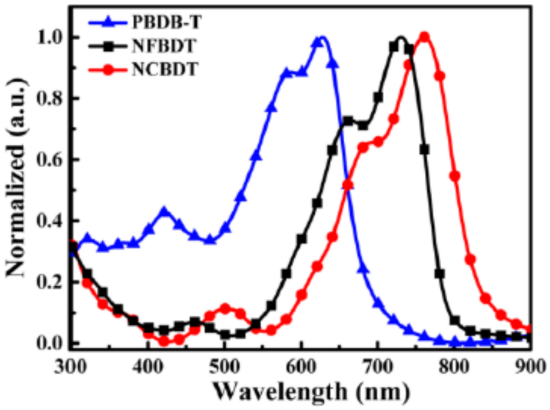

Fig. 6.2 The absorption spectra of PBDB-T, NFBDT and NCBDT pristine films. Extracted from [1].

Under excitation, bound electron-hole pair (exciton) initially forms. From transient absorption (TA) measurements, we know the spectroscopic feature of excitons and how the exciton decays. Due to the disorder in the solid state, self-dissociation of excitons may occur to some degree, and therefore the spectra of relatively long-lived polarons can also be obtained. On the other hand, inter-system crossing cannot be neglected, which may generate triplet states. Further evidence are needed to distinguish charge and triplet states. Such understanding lays the basics for understanding the more complex interaction between donor and acceptor in the bulk-heterojunction structure.

Laser pulses at 600 nm can excite both donor and acceptor materials. In this section, we focus on the probe region between 800 nm and 1600 nm where PIA signals of exciton and polaron mainly reside. Fig. 6.3 represents the spectra at different time delays. In general, the excited species in the pristine phase at early time, i.e. < 1 ps, is assigned to excitons. The signal at later time (1 ns to 6 ns) is associated with polarons or triplets, from exciton self-dissociation between adjacent molecules or the inter-system crossing, respectively. Despite PIA signals, some other types of spectral features, such as stimulated emission (SE) and ground-state bleach (GSB), are also present near 800 nm. To distinguish them, SE signal decays when excitons are dissociated or recombined, while GSB signal maintains, regardless of as exciton or other excited states.

For PBDB-T, the exciton has a broad PIA which peaks around 1150 nm; the long-lived signal is also broad, peaking at 900 nm,together with probably another broad peak near 1400 nm. In both acceptor films, a narrow peak, assigned to exciton PIA, exists at 1050 nm, and a broad PIA peaks around 1250 nm and 1300 nm for NFBDT and NCBDT, respectively. We will discuss whether they are triplets or polaron in later sections. A negative signal before 950 nm represents contribution from GSB and/or SE. We note that exciton PIA may extend

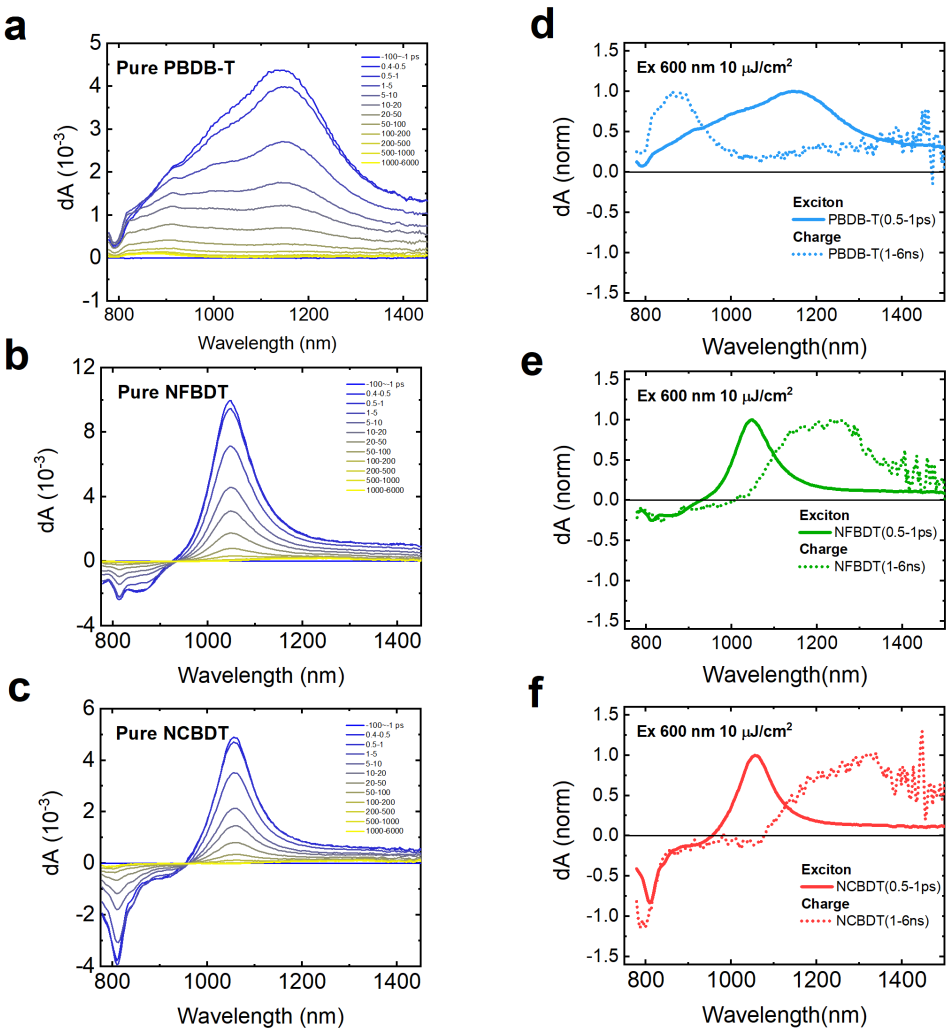

Fig. 6.3 Time resolved spectra in NIR region from transient absorption measurements of pristine films (a) PBDB-T (b) NFBDT and (c) NFBDT. (d)-(f) are the figures containing the early spectra (0.5-1 ps) and late spectra (1-6 ns). The excitation wavelength is 600 nm and the fluence is around 10 $\mu W\,cm^{-2}$.

into this region and decays in the way as SE, so it would be difficult to exactly determine the shape of PIA and SE signals. Following the guideline, we can assign peaks in the spectra to various species. The early and late spectra are summarised in Figure 6.4. In the kinetics, the half-amplitude lifetime is 4.5 ps for the exciton signal at around 1150 nm for PBDB-T and 5.5 ps at around 1050 nm for NCBDT and NFBDT.

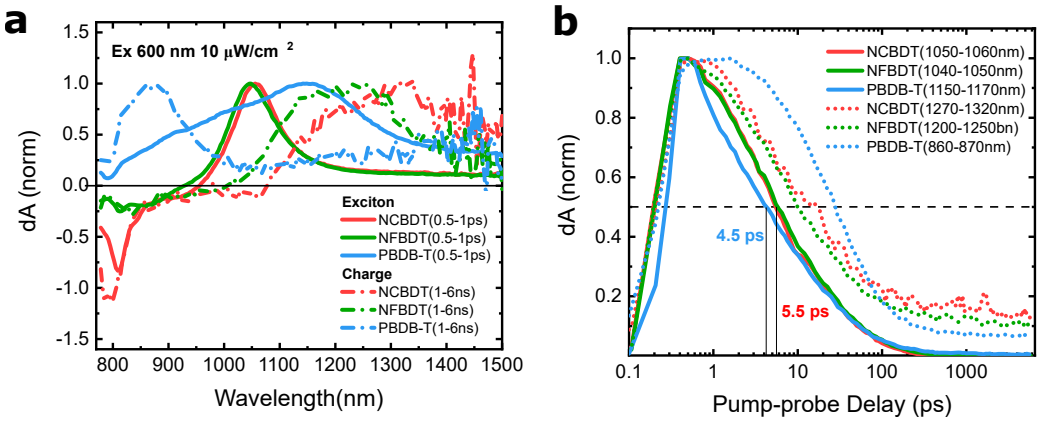

Fig. 6.4 (a) The representative spectra at early time (0.5-1 ps) and late time (1-6 ns) in PBDB-T, NFBDT and NCBDT pristine films; (b) the representative kinetics at chosen wavelengths according to their signal strength at early time and late times. and decay curves from pristine films.

6.2.2 Selective Excitation of Donor and Acceptor in D-A blend films

In the molecular blend, we are interested in how the heterojunction helps dissociate the excitons and how charges are generated and recombined. As both donor and acceptor contribute to light absorption, excitation of either component is important. We use light at different wavelengths to selectively excite the donor or acceptor.

Figure.6.5 presents the results of ultrafast transient absorption (TA) experiments after photoexcitation of the studied PBDB-T:NCBDT blend with 750-nm and 425-nm light. Excitation at 750 nm selectively excites the acceptor as the donor material does not absorb at this wavelength at all. Excitation at 425 nm can excite both materials, but donor absorbs much stronger than the acceptor (see Fig.6.2), thus should largely excite the donor material. To avoid the complicated influences of ground-state bleach as well as thermal and electro-absorption contributions to the response, we analysed the spectra in the >900 nm region where only the PIA features of charges and excitons (singlets and triplets) are present in this section. We chose three representative wavelengths, 940 nm, 1050 nm, and 1320 nm, to watch the kinetics of D polaron, A exciton, and A polaron/triplet, respectively. Here in the 750-nm excitation case, we choose 940 nm to observe polaron signal because the exciton signal does not contribute at this region. In the normalised graph, a clear signature of D polarons and A polarons/triplets agrees with the assignments in Figure.6.4.

At 425 nm excitation, we mainly excite the D material and the decay of D exciton signal around 1150 nm is very fast as the signal disappears within 1 ps. Either energy transfer or charge transfer must happen. The decay of D exciton is correlated with the rise of A exciton signal, thus energy transfer is more likely. This is possible as the emission of polymer and

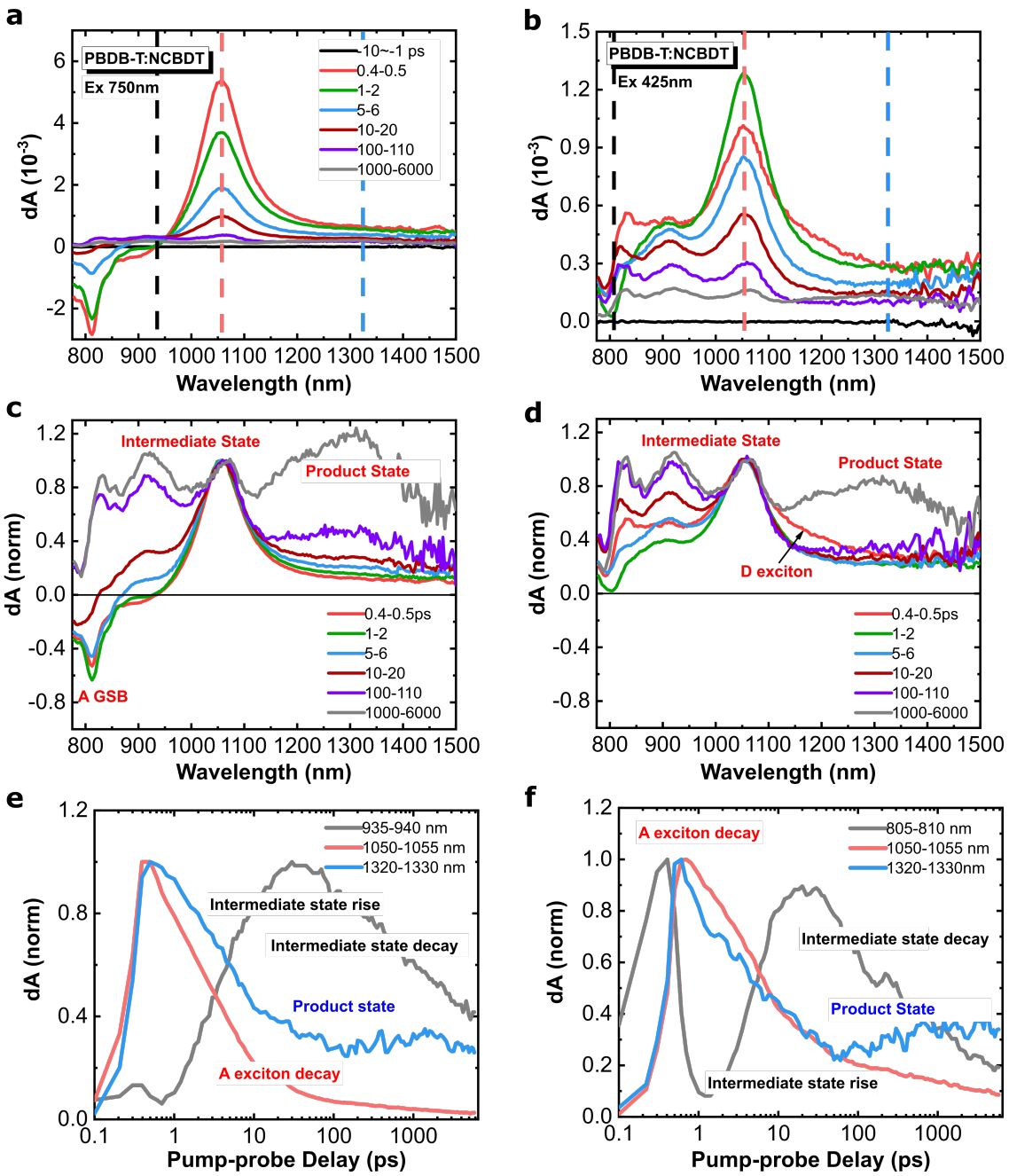

Fig. 6.5 Transient absorption spectroscopy of PBDB-T:NCBDT with 750 nm and 425 nm excitation. (a-b) Spectral slices at various time scales from several hundred femtosecond to 6 nanosecond. The vertical lines are representative wavelengths for different excited species: 935-940 nm/805-810 nm (black) for the intermediate state, 1050-1055 nm (red) for acceptor exciton, and 1320-1330 nm (blue) for product state (c-d) Normalised spectra at the peak around 1050 nm with the notation of the excited species; (e-f) Selected kinetics at wavelength indicated in (a-b) and with the species notation.

the absorption of donor overlap in the spectrum. The weak PLQY of polymer does not harm the energy transfer efficiency in FRET, as long as its rate much exceeds the radiative and non-radiative rates. However, we cannot completely exclude the possibility of charge transfer here. In later part of signal decomposition, we will further analyse the signal at early times. We note that the acceptor exciton generated from energy transfer decays slower compared to that from direct acceptor excitation. This has been observed also in other NFA blends, like P3HT:O-IDTBR where geminate recombination is different at selective excitation.[177].

In the kinetics curves shown in Fig.6.5 (e) and (f), after 1 ps, the intermediate state signal increases, peaking at around 25 ps. We assign this rise to *hole transfer* process. Using the rise of donor polaron to quantify the hole-transfer process is a better way than observing the exciton decay, in particular when the hole transfer is not ultrafast that other processes such as exciton diffusion, exciton recombination, and exciton-exciton annihilation will come into play. This gives a charge transfer rate of around 5 ps. We note that at the same time range, the blue curve is decaying, which is caused by the acceptor exciton decay as acceptor exciton has some contribution at around 1320-1330 nm when the population is large. After 100 ps, the decay of the intermediate state signal, which is usually interpreted as geminate recombination, is strangely correlated with the rise of the product state. In the later sections we will further decompose the signal using global analysis to distinguish them.

6.2.3 Spectral Decomposition by Genetic Algorithm

Separating heavily overlapping signals is a difficult process in interpreting charge dynamics in organic systems. As introduced in the Chapter 2, we use genetic algorithm to analyse the data discussed in the previous section.

Global analysis of the multidimensional spectroscopic data shows that three types of species contribute to the PIA signals. For PBDB-T:NCBDT, the decomposed spectral signatures of these species are shown in Figure.6.6 (a) and the corresponding dynamics of these species are presented in Figure.6.6 (b). The first species (blue curve) is assigned to excitons as the spectral response matches that of pure acceptor. The second species (grey solid line) is assigned to an excited species from free charges in PBDB-T, as its spectral shapes also match the long-lived spectra from the pure materials (dashed lines), and it exists in both 750 nm and 425 nm excitation cases. From the decay curves of the red curve, we call it the *intermediate states*. The population of this species first grows until 30 ps, which is on the same timescale as hole transfer in Fig.6.5 (e). The population then decays steadily with a 400 ps time constant, as the population of charges increases. The third species (red lines) exhibits spectral signatures that are very similar to those appearing in the pristine materials, which is called *product states*. Thus, this can either be polaron or triplet states.

From the kinetics, this species rises as the intermediate species decays. We note that GA decomposition cannot catch the spectral shift of the excited species, which may happen as those excited states thermalise, but should be able to mostly catch the excited species when their spectral shapes are separate and different.

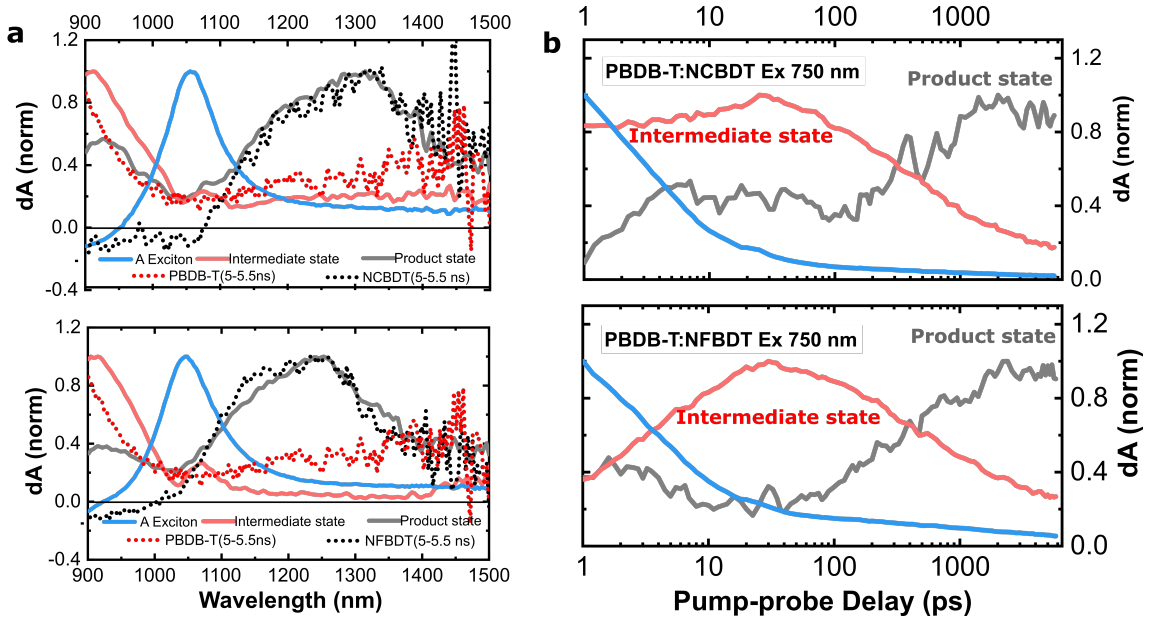

Fig. 6.6 Global analysis of the transient absorption spectra of PBDB-T:NCBDT and PBDB-T:NFBDT under the excitation of 750 nm. (a) The solid lines are evolved spectral shape for three excited species, and dashed lines are curves from the pristine films extracted from Fig.6.3; (b) The decay kinetics for three excited species. The blue one should be acceptor exciton as 750 nm excites the acceptor material first and it spontaneously forms and decays; the *intermediate state* (red) has contributions around 900 nm from donor polaron, and might have some contribution from acceptor late spectra; the *product state* (grey) has very similar spectra as the late spectra in the pristine acceptor materials, and should be either polaron or triplet states.

We also performed fluence-dependent measurements, from 50 nJ/pulse to 100 and 200 nJ/pulse. In the GA program, all the data of three fluences are decomposed together. The spectral shape for individual species is very similar to Fig.6.6 and the respective decay curves are shown in Fig.6.7. In this figure, the exciton decays faster at higher fluence possibly due to exciton-exciton annihilation effect. For the intermediate state, the rise disappears at higher fluence which reveals that this species decays faster at higher fluence. This indicates that 50 nJ is not a fluence that can see fluence-independent region. However, we do not have lower fluence data taken together. Strangely, the third species does not show fluence dependence between 10-200 ps, which seems to indicate it is a geminate-like species. After 200 ps, the signal rises but lower at higher fluence. As triplet state is normally a bimolecular process from the electron-hole recombination and normally happens at time scale later than ns. Such

bimolecular recombination should show a faster formation rate at higher excitation fluence, which seems to erase the possiblity of triplet state.

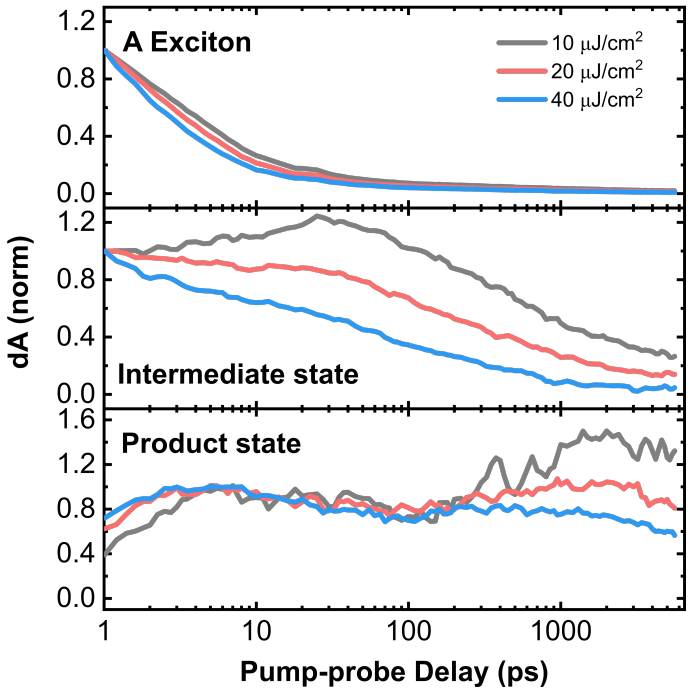

Fig. 6.7 Global analysis of fluence-dependent transient absorption spectroscopy of the PBDB-T:NCBDT blend with pulse energy from 50 nJ to 200 nJ. The second species is the intermediate state related to the donor polaron, and the third species is the product state, either polaron or triplet state related to the acceptor.

For 425 nm excitation, we decomposed the signal to see its energy transfer using global analysis. Here, the spectra of D exciton also needs to be considered. We limit the time range to 15 ps from 0.5 ps, which fully includes the energy transfer process and excludes other later processes. From the decomposed spectra and kinetics in Fig.6.8, the first two components (blue line and red line) were assigned to the polymer exciton and the acceptor exciton respectively as their spectra were extracted from pristine materials (Figure.6.3). The third species (black line) was assigned to intermediate state as the spectral shape is similar to that obtained in Figure.6.6. We find that the energy transfer from its possibly 'hot' excited state (S_n) to the acceptor material finishes within 1 ps. This energy transfer is possible as a result of the overlap of spectra of the donor emission and the acceptor absorption.

Fig.6.9 presents the kinetics of intermediate state and product state under different excitation conditions. We note that after 100 ps the signal from exciton absorption is negligible. This enables the execution of global analysis using two species. Their dynamics under

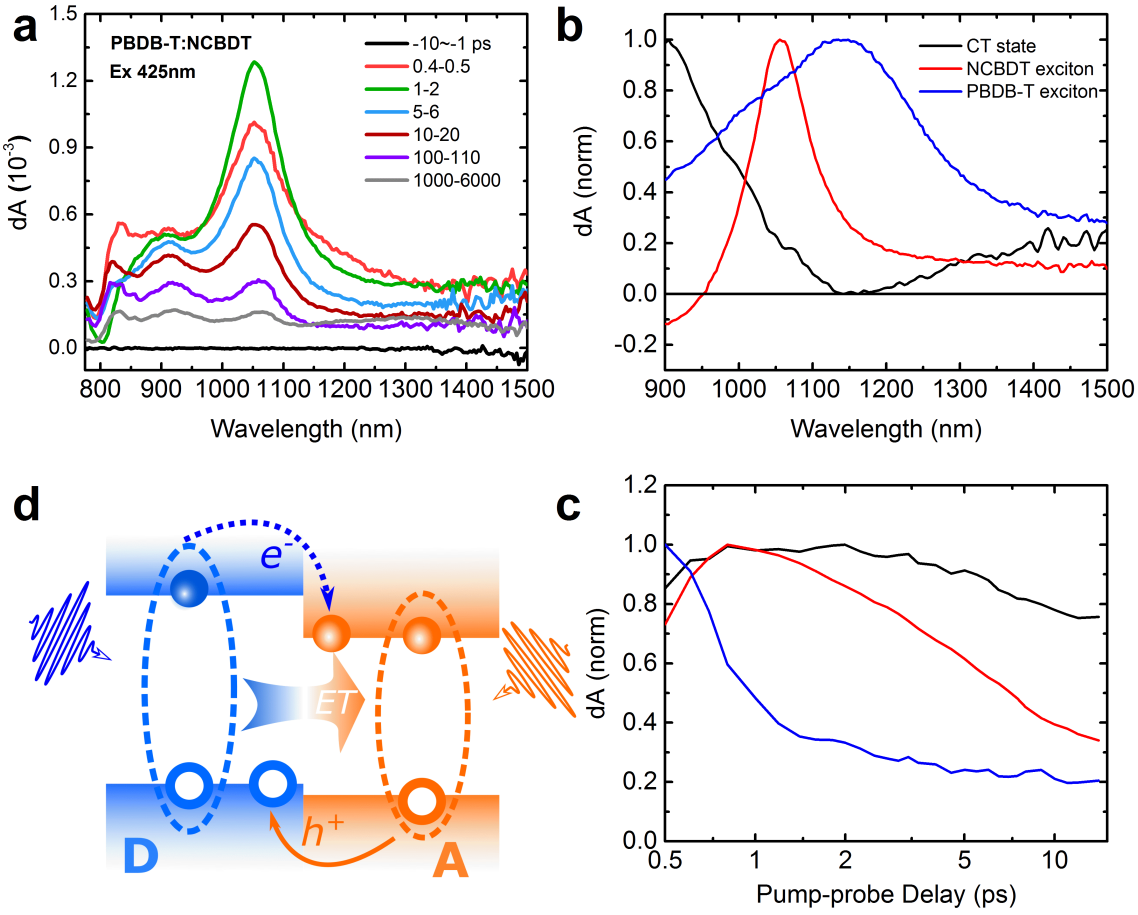

Fig. 6.8 Transient absorption spectroscopy of PBDB-T:NCBDT with excitation at 425 nm. (a) Transient absorption spectra of the original spectra; (b-c) Spectra and kinetics from global analysis of TA spectra in first 15 ps starting from 0.5 ps; (d) The diagram showing the energy transfer channel from the donor to the acceptor as well as the electron transfer and hole transfer processes.

425 nm and 750 nm excitations are quite similar, which means that the photophysics after 100 ps makes hardly any difference. This gives the rate at ∼400 ps for the interconversion from intermediate state into the product state.

6.3 Model 1

The difficulty of signal analysis comes from the nature of the product state in the transient absorption data. Here, we analyse two alternative models.

In this section, we first discuss one possibility that the intermediate state is charge pair state and the product state is free charge. Intermediate states have clear donor polaron

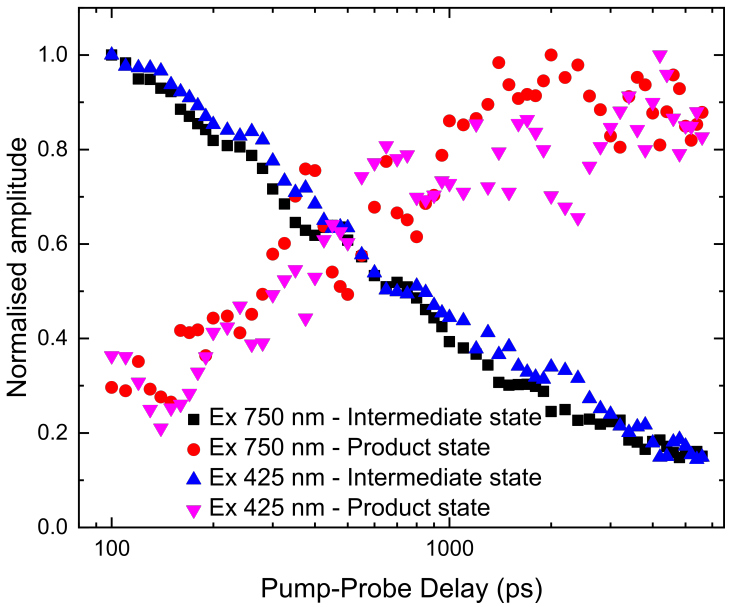

Fig. 6.9 Comparison of electron and hole transfer after 100 ps using the global analysis, assuming that exciton signal contribution is negligible. The rate of conversion from the intermediate state into product state is around 400 ps.

character and are probably related to the charges residing in the donor-acceptor mixed phase. We note that though interfacial charge pairs are in a sense similar to widely discussed charge-transfer excitons, we avoid to use this notation as we cannot quantify the level of interaction between the electron and the hole. The characteristic spectral signatures of interfacial charge pairs, dissimilar from those of free carriers, may be the result of specific structural conformations of the molecules not well packed in pure material domains. Additional minor contribution may come from donor-acceptor electronic couplings. Fluence-dependence kinetics after 200 ps in Fig.6.7 of the product states supports more the free charge assignment, rather than triplet states from bimolecular recombination. However, we do notice that triplet-triplet or triplet-charge annihilation will give the same trend. These processes are prominent at very high photoexcitation density and can be detected in TA, but should not play an important role at solar illumination conditions. The results of PBDB-T:NFBDT blend (Figure.6.6, bottom) appeared to be qualitatively very similar to PBDB-T:NCBDT consistent with the morphology discussed above, which means the photophysics of both materials can be described using the same model.

From the above discussion, we arrive at one possible model, shown in Figure.6.10. Acceptor excitation due to the light absorption, or due to the energy transfer from donor, leads to the (i) direct free charge generation or (ii) formation of intermediate state. We

estimate that around two thirds of free carriers come from the separation of intermediate state and another one third from the direct generation. This is seen in Fig.6.6 (b), where the signal at 100 ps is around 0.35 and the signal peaking at around 2 ns is around 1 after normalisation. One possible reason for this, can be that 35% efficient generation of free charges is happening through the 'hot' charge-transfer states, while the rest of photocurrent is generated through the 'cold' intermediate states. Another possibility is that different local morphologies lead to the different charge generation pathways, direct or intermediate-state mediated. Based on the existing data, we cannot differentiate between these two different mechanisms. The timescale of conversion from intermediate states to free charges is estimated to be around 400 ps, which is in striking contrast to sub-ps free carrier formation observed in most polymer-fullerene blends and some other NFA materials. This highlights the conceptually different molecular mechanism of charge generation in high-performance NFA acceptors like NFBDT and NCBDT. Interestingly, the photophysics for both studied materials are very similar despite the HOMO-HOMO offset in NCBDT-based blend is smaller by $\sim$ 40 meV. This indicates that the charge generation in the studied class of donor-acceptor systems is not very sensitive to the driving energy for charge separation, allowing further optimisations of acceptor bandgaps and open-circuit voltage. Delicate control of band offsets via energy level optimisation might be a powerful approach to design optimal combinations of acceptor and donor materials, to increase solar light absorption (for higher J_{SC}) while minimizing the loss of V_{OC}.

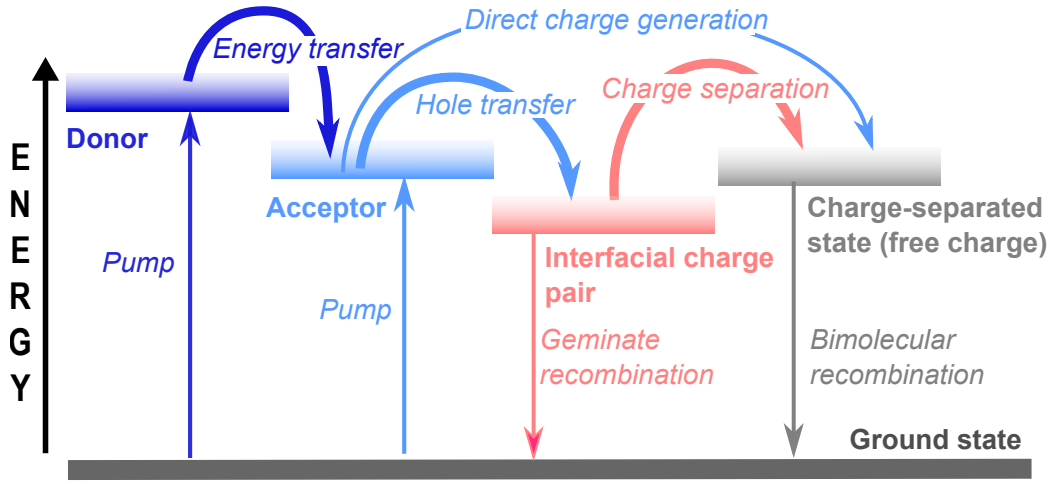

Fig. 6.10 State energy diagram showing the relevant photophysical processes. Excitation of donor is followed by an ultrafast energy transfer process; the following hole transfer process from the acceptor to the donor generates interfacial charge pair state, and the further separation from this pair state, or directly from the acceptor leads to charge-separated states.Geminate recombination from ICP state and bimolecular recombination to the ground state occur.

6.4 Model 2

The above results are mostly published in the paper[1]. However, the model described earlier does not give any direct evidence to exclude the possibility of triplet states. Thus, more experiments were performed later, and we will discuss this part of data in this section.

We also note that the yield, defined as the amplitude of the third species divided by the amplitude of the exciton signal. In the pristine NCBDT, this ratio is 1.0×10^{-4} / 5.0×10^{-3}, and in the blend, the ratio is 2.0×10^{-4} / 5.3×10^{-3}. Therefore the polaron yield in the blend is around twice higher in the blend compared to the pristine. This is not normal as for such efficient blends, the polaron yield should be much higher. In this section, we will discuss another possible model including the triplet states, probed from triplet sensitisation and enhanced inter-system crossing. The corresponding states for the intermediate states and product states are free charges and triplet state, respectively.

6.4.1 Triplet Sensitisation

Low-lying triplet states can be a significant loss in fullerene-based organic solar cells.[179] In efficient polymer:NFA blends, the energy level of the triplet states of the NFA is the lowest among excited states. In other words, if triplet states are formed, additional forces are unavoidably needed to separate them to form charges, thus attention should be paid whether and how much triplet states are formed. If not, understanding how the formation of triplet states are suppressed is also important.

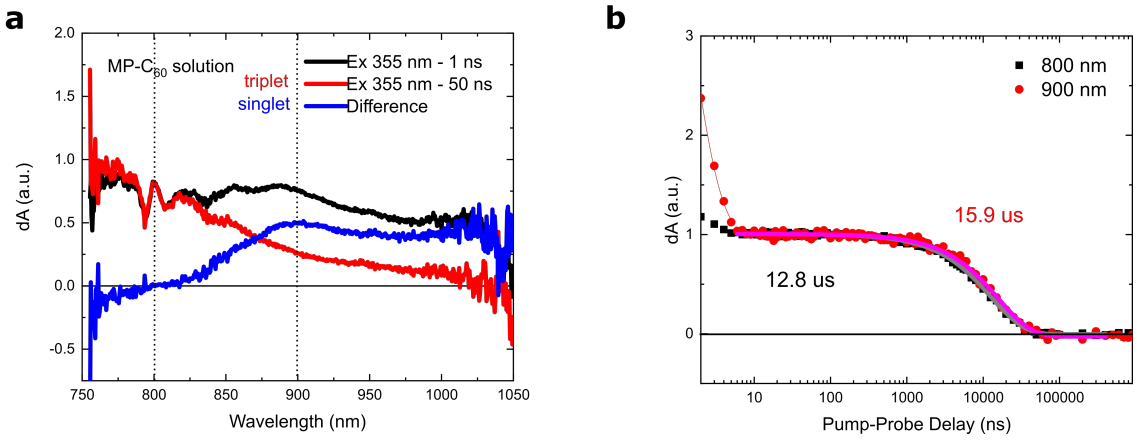

Fig. 6.11 Transient absorption spectra of MP-C_{60} solution in DCM, covering the time scale between 2 ns and 1 ms. (a) The normalised transient absorption spectra at 1 ns (black) and 50 ns (red). The spectrum at 50 ns is purely from triplet state, while the difference signal (blue) is assigned to the singlet state. (b) The kinetics at 800 nm and 900 nm with single exponential fitting, giving an estimate of the lifetime of triplet state. The excitation wavelength is 355 nm.

An obvious prior step is to generate and see triplet states in some way. To find the signature of triplet states, we study the solution phase first in this section. To enable the sensitisation, the triplet states must stay long enough to interact with the other molecule. The triplet lifetime is thus a fundamental quantity to measure first. We thus perform experiments to probe the lifetime of the triplet states. The triplet states are formed from singlet states via inter-system crossing under optical excitation. We use N-methylfulleropyrrolidine (MP-C_{60}) as the sensitiser, which is often used in singlet fission studies.

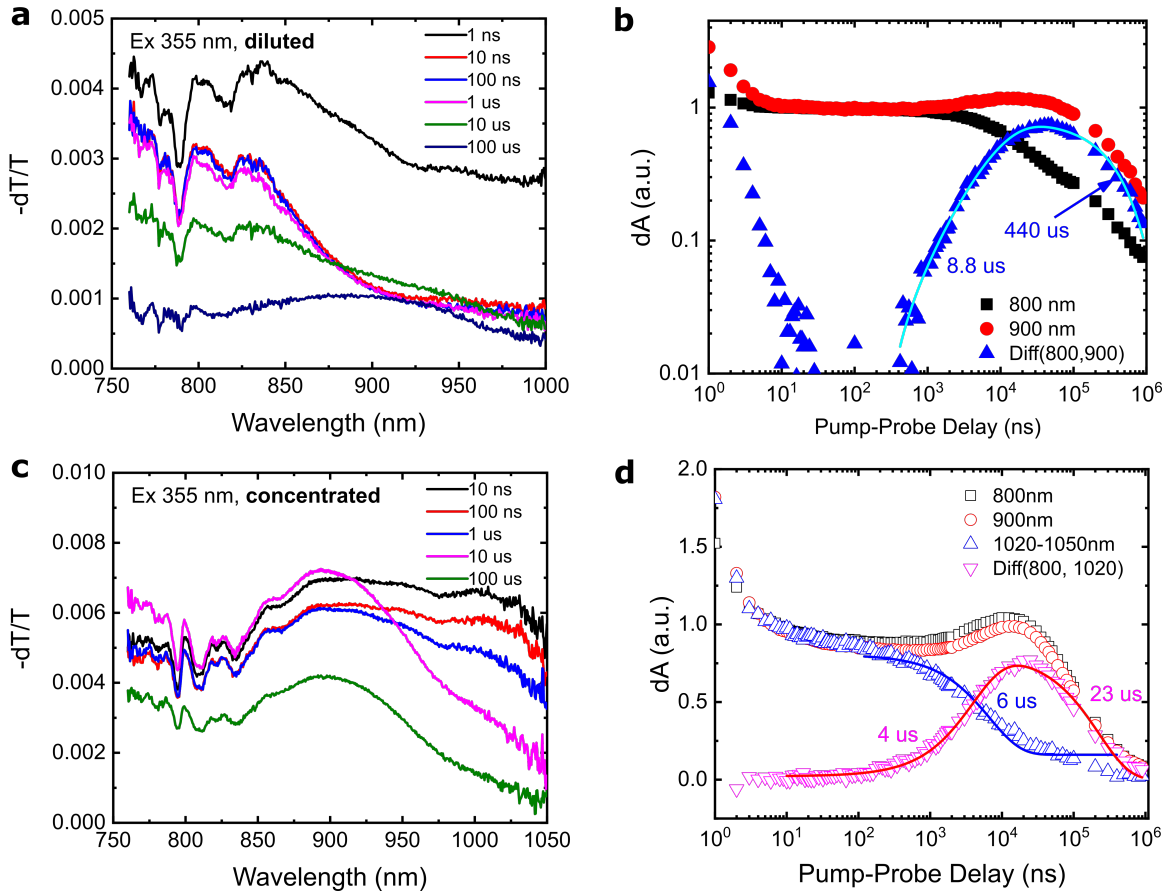

Fig. 6.12 Transient absorption spectra of PBDB-T-MP-C_{60} solution in DCM, covering the time scale between 1 ns and 1 ms. Spectra at various time delays in (a) diluted solution and (c) concentrated solution; (b,d) representative decay curves. In (b) and (d), the difference signal is obtained from subtracting the two kinetics normalised to the overlapping amplitude around 100 ns. The fitting line are exponential fitting with two components. The excitation wavelength is 355 nm.

MP-C_{60} solution in dichloromethane was excited with UV light. In Fig.6.11, the long-lived PIA signal located mainly between 750-850 nm is due to triplet state, and the early time signal, with a different feature at 900 nm, is assigned to the singlet state. From their kinetics, the lifetime of the triplet state, is between 12.79±0.16 ns and 15.91±0.47 ns, fitted

from the kinetics at 800 nm and 900 nm, respectively. The internal system cross to form the triplet states is complete before 10 ns, as seen in the rapid decay at 900 nm.

We now turn to study the PBDB-T and PBDB-T-MP-C_{60} in the solution. Fig.6.12 presents the transient absorption signal of PBDB-T-MP-C_{60} solution with high and low concentrations. The triplet state of MP-C_{60} has a finite lifetime, which is related to a distance range that triplet energy transfer from MP-C_{60} to PBDB-T can happen. The concentration mainly changes the average distance between PBDB-T and MP-C_{60}.

At low concentration in Fig.6.12 (a), the same spectral shape (red and blue) between 10 ns and 100 ns as the earlier measured triplet state (red) in MP-C_{60} (purple) in Fig.6.11 supports the formation of triplet state of MP-C_{60}. In Fig.6.12 (b), the difference signal between 800 nm and 900 nm (blue line) before 20 µs gives a lifetime around 8.8 µs. This can be either triplet energy transfer process, or charge transfer from MP-C_{60} triplet state to PBDB-T. Later, a slow decay around 440 µs shows the recombination of the excited state to the ground state. This lifetime is really long and we cannot exclude triplet or free charges in the solution. This ends with with a quite broad and featureless signal around 900 nm (green line), which is similar to the PBDB-T polaron in the pristine film (peak at 880 nm) in Fig.6.13 (a) and 920 nm in the blend in Fig.6.5 (c) and (d).

In solution with a higher concentration of MP-C_{60}, Fig.6.12 (c-d) shows that the singlet signal at around 1020-1050 nm decays slower than before before 10 ns. Interestingly, both signals at 800 nm and 900 nm rise at a similar pattern, quite different from the dilute case. The interaction time scale is also different - the rising time from the difference signal (pink) is 4 µs, twice faster than the dilute one. The long-lived component decays at a rate of 23 µs, more than one magnitude faster than the diluted solution. This can be due to either charge recombination, or triplet-triplet annihilation, as both processes are related to diffusion and become faster at higher concentration. To distinguish charge transfer, or triplet transfer, one way is to check the GSB region in the visible region where triplet energy transfer should not contribute to the GSB of MP-C_{60}. Another way to check is to see if emission from triplet-triplet annihilation can happen, which can confirm the existence of triplet states.

After explaining the concentration-dependent PBDB-T:MP-C_{60} data, we now turn to NCBDT-MP-C_{60} solution. Here, we performed fluence-dependent measurements. Fig.6.13 (a) and (d) show very similar pattern for the signal evolve. At early time such as 1 ns (black line), a peak around first decays until 10 ns. After 10 ns, the signalat around 1020 nm slowly rises until 20 µs, together with the rise of GSB signal before 800 nm, which should be NCBDT-related signal as NCBDT GSB/SE is around 750 nm. After 20 µs, there is no spectral evolve but a simple decay trend.

To analyse the data better, we use the genetic algorithm mentioned earlier to decompose the signal into two components. The long-lived signal has its peak around 1020 nm, which can be either NCBDT polaron or triplet. This spectrum actually resembles the NCBDT singlet exciton, shown in Fig.6.3 (c). The decay rate at higher fluence (76 µs) in (a) is faster than the lower fluence (108 µs) in (d), which is probably related to triplet-triplet annihilation. However, charge-charge annihilation cannot be completely excluded.

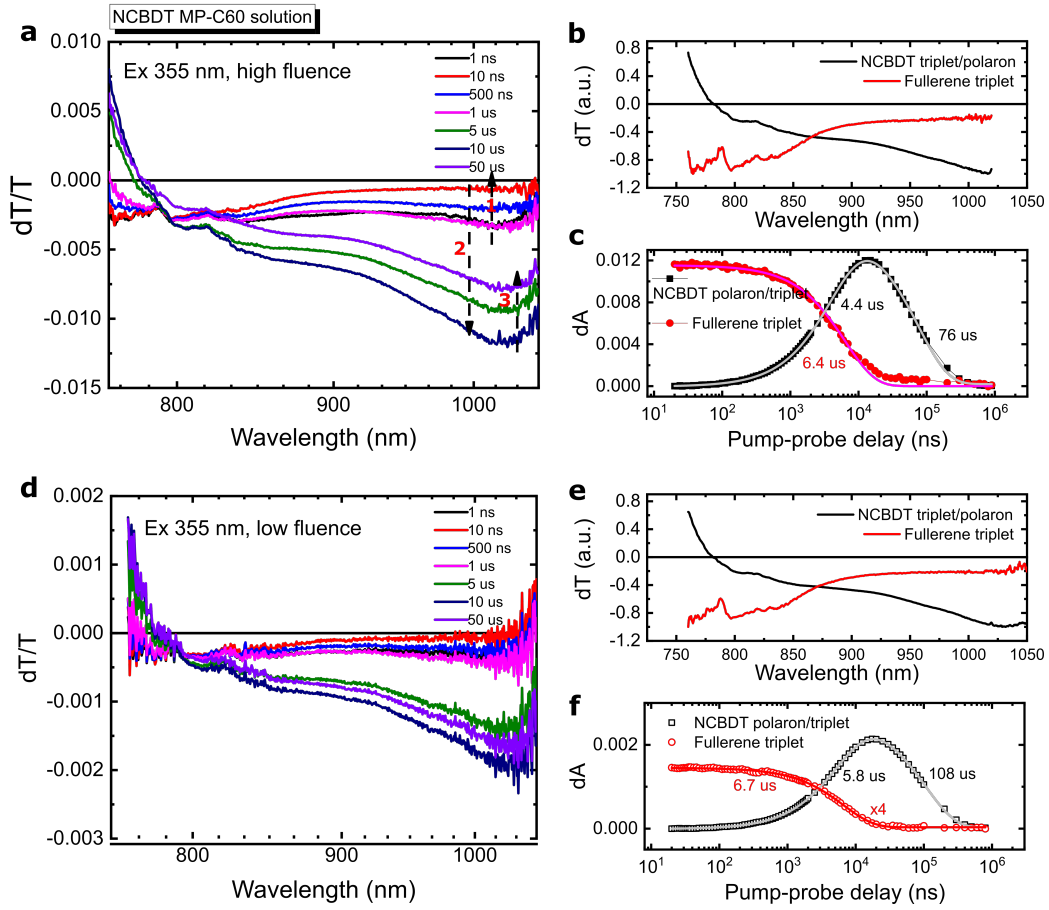

Fig. 6.13 Transient absorption spectra of NCBDT-MP-C_{60} solution in DCM, covering the time scale between 2 ns and 1 ms. Spectra at various time delays at (a) higher fluence and (d) lower fluence; (b,e) The deconvoluted spectra for MP-C_{60} triplet and possibly NCBDT triplet; (c,f) The deconvoluted kinetics for respective spectra. The excitation wavelength is 355 nm.

For the solution sensitisation experiments, we note that the signal between 1000-1600 nm is not measured which should provide more evidence for the spectra of triplet states.

To further determine whether the excited states in the solution are triplets or free charges, we also measure the time-resolved photoluminescence in additional to transient absorption measurements. The absorption onset of MP-C_{60} is around 550 nm. In Fig.6.14 (a), we thus use 650 nm to selective excite the NCBDT molecules, resulting in short-lived signal at its

emission wavelength. In contrast, excitation at 400 nm leads to long-lived PL, shown in Fig.6.14 (b). Combining with the TA data, the long-lived signal is luminescent. From the PL shape in Fig.6.14 (c), the black line represents NCBDT singlet emission, and the delayed emission spectra is only slightly blue shifted and possibly from the same state. The difference between 2 ns and 2 µs at 400 nm is probably due to reduction in singlet MP-C_{60} emission. We therefore conclude that the delayed emission is from triplet-triplet annihilation.

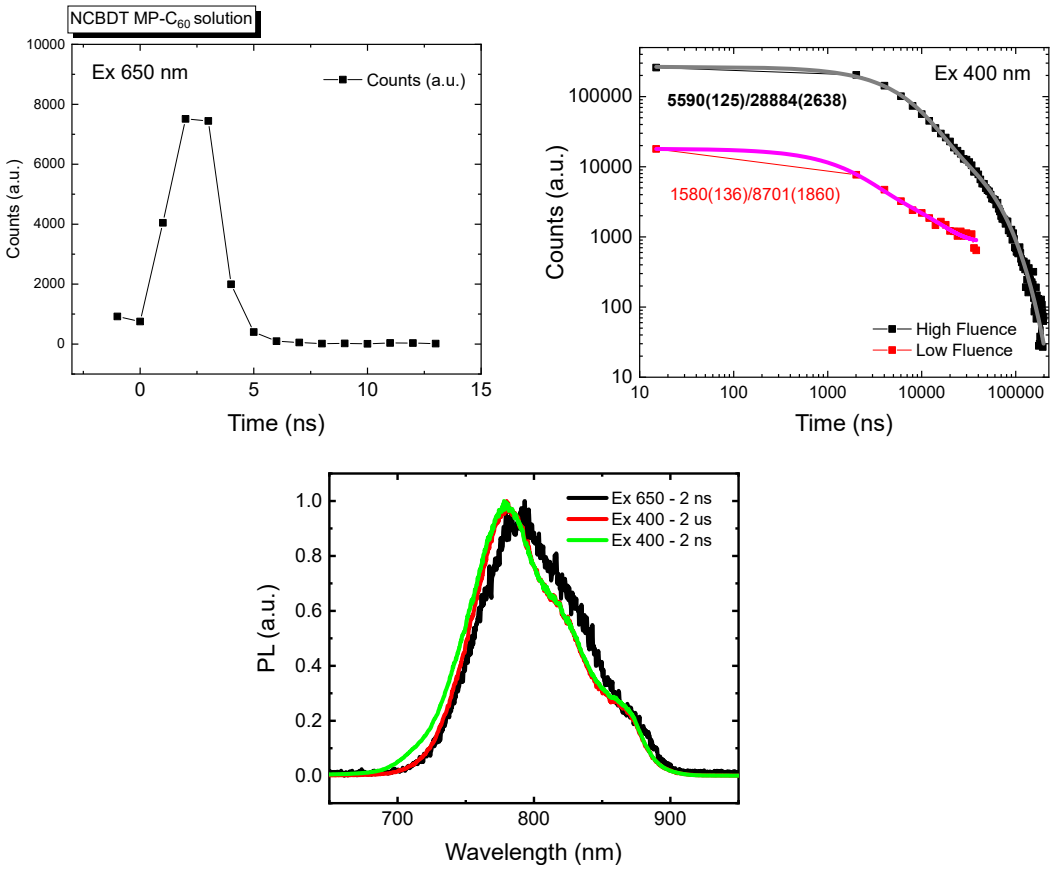

Fig. 6.14 Time-resolved PL of NCBDT-MP-C_{60} solution with excitation at 650 nm and 400 nm, respectively; the representative PL spectra at 2 ns and 2 µs.

6.5 Enhanced ISC via Heavy-Metal Effect

From the previous section, we discuss the model that the long-lived product state is triplet state, which is probably the loss channel. In this section, we use another method to probe the triplet state by using molecules containing heavy atoms to influence the inter-system crossing behaviours of the studied materials.

Fig.6.15 shows the transient absorption spectra of NCBDT film excited by 750 nm. This film is fabricated the same way as Fig.6.3 (c).

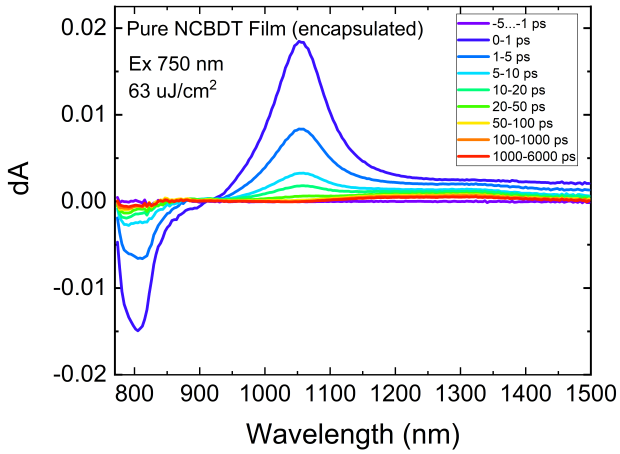

Fig. 6.15 Transient absorption spectra of NCBDT film up to 6 ns with the excitation fluence of 63 $\mu J\,cm^{-2}$ at 750 nm.

Here, we also measured the fluence-dependent spectra of NCBDT film at 2 $\mu J\,cm^{-2}$ and 10 $\mu J\,cm^{-2}$ in Fig.6.16 with 750-nm excitation light, shown below.

We compared the early (0-1 ps) and late (1-6 ns) spectra of NCBDT film shown in Fig.6.16 (a-c), and the representative kinetics of selected wavelengths in Fig.6.16 (d-f). These wavelengths (800-810 nm, 1050-1060 nm, and 1200-1300 nm) are chosen to represent GSB, PIA and the long-lived signal, respectively. At higher fluence, the long-lived signal is much stronger than lower fluences. Comparing the sub-figures (a-c), the yield of the long-lived signal is higher at higher fluence. This is confusing as inter-system crossing is a single-particle process and should not depend on the fluence. If the product state is triplet, it should give less yield as two-particle annihilation processes may happen.

In this section, we only choose to excite NCBDT molecule rather than PtOEP and will show why.

Next, we fabricated NCBDT pristine films (5 mg/ml in CF) and doped films with PtOEP (weight ratio, 13%). PtOEP is a well studied molecule which has very strong spin-orbital coupling and phosphorescence at room temperature. The common use of PtOEP is to introduce triplet states in other molecules by exciting the PtOEP first. In Fig.6.17 shows the transient absorption spectra of NCBDT doped with PtOEP. We find that the amplitude of the long-lived signal is much stronger than the pristine NCBDT films in Fig.6.15. The fluence-dependent TA data is also measured in Fig.6.18, covering from 2.8 $\mu J\,cm^{-2}$ to 63 $\mu J\,cm^{-2}$. At higher fluence, the yield of the long-lived signal decreases, in contrast to the pristine film

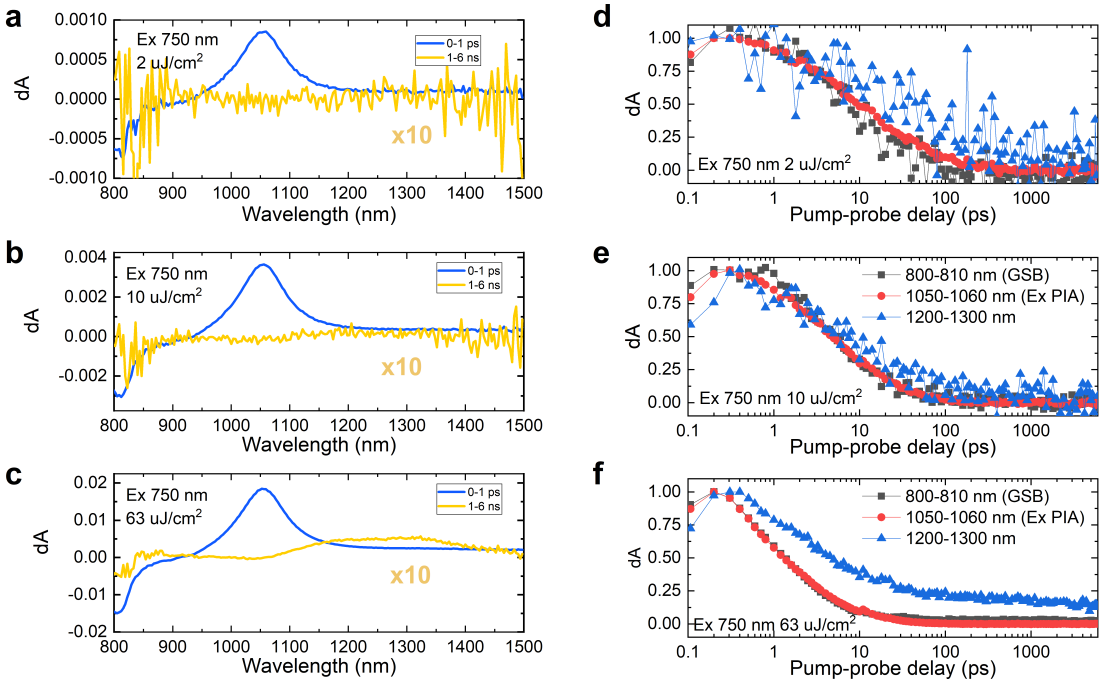

Fig. 6.16 Transient absorption spectra of NCBDT film at various fluences excited at 750 nm. (a-c) Selected spectra at 0-1 ps and 1-6 ns with the fluence of 2 $\mu J\,cm^{-2}$, 10 $\mu J\,cm^{-2}$ and 63 $\mu J\,cm^{-2}$; (d-f) Selected kinetics at wavelength range of 800-810 nm (GSB), 1050-1060 nm (PIA signal), 1200-1300 nm (the main feature of the long-lived signal).

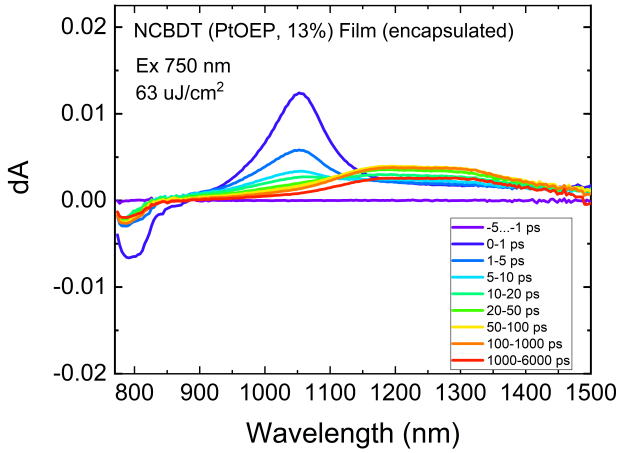

Fig. 6.17 Transient absorption spectra of NCBDT film doped with PtOEP (13% weight ratio) up to 6 ns with the excitation fluence of 63 $\mu J\,cm^{-2}$ at 750 nm.

in Fig.6.16. From the kinetics in Fig.6.18 (d-f), there is a clear interconversion from singlet

states (red) to triplet states (blue) before 100 ps. After 100 ps, the triplet signal starts to decay and its decay rate is faster at higher fluence.

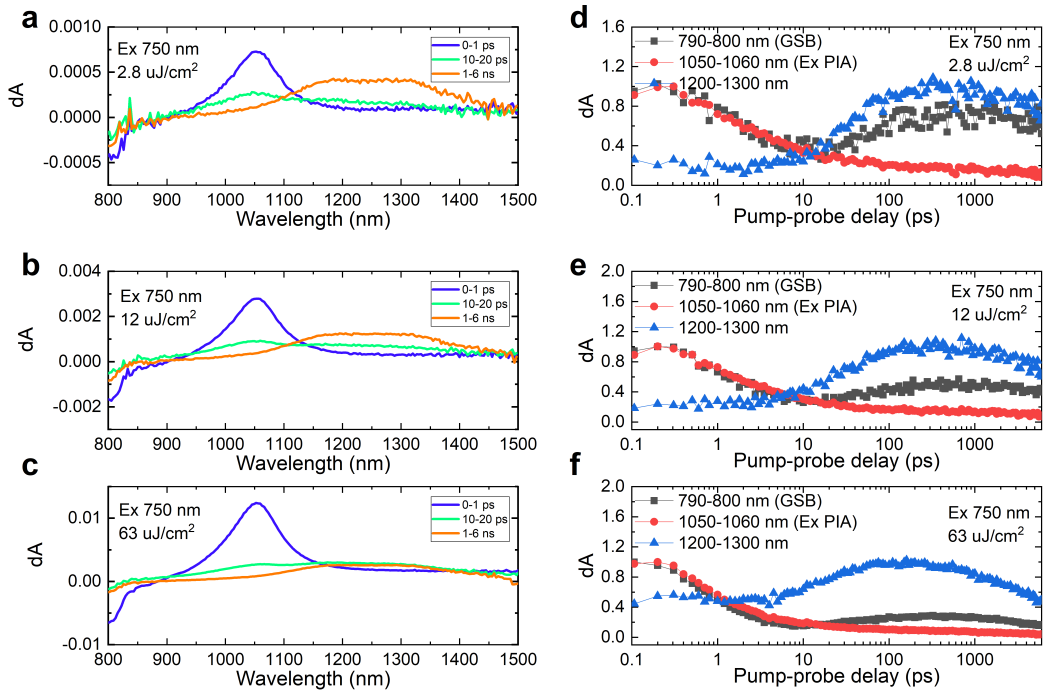

Fig. 6.18 Transient absorption spectra of NCBDT film doped with PtOEP (13% wt) at various fluences excited at 750 nm. (a-c) Selected spectra at 0-1 ps and 1-6 ns with the fluence of 2 $\mu J\,cm^{-2}$, 10 $\mu J\,cm^{-2}$ and 63 $\mu J\,cm^{-2}$; (d-f) Selected kinetics at wavelength range of 790-800 nm (GSB), 1050-1060 nm (PIA signal), 1200-1300 nm (the main feature of the long-lived signal).

The solid state film shows the enhancement of inter-system crossing probably due to the heavy-metal effect. We also performed solution measurement shown below to check if such effect still exists. Fig.6.19 and Fig.6.20 show that PtOEP has almost no effect on the overall spectral shape and kinetics. One possible reason is that the used concentration is not high enough for excited state to diffuse and interact. In such measurements, the lifetime of NCBDT triplets is 400±10 ns fitted from Fig.6.19 (d).

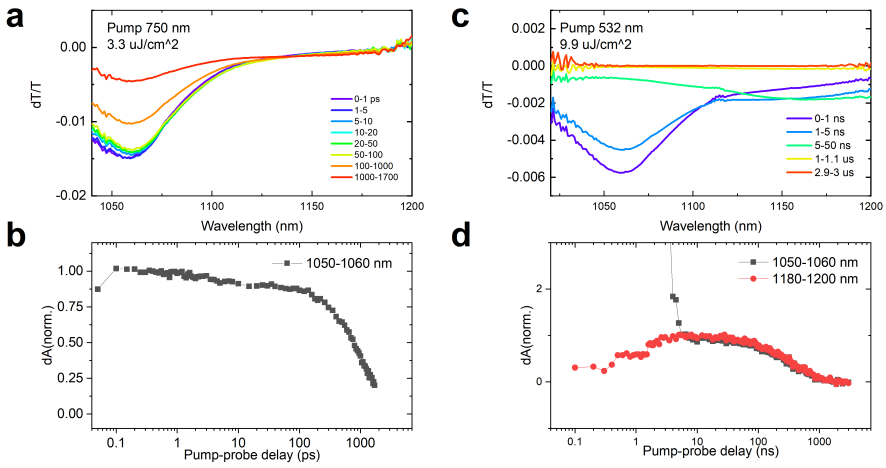

Fig. 6.19 Transient absorption spectra of NCBDT solution. (a-b) Short-time spectra up to 1700 ns excited with 750-nm light. (c-d) Long-time spectra up to 3 µs excited with 532-nm pulses.

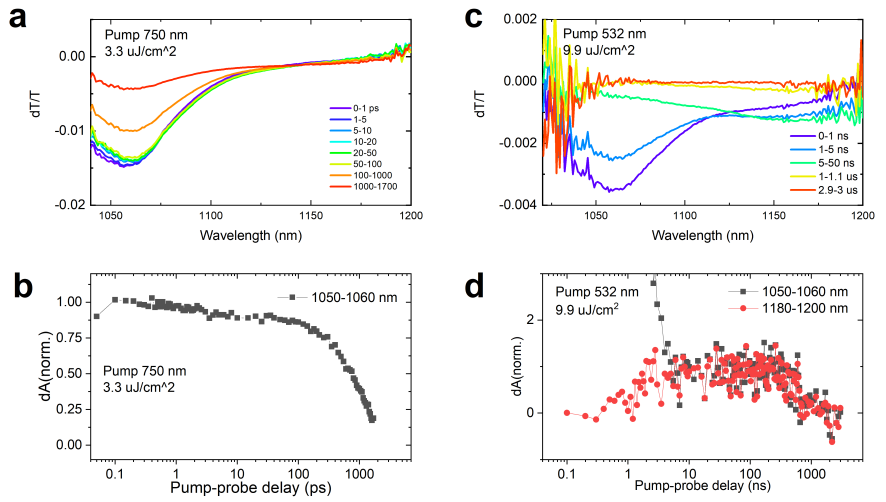

Fig. 6.20 Transient absorption spectra of NCBDT solution doped with PtOEP (17% weight ratio.(a-b) Short-time spectra up to 1700 ns excited with 750-nm light. (c-d) Long-time spectra up to 3 µs excited with 532-nm pulses.

However, we still cannot fully exclude another possibility that charge transfer from NCBDT to PtOEP occurs. One way is to vary the HOMO and LUMO properties of the heavy-metal molecules to form type-I heterojunction to prevent the charge transfer pathways.

6.6 Conclusion

To summarise, we studied the charge dynamics in high-efficiency NFA-based blends, PBDB-T:NCBDT and PBDB-T:NFBDT using transient absorption spectroscopy.

Firstly, in such blends, we find ultrafast energy transfer happens under donor excitation after which hole transfer occurs; excitation of the low-bandgap NFA also leads to hole transfer and the charge generation process lasts around 25 ps. Such slow charge generation is in sharp contrast with ultrafast (sub-ps) charge generation in the fullerene-based blends.

Secondly, using genetic algorithm, we decompose the measured spectra and find two key states, critical for understanding the signals, namely, the intermediate state and the product state. The intermediate species has donor polaron signature, and long-lived product state has acceptor-related signature. The conversion rate from the intermediate states into product states is around 400 ps. To study these two tates, we discuss two alternative models with experimental evidence.

In model 1, we assign the intermediate states to interfacial charge pair states and the product states to free charges. The main supporting evidence includes the fluence-dependence kinetics in both pristine NFA materials and blends. The time scale for formation of intermediate states and the separation of intermediate states into the free charges are reasonable. However, this model cannot explain the low yield of free charges in such high-efficiency blends.

In model 2, we assign the intermediate states to free charges and the long-lived product states to triplet states, with evidence from fullerene sensitisation, TTA-based photoluminescence, and solid-state heavy-atom enhanced ISC measurements. But the model involving triplet states cannot well explain the fluence-dependent kinetics. Even though triplet state can become a loss channel. In working devices, as long as the ratio of triplet states compared to the free charges is low, the polymer:NFA blends may still perform well under solar excitation conditions. One field not explored in this thesis is the possibility of separating the low-energy triplet states into free charges. To suppress the loss of triplets, further studies are needed to better understand its suppression mechanism.

Our results provide a new framework to study the charge dyanmics, in particular triplet-related behaviours, in the NFA-based blends.

Chapter 7

Efficient Nonfullerene Organic Solar Cells via Sequential Deposition

Note: This chapter is closely adapted from the following publication: J. Zhang†, B. Kan†, A. J. Pearson, A. J. Parnell, J. F. K. Cooper, X. -K. Liu, P. J. Conaghan, T. R. Hopper, Y. Wu, X. Wan, F. Gao, N. C. Greenham, A. A. Bakulin, Y. Chen*, R. H. Friend*. "Efficient non-fullerene organic solar cells employing sequentially deposited donor–acceptor layers" *J. Mater. Chem. A*, **2018**, 6, 18225-18233; (Reproduced from Ref. [261] with permission from the Royal Society of Chemistry.)

B. Kan and X. Wan. synthesised the non-fullerene acceptor. B. Kan and J. Zhang. optimised and characterised the conventional devices. J. Copper. performed NR measurements with data analysed by A. Pearson and A. Parnell. X. Liu. measured EQE of EL. J. Zhang performed the exciton diffusion length measurements and ultrafast measurements. R. Friend., A. Bakulin., Y. Chen, N. Greenham. and F. Gao supervised the project. J. Zhang wrote the manuscripts with contribution from all co-authors.

7.1 Introduction

Organic solar cells (OSCs) retain their flexibility and processability over large areas at relatively low cost, and have clear potential for assimilation into emerging technologies, such as building-integrated photovoltaics and wearable electronics.[6, 262] The active layers of OSCs typically incorporate a heterojunction between electron donor (D) and electron acceptor (A) organic semiconductors to facilitate efficient photocurrent generation. This concept, first introduced by Tang in 1986 using a planar heterojunction (PHJ) active layer architecture,[49] was modified in 1995 toward bulk-heterojunction (BHJ) layers that overcome clear limitations of the PHJ approach. Specifically, the mismatch between absorption depth and D:A interfacial area in a PHJ device results in a low efficiency for harvesting photogenerated excitons. By forcing a phase separation length scale between D and A that is commensurate with the exciton diffusion length (10-20 nm), BHJs enable much higher quantum efficiencies and overall power conversion efficiencies (PCEs).[51, 52] Since the introduction of the BHJ concept, morphological control of BHJs (e.g. D:A ratio, active layer processing conditions) has remained a key factor in the development of high-efficiency OSCs[263–265, 69, 67, 70, 266], despite the fact that a detailed mechanistic understanding of it remains under-developed.[267, 268, 245, 269]

As an alternative to co-depositing D and A semiconductors to form a BHJ, a two-step solution deposition process can be used, wherein the electron acceptor layer (usually based on a fullerene derivative small molecule) is deposited onto the electron donor layer (usually a polymer). This structure, termed a sequentially deposited BHJ (sq-BHJ), has been used in fullerene-based OSCs, sometimes yielding quantum efficiencies comparable to an as-cast BHJ (c-BHJ) based on D:A co-deposition.[270–283] For example, the state-of-the-art sq-BHJ OSCs based on poly[4,8-bis(5-(2-ethylhexyl)thiophen-2-yl)benzo[1,2-b;4,5-b']dithiophene-2,6-diyl-alt-(4-(2-ethylhexyl)-3-fluorothieno[3,4-b]thiophene-)-2-carboxylate-2-6-diyl)] (PTB7-Th) and $PC_{71}BM$ after post-annealing show maximum PCEs of 8.6%.[270] Compared to the c-BHJ approach, sq-BHJ OSCs potentially offer several advantages from the perspective of device fabrication, namely: (i) individual layer properties such as thickness and crystallinity can be independently controlled, thereby simplifying BHJ morphology optimisation. (ii) As a consequence of (i), OSCs can be fabricated with high reproducibility. (iii) The morphology of a sq-BHJ layer might be closer to thermal equilibrium and therefore more stable under conventional OSC operating temperatures.

With fullerene-based semiconductors remaining the archetypal electron acceptor for OSCs, the recent fast advancement of high-performance non-fullerene acceptors (NFAs) has motivated a careful evaluation of the future direction of OSC research. Beginning in 2015, the PCEs of champion NFA-based single-junction OSCs have been higher than those fabricated

using fullerenes, and now stands at an impressive 17%.[284, 105, 285, 102, 81, 286–290] Following this progress, the performance of OSCs based on other types of active layer architectures, such as ternary-blend OSCs[291, 292, 91, 89] tandem-junction OSCs[293, 294] and semitransparent OSCs[295–297], have all benefited from substitution of a fullerene-based electron acceptor for a NFA.

In this contribution, we report an efficient sq-BHJ device using poly[(2,6-(4,8-bis(5-(2-ethylhexyl)thiophen-2-yl)-benzo[1,2-b:4,5-b']dithiophene))-alt-(5,5-(1',3'-di-2-thienyl-5',7'-bis(2-ethylhexyl)benzo[1',2'-c:4',5'-c']dithiophene-4,8-dione)] (PBDB-T) as the donor and NCBDT as the acceptor. Optimised sq-BHJ layers are prepared using dichloromethane (DCM) as the solvent for NFA without post-treatments or solvent additives. The resultant OSCs show >10% PCE, comparable to that achieved by OSCs based on as-cast BHJ layers. This efficiency is one of the highest reported for sq-BHJ OSCs. As PBDB-T remains a benchmark polymer for NFA OSCs, we also determined its exciton diffusion length to be 10 ± 3 nm from external quantum efficiency (EQE) measurements. To understand the performance of both sq-BHJ and c-BHJ OSCs we characterise the factors governing voltage loss using stead-state and time-resolved optical and electrical measurements.

7.2 Experimental Section

7.2.1 Conventional Structure

The device structure was glass/ITO/PEDOT:PSS (poly(3,4-ethylenedioxythiophene) polystyrene sulfonate)/active layer/PDINO (perylene diimide functionalized with amino N-oxide)/Al. The glass substrate with ITO was cleaned sequentially by deionized water, acetone and isopropyl alcohol under ultrasonication for 10 min each. The subsequent PEDOT:PSS layer was spin-coated at 5000 RPM for 45 s, and then baked at 150 °C for 20 min in ambient atmosphere. For the sq-BHJ film, the donor layer was deposited from 6 mg mL^{-1} solution in chloroform at 1900 RPM for 20 s, and the subsequent acceptor layer was cast from ∼60 µL solution in DCM (6 mg mL^{-1}) at 2500 RPM for 40 s right before spin-coating. PDINO (1 mg mL^{-1} in CH_3OH) was spin-coated on the active layer at 3000 RPM for 40 s. Finally, a 100 nm Al layer was deposited under high vacuum. The effective area of each cell was 4.5 mm^2.

7.2.2 Device Photovoltaic Performance

Current density-voltage curves of the solar cells were recorded by a Keithley 2635 source meter under illumination of a solar simulator (SS50AAA, Photo Emission Tech). The

intensity of the simulated sunlight (100 mW cm^{-2}) was calibrated with a standard silicon reference cell and a KG3 filter. The external quantum efficiency (EQE) spectrum was measured by an Oriel Cornerstone 130 monochromator. Reporting a reliable photovoltaic performance requires careful calibration, for which readers are suggested to read the following papers.[298–301]

7.2.3 EL Efficiency, Field-Dependent PL and EL

EQE_{EL}, field-dependent PL and EL. EL emission from the device was collected by a silicon photodiode with an active area of 100 mm, with fixed distance between the device and the photodiode. The current-voltage characteristics of the device were measured with a Keithley 2400 source meter and the current outputs of the photodiode were measured with a Keithley 2000 source meter. Steady-state PL was measured from encapsulated films using a home-built setup with a 405 nm laser (Coherent) as the excitation source. The collected PL was focused into a spectrometer (Andor). For field-dependent PL, the encapsulated devices were connected to and biased by a source meter (Keithley 2400). With the same setup, the bias-dependent EL was measured in the injection region. A 500 nm long-pass filter was used to block the excitation scattering.

7.2.4 Neutron Reflectivity

NR measurements of thin film layers were made using the same spin coating parameters as for the actual devices. The substrates were 5 mm thick circular silicon wafers (Prolog Semicor, Ukraine) with diameter of 50.8 mm. The NR data was measured at the ISIS pulsed Neutron and Muon Source (Oxfordshire, UK) using the instrument OFFSPEC, which has a useable incident neutron wavelength range from 2-12 Å. A number of incident angles were collected to cover the measured momentum transfer range 0.008-0.238 Å^{-1}. We measured reference samples for each pure material (PEDOT:PSS, PBDB-T and NCBDT) which allowed us to unambiguously measure the scattering length density (SLD) of each layer independently. The PEDOT:PSS layer SLD, thickness and roughness were constrained in the device layer films, whilst silicon oxide thickness was allowed to vary. The NR data was modelled using the scheme of Névot and Croce as a number of layers each having a roughness, thickness and a SLD. For the as-cast BHJ layer a single fit was used. For the sequentially processed layers, fitting was performed for two possible cases, that of a bilayer architecture and a single layer. In the former, the SLD of each layer was constrained to the values measured for the single layer films.

7.2.5 Pump-Probe Spectroscopy

800 nm, ∼200 fs pulses were generated by a regenerative Ti:sapphire regenerative amplifier (Spectra Physics, Solstice Ace) operating at 1 kHz. A portion of the seed pulses were directly sent into the sample area, while another portion was sent to a delay stage, followed by generation of the broadband probe pulses (∼950-1350 nm). Part of the probe light was split off and used as the reference to reduce the pulse fluctuation. Both probe and reference beams were detected using a pair of linear image sensors (Hamamatsu). The signal was read out at the full laser repetition rate by a custom-built board (Stresing Entwicklungsburo). The beam size of pump and probe pulses were estimated to be ∼0.5 mm. The sq-BHJ and c-BHJ films were prepared following the procedures for device fabrication. Pure NCBDT film was spin-coated at 3000 RPM for 40 s from a 6 mg/ml solution in CF, while the NCBDT:PS (weight ratio, 1:49) blend film was cast from chlorobenzene. The pump pulse energy was 250 nJ for NCBDT:PS film and 50 nJ for other films.

7.3 Conventional Device Fabrication and Characterisation

7.3.1 Materials

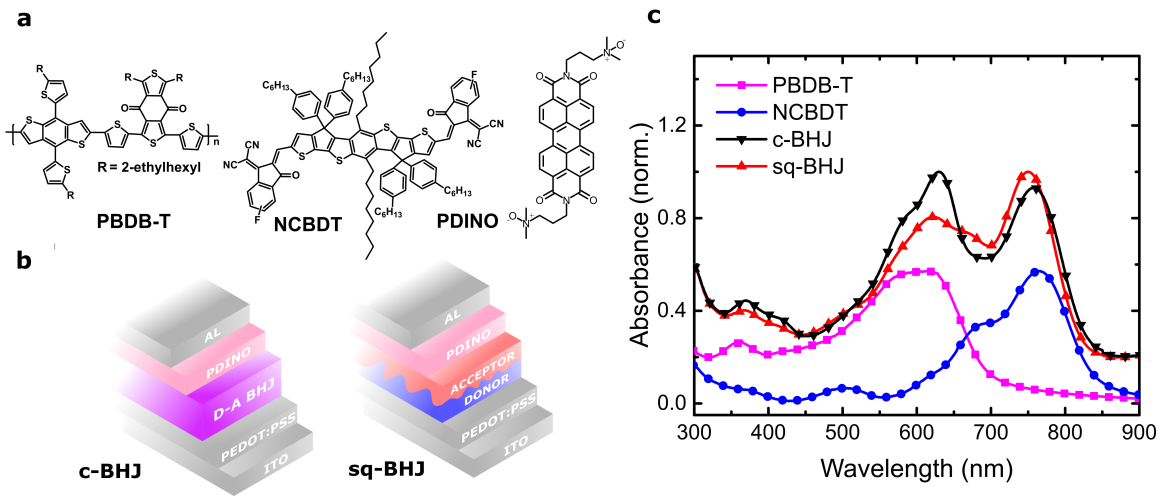

Fig. 7.1 Molecule structure absorption and the device structure. (a) Chemical structures of PBDB-T (donor), NCBDT (acceptor) and PDINO (electron-transport layer). (b) Device structures where the photoactive layer is based on a c-BHJ or sq-BHJ architecture. (c) Absorption spectra of pristine PBDB-T and NCBDT films. The blend absorbance is normalised to 1 and the pristine data is normalised to 1/2.

Fig.7.1(a) presents the chemical structures of the electron donor (PBDB-T), electron acceptor (NCBDT) and electron transport layer (PDINO, perylene diimide functionalized with amino N-oxide). PBDB-T is widely used as a benchmark electron donor for blending with emerging electron acceptors.[302] The central electron-donating BDT unit has also featured in many ladder-type NFAs [252], such as NCBDT in this study.[1] For the sq-BHJ film, the donor layer was deposited from solution in chloroform, and the upper acceptor layer was cast from DCM solution. For the bulk-BHJ film, the donor and acceptor mixed layer was deposited from chloroform. Fig.7.1(c) shows the complementary absorption of the pristine materials across the visible and near-IR region together with the absorption spectra of c-BHJ and sq-BHJ blends. As shown in our previous study, the peak optical absorption of NCBDT shifts from $\sim$ 730 nm in dilute solution to $\sim$ 760 nm in an as-cast film, suggesting ordered molecular packing in the solid state.[1]

7.3.2 Device Fabrication

The device structure, shown in Fig.7.1(b), is ITO/PEDOT:PSS (poly(3,4-ethylenedioxythiophene) polystyrene sulfonate), $\sim$ 30 nm)/active layer/PDINO ($\sim$ 5 nm)/Al (100 nm). PDINO was then spin-coated from methanol solution on the active layers, followed with an evaporated Al layer. To simplify device fabrication, we do not subject either active layer architecture to any post-film deposition annealing.

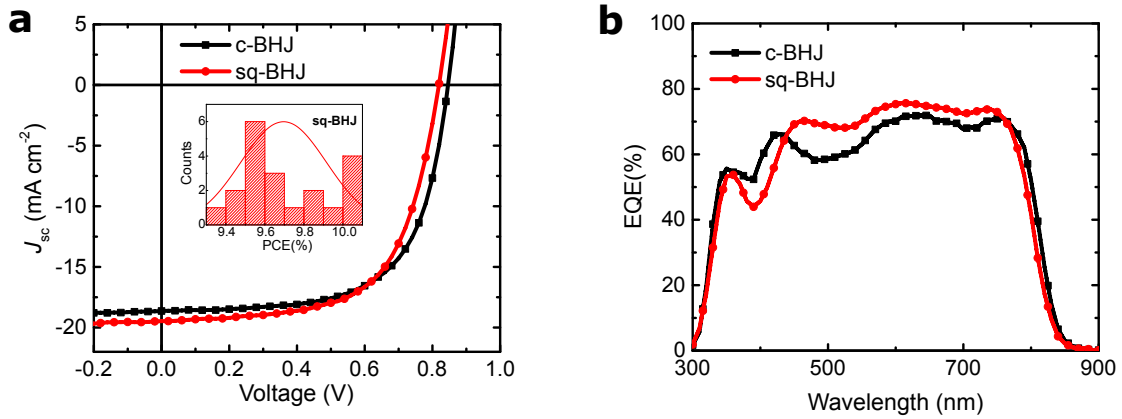

Fig. 7.2 Photovoltaic performance measurements. (a) Current-density voltage measurements under one-sun illumination. Inset: the distribution of PCE in 20 sq-BHJ devices. (b) Spectral dependence of the EQE.

C-BHJ OSCs with an active layer thickness of 100 ± 5 nm show a PCE of $\sim$ 10%, reproducing the results from our previous study.[1] Optimisation of the sq-BHJ OSCs considered the following processing variables: PBDB-T and NCBDT solution concentration,

Table 7.1 Characteristics of the c-BHJ and sq-BHJ devices.

active layer layout	V_{OC} (V)	J_{SC} (mA cm^{-2})	FF (%)	PCE (%)	J_{SC} EQE (mA cm^{-2})	Hole mobility (10^{-4} m^2 V^{-1} s^{-1})	Electron mobility (10^{-4} m^2 V^{-1} s^{-1})
c-BHJ	0.847 (0.842±0.003)	18.64 (18.32±0.20)	64.6 (63.5±0.5)	10.19 (10.05±0.12)	18.65	1.28 (1.21±0.04)	1.18 (1.09±0.05)
sq-BHJ	0.824 (0.820±0.003)	19.45 (19.14±0.15)	62.9 (61.8±0.6)	10.04 (9.70±0.24)	19.30	0.88 (0.81±0.05)	0.92 (0.85±0.07)

Table 7.2 Determination of non-radiative and radiative energy loss in c-BHJ and sq-BHJ devices.

active layer layout	E_{gap} (±0.01)	$q\,V_{OC}$ (±0.005)	$q\Delta V$	$\Delta E_1 = E_{gap} - q\,V_{OC}^{SQ}$	$\Delta E_2 = q\,V_{OC}^{SQ} - q\,V_{OC}^{rad}$	$\Delta E_3 = q\,V_{SQ}^{rad} - q\,V_{OC}$	EQE_{EL} $(exp.)$	$q\,\Delta V_{OC}^{non\text{-}rad,exp}$
c-BHJ	1.54	0.847	0.693	0.282	0.038	0.373	9.1×10^{-7}	0.347
sq-BHJ	1.54	0.824	0.716	0.281	0.033	0.402	2.2×10^{-7}	0.383

1. The EQE_{EL} was determined at the injection current of 155 mA cm^{-2}. In the table, q is the element charge, ΔV is the voltage loss, E_{gap} is the lower bandgap of D or A, V_{OC}^{SQ} is the maximal voltage by the Shockley-Queisser limit, V_{OC}^{rad} is the open-circuit voltage when there is only radiative recombination. EQE_{EL} is the radiative quantum efficiency of the solar cell when charge carriers are injected into the device in the dark. $\Delta V_{OC}^{non\text{-}rad,exp}$ is the voltage loss calculated from EQE_{EL}.
2. The unit is eV for energy quantities.

Table 7.3 Device optimisation of sq-BHJ devices by changing the solvent, the spin speed for the acceptor and donor layers. The donor and acceptor concentration are both 6 mg ml^{-1}, respectively.

Variant	Parameter	V_{OC} (V)	J_{SC} (mA cm^{-2})	FF (%)	PCE (%)
Solvent (1500 RPM for donor and 3000 for acceptor)	DCM	0.803	19.24	53.8	8.32
	DCE	0.811	5.08	43.6	1.79
	TCE	0.811	10.15	53.0	4.37
Spin speed of acceptor layer (1500 RPM for donor layer)	1500	0.790	18.80	52.7	7.82
	2000	0.799	19.29	53.2	8.19
	2500	0.804	19.64	56.7	8.95
	3000	0.803	19.24	53.8	8.32
	3000+SVA[1]	0.792	19.57	53.6	8.30
Spin speed of donor layer (2500 RPM for acceptor layer)	1500	0.804	19.64	56.7	8.95
	1700	0.824	19.05	61.7	9.68
	1900	0.824	19.45	62.9	10.04
	2100	0.791	18.08	58.9	8.42
	2300	0.791	18.06	59.2	8.51
	1900+ZnO[2]	0.803	18.92	59.9	9.10

1. SVA: solvent vapour annealing
2. ZnO: the electron transport PDINO interlayer was replaced by ZnO.

film deposition spin-speed, and casting solvent, the outcomes of which are tabulated in Table.7.3. From this exercise, devices with PCE of $\sim$ 10% were obtained. The efficiency distribution is shown in the inset of Figure.7.2(a). The bars are not so well fitted with a Gaussian line, showing an average efficiency around 9.7%. Here, the nominal thicknesses of the donor and acceptor layer were 45 ± 5 nm and 50 ± 5 nm, respectively, and the total active layer thickness was 90 $\pm$ 5 nm.

Fig.7.2 shows the overall photovoltaic behaviour for both c-BHJ and sq-BHJ OSCs with related performance metrics summarized in Table.7.1. Compared with the c-BHJ OSCs, sq-BHJ OSCs have larger short-circuit current density (J_{SC}) up to 19.45 mA cm^{-2}, which likely results from optimised vertical stratification.[277] The larger open-circuit voltage (V_{OC}) of the c-BHJ OSCs has previously been observed in a polymer:fullerene OSC, but the origin of this difference was not investigated in detail.[280] The fill factor (FF) for the sq-BHJ OSCs, was found to be relatively more sensitive to the thicknesses of the donor and acceptor layers (Table.7.3), which may reflect a greater imbalance between electron and hole mobilities, and/or enhanced bimolecular recombination (BR). We measured the dark current density-voltage behaviour of single carrier devices in the space-charge limited current regime to determine respective charge carrier mobilities (Fig.7.3). From this experiment, the ratio of electron to hole mobilities were found to be smaller in the sq-BHJ devices than those in

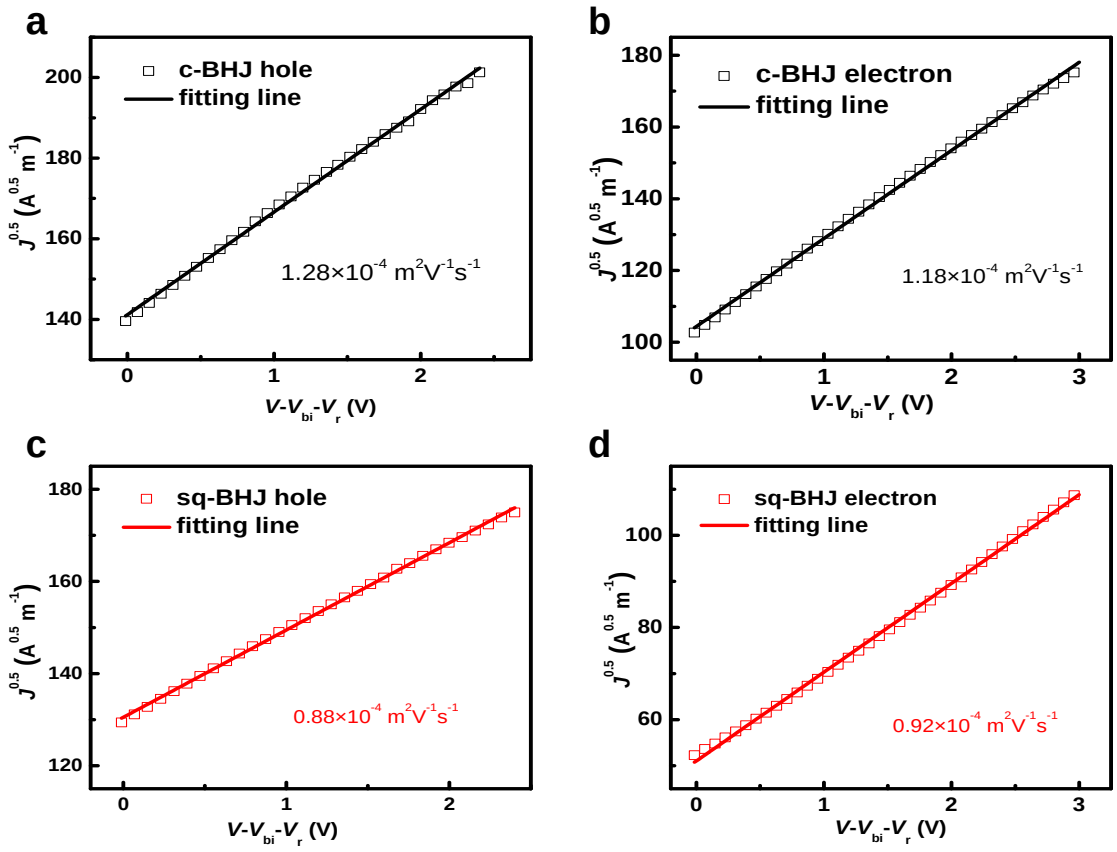

Fig. 7.3 Hole and electron mobilities extracted from the space-charge limited current.

c-BHJ devices, consistent with the FF values found for the corresponding OSCs as a higher mobility means better charge transport ability.

7.3.3 Device Stability

Fullerene-based OSCs are not photo-stable mainly due to sensitivity of fullerene to the environment, for example, the oxygen and water in the air. Sq-BHJ devices often show an improved stability over c-BHJ devices in fullerene-based OSCs.[270] The efficiency increase in NFA OSCs also accompanies its improved device in c-BHJ devices probably due to elimination of fullerene derivatives. In such scenario, the device stability of NFA-based sq-BHJ devices is not reported yet. Fig.7.4(a) shows that sq-BHJ devices preserve 65% of its original efficiency after 3 weeks while c-BHJ devices maintain 72%. We find that the efficiency drop is mainly due to decreased J_{SC} while V_{OC} and FF degraded similarly. The inferior stability of sq-BHJ devices might be due to its not thermally stabilized interfacial morphology, and or trap states at the interface.

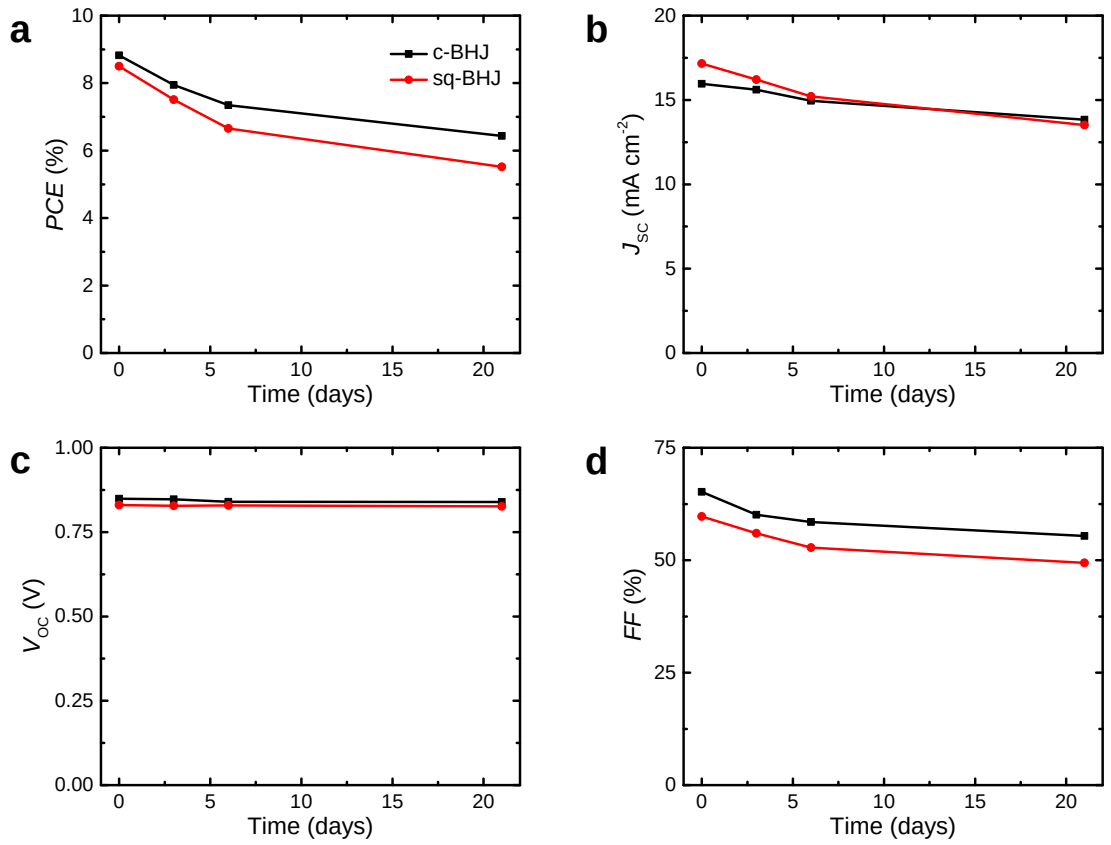

Fig. 7.4 Device stability of c-BHJ and sq-BHJ devices over 3 weeks. During measurements, the device is kept in dark nitrogen environment. The data is averaged of 3 devices.

7.4 Charge Generation and Recombination

Fig.7.2 shows the EQE spectra for both OSC types. Between 450 and 800 nm, the EQE for the sq-BHJ OSC is higher and more uniform than that for the c-BHJ OSC, which contains a clear local minimum around 500 nm. This dip in EQE may be due to lower absorption efficiency of the c-BHJ layer and/or suboptimal optical management of the device stack. We note, however, that the sq-BHJ layer is more likely to exhibit vertical heterogeneity, and the photocurrent generation efficiency could therefore exhibit a greater dependence on position within the OSC stack.[303] This optical management factor can be understood by substantially increasing the PBDB-T layer thickness. Data presented in Fig.7.5 shows that the EQE at long wavelengths (>600 nm) becomes lower as a result.

Alongside improved semiconductor design, future device optimisation should carefully consider the distribution of materials within a sq-BHJ layer in order to accurately predict the device structure which enables maximal EQE.[277] In our case, it becomes interesting that

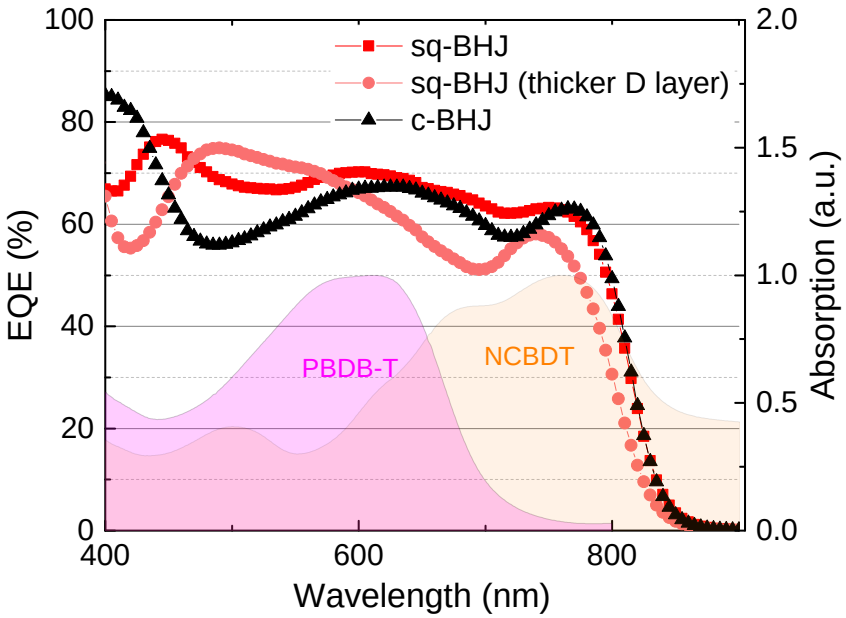

Fig. 7.5 EQE profile of the c-BHJ, and the sq-BHJ devices with different thicknesses of the PBDB-T layer. The filled area shows the absorption profile of PBDB-T and NCBDT. The sharp contrast at 500 nm and 700 nm can be rationalised by cavity effect - the stronger light absorption at higher wavelength away from the metal electrode.

sq-BHJ structure seems to exhibit features of both BHJ (efficient exciton dissociation) and PHJ (heterogeneity effect). The cavity effect results in better absorption of high wavelength light far away from the metal electrode. This effect can be utilised when D and A absorb light at complementary bands which is enabled by the development of NFA. Future experiments should use high-bandgap material closer to the electrode. Certain simulation can be conducted to calculate the optimum mixing of D and A at their contacts. We will discuss this in later session.

We also measured the dependence of photocurrent density on effective bias (V_{eff}, defined as the applied bias minus the built-in voltage of the OSC) and light-intensity dependence of J_{SC} and V_{OC}. Each of these measurements does not show significant differences between these device types (Fig.7.6), supporting the notion of similar charge generation and recombination in both OSCs.

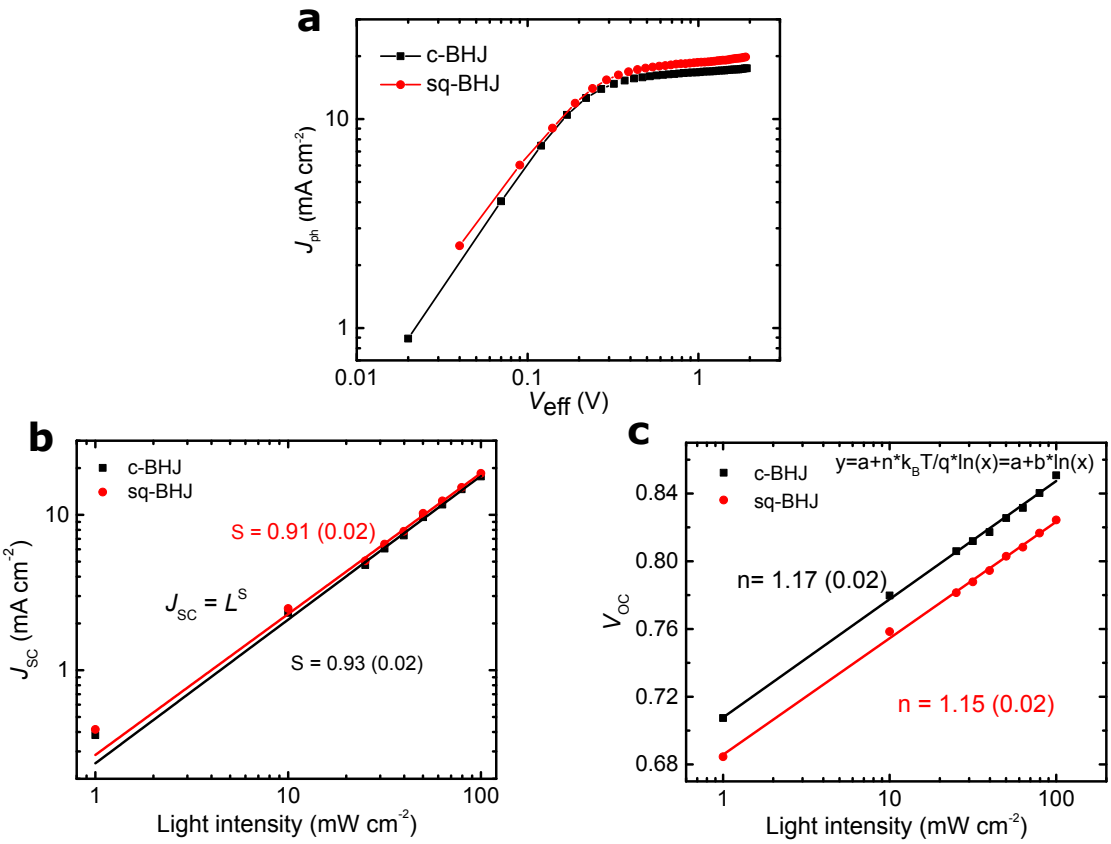

Fig. 7.6 Light-intensity-dependent measurement. (a) Photocurrent generation versus the effective voltage of c-BHJ and sq-BHJ devices. (b-c) Light-intensity dependent J_{SC} and V_{OC}. The dependence of J_{SC} under different light illumination was fitted as $J_{SC} \propto L^S$, where L is the light intensity, S is the fit parameter. The dependence of V_{OC} on light intensity was fitted with $V_{OC} = a + (n\,k_B\,T/q) \times \ln L = a + b \times \ln L$, where the slope b is linked to idealty factor n, k_B is the Boltzmann constant, T is the temperature and q is the element charge.

7.5 Voltage Loss and Non-Radiative Recombination

Within the literature, state-of-the-art NFA-based OSCs exhibit a much lower voltage loss compared to state-of-the-art fullerene-based OSCs, overcoming the traditionally severe trade-off between high J_{SC} and high V_{OC}. This is primarily due to their high charge generation efficiency despite the minimal driving force for exciton dissociation, in addition to their much improved electroluminescence (EL) efficiency. These characteristics motivate us to reflect on the larger V_{OC} (by ~ 23 meV) of the c-BHJ OSCs compared to the sq-BHJ OSCs, and to characterize the detailed energy losses in both devices. As discussed by Nelson [304] and Yan [78], energy loss can be separated into three categories: 1) $\Delta E_1 = E_{gap} - q\,V_{OC}^{SQ}$, mainly radiative recombination due to the absorption above the bandgap; 2) $\Delta E_2 = q\,V_{OC}^{SQ} - q\,V_{OC}^{rad}$,

due to additional radiative recombination from the absorption below the bandgap; 3) $\Delta E_3 = q\,V_{SQ}^{rad} - q\,V_{OC} \approx -kT \ln EQE_{EL}$ from the non-radiative recombination.

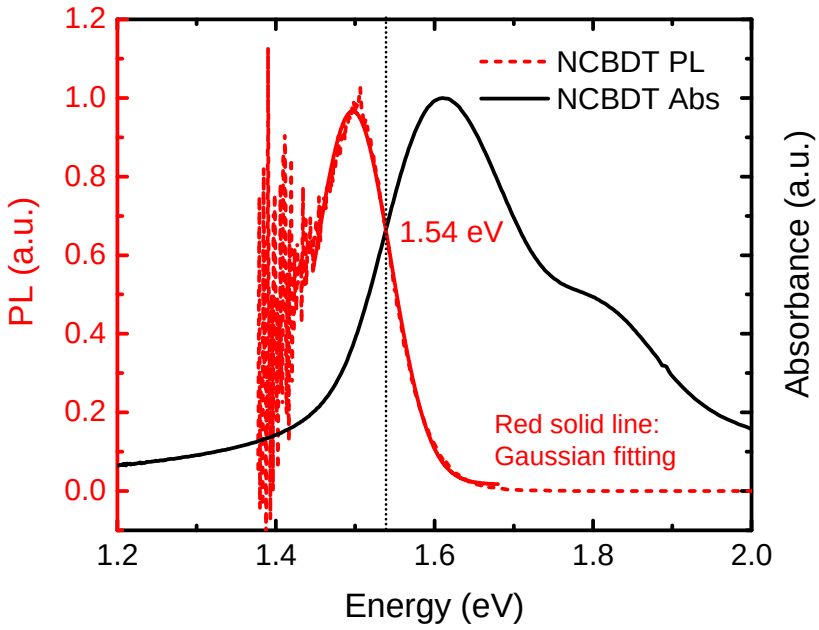

Fig. 7.7 Optical bandgap energy of NCBDT acceptor determined by the cross point of the absorption (black) and emission (red) spectra.

The bandgap of NCBDT is ~ 1.54 eV, determined by the cross point of the absorption and emission spectra (Fig.7.7).[10] With the same material combination and similar EQE in both structures, there is only a small difference in the energy loss from ΔE_1 (1 meV) and ΔE_2 (~ 5 meV) as determined by EQE spectra according to the published method.[39] Thus, the dominant loss channel should be non-radiative recombination, estimated to be ~ 29 meV. This parameter is fundamentally connected with the EL efficiency. We directly measured EQE_{EL} by recording the EL intensity from both OSCs under forward bias conditions (Fig.7.8). The ratio of EL (Table.7.2) efficiencies corresponds to a voltage difference of ~ 36 meV, which is comparable with the predicted ΔE_3 of ~ 29 meV. This is also reflected by the measured dark current density-voltage behaviour, which inversely correlates with EL efficiency (Fig.7.9). The relevant energy losses are summarised in Table. 7.2 on page 145.

For P3HT:PC_{61}BM OSCs reported elsewhere, an identical V_{OC} was obtained using sq-BHJ and c-BHJ active layers (with thermal annealing treatment).[272] However, polymer:fullerene OSCs utilising poly[N-9'-heptadecanyl-2,7-carbazole-alt-5,5-(4',7'-di-2-thienyl-2',1',3'-benzothiadiazole)] (PCDTBT) demonstrated a higher V_{OC} in sq-BHJ devices.[283] Thus the voltage output depends on material combination and post-treatment, both of which

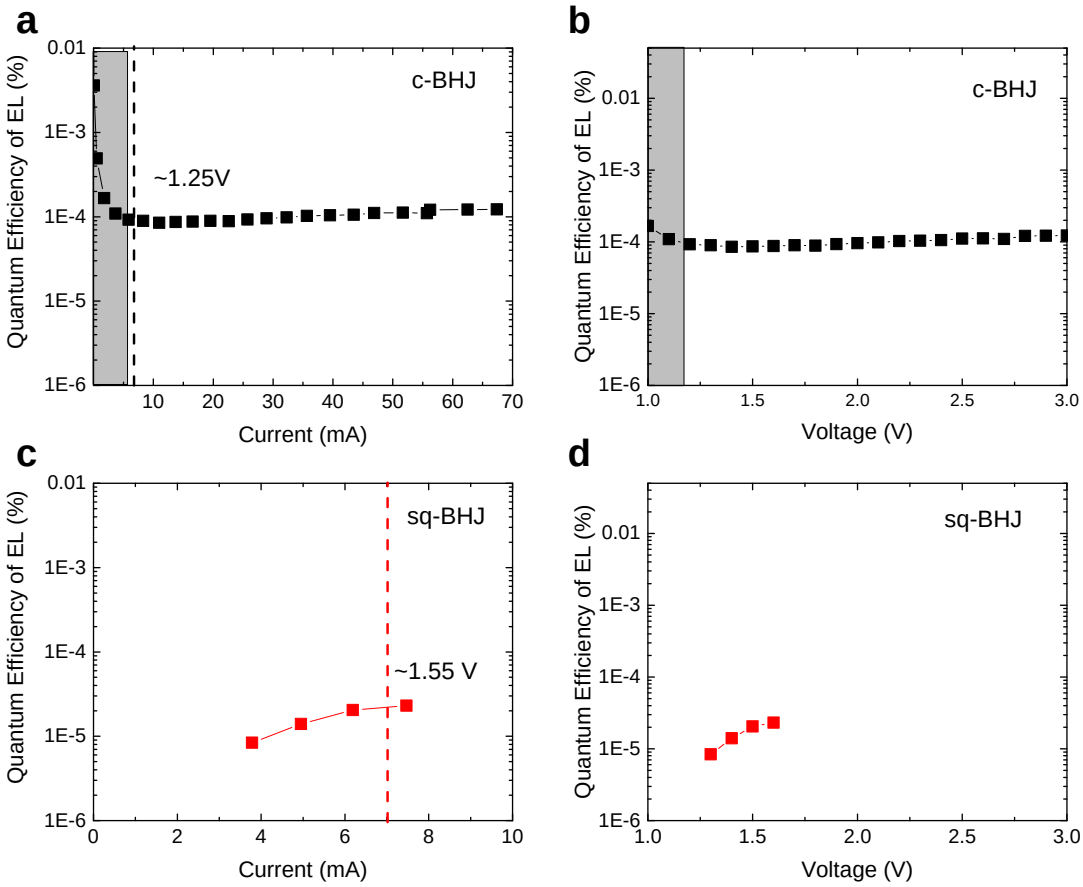

Fig. 7.8 Quantum efficiency of EL of the c-BHJ and sq-BHJ devices. The data in gray region in (a) and (b) is abandoned due to its low luminescence. The EQE_{EL} is determined at the injection current of 7 mA.

strongly influence the D:A interfacial morphology. In our work, V_{OC} in the sq-BHJ OSCs studied here is smaller than that in the c-BHJ devices, which can be explained by higher non-radiative recombination.

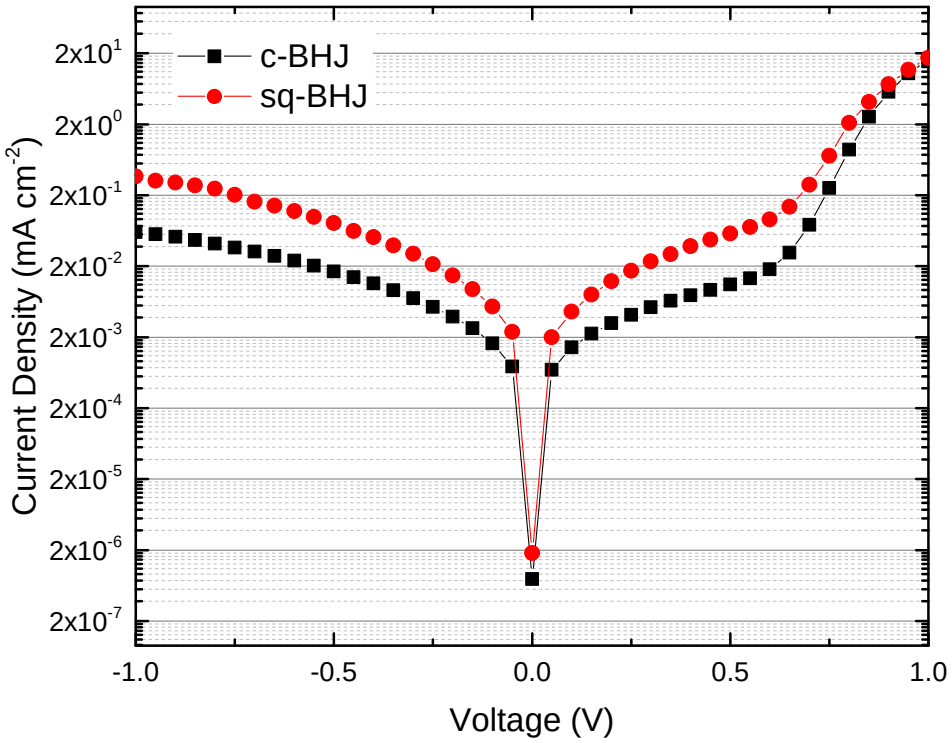

Fig. 7.9 Dark current-density voltage curves of the c-BHJ and sq-BHJ devices.

7.6 Atomic-Force Microscope and Neutron Scattering

To realise efficient sq-BHJ OSCs, a processing solvent with partial solubility for the bottom layer and good solubility for the top layer is required. Dichloromethane (DCM) meets these criteria as it only partially dissolves PBDB-T, in contrast to tetrahydrofuran (THF) which washes away the polymer layer entirely as shown in Fig.7.10. In detail, we spin-coated the pristine donor layer with pure THF and DCM, and measured its absorption change as well as its surface roughness. DCM slightly removed the donor layer (5 nm less in thickness and 4% less in absorption) with a smooth surface (R_a = 1.7), while THF largely dissolved the donor layer (40 nm less in thickness and 30% less absorption) with a rougher surface (R_a = 2.0).This contrasts with the results of Kim et al. on PTB7 films, where it was found that DCM washed away 90% of material, mostly likely regions of relatively low molecular weight and high disorder.[278]

Scanning probe microscopy images in Fig.7.12(a) show the evolution of the PBDB-T film surface structure during these processing steps. Following diiodomethane (DIM) washing,

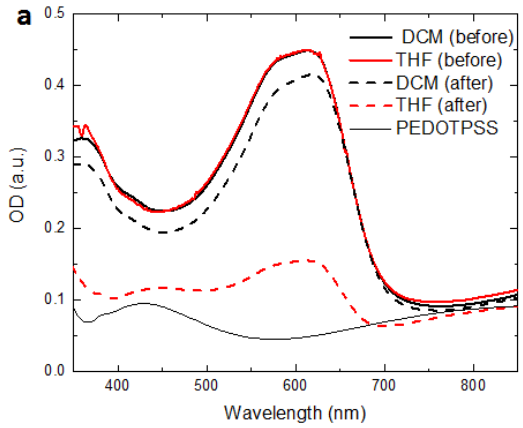

c

Sample	Thickness* (nm)	Ra (nm)
Pure PBDB-T	90	0.9
DCM Wash	85	1.7
THF Wash	50	2.0

Fig. 7.10 Film washed by THF and DCM solvents. (a) Films absorption before and after washing the pure PBDB-T layer with THF and DCM. (b) The images of the films after washing. (c) The film thickness (including PEDOT:PSS layer, $\sim$ 30 nm) and surface roughness measured by AFM.

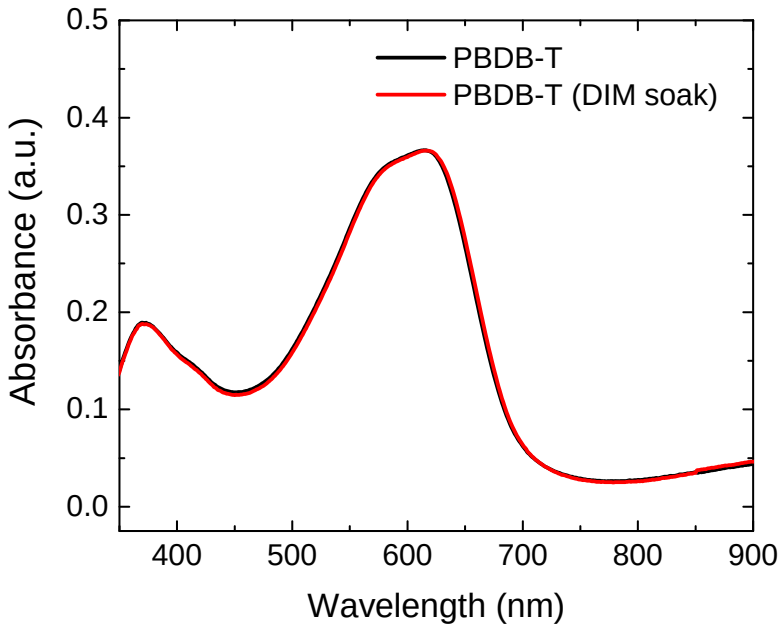

Fig. 7.11 Absorption of PBDB-T film with and without DIM soaking.

NCBDT is successfully removed as inferred from UV-Vis measurements (Fig.7.12(b)). The reduction in PBDB-T absorption results from the process of NCBDT deposition and its exposure to DCM solvent as DIM is an orthogonal solvent to PBDB-T (Fig.7.11).

We note that DIM is toxic and reactive and should not be used for device fabrication. The resultant increase in PBDB-T surface roughness (to 1.70 nm) indicates that polymer reorganisation can take place during second layer deposition, which likely encourages intermixing between PBDB-T and NCBDT. Data obtained using neutron reflectivity (Fig.7.12(c)) is fitted to a model that implies uniform mixing of sq-BHJ film rather than a strict bilayer structure. However, as the small difference in SLDs between PBDB-T and NCBDT ($\sim 0.2 \times 10^{-6}$ Å^{-2}) places a relatively large uncertainty on any model output, we are not able to determine the gradient in NCBDT distribution using this data. More advanced characterisation techniques are required to precisely image the vertical heterogeneity of the BHJ active layer.

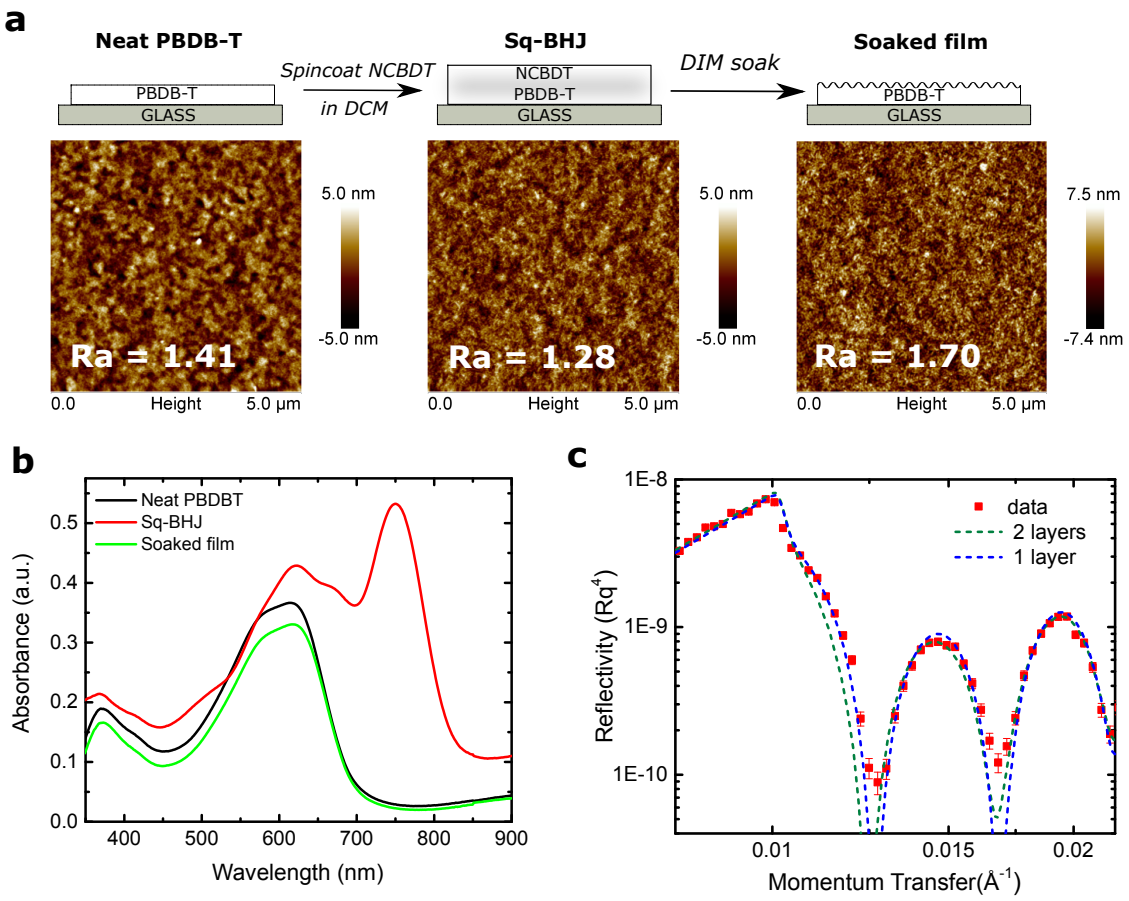

Fig. 7.12 Morphological characterisation of PBDB-T and PBDB-T:NCBDT blend films. (a) AFM images showing the surface nanostructure of pristine PBDB-T layer, and a PBDB-T:NCBDT sq-BHJ before and after NCBDT removal. Here the NFA was washed from the sample using DIM solvent (b) Absorption spectra corresponding to samples in (a). (c) Measured and simulated neutron reflectivity data of a sq-BHJ film, with simulated data considering either a homogeneous PBDB-T:NCBDT blend layer or strict PBDB-T:NCBDT bilayer.

7.7 D-A Interfacial Energetics

We naturally question whether the differences in c-BHJ and sq-BHJ films influence the energetics inside the D:A intermixed regions. As mentioned previously, NFA OSCs often benefit from high charge generation efficiencies despite a small driving energy. In contrast, for fullerene-based OSCs, a small driving energy leads to poor charge generation efficiency.[97]

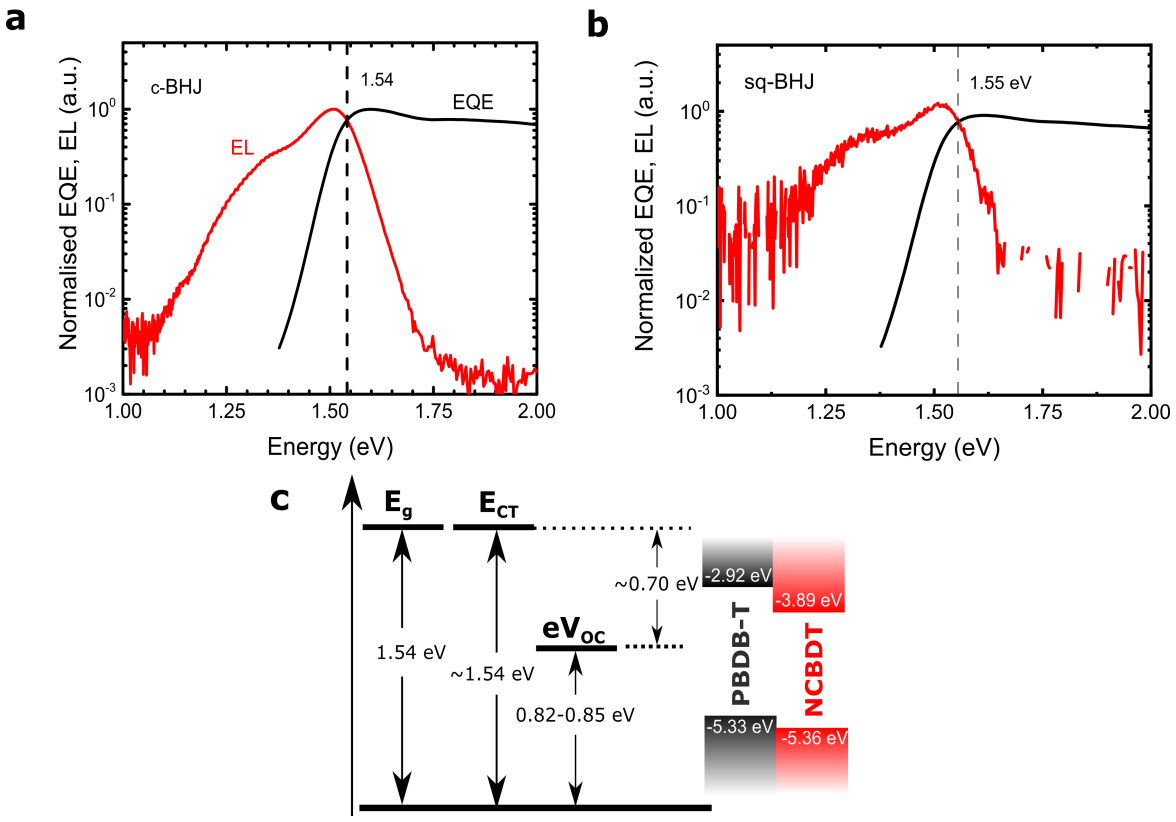

Fig. 7.13 EL, EQE and its related energy levels. (a) c-BHJ and (b) sq-BHJ: EL and EQE profile for determination of bandgap of possible interfacial states. (c) Left: the energy level of the optical bandgap and possible charge-transfer (CT) states (1.54 eV) with a device V_{OC} around 0.82-0.85 V and recombination energy loss of $\sim$ 0.70 eV; Right: highest occupied molecular orbital (HOMO) and lowest unoccupied molecular orbital (LUMO) energy levels of PBDB-T and NCBDT.

From Fig.7.13(b), the energetic difference between PBDB-T and NCBDT HOMO levels is $\sim$ 30 meV. However, the high peak EQE ($\sim$ 75%) implies efficient light harvesting. Our high-performance devices thus serve as a model system for investigating D:A interface energetics in a sq-BHJ OSC that contains an A-D-A type NFA. In the EQE graph and EL emission, a Gaussian-type shoulder is usually characteristic of CT states. As shown in Fig.7.13(a), it is difficult to confirm such a shoulder in the EQE and EL data. The cross point energy of EQE and EL spectra [95, 305] is 1.54 eV, the same as the bandgap of the pure

acceptor (Fig.7.7). From this we conclude that there is a negligible driving force for charge transfer. This result agrees with measurements made on another category of NFAs based on fused aromatic diimides reported by Yan et al.[78]

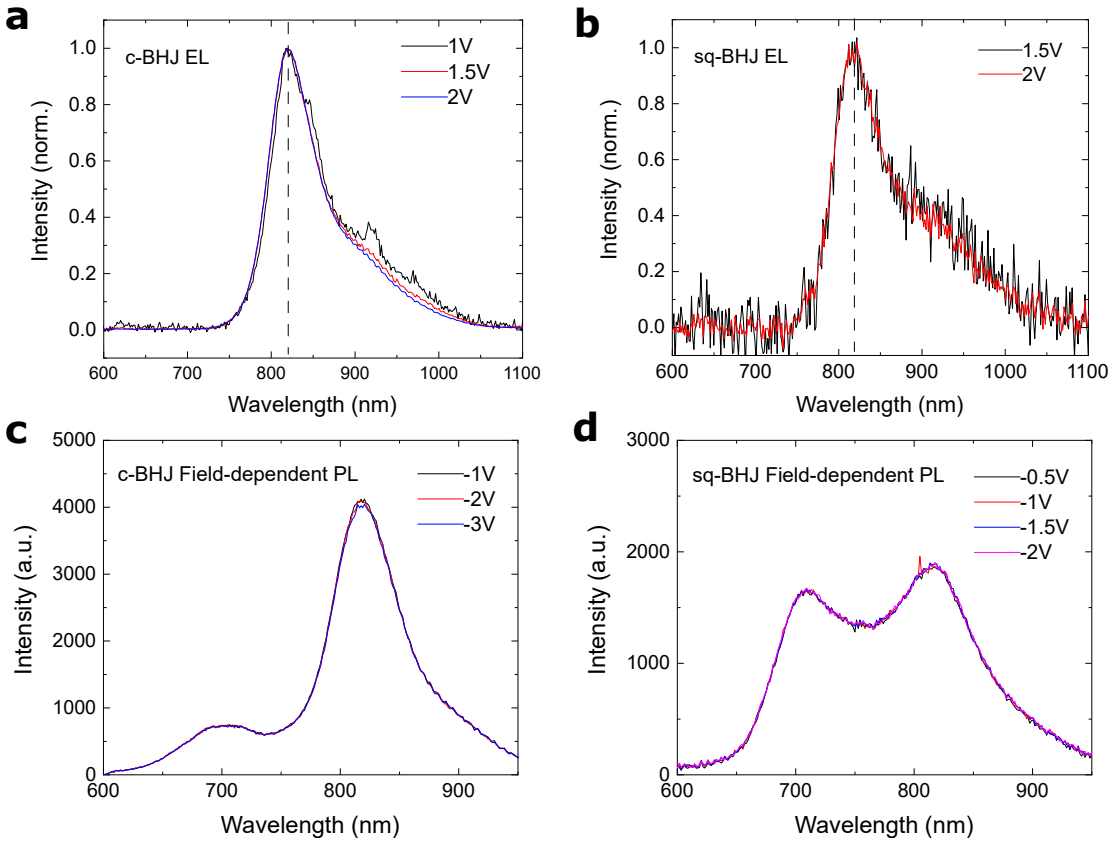

Fig. 7.14 Field-dependent PL and EL. (a-b) Field-dependent EL of c-BHJ and sq-BHJ devices under forward biases. (c-d) Field-dependent PL of c-BHJ and sq-PHJ OSCs with excitation at 400 nm. The peak at 700 nm is from the emission of PDINO layer. The peak at 820 nm is from the active layer.

No change in EL and PL spectra under various biases was observed as shown in Fig.7.14, which indicates that the emissive spectra are from the same species, possibly singlet excitons. This is quite different from the low energy offset ($\sim$ 50 meV) fullerene-based blends PIPCP:$PC_{61}BM$, where the PL intensity of the BHJ blend is field-dependent.[306] Intramolecular vibrations in CT states have been suggested to explain the intrinsic limit for the non-radiative recombination in fullerene-based OSCs[95] , but in these novel NFA OSCs, the intrinsic limit of non-radiative recombination has not been determined. A systematic investigation of the charge generation mechanism is still missing, and the effect of charge delocalization and non-uniform electronegativity in strong intramolecular push-pull molecules requires further attention.[307] At this stage of our research, we do not find substantial ener-

getic difference between the c-BHJ and the sq-BHJ OSCs despite their different preparation methods.

7.8 Transient Absorption

To observe ultrafast kinetics, we used femtosecond optical spectroscopy. In the optical pump-probe measurement, we selectively excited NCBDT with 800 nm pulses. Figure. 7.15 shows the kinetics of the exciton peak (averaged between $1000-1100$ nm) extracted from the full spectra in Figure. 7.16 on the facing page. A faster exciton decay in the D-A blend than that in the NCBDT: polysterene (PS) blend suggests efficient exciton quenching in both c-BHJ and sq-BHJ blends. Interestingly, kinetics at short timescales (<20 ps) from D:A blends are very similar to that from pure NCBDT blend. This indicates a slow charge-transfer rate under such low offset in HOMO energies (Fig. 7.13 on page 157(b)). The signal after 100 ps in D-A blends cannot come from excitons which are expected to decay completely (as seen in measurements on pure NCDBT film), but possibly from polarons. The smaller amplitude at around 200 ps in c-BHJ films thus might come from faster BR due to its finer phase separation. Such fast recombination has been observed in PIPCP:PCBM blends.[183] Overall, from transient absorption measurements, there is not much difference in charge generation in c-BHJ and sq-BHJ films.

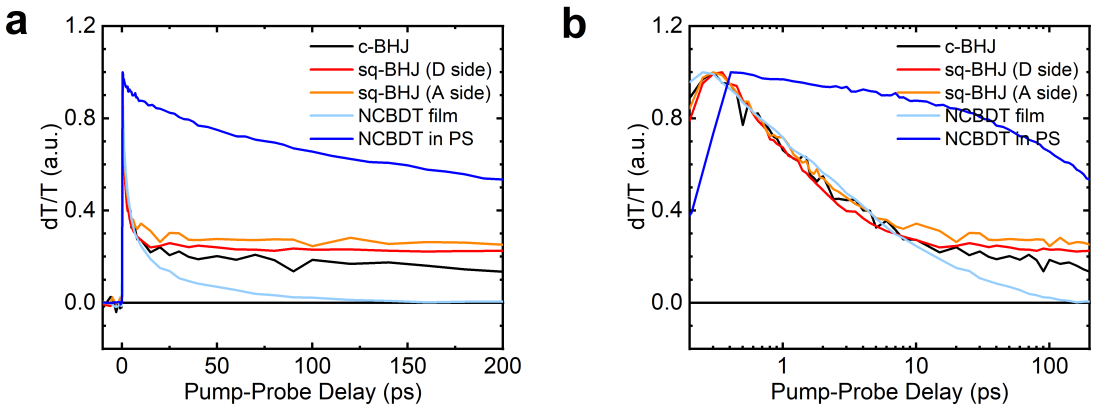

Fig. 7.15 Kinetics from pump-probe spectroscopy with selective acceptor excitation at 800 nm. The kinetics is averaged between 1000 and 1100 nm. The sq-BHJ film was excited at two directions, either donor side first, or acceptor side first. The kinetics from the pure acceptor film and the NCBDT:PS blend film are for reference. (a) x and y are both in linear scales; (b) x is in logarithm scale.

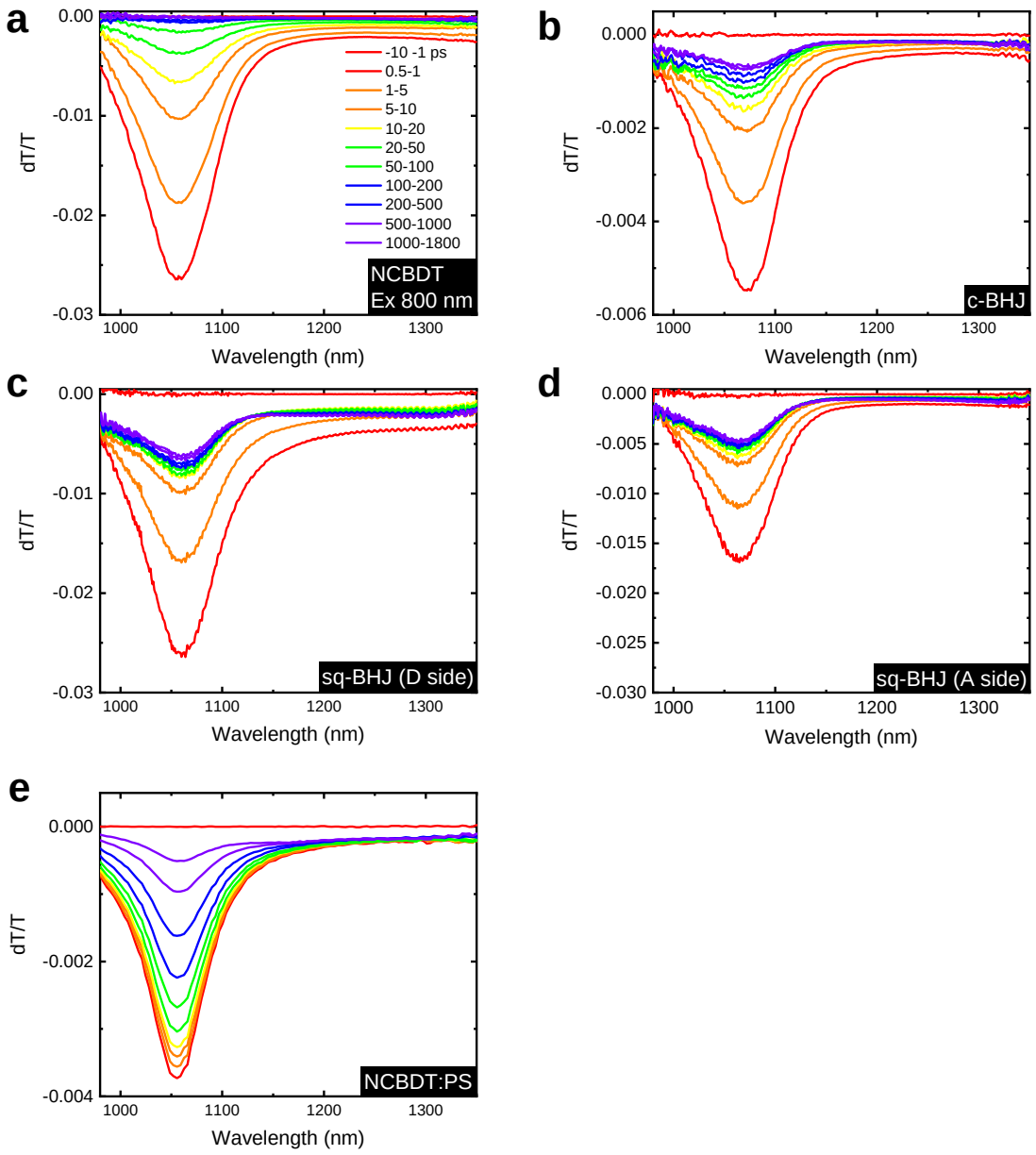

Fig. 7.16 Transient absorption spectra with excitation at 800 nm. (a) pure NCBDT film. (b) c-BHJ film. (c) sq-BHJ film excited with donor side first. (d) sq-BHJ film excited with acceptor side first. (e) NCBDT:PS blend.

7.9 Sequentially Deposited Devices using Different Materials

To further test this sequential deposition method, we also fabricated a series of NFA-based OSC devices using a combination of several donors and acceptors (PBDB-T, PTB7-Th, PDCBT, NCBDT and ITIC). As shown in Table. 7.4 on the facing page, for PBDB-T and PTB7-Th, the device efficiencies using c-BHJ and sq-BHJ architectures are similar, while for PDCBT, sq-BHJ device efficiencies are much lower than c-BHJ ones. This is probably due to DCM used for processing. We note that some other solvents may work better for PDCBT blends. The lower J_{SC} and FF in sq-BHJ devices may indicate an inefficient exciton dissociation and/or severe charge recombination, probably relating to not intermixed morphology and limited exciton diffusion length of organic materials.V_{OC}s of sq-BHJ devices are within 50 meV difference compared with c-BHJ ones. Overall, these device results agree with our previous discussion that the formation of BHJ-like morphology greatly depends on the properties of polymer and the solvent for the NFA layer, and various solvents may be needed to optimise a specific blend.

Table 7.4 Device performance comparison of c-BHJ and sq-BHJ devices based on different donor and acceptor combinations. The solvent for these devices is DCM.

active layer	layout	V_{OC} (V)	J_{SC} ($mA\,cm^{-2}$)	J_{SC} EQE ($mA\,cm^{-2}$)	FF (%)	PCE (%)
PBDB-T: ITIC	c-BHJ	0.898 (0.899±0.002)	14.11 (14.19±0.09)	14.07	56.7 (55.0±1.2)	7.14 (7.00±0.10)
	sq-BHJ	0.835 (0.833±0.004)	14.82 (15.08±0.16)	14.28	47.7 (45.9±0.9)	5.86 (5.77±0.09)
PTB7-Th: NCBDT	c-BHJ	0.781 (0.780±0.001)	17.39 (17.62±0.16)	17.17	65.6 (64.0±1.0)	5.86 (5.77±0.09)
	sq-BHJ	0.759 (0.759±0.002)	17.37 (17.20±0.13)	-	62.8 (62.7±0.3)	8.27 (8.19±0.06)
PTB7-Th: ITIC	c-BHJ	0.805 (0.807±0.001)	14.60 (14.63±0.10)	14.46	60.3 (59.5±0.6)	7.09 (7.03±0.04)
	sq-BHJ	0.794 (0.792±0.004)	14.88 (14.70±0.14)	14.64	60.3 (59.5±0.6)	7.13 (6.97±0.15)
PDCBT: NCBDT	c-BHJ	0.872 (0.870±0.002)	12.91 (12.93±0.09)	12.46	61.3 (60.2±2.2)	6.91 (6.77±0.30)
	sq-BHJ	0.873 (0.870±0.002)	8.39 (8.02±0.30)	-	44.7 (44.9±0.2)	3.28 (3.14±0.14)
PDCBT: ITIC	c-BHJ	0.927 (0.923±0.004)	14.15 (14.05±0.19)	14.08	64.9 (64.2±0.6)	8.51 (8.33±0.22)
	sq-BHJ	0.905 (0.902±0.004)	5.99 (5.59±0.33)	-	43.9 (42.4±1.7)	2.38 (2.15±0.21)

7.10 Exciton Diffusion Length of PBDB-T

As a benchmark polymer, the exciton diffusion length of PBDB-T is still yet to be determined. We fabricated PBDB-T:C_{60} PHJ with various donor layer thicknesses (∼8 nm to 60 nm, measured by spectroscopic ellipsometry). The thickness of the C_{60} layer is fixed at 60 nm to have the constructive interference at ∼500 nm for the optimum device efficiency.[308] As shown in Fig.7.17c, the donor thickness of ∼20 nm gave the highest efficiency. According to the simple relationship[309],

$$x_{\max} = \frac{L \ln \alpha L}{\alpha L - 1} \tag{7.1}$$

where $x_{\max}$ is the distance from the electrodes (excluding PEDOT:PSS layer), L is the exciton diffusion length, α is the absorption coefficient. The absorption coefficient of PBDB-T was determined to be 2.3×10^5 cm^{-1}. According to Fig. 7.17 on the next page the exciton diffusion length is 10±3 nm.

We note that some interdiffusion might happen at the interface, but is not a big issue in this section. First, characterisation of the nanometer length scale interdiffusion of two organic molecules is not easy, although some advanced techniques, such as cross-sectional TEM may work. Secondly, the existence of interdiffusion might result in an overestimation of the value of exciton diffusion length. Finally, the resultant fitting value is around 10 nm for PBDB-T, a quite common value for organic polymers, which supports that our bilayer model is close to the real situation.

The EQE only decreased by one third at thick donor layer of ∼60 nm, while for PPV, although the exciton diffusion length is similar, the EQE peak amplitude dropped by >50%. From previous transient measurements, we observed very short-lived excitons (∼9 ps at 1/e of maximal amplitude). According to Einstein diffusion equation, $L = \sqrt{D_{exc} \times \tau_{exc}}$, D_{exc} is ∼0.11 cm^2 s^{-1}. This diffusion coefficient is very high in disordered organic semiconductors.

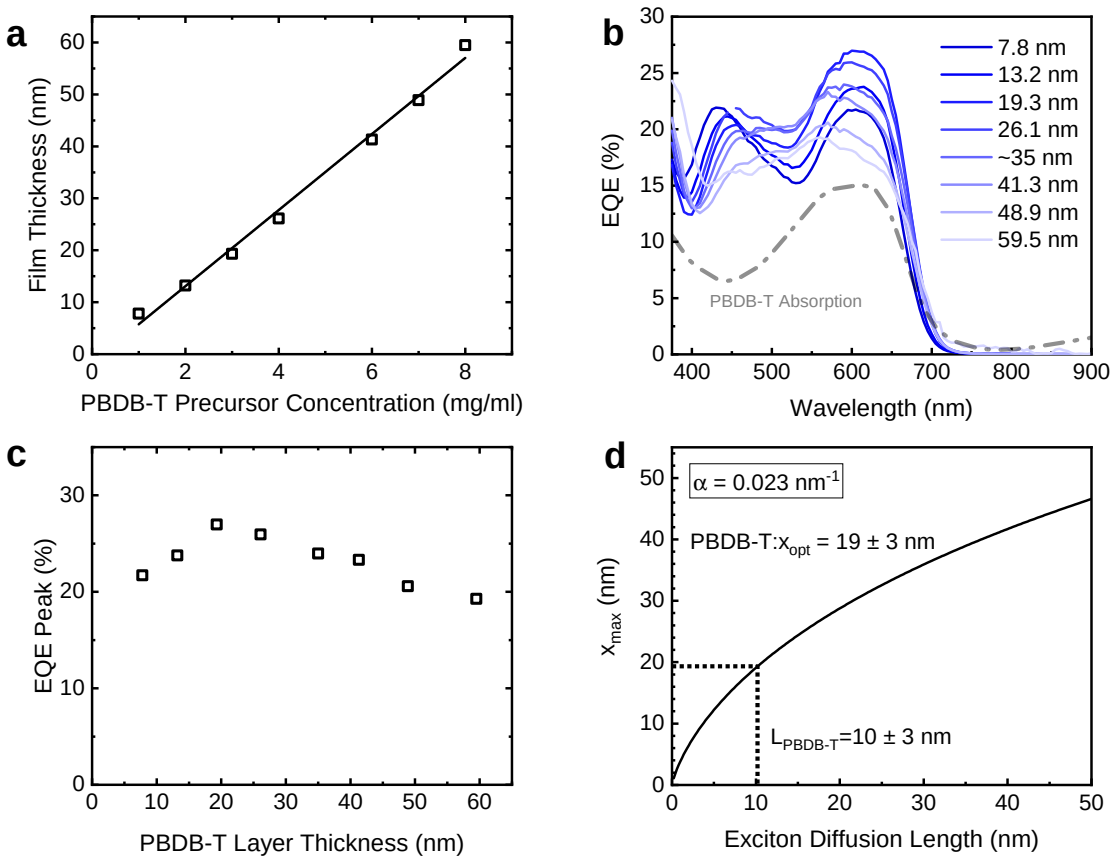

Fig. 7.17 Measurements on exciton diffusion length of PBDB-T. (a) Film thickness of PBDB-T layer deposited from various precursor concentrations (1 mg mL^{-1} to 8 mg mL^{-1}). (b) EQE spectra of PBDB-T:PCBM PHJ devices. Gray line is the absorption spectrum of PBDB-T. (c) Peak EQE as a function of thicknesses of the PBDB-T layer. (d) Exciton diffusion length (10±3 nm) determined from the optimum donor layer thickness (19±3 nm). The absorption coefficient of PBDB-T film is 2.3×10^5 cm^{-1}

7.11 Outlook and Conclusion

BHJ morphological optimisation has been relatively well studied and optimised in the past twenty years, while there are still limited efforts on understanding the sq-BHJ devices. Here we show that sq-BHJ layout carries high potential and can demonstrate performance comparable to as-cast co-depositing BHJ without any post treatments or solvent additives. At the same time, this structure may process several technology relevant advantages compared with one-step BHJ formation for future exploration, such as i) straightforward device fabrication and optimisation; ii) control of interfacial disorder for eliminating trap states; iii) engineering of distortion of EQE spectra for higher photocurrent; iv) device with higher morphological stability. We believe that future work will make it possible to combine the high-PCE achievement of this study with one or several outlined potential advantages and make sq-BHJ suitable for practical applications.

Chapter 8

Photophysical Studies of Sequentially Deposited Nonfullerene Organic Solar Cells

B. Kan and X. Wan synthesised the non-fullerene acceptor. A. Pearson performed TPV and TPC measurements. V. Lami performed the depth-profile UPS. C. Cho simulated the exciton dissociation efficiency. A. Sadhanala performed PDS measurements. F. Kosasih. and G. Divitini performed STEM characterisation and analysis. M. Futscher performed the electrochemical measurement. J. Zhang and Q. Gu fabricated the inverted devices. R. Friend, A. Bakulin, Y. Chen., C. Ducati, N. Greenham, D. Credgington, B. Ehrler and Y. Vaynzof supervised the project. J. Zhang wrote the manuscript with contribution from all co-authors.

8.1 Introduction

Organic solar cells (OSCs), made from solution-processable carbon-based materials, have the potential to be flexible, light-weight and low-cost.[6] Using fullerene and its derivatives as benchmark electron-accepting materials, tremendous efforts in developing electron-donating polymers and small molecules, particularly low-bandgap materials, have taken the device power conversion efficiency (PCE) over 10%.[262, 267, 70, 310, 69, 268, 112, 67] The drawback of fullerene, such as being expensive, unstable and not absorptive in the near-IR region has largely been overcome by the fast development of small-molecule acceptors, so-called non-fullerene acceptors (NFAs).[77, 284, 311, 82, 84, 312, 286, 73, 75, 269, 54, 1, 313, 91, 295] These molecules exhibit tuneable absorption and energy levels, and contribute to efficient photocurrent generation even at negligible driving force.[78, 39, 169]. As such, PCEs of binary and tandem devices have reached over 16% and 17.3%, respectively.[8, 80]

The efficiency of the planar heterojunction (PHJ) devices, when donor and acceptor layers are placed on top of each other, is mainly limited by the so-called "exciton bottleneck", the competition requirement for efficient optical absorption and limited exciton diffusion.[49] A major breakthrough was the invention of bulk-heterojunction (BHJ) – an inter-penetrating donor and acceptor network.[51, 52] This structure can be easily obtained by spin-coating the blended donor and acceptor solutions, but the morphology is very sensitive to the materials and processing conditions, such as the blend ratio, solvent and solvent additives as well as the thermal and solvent annealing processes.[314] An intermediate active layer nanomorphology between PHJ and BHJ is termed the graded bulk heterojunction (GBHJ).[315] The gradient morphology contributes to increased exciton dissociation efficiency relative to the PHJ and an enhanced charge collection efficiency compared to a uniformly mixed BHJ.[315, 316] The morphology of the GBHJ can be controlled in vacuum deposited binary films where the ratio of donor/acceptor deposition rate is ramped linearly, or a stack of thin layers with varied donor-acceptor concentration ratios.[316] Experimental methods to prepare the GBHJ via solution processing are less straightforward, and can involve manipulating the surface energy of substrates, substrate temperature, solvent fluxing, and graded nanoparticle layers.[273, 317–319]

A method to prepare GBHJ originating from fullerene-based cells, called sequential deposition (sq-BHJ), or layer-by-layer approach attracted much attention last year in developing high-efficiency NFA OSCs.[270, 278, 277, 283, 274, 320–322] To better control the phase separation, Hou et al. used a mixed solvent for a new polymer (PBDB-TFS1) in combination with a high-performance NFA (IT4F) where the interdiffusion was controlled by the amount of a second solvent (THF and o-DCB). This exercise led to an efficiency at 13% for sq-BHJ devices, higher than 11.8% obtained by one-step processing.[323] Huang et al. and Min et al

successfully applied this method to fabricate large-area (1 cm) devices with a performance of over 10% and improved device stability.[324, 325] Yang et al. fabricated ternary blends in which a BHJ was mixed with a new donor or acceptor layer.[326] In the same period, our group found that sequentially depositing the donor and acceptor layers led to a high efficiency (>10%), comparable to the as-cast one-step formation of BHJ (c-BHJ) using novel NFAs.[261] Such advancements in device efficiency, stability, green-solvent and large-area processing make this sequential deposition method universal and attractive.

So far, most studies on sq-BHJ systems have focused on device performance rather than a detailed mechanistic study of the underlying photophysics. The reasons and mechanism for the comparable performance need to be understood, and obvious questions remain behind sq-BHJ functionality. For example, to realize high (close to unity) charge generation efficiency in sq-BHJ devices, most excitons must be separated at the donor-acceptor (D-A) interface. Characterising this process is a prior to understanding efficient device operation. In this work, we focus on interfacial properties in sq-BHJ together with morphological characterisations to study their relationship with the initial exciton dissociation and device performance. Using a range of spectroscopic techniques, we focus on the interfacial states at the D-A interfaces in blends prepared by sequential deposition as well as as-cast one-step methods, and correlate our observations with the device performance. To directly visualise the vertical stratification, we characterize the D-A vertical distribution using cross-sectional transmission electron microscopy-energy dispersive X-ray spectroscopy (TEM-EDX) and ultraviolet photoemission spectroscopy (UPS) depth profiling. To understand the effect of D-A distribution on exciton dissociation, a "needle" model is proposed to simulate the structure of sq-BHJ compared with a "cubic" structure for c-BHJ.

8.2 Experimental Section

8.2.1 Device Fabrication

For the conventional devices, the same recipe in Chapter 7 was used. For the inverted devices, the device structure was glass/ITO/ZnO/active layer/MoO_3/Ag. The ZnO precursor was prepared from dissolving 1.098 g zinc acetate dehydrate in 10 mL 2-methoxyethanol mixed with 301.8 µL ethanolamine as a stabilizer. The precursor was stirred on a hot plate at 1000 RPM at 60 °C for at least 2 hours. The fully dissolved solution was filtered using 0.2 µm PTFE filters, and then the ZnO layer was spin-coated at 3000 RPM for 60 s before being baked at 80 °C for 10 min and 130 °C for 1 hour in ambient atmosphere, resulting in a ∼30

nm-thick film. The active layer was deposited in the same way as the conventional devices and a 10 nm MoO_3 as well as a 100 nm silver layer was deposited under high vacuum.

8.2.2 Capacitance Measurements

Capacitance measurements were performed at a pressure below 3×10^{-6} mbar in the dark at 300 K with an AC perturbation of 20 mV. For the fitting, the thickness of the active layer thickness was set to (100 $\pm$ 5) nm for the c-BHJ and (90 $\pm$ 5) nm for the sq-BHJ devices.

8.2.3 Transient Photocurrent Spectroscopy

A 465 nm light-emitting diode (LED465E, Thorlabs) was used as the light source for transient experiments, connected to an Agilent 33500B wavefunction generator and a purpose-built low-noise power supply. Solar cell transients were recorded by connecting the device to a Tektronix DPO 3032 oscilloscope.

8.2.4 X-ray Photoelectron Spectroscopy

The structure of samples for XPS measurements was ITO/PEDOT:PSS/active layer, using the same procedures as for device fabrication. Some films were ready for further measurements, while other films were cut into $\sim$3×3mm^2 and immersed in water. The floating pieces were then carefully transferred to silicon wafer substrates with and without flipping. The samples (either glass substrates or silicon wafer) were then transferred to an ultrahigh vacuum (UHV) chamber (ESCALAB 250Xi) for XPS measurements, using an XR6 monochromated Al K Alpha X-ray source ($h\mu = 1486.68$ eV) with a 400 μm spot size and 200 eV pass energy.

8.2.5 Scanning Transmission Electron Microscopy – Electron Energy Loss Spectroscopy

Sample lamella was prepared with a FEI Helios Nanolab focused ion beam/scanning electron microscope (FIB/SEM). STEM imaging and STEM-EELS were conducted in a FEI Tecnai Osiris TEM fitted with a Schottky X-FEG gun and operated at 80 kV acceleration voltage. All imaging was done in STEM-HAADF mode. EELS spectrum images were acquired with a Gatan Enfinium ER 977 spectrometer in Dual EELS mode with a pixel size of 1.25 nm and energy dispersion of 0.25 eV/channel. The spectrometer aperture was 2.5 mm in diameter and the camera length was 34 mm, resulting in convergence and collection semi-angles of

11.0 and 24.5 mrad respectively. EELS data was obtained with Tecnai Imaging and Analysis software and analysed in DigitalMicrograph and HyperSpy.

8.2.6 Depth-Profile Ultraviolet Photoelectron Spectroscopy

After preparation, the samples were stored in N_2 and afterwards transferred into an UHV chamber of a photoelectron spectroscopy system (Thermo Scientific ESCALAB 250Xi) for measurements. The samples were exposed to air only for a short time span of approximately 30 seconds during this transfer. All measurements were performed in the dark. UPS measurements were carried out using a double-differentially pumped He discharge lamp ($h\nu = 21.22$ eV) with a pass energy of 2 eV) and a bias at -5 V. Etching was performed using an Argon cluster (MAGCIS) source with a cluster energy of 4000 eV and a raster size of 2.5×2.5 mm^2. Otherwise, UPS depth profiling was performed the same way described elsewhere.[327]

8.3 Trap States and Charge-Transfer States

8.3.1 Capacitance Spectroscopy

From the device performance in Table.7.1, we observed that the V_{OC} of sq-BHJ devices was $\sim$30 meV smaller than that of the c-BHJ devices. Such loss is correlated with increased non-radiative recombination, observed from their electroluminescence (EL) efficiency, as summarised in Table.7.2. In comparing devices of the same material combination, the most probable explanation for the difference in EL efficiency is the relative population of trap states. Because the donor and acceptor stoichiometry is similar in both blends, we expect that the trap states are interfacial and depends on the processing history.[328]

We characterise these interfacial trap states using capacitance measurements. Fig.8.1 shows the capacitance as a function of voltage, where a close-to plateau curve at low voltages indicates close to full depletion at the short-circuit condition. At low forward bias, we observe a capacitance increase which is correlated to a decrease in depletion-layer width. From above 0.5 V, the change in capacitance can be approximated by the Mott-Schottky relation as

$$C^{-2} = \frac{2}{\varepsilon_0 \varepsilon q N A^2}(V_{bi} - V) \tag{8.1}$$

where ε_0 is the vacuum permittivity, ε the blend permittivity, q the elementary charge, N the doping density, A the device active area, V_{bi} the built-in potential, and V the external bias. From the Mott-Schottky plot we obtained a doping density of $(7.3\pm0.6)\times10^{16}$ cm^{-3} for the

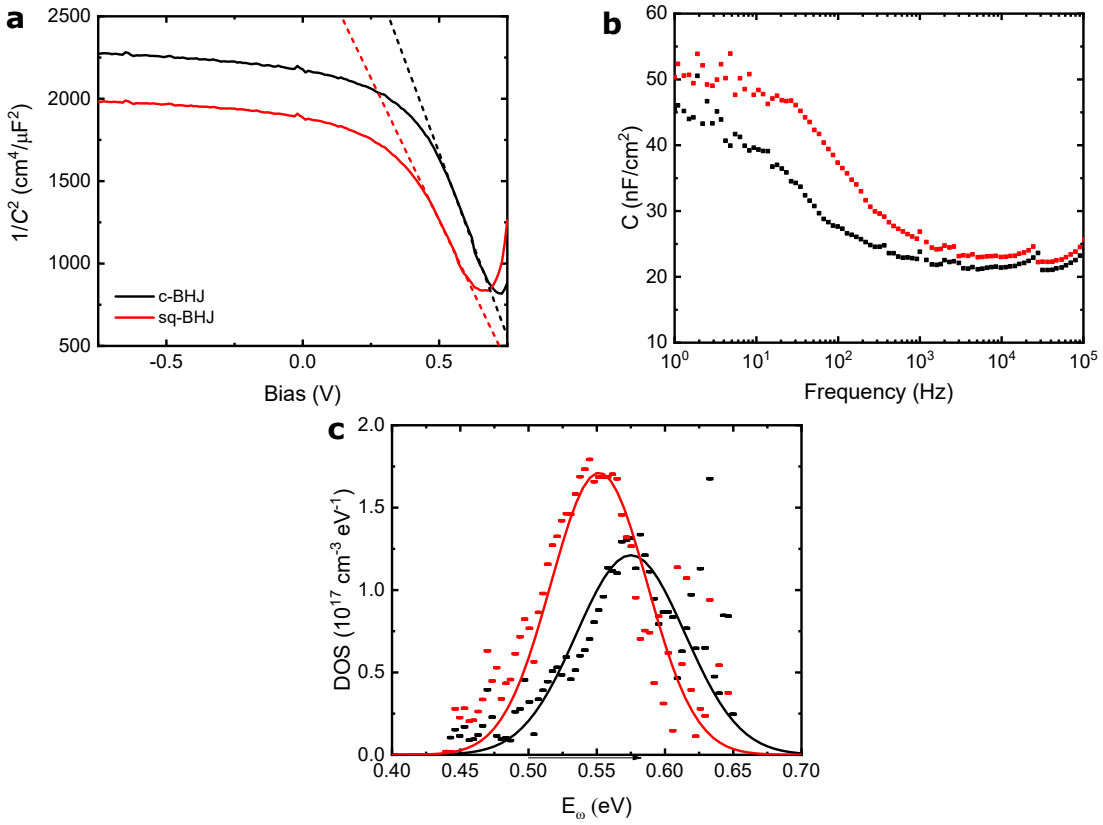

Fig. 8.1 Capacitance measurement to quantify the density of trap states. (a) Mott-Schottky plot measured at 10 kHz. The linear fit reveals the doping density and the built-in potential. (b) Capacitance spectra measured at zero bias. (c) Density of trap states (DOS) calculated using the capacitance spectra shown in (b). The continuous line corresponds to the fit of a Gaussian defect distribution.

sq-BHJ, slightly higher than the value of $(6.2\pm0.5)\times10^{16}$ cm^{-3} for the c-BHJ, and a built-in potential of 0.87±0.22 V and a blend permittivity of 2.4±0.2 V for both the c-BHJ and the sq-BHJ. To quantify the density and energetics of trap states in both devices, we measured the capacitance as a function of frequency at zero bias in the dark (see Fig.8.1(b)). At low frequencies, we observe an increase in capacitance due to charging and discharging of defect states.[329] At high frequencies, the defects cannot follow the applied AC signal. Using these capacitance spectra, the defect distribution can be estimated as

$$N_T(E_\omega) = -\frac{V_{\mathrm{bi}}\omega}{qwk_{\mathrm{B}}T}\frac{dC}{d\omega} \tag{8.2}$$

where E_ω is the demarcation energy of the defects, k_{B} is the Boltzmann constant, w is the depletion width, and ω the modulation frequency.[329] E_ω is calculated as

$$E_\omega = k_{\mathrm{B}}T\ln\frac{\omega_0}{\omega} \tag{8.3}$$

where ω_0 is the attempt-to-escape frequency. Assuming a typical attempt-to-escape frequency of 10^{12} s^{-1}, we find a Gaussian density of trap states centred between 0.5 eV and 0.6 eV of $(1.7\pm0.1)\times10^{17}cm^{-3}$ for the sq-BHJ, around 50% higher than the value of $(1.2\pm0.1)\times10^{17}cm^{-3}$ for the c-BHJ (see Fig.8.1(c)).[330] The density of the trap states is higher than the acceptor density obtained from the Mott-Schottky analysis because the capacitance-voltage characteristics were measured at a frequency (10 kHz) at which the defects cannot follow the applied AC signal. We furthermore find that density of trap states of the c-BHJ (40 meV) is broader than that of the sq-BHJ (35 meV), suggesting less molecular disorder at the interface in the latter case. This molecular disorder is related to the fabrication method and is discussed together with the photothermal deflection spectroscopy (PDS) data below.

We notice that the data is quite noisy, and we measured multiple devices to ensure the reproducibility. Although the detailed value varies, the overall trend of the density distribution is similar and can be fitted in the same way using the Gaussian function. The trap density of c-BHJ from 4 measurements is $(1.1\pm0.1)\times10^{17}cm^{-3}$ and sq-BHJ from 7 measurements is $(1.3\pm0.1)\times10^{17}cm^{-3}$.

8.3.2 Transient Photocurrent Spectroscopy

We also characterize the trap states from transient photocurrent measurements. Fig. 8.2 on the following page (a) shows a larger steady-state current between 200 and 400 µs for the sq-BHJ OSC. The higher photocurrent is due to its higher EQE of the sq-BHJ device at the illumination wavelength (460 nm). The signal decays to a constant value after 200 µs, which reflects an equilibrium between the trapping and detrapping of free carriers. When the light is switched off (400 µs after the initial excitation), the trapping channel is stopped and only the detrapping of free carriers contributes to the decay curve.[331] Following the normalization, the relative amplitude or the area below the decay curve is independent of the carrier density, and thus represents the relative density of trap states. From Fig. 8.2 on the next page (b), we observe a larger area below the decay curve for the sq-BHJ device, which we assign to a higher relative density of trap sites, agreeing with the capacitance measurements.

Trap states have been shown to act as non-radiative recombination centres in Shockley-Reed-Hall type recombination, resulting in a lowering of the quasi-Fermi level of the electrons and a limitation in the V_{OC}.[258, 332] The higher density of trap states in sq-BHJ devices are probably related to its lower EQE_{EL} and slightly lower V_{OC} compared with c-BHJ devices. We note that sequential deposition generally leads to more stable devices.[270, 321] However in our blends, under light illumination, generation of deep trap states may exacerbate the degradation of solar cells. Such trap states might originate from a fast solvent evaporation

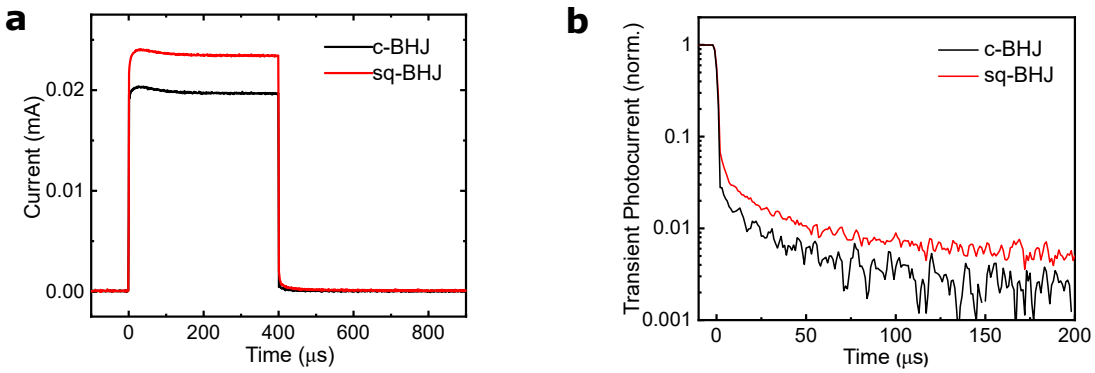

Fig. 8.2 Transient photocurrent spectroscopy to quantify the density of trap states. (a) Decay curves from transient photocurrent spectroscopy with excitation at 460 nm. (b) Normalised photocurrent decay in the log scale with the time zero shifted by around 400 μs relative to (a).

during spin-coating and are probably morphology dependent. Future effort is needed to eliminate these trap states to improve the performance of devices prepared by the sequential deposition method.

8.3.3 Photothermal Deflection Spectroscopy

The process of CT at D-A interfaces is also important in determining the device photophysics. Due to the limited exciton diffusion length of 10-20 nm in organic materials, sufficient interfacial area between donor and acceptor is necessary to separate the photo-generated excitons. CT states at these interfaces can be difficult to characterise, since their optical response is typically much lower than that of the bulk states. To probe the relative quantity of interfacial CT states, we used a scattering-free and highly sensitive PDS technique. For the technical details of PDS, please refer to Section 3.1.2. Fig.8.3 (a) shows the measured absorption of a pristine NCBDT film. Through analysis of the band gap and the band tail absorption, PDS allows the full band gap of the solar cells and the density of mid-gap trap states to be measured.[333, 334]

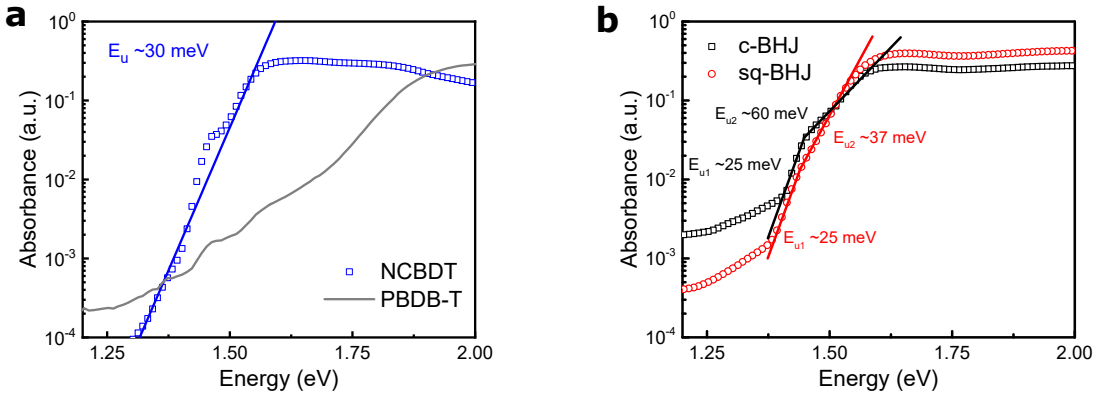

Fig. 8.3 Absorption spectra of (a) pristine NCBDT and PBDB-T films, (b) c-BHJ and sq-BHJ films using photothermal deflection spectroscopy. The straight lines in (b) are the exponential fits used to extract the Urbach energy shown nearby.

The Urbach energy is fitted from the exponential tail of the absorption spectrum,

$$A = A_0 \exp(\frac{h\nu}{E_u}) \tag{8.4}$$

Taking logarithm on both sides, we can obtain

$$\ln(A) = \ln(A_0) + \frac{h\nu}{E_u} \tag{8.5}$$

Therefore, we can fit the slope of the line to get the Urbach energy E_u. The sharp tail in Fig.8.3 (a) gave an Urbach energy around 30 meV for NCBDT, suggesting a high degree of order, and ruling out possibility of associating absorption tail with defects. The blend absorption is shown in Fig. 8.3) (b).

Between 1.37 and 1.54 eV, the signal can be fitted with two exponential or one exponential components. (1) Two exponential components. This corresponds to the Urbach energies of around 25 meV and 37-60 meVThe fused ring core in NCBDT facilitates dense π-π stacking and probably gives very ordered regions as characterised by a small Urbach energy. The packing near the interface is likely less ordered and thus gives a second component of a larger Urbach energy. The latter Urbach energy in the sq-BHJ film is $\sim$37 meV, smaller than $\sim$60 meV in the c-BHJ film. This comparison suggests more ordered molecular packing close to the acceptor band gap in sq-BHJ compared to c-BHJ, possibly benefiting from the sequential deposition process. This agrees with the Gaussian-fitted width as shown in Fig.8.1 (c). (2) One exponential component. Normally we fit the tail using one exponential component. The kink at around 1.4 eV might come from the instrument error. We further confirm this by taking the spectrum of the halogen bulb as shown in Fig.8.4. Thus, the kink is caused by the large variation of the spectral intensity, and can be mitigated by using another light source. In summary, from the PDS measurements, one information we can obtain is that the interface is quite ordered mainly due to the easily aggregated NFAs.

The absorption amplitude of the sub-bandgap region (1.2 – 1.4 eV) is larger than that from the pure acceptor film, suggesting that the signal is not purely from the bulk and/or trap states in donor or acceptor materials. We notice that the signal in this region in the blends seems to resemble the signal of PBDB-T, but the PBDB-T composition variation is much smaller than the signal contrast in the blend. Instead, we assign the signal to the interfacial CT states. The absorption of CT states is usually seen as a Gaussian peak in blends with a large energetic offset. In the studied blend, the HOMO offset is so small (<30 meV) that the Gaussian peak from CT states may overlap with the singlet states from the acceptor. One possible explanation comes from hybridization of local exciton and CT states[166], but direct evidence is still missing. Vandewal et al. have related the amplitude of the sub-bandgap absorption in BHJ blends to the D-A interfacial area in large-offset fullerene-based blends.[193] In our case, the smaller amplitude in the sq-BHJ film possibly originates from less D-A interface than the more mixed c-BHJ film. As we note that highly efficient exciton dissociation still occurs at the donor-acceptor interface, the morphological requirement for efficient sq-BHJ devices might be different.

8.3.4 Pump-Push Photocurrent Spectroscopy

To study these interfacial CT states further, we probed their geminate recombination (GR) in both operational devices using ultrafast spectroscopy. Pump-push photocurrent (PPP) spectroscopy is a device-based ultrafast technique.[30, 184, 324] It is sensitive to GR of CT states through pushing such states away from the interface and sensing the resultant photocurrent increase. Fig.8.4 shows that in both devices the push-induced effect (dJ/J) is tiny (on the order of magnitude of 10^{-4}), suggesting that GR is not a limiting loss channel in either device.[174] This is in agreement with the high charge generation efficiency in our studied blend, and the unity quantum efficiency in other NFA blend with minimum GR[290]. The amplitude is smaller in the sq-BHJ device than that in the c-BHJ device, suggesting that GR is less substantial in former devices. Because GR occurs at the interface, these observations might be explained by the less interfacial area, and hence lower number of CT states in the sq-BHJ devices, as suggested by our PDS results. We also note that any shallow or deep trap states should not influence the amplitude and kinetics of GR at such early (sub-nanosecond) time scales.

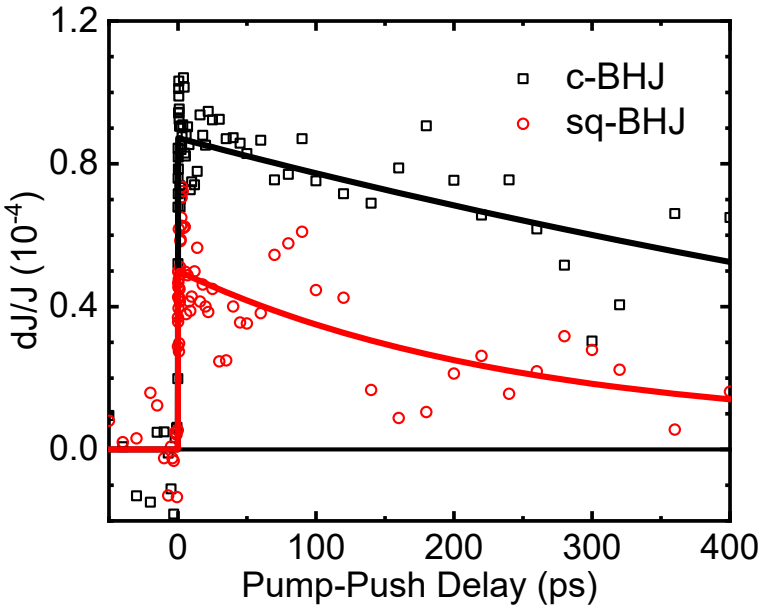

Fig. 8.4 Geminate recombination probed with pump-push photocurrent spectroscopy with excitation at 575 nm.

8.3.5 Discussion

The presence of fewer interfacial CT states in the sq-BHJ devices relates to the reduced phase separation that has been suggested to increase the performance of BHJ OSCs as long as the exciton dissociation remains efficient.[335] Elsewhere, in sequentially deposited PTB7-Th:$PC_{61}BM$ blends less interfacial area for carrier recombination has been correlated with higher V_{OC} values.[270] The recent high-efficiency sqBHJ devices exhibited a higher (around 30 meV) V_{OC} accompaying the higher PCE.[323] This confirms that achieving higher V_{OC} in sq-BHJ is reachable with the reduction in interfacial area.

8.4 Imaging Vertical Heterogeneity

The vertical stratification of binary composition greatly influences charge recombination and transport and is of great relevance to device performance.[281] The view on the resultant vertical phase separation in sq-BHJ films, whether homogeneous or inhomogeneous, is actually not convergent[270, 280, 336, 279], largely depending on the characterisation methods. Using cross-sectional EDX and depth-profile UPS, we directly visualise the vertical phase separation of donor and acceptor and our result is important for studying the morphology in sq-BHJ devices.

8.4.1 X-Ray Photoemission Spectroscopy

From the measurement of interfacial area and previous neutron scattering modelling, the morphology of the sq-BHJ is more akin to a homogeneous BHJ than a two-layer PHJ. The detailed morphology distribution of sq-BHJ probably lies between BHJ and PHJ, but its 3D morphology at nm length scale is difficult to determine from experiments. Initial evidence for D:A intermixing throughout the sq-BHJ blend was obtained from XPS measurements. As NCBDT contains N and F atoms and PBDB-T does not, these elements are used as chemical markers for the presence of the acceptor. Fig.8.5 (b) presents binding energy spectra for c-BHJ and sq-BHJ films, which give insight into the elements within the top few nm of each film surface. The spectrum for the sq-BHJ sample contains more intense F 1s and N 1s features but less O 1s than the spectrum for the c-BHJ sample (See Table. 8.1 on the next page for atom% values), indicating surface enrichment of the acceptor in the top part. We also measured the bottom surface which interfaces with PEDOT:PSS to confirm the presence of NCBDT in this region. We prepared the film similarly but flipped the active layer using the water soluble PEDOT:PSS before attaching to the Si/SiO_x substrates as shown in Fig.8.5 (a). Fig.8.5 (c) shows similar spectra of N, F and O peaks, supporting its homogeneous

distribution. In Fig.8.5 (d), even though the N 1s and F 1s intensities are similar to those in the top part, the O 1s intensity is clearly showing that the bottom part has a higher concentration of donor materials than the top.

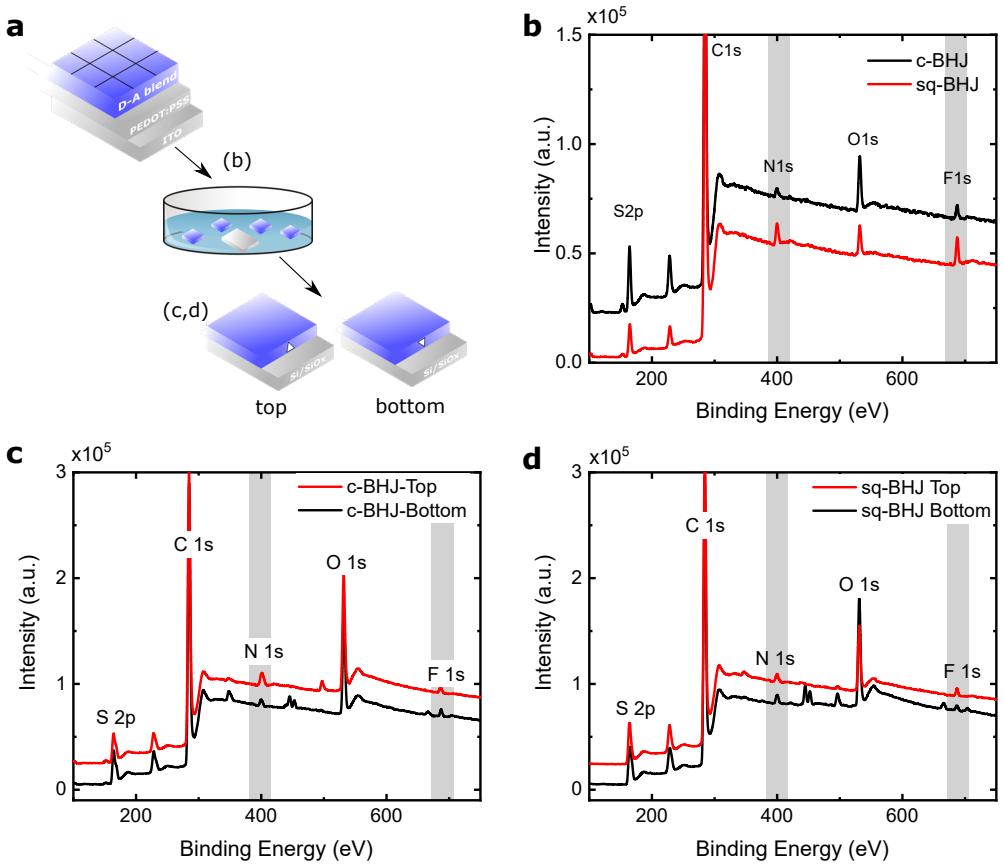

Fig. 8.5 XPS measurements on sq-BHJ and c-BHJ films. (a) Preparation of samples with and without the active layer flipped. After cutting the film into smaller pieces, the substrate is immersed in the water where PEDOT:PSS layer is dissolved. (b) XPS directly on ITO/active layer. (c-d) XPS on Si/SiOx/active layer of c-BHJ and sq-BHJ films with the sample prepared in (a).

Table 8.1 The atomic concentration (at) of atoms in the top surface of c-BHJ and sq-BHJ devices measured by XPS. The device structure is ITO/PEDOT:PSS/active layer.

Name	Position eV	c-BHJ atomic concentration (%)	sq-BHJ atomic concentration (%)
O 1s	532.22	4.12	2.12
C 1s	285.22	86.74	90
N 1s	399.22	0.73	2.56
F 1s	687.22	0.53	1.22
S 2p	165.22	7.88	4.10

8.4.2 Cross-Sectional Electron/X-ray Microscope

To confirm our XPS results, we prepared cross-sectional lamellae (∼70 nm) of full devices using a focused ion beam miller for transmission electron microscopy (TEM) characterization. Unfortunately, we were not able to observe noticeable differences in D:A distribution from bright-field as well as high resolution TEM imaging (Fig.8.6). We then switched our TEM to scanning mode and used energy dispersive X-ray spectroscopy (STEM-EDX) to map the elemental distribution in the c-BHJ and sq-BHJ blends. For the EDX measurement, the device configuration is ITO/PEDOT:PSS/active layer/Ca (10 nm)/Al, where PDINO with nitrogen inside was replaced with the 10-nm Ca layer.

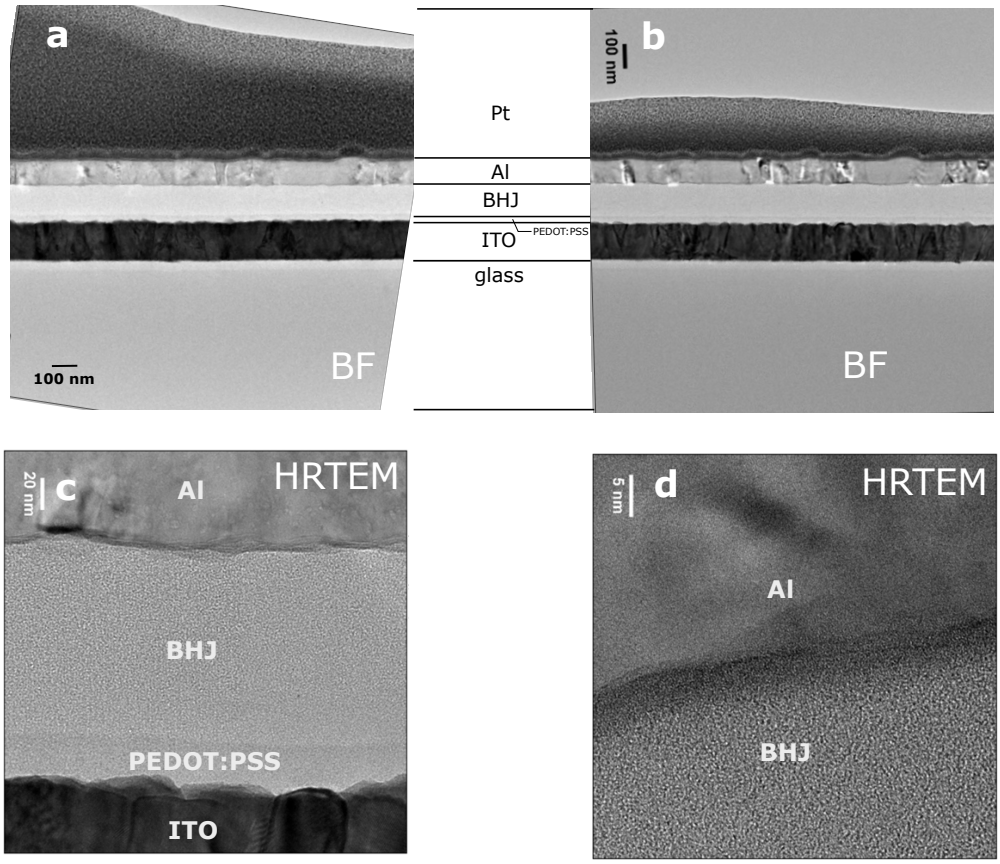

Fig. 8.6 In-focus bright-field TEM of (a) c-BHJ and (b) sq-BHJ cross-sectional images. High-resolution TEM of (c) c-BHJ and (d) sq-BHJ cross-sectional images. The scale bar is shown in each image. We cannot distinguish donor and acceptor phases from these measurements.

After acquiring EDX spectrum images of c-BHJ and sq-BHJ layers, we performed principal component analysis (PCA) in HyperSpy to denoise the dataset from which we finally produced semi-quantitative elemental maps.[337] While EDX is generally not capable of measuring concentrations of light elements to a very high accuracy, the elemental distribution

trends shown in the maps are clear.[338] Considering the 2D map showing the elemental distributions of F and N in Fig.8.7 (a-b), we averaged the signal vertically, and obtained a 1D line in Figure Fig.8.7 (c-d). We note that the small peak in N and F concentration around x = 40 nm, supposedly for Ca layer, is possibly due to an intense signal for O-K_α at 525 eV which also spreads into N-K_α (392 eV) and F-K_α (677 eV) after decomposition. The strong rise of nitrogen signal after 150 nm might be caused by some impurities in the ITO layer. We determined the active layer region as highlighted in grey. The thicknesses of c-BHJ and sq-BHJ active layer agrees with previous thickness measurements using atomic-force microscope. For the c-BHJ layer, the F distribution is not uniform, but rather shows a gradual increase in the bottom half of the active layer within 10% variation and the N distribution changes following a similar pattern. This variation is probably caused by two acceptor clusters seen in Fig.8.7 (a), and the concentration at both ends is quite similar, in agreement with the XPS results. We thus concluded that c-BHJ film is fairly homogenous. In contrast, in sq-BHJ films shown in Fig.8.7 (b), both N and F distribution shows a gradual decrease in concentration ($\sim$ 15% for N and $\sim$ 30% for F) from the top surface of the active layer up to about half of the layer's thickness. These results support the conclusion that the top half of the film exhibits a gradual change in the D-A composition, while the bottom half of the film has a homogenous D and A distribution.

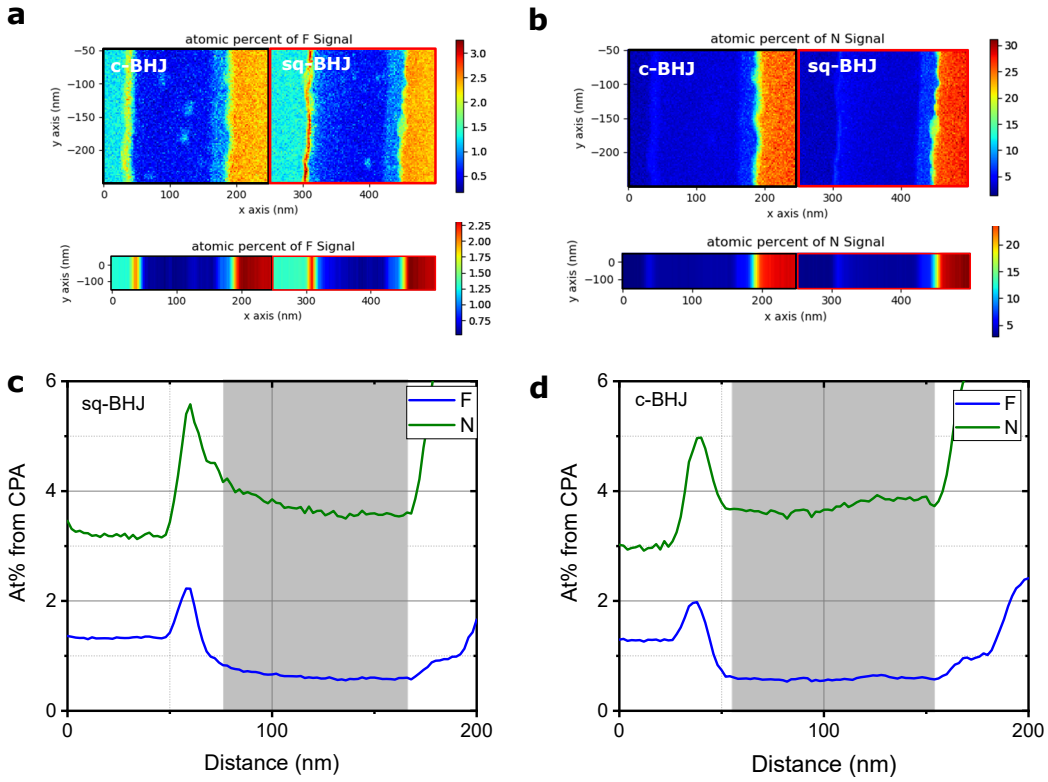

Fig. 8.7 EDX-STEM measurements on sliced lamella. (a-b) Maps of N and F concentrations as measured with STEM-EDX. (c-d) The N and F concentration plotted from the Al layer (x = 0 nm) up to ITO (x = 200 nm). This information is averaged from vertical slices; the grey area is determined to be the active layer.

8.4.3 Depth-Profile Ultraviolet Photoemission Spectroscopy

The vertical stratification of binary composition greatly influences charge recombination and transport and is of great relevance to device performance.[281] We note that the view on the resultant vertical phase separation in sq-BHJ films, whether homogeneous or inhomogeneous, is actually not convergent[270, 280, 279, 336], largely depending on the characterisation methods.

To visualise the vertical distribution further, we employed a newly developed technique: UPS depth profiling.[327] UPS measures the kinetic energy spectrum of emitted photoelectrons after absorbing ultraviolet photons, and thus determines the occupied molecular orbital energies, and the density of states (DOS) in the valence band region. Depth profiling uses Argon (Ar) ion cluster sputtering which does not induce damage to the electronic and chemical structures of the organic materials.[339] The combination of Ar cluster etching with the highly surface-sensitive UPS offers a superior vertical resolution of 1-2 nm, surpassing the capabilities of traditional XPS depth profiling (normally 5-10 nm).

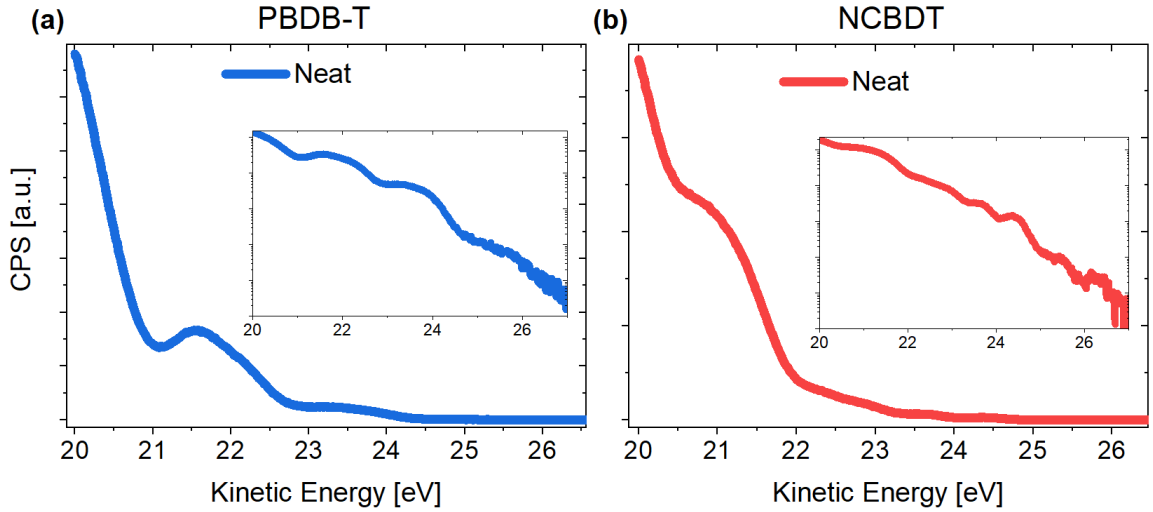

Fig. 8.8 UPS spectra of neat PBDB-T and NCBDT films. The inset is the logarithm representation of the data.

We first probe the spectra of pure PBDB-T and NCBDT films (Fig.8.8), which show different distribution of filled states and will be later be used for fitting. The results of UPS depth profiling for both c-BHJ and sq-BHJ are shown in Fig.8.9.

On the one hand, the change of the DOS over the entire c-BHJ active layer is not significant, except for a small variation at the very surface, probably induced by surface contamination and by a slightly shifted energetics. On the other hand, the DOS of the sq-BHJ sample shows a continuous change in the top half of the film. Four representative depths are

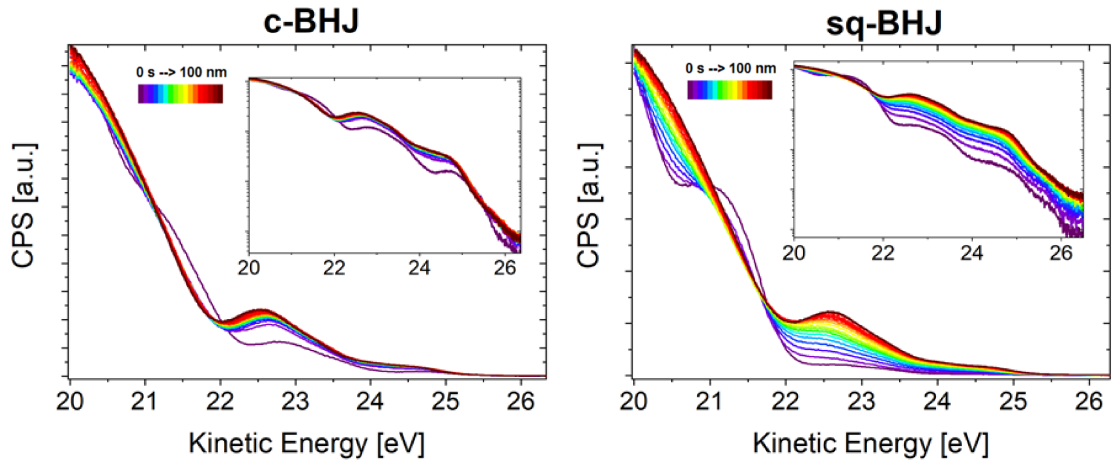

Fig. 8.9 UPS spectra of c-BHJ and sq-BHJ at all etching depths. The inset is the logarithm representation of the data.

also shown in Fig.8.10, showing that the difference between spectral slices from the c-BHJ and the sq-BHJ vanishes with the increasing etch depth.

Since we are primarily interested in these differences between the c-BHJ and sq-BHJ films, we calculated their UPS signal difference for each measured depth as shown in Fig.8.9(a). The spectral shape of this difference spectrum (c-BHJ minus sq-BHJ) remains almost the same for each depth, except for the very first spectrum showing small variations at a kinetic energy of ~ 22 eV due to surface effects. As the spectral shape stays the same, the magnitude of the spectrum (taken as the integral of the signal) is a measure for the difference in the amount of A (or D) in the c-BHJ and in the sq-BHJ. To explain how we obtain Fig.8.9(b) from Fig.8.9(a), we introduce some formulae here. In both the c-BHJ and sq-BHJ blends, only two components exist – donor and acceptor. If we assume the proportion of A at a given depth is x, then the proportion of D at that depth is $(100-x)$. We define x to represent the proportion of A in c-BHJ and y to represent that in sq-BHJ, the UPS spectra can be expressed as:

$$\mathrm{UPS}_{\text{c-BHJ}}(E) = x \times \mathrm{UPS}_{\mathrm{A}}(E_1) + (100-x) \times UPS_{\mathrm{D}}(E_2) \tag{8.6}$$

$$\mathrm{UPS}_{\text{sq-BHJ}}(E) = y \times \mathrm{UPS}_{\mathrm{A}}(E_1) + (100-y) \times UPS_{\mathrm{D}}(E_2) \tag{8.7}$$

where $\mathrm{UPS}_{\mathrm{A}}$ and $\mathrm{UPS}_{\mathrm{D}}$ are UPS spectra for A and D (obtained from Fig.8.8), respectively. The E_1 and E_2 are defined due to the energy shift in UPS spectra. The difference spectrum at

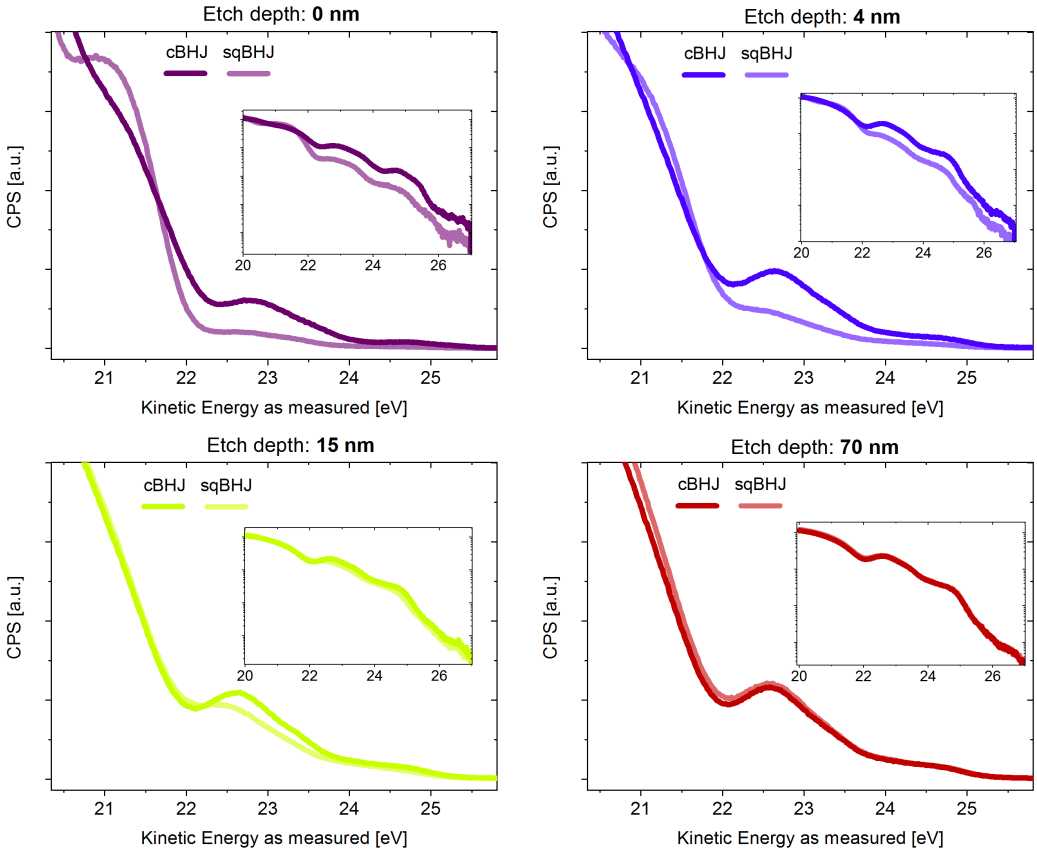

Fig. 8.10 UPS spectra of c-BHJ and sq-BHJ at four depths of 0 nm, 4 nm, 15 nm and 70 nm. The insets are the logarithm representation of the data.

energy E is:

$$\mathrm{UPS_{c\text{-}BHJ}}(E) - \mathrm{UPS_{sq\text{-}BHJ}}(E) = (\mathrm{UPS_A}(E_1) - UPS_{\mathrm{D}}(E_2)) \times (x-y) \tag{8.8}$$

It is clear from Fig.8.11(a) that the spectral shape of the difference spectrum $\mathrm{UPS_A}(E_1)$-$\mathrm{UPS_D}(E_2)$ is constant at all depths. Therefore, the difference spectrum is proportional to the proportion difference $(x-y)$. We thus use the difference spectra as a measure for the excess acceptor material in sq-BHJ.

We thus can determine the relative excess of A in the sq-BHJ versus the c-BHJ. However, the absolute values still need a calibration. To quantify this excess, we fitted the very top surface of both c-BHJ and sq-BHJ using the spectra obtained from pure PBDB-T and NCBDT films (Fig.8.8) with the fits shown in Fig.8.12. We can obtain the A percentage to be 44.4% and 77.6% in the c-BHJ and sq-BHJ, respectively. Thus, the excess acceptor percentage is

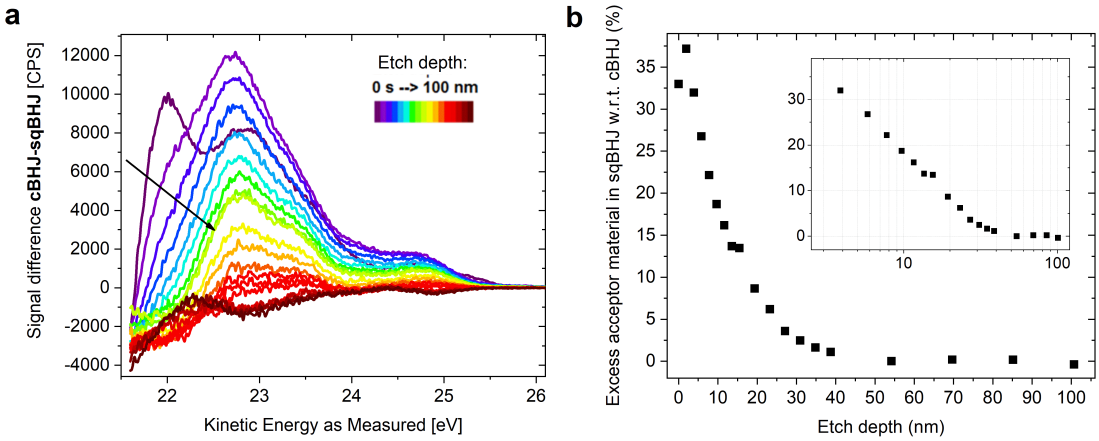

Fig. 8.11 Depth-profile UPS measurements on c-BHJ and sq-BHJ films. (a) The kinetics energy spectra at different etching depth, measured using depth-profile UPS. The resolution is 1-2 nm. (b) The excess acceptor material in sq-BHJ compared to c-BHJ with a function of the etching depth. The data is fitted assuming that a uniform mixing is at a ratio of 5:4.

∼33%, being thus the first value in Fig.8.11(b). As the final spectral shape of c-BHJ and sq-BHJ is almost the same (bottom right graph in Fig.8.10, the proportion of D:A ratio for sq-BHJ is also 5:4 (44.4% acceptor) in the bottom. This is summarized in Fig.8.11(b), confirming that the upper half (top ∼40 nm) of the sq-BHJ film exhibits a gradually decreasing amount of excess acceptor material, while the bottom half is compositionally equivalent to the c-BHJ. This vertical trend is in excellent agreement with the results of the EDX measurements.

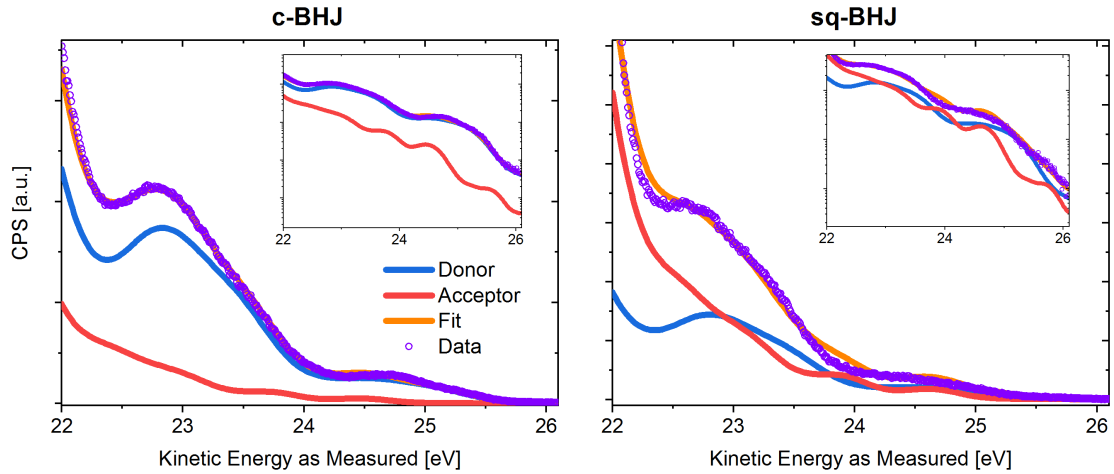

Fig. 8.12 The fitting of the first spectra in c-BHJ and sq-BHJ with the spectra from pristine PBDB-T (blue) and NCBDT (red) films. The measured data is represented with purple circles, while the fitting line is orange.

8.5 Inverted Device

8.5.1 Device Fabrication and Characterisation

Using the sequential deposition method, acceptor material is enriched on the top layer. This structure is beneficial for the charge transport in the regular device architecture, but not good for the inverted devices. To show this effect, we fabricated inverted devices using c-BHJ and sq-BHJ active layers. Their photovoltaic performance is summarised in Table.8.2. We find that sq-BHJ is more sensitive to the device structure, as the device average PCE dropped by 20% in contrast to 4% for the c-BHJ layer. To take advantage of the field distribution, the larger bandgap material in D:A blends is preferred to be positioned near the metal electrode to increase light absorption. We note that recent sq-BHJ blends are disadvantageous in such aspect, and we believe such strategy may further improve the device performance of sq-BHJ devices.

Table 8.2 Photovoltaic performance of regular and inverted PBDB-T:NCBDT devices prepared with one-step formation of BHJ and sequential deposition without post-annealing or solvent additives.

Device structure	Active layer layout	V_{OC} (V)	J_{SC} (mA cm^{-2})	FF (%)	PCE (%)
Regular	c-BHJ[a]	0.847 (0.842±0.003)	18.64 (18.32±0.20)	64.6 (63.5±0.5)	10.19 (10.15±0.12)
	sq-BHJ[a]	0.824 (0.820±0.003)	19.45 (19.14±0.15)	62.9 (61.8±0.6)	10.04 (9.70±0.24)
Inverted	c-BHJ	0.855 (0.847±0.006)	20.13 (18.56±0.88)	61.65 (61.21±1.78)	10.62 (9.63±0.54)
	sq-BHJ	0.839 (0.814±0.010)	18.39 (17.24±1.22)	61.50 (54.56±2.59)	9.49 (7.67±0.84)

a. data from reference [261]

8.5.2 Transfer Matrix Simulation

To establish the design rule, we calculated the internal electric field $|(E-field)|^2$ profiles formed inside the device using transfer-matrix formalism with the refractive indices from a literature. A general insight can be obtained from the homogeneous structure consisting of an arbitrary thick dielectric ($n = 1.8$, n is the refractive index) and metal reflector as shown in Fig.8.13 (a). Under the illumination with a normal incident angle, the local maxima of $|(E-field)|^2$ are generated by the constructive interference between the incident light and reflected light, hence the first local maxima appear near the distance of wavelength $\lambda/4n$

from the reflector, with a slight shift (∼25 nm) towards the metal side due to the imperfect reflectivity of Ag. Those local maxima are rarely changed by inserting more layers such as ITO, ZnO, and MoO_3 in the practical devices as shown in Fig.8.13 (b), despite the additional interference modes shown. Therefore, to achieve the efficient light absorption and higher photocurrent, the active layer should be positioned near such regions having strong E-field intensity. For c-BHJ devices, donor and acceptor materials are uniformly mixed over the thick region and the optical design has the limited degree of freedom. On the other hand, in PHJ devices, donor and acceptor can be selectively positioned according to their optical properties and the overall absorption has a further room for enhancement. For example, in our system, PBDB-T (donor) with a large bandgap (i.e. absorbing wavelength < 650 nm) and NCBDT (acceptor) with a smaller bandgap (i.e. absorbing wavelength > 650 nm) may prefer to be positioned near the metal side and ITO side, respectively (i.e. inverted structure). Sq-BHJ structure can be considered as a good compromise achieving both efficient exciton dissociation of c-BHJ and optical benefit of PHJ with a dedicate design. Further optimisation of the sq-BHJ device maximising the selective absorption of each layer remains as a future work.

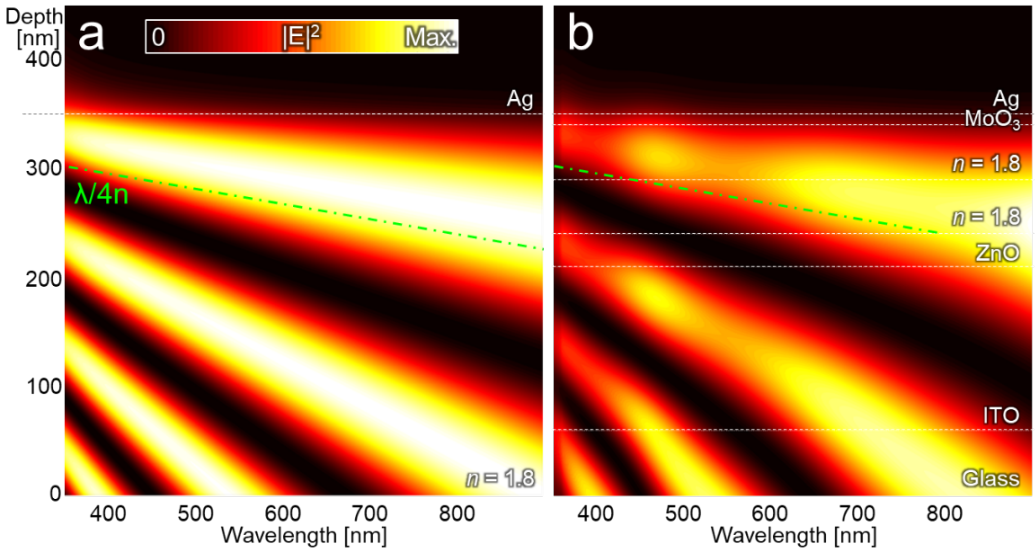

Fig. 8.13 Calculated internal $|E - field|^2$ profiles along the depth for (a) a homogeneous dielectric (n = 1.8) with a back metal reflector and (b) full PV structure. Green lines indicate the theoretically expected local maxima with a distance of $\lambda/4n$ from the reflector.

8.6 Simulating the Exciton Dissociation Efficiency

For the exciton dissociation step, here we propose a simple model for sq-BHJ structure assuming that acceptor phase columns with ignorable volume like a "needle" are grown in the planar donor layer. Inset in Fig.8.14 (a) shows its schematic where the distance for an exciton to meet the interface (D_{min}) is the minimum horizontal distance to the column or the vertical distance to the planar interface. From the calculated probability distribution, the most probable D_{min} increases with the distance between the columns (L). In the extreme case when L is infinite, this structure turns into a PHJ. As excitons in the PHJ can only dissociate through the D-A interface, the population function is uniform over D_{min} = 0-T (T = 50 nm), while excitons in the sq-BHJ can be more easily dissociated through the columns. Fig.8.14 (b) shows the "cubic" model for the c-BHJ structure, where excitons are generated in small cubes with a size of L, having a large area of interfaces per volume. The D_{min} here is defined as the minimal distance to the surrounding surfaces of another material. Considering the realistic exciton diffusion length of organic materials, we assume that excitons within $D_{\text{min}} < 10$ nm are fully dissociated. By comparing the fraction of dissociated excitons to those with $D_{\text{min}} >$ 10 nm, we calculate the exciton dissociation efficiency shown in Fig.8.14 (c). C-BHJ (blue) achieves the unity dissociation efficiency for $L < 20$ nm, and the efficiency is maintained to be >78% with a very large L of 50 nm, showing reliable exciton dissociation with a relatively small dependence on the morphology. On the other hand, the optimisation of morphology is shown to be more important in the sq-BHJ, as depicted by the rapid drop of dissociation efficiency for an increased L. Such sharp dependency on morphology can be attributed to the relatively small interfacial area of the structure, where the excitons have no alternative path to be dissociated if a column moves far apart. With a well-controlled morphology, the exciton dissociation efficiency of the sq-BHJ can also reach 100%, when $L < 14.2$ nm, while such efficiency of PHJ is only 20%. To secure efficient exciton dissociation, we can infer that L should be small and this agrees with the high device performance already achieved in sq-BHJ devices. Such morphology with a small L is highly possible in sq-BHJ, considering its rough surface and the possibly vertical heterogeneity. Thus, our model provides a simple picture to show the promise of efficient exciton dissociation in sq-BHJ.

8.7 Conclusion

In summary, we have characterised the interfacial trap states and CT states in a highly efficient polymer:NFA blend prepared by sequential deposition and conventional one-step processing methods. We consistently found less interfacial area and more trap states in

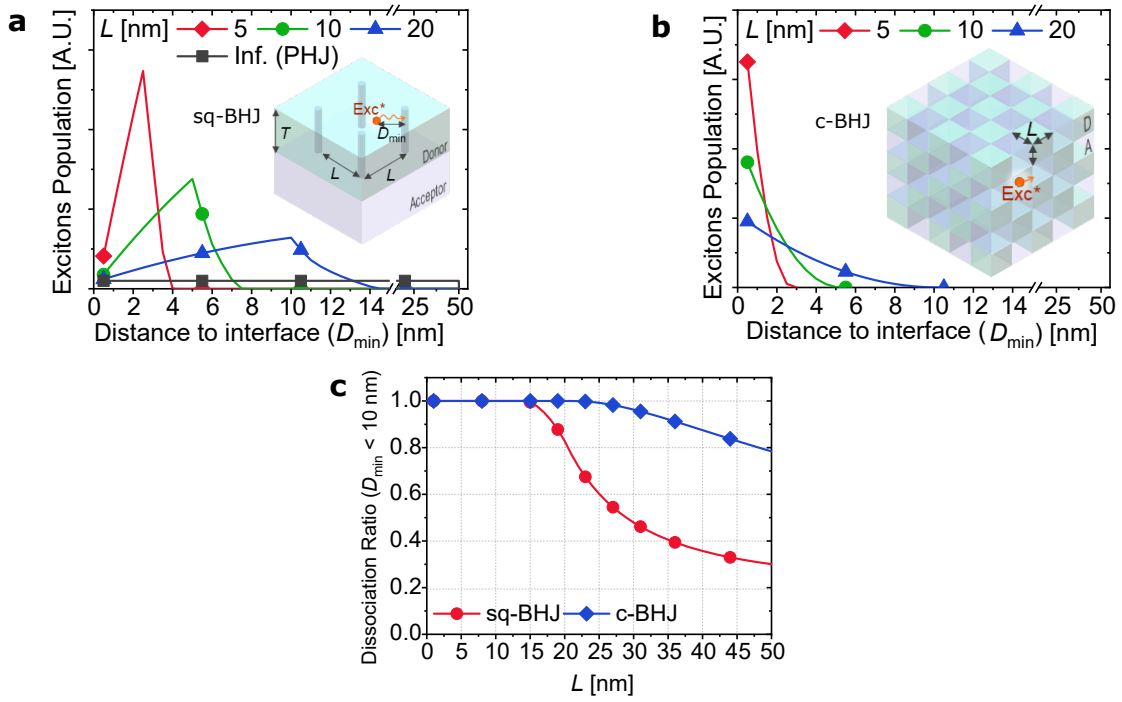

Fig. 8.14 A simple model of D:A morphology to simulate the exciton dissociation in sq-BHJ, c-BHJ and PHJ. (a, b) Modelled exciton population ratio as a function of the minimum distance to donor/acceptor interface (D) in the (a) sq-BHJ and (b) c-BHJ. For the sq-BHJ, donor and acceptor are assumed to be thin-films sequentially deposited with a thickness of $T = 50$ nm. Acceptor is assumed to be mixed to donor in a shape of ultrathin columns, having a period of L and height equal to T. For the c-BHJ, donor and acceptor are equally mixed as shown in the inset, where each cube has an edge length of L. It should be noted that the sq-BHJ with infinite L corresponds to the PHJ. Excitons are assumed to be uniformly generated in the donor region and those in the acceptor region can be calculated in the same way. (c) Exciton dissociation ratio of the sq-BHJ and c-BHJ structures as a function of L, assuming that excitons with $D_{\text{min}} < 10$ nm are fully dissociated.

sq-BHJ devices compared with c-BHJ devices. Sq-BHJ devices have the potential to achieve a higher voltage output due to reduced interfacial states for recombination. On the other hand, trap states at the interface can adversely influence the device performance, such as the non-radiative recombination, limiting voltage improvement. The vertical stratification is directly visualised using two advanced techniques, cross-sectional TEM-EDX and depth-profile UPS, supporting gradual D-A composition change in top half of the film and a uniform distribution in the bottom half. Our proposed simple model to simulate the sq-BHJ structure demonstrates that sq-BHJ devices can achieve unity exciton dissociation without such strong morphological requirements as in traditional BHJ systems. Our results highlight the need to eliminate these trap states to achieve higher V_{OC} and PCE in sq-BHJ devices.

Chapter 9

Conclusion and Future Work

In this dissertation, we have investigated charge dynamics in different types of organic solar cells using existing and new ultrafast techniques. The studied OPV blends, including fullerene-based and NFA-based blends, exhibit a large energy offset.

To realise efficient solar cells, the potential barrier from Coulomb interaction at the donor-acceptor interface must be overcome. This process is difficult to directly probe, since that the involved states (CT states and charge-separated states) have the spectroscopic signals at the similar positions in transient absorption measurements. In contrast, the relatively new technique, PPP spectroscopy, offers a delicate method to probe such separation process by activating charge transfer pathways with optical pulses. Here we presented the newly developed temperature-dependent extension of the PPP, which we applied to probe the energetics of CTSs and extract an important quantity, the binding energy of localised CTSs, a proportion of CTSs that are most prone to recombination. Surprisingly, we found out that the fullerene aggregation and the molecular energetics does not strongly affect the binding energy of CTSs which is measured to be around 90 meV, well above the thermal energy at room temperature. Instead, aggregation and energy offsets influence the relative concentration of strongly and weakly bound states. We thus conclude that access to delocalised states not through localised CTS, is crucial for fullerene-based material systems, rather than the energy level of CTSs. Furthermore, we studied the geminate recombination, the rate of which can compete with that of charge separation. The CT lifetime is measured to be 130 ps, coherent and independent of the morphology in the studied material, supporting that morphological optimisation cannot change the energetics, but mainly increases the coupling to charge-separated states. One additional observation is that the dissociation of excitons is diffusive, resulting in a slow rate of charge generation, in contrast to an ultrafast charge-transfer event in the well mixed blend. This connects to the slow charge generation in the state-of-the-art materials systems.

Morphology optimisation is the key to achieving high performance in OSCs, but usually requires trial-and-error device fabrication. For emerging NFAs, we demonstrated a very simple method, using sequential deposition to achieve the efficient OSCs. resultant morphology is very close to the optimal, in which the solvent choice is most critical. Environmentally friendly solvent is also applicable, to replace the toxic organic solvent. In addition, this method can be easily integrated into industrial fabrication methods, such as slot-die and roll-to-roll. Such simple and green processing is particularly useful for large-scale production and future commercialisation.

In the state-of-the-art photovoltaic blends with a low energy offset, the understanding is still far from being satisfactory. New experimental evidence, different from fullerene-based blends, includes slow charge generation from ultrafast measurements, the disappearance of CT transition from the sensitive photon action spectra, electroluminescence spectrum shape similar to photoluminescence, and high electroluminescence efficiency. The current explanation is based on the hybridisation of CTSs and local excitons, where CTS can borrow oscillator strength from the singlet state thus become brighter. However, the direct supporting evidence to support such coupling is still missing. Future experimental efforts should focus on resolving the mechanism behind the slow charge generation by probing the properties of the material system, dependent on temperature, electric and magnetic field. Some tools, used in OLED studies, may become useful as well to study the more luminescent OSCs.

Following the success of NFA-based OSCs, a fundamental question of how to avoid the formation of local triplet states is naturally raised, as triplet states with lowest energy levels may become a significant loss channel in OSCs. There is still no clear evidence to show the triplet states in state-of-the-art NFA blends. Initial study can start from material systems to observe the triplet states at the first place, such as from solution systems where triplet-triplet annihilation is an easy proof to show the existence of triplet states, or in the solid-state films where high excitation density may deliberately form triplet states.

To continue the research line, it would be interesting to explore other types of heterojunctions assembly by nanomaterials. I also have interest to study new emerging optoelectronic fields to combine photons and electrons together, such as ultrafast transmission electron microscopy and nuclear optical clocks. One short-term direction can be working towards better understanding the organic-organic interface. The charge recombination at the organic-organic interface is also important in OLEDs. The exciplex system in OLEDs, similar to CT interface in OSCs, represents a type of efficient emitters, where the interfacial state can have a significant long lifetime before its recombination. From the heterojunction similarity, one possible direction is to explore the design rules which control the lifetime of CT states. This fundamental study may enable the luminescent OSCs with minimal energy loss. Another

direction can be improving the understanding of the inorganic-inorganic interface. For example, interlayer exciton in two-dimensional transition-metal dichalcogenide materials, similar as CT exciton, can be an exciting field to explore.

References

[1] Bin Kan, Jiangbin Zhang, Feng Liu, Xiangjian Wan, Chenxi Li, Xin Ke, Yunchuang Wang, Huanran Feng, Yamin Zhang, Guankui Long, et al. Fine-tuning the energy levels of a nonfullerene small-molecule acceptor to achieve a high short-circuit current and a power conversion efficiency over 12% in organic solar cells. *Advanced Materials*, 30(3):1704904, 2018.

[2] UK renewable energy percentage 2018 and 2019. https://smarterbusiness.co.uk/uk-renewable-energy-percentage-2018/. Accessed: 2019-09-11.

[3] Pabitra K Nayak, Suhas Mahesh, Henry J Snaith, and David Cahen. Photovoltaic solar cell technologies: analysing the state of the art. *Nature Reviews Materials*, 4(4):269, 2019.

[4] Martin A Green, Ewan D Dunlop, Dean H Levi, Jochen Hohl-Ebinger, Masahiro Yoshita, and Anita WY Ho-Baillie. Solar cell efficiency tables (version 54). *Progress in Photovoltaics: Research and Applications*, 27(NREL/JA-5K00-74116), 2019.

[5] Solar PV deployment in the UK. https://en.wikipedia.org/wiki/Solar_power_in_the_United_Kingdom. Accessed: 2019-09-11.

[6] Gang Li, Rui Zhu, and Yang Yang. Polymer solar cells. *Nature Photonics*, 6(3):153, 2012.

[7] Stephen R Forrest. The path to ubiquitous and low-cost organic electronic appliances on plastic. *Nature*, 428(6986):911, 2004.

[8] Lingxian Meng, Yamin Zhang, Xiangjian Wan, Chenxi Li, Xin Zhang, Yanbo Wang, Xin Ke, Zuo Xiao, Liming Ding, Ruoxi Xia, Hin-Lap Yip, Yong Cao, and Yongsheng Chen. Organic and solution-processed tandem solar cells with 17.3% efficiency. *Science*, 361(6407):1094–1098, 2018.

[9] Samuel D Stranks. Nonradiative losses in metal halide perovskites. *ACS Energy Letters*, 2(7):1515–1525, 2017.

[10] Jianhui Hou, Olle Inganäs, Richard H Friend, and Feng Gao. Organic solar cells based on non-fullerene acceptors. *Nature Materials*, 17(2):119, 2018.

[11] Martin Pope and Charles E Swenberg. *Electronic processes in organic crystals*. Clarendon Press, 1982.

[12] Alan J Heeger, Alan G MacDiarmid, and Hideki Shirakawa. The Nobel Prize in Chemistry, 2000: conductive polymers. *Stockholm, Sweden: Royal Swedish Academy of Sciences*, pages 1–16, 2000.

[13] Jeremy H Burroughes, Donal DC Bradley, AR Brown, RN Marks, K Mackay, Richard H Friend, PL Burns, and AB Holmes. Light-emitting diodes based on conjugated polymers. *Nature*, 347:539–541, 1990.

[14] Alan J Heeger. Semiconducting polymers: the third generation. *Chemical Society Reviews*, 39(7):2354–2371, 2010.

[15] Ho-Wa Li, Zhiqiang Guan, Yuanhang Cheng, Taili Lui, Qingdan Yang, Chun-Sing Lee, Song Chen, and Sai-Wing Tsang. On the study of exciton binding energy with direct charge generation in photovoltaic polymers. *Advanced Electronic Materials*, 2(11):1600200, 2016.

[16] Jean Luc Brédas and Seth R Marder. *The WSPC Reference on Organic Electronics: Organic Semiconductors*, volume 1. World Scientific, 2016.

[17] Stefan Kraner, Reinhard Scholz, Christian Koerner, and Karl Leo. Design proposals for organic materials exhibiting a low exciton binding energy. *The Journal of Physical Chemistry C*, 119(40):22820–22825, 2015.

[18] Anna Köhler and David Beljonne. The singlet–triplet exchange energy in conjugated polymers. *Advanced Functional Materials*, 14(1):11–18, 2004.

[19] Akshay Rao and Richard H Friend. Harnessing singlet exciton fission to break the Shockley–Queisser limit. *Nature Reviews Materials*, 2(11):17063, 2017.

[20] Andrew J Musser and Jenny Clark. Triplet-pair states in organic semiconductors. *Annual Review of Physical Chemistry*, 70:323–351, 2019.

[21] Markus Einzinger, Tony Wu, Julia F Kompalla, Hannah L Smith, Collin F Perkinson, Lea Nienhaus, Sarah Wieghold, Daniel N Congreve, Antoine Kahn, Moungi G Bawendi, et al. Sensitization of silicon by singlet exciton fission in tetracene. *Nature*, 571(7763):90, 2019.

[22] Hiroki Uoyama, Kenichi Goushi, Katsuyuki Shizu, Hiroko Nomura, and Chihaya Adachi. Highly efficient organic light-emitting diodes from delayed fluorescence. *Nature*, 492(7428):234, 2012.

[23] Yasuhiro Kondo, Kazuki Yoshiura, Sayuri Kitera, Hiroki Nishi, Susumu Oda, Hajime Gotoh, Yasuyuki Sasada, Motoki Yanai, and Takuji Hatakeyama. Narrowband deep-blue organic light-emitting diode featuring an organoboron-based emitter. *Nature Photonics*, pages 1–5, 2019.

[24] Ryo Nagata, Hajime Nakanotani, William J Potscavage Jr, and Chihaya Adachi. Exploiting singlet fission in organic light-emitting diodes. *Advanced Materials*, 30(33):1801484, 2018.

[25] O Armet, J Veciana, C Rovira, J Riera, J Castaner, E Molins, J Rius, C Miravitlles, S Olivella, and J Brichfeus. Inert carbon free radicals. 8. Polychlorotriphenylmethyl radicals: synthesis, structure, and spin-density distribution. *Journal of Physical Chemistry*, 91(22):5608–5616, 1987.

[26] Qiming Peng, Ablikim Obolda, Ming Zhang, and Feng Li. Organic light-emitting diodes using a neutral π radical as emitter: the emission from a doublet. *Angewandte Chemie International Edition*, 54(24):7091–7095, 2015.

[27] Xin Ai, Emrys W Evans, Shengzhi Dong, Alexander J Gillett, Haoqing Guo, Yingxin Chen, Timothy JH Hele, Richard H Friend, and Feng Li. Efficient radical-based light-emitting diodes with doublet emission. *Nature*, 563(7732):536, 2018.

[28] Haoqing Guo, Qiming Peng, Xian-Kai Chen, Qinying Gu, Shengzhi Dong, Emrys W Evans, Alexander J Gillett, Xin Ai, Ming Zhang, Dan Credgington, et al. High stability and luminescence efficiency in donor–acceptor neutral radicals not following the aufbau principle. *Nature Materials*, 18(9):977–984, 2019.

[29] Ernest Pastor, Ji-Sang Park, Ludmilla Steier, Sunghyun Kim, Michael Grätzel, James R Durrant, Aron Walsh, and Artem A Bakulin. In situ observation of picosecond polaron self-localisation in α-Fe_2O_3 photoelectrochemical cells. *Nature Communications*, 10(1):1–7, 2019.

[30] Artem A. Bakulin, Akshay Rao, Vlad G. Pavelyev, Paul H. M. van Loosdrecht, Maxim S. Pshenichnikov, Dorota Niedzialek, Jérôme Cornil, David Beljonne, and Richard H. Friend. The role of driving energy and delocalized states for charge separation in organic semiconductors. *Science*, 335(6074):1340–1344, 2012.

[31] Christina Enengl, Sandra Enengl, Sandra Pluczyk, Marek Havlicek, Mieczyslaw Lapkowski, Helmut Neugebauer, and Eitan Ehrenfreund. Doping-induced absorption bands in P3HT: Polarons and bipolarons. *ChemPhysChem*, 17(23):3836–3844, 2016.

[32] Ronald Österbacka, Chong P An, XiaoMei Jiang, and Z Valy Vardeny. Two-dimensional electronic excitations in self-assembled conjugated polymer nanocrystals. *Science*, 287(5454):839–842, 2000.

[33] Michael Baer. *Beyond Born-Oppenheimer: electronic nonadiabatic coupling terms and conical intersections*. John Wiley & Sons, 2006.

[34] Andreas Christian Jakowetz. *Spectroscopic Studies of Excited States in Polymer:Fullerene Heterojunctions and Covalent Organic Frameworks*. PhD thesis, University of Cambridge, 2016.

[35] Rudolph A Marcus. Chemical and electrochemical electron-transfer theory. *Annual Review of Physical Chemistry*, 15(1):155–196, 1964.

[36] Rudolph A Marcus. On the theory of oxidation-reduction reactions involving electron transfer. I. *The Journal of Chemical Physics*, 24(5):966–978, 1956.

[37] Andreas C Jakowetz, Marcus L Böhm, Jiangbin Zhang, Aditya Sadhanala, Sven Huettner, Artem A Bakulin, Akshay Rao, and Richard H Friend. What controls the rate of ultrafast charge transfer and charge separation efficiency in organic photovoltaic blends. *Journal of the American Chemical Society*, 138(36):11672–11679, 2016.

[38] Brett M Savoie, Akshay Rao, Artem A Bakulin, Simon Gelinas, Bijan Movaghar, Richard H Friend, Tobin J Marks, and Mark A Ratner. Unequal partnership: asymmetric roles of polymeric donor and fullerene acceptor in generating free charge. *Journal of the American Chemical Society*, 136(7):2876–2884, 2014.

[39] Deping Qian, Zilong Zheng, Huifeng Yao, Wolfgang Tress, Thomas R Hopper, Shula Chen, Sunsun Li, Jing Liu, Shangshang Chen, Jiangbin Zhang, et al. Design rules for minimizing voltage losses in high-efficiency organic solar cells. *Nature Materials*, 17(8):703, 2018.

[40] Sreelakshmi Chandrabose, Kai Chen, Alex J Barker, Joshua J Sutton, Shyamal KK Prasad, Jingshuai Zhu, Jiadong Zhou, Keith C Gordon, Zengqi Xie, Xiaowei Zhan, et al. High exciton diffusion coefficients in fused ring electron acceptor films. *Journal of the American Chemical Society*, 141(17):6922–6929, 2019.

[41] Caroline Murawski, Karl Leo, and Malte C Gather. Efficiency roll-off in organic light-emitting diodes. *Advanced Materials*, 25(47):6801–6827, 2013.

[42] Dawei Di, Le Yang, Johannes M Richter, Lorenzo Meraldi, Rashid M Altamimi, Ahmed Y Alyamani, Dan Credgington, Kevin P Musselman, Judith L MacManus-Driscoll, and Richard H Friend. Efficient triplet exciton fusion in molecularly doped polymer light-emitting diodes. *Advanced Materials*, 29(13):1605987, 2017.

[43] Nicholas J Hestand and Frank C Spano. Expanded theory of H-and J-molecular aggregates: the effects of vibronic coupling and intermolecular charge transfer. *Chemical Reviews*, 118(15):7069–7163, 2018.

[44] Frank Würthner, Theo E Kaiser, and Chantu R Saha-Möller. J-aggregates: from serendipitous discovery to supramolecular engineering of functional dye materials. *Angewandte Chemie International Edition*, 50(15):3376–3410, 2011.

[45] Hwang-Beom Kim and Jang-Joo Kim. A simple method to measure intermolecular charge-transfer absorption of organic films. *Organic Electronics*, 62:511–515, 2018.

[46] Sascha Ullbrich, Johannes Benduhn, Xiangkun Jia, Vasileios C Nikolis, Kristofer Tvingstedt, Fortunato Piersimoni, Steffen Roland, Yuan Liu, Jinhan Wu, Axel Fischer, et al. Emissive and charge-generating donor–acceptor interfaces for organic optoelectronics with low voltage losses. *Nature Materials*, 18(5):459–464, 2019.

[47] CW Tang and AC Albrecht. Chlorophyll-a photovoltaic cells. *Nature*, 254(5500):507–509, 1975.

[48] Chwan K Chiang, CR Fincher Jr, Yung W Park, Alan J Heeger, Hideki Shirakawa, Edwin J Louis, Shek C Gau, and Alan G MacDiarmid. Electrical conductivity in doped polyacetylene. *Physical Review Letters*, 39(17):1098, 1977.

[49] Ching W Tang. Two-layer organic photovoltaic cell. *Applied Physics Letters*, 48(2):183–185, 1986.

[50] Niyazi S Sariciftci, L Smilowitz, Alan J Heeger, and F Wudl. Photoinduced electron transfer from a conducting polymer to buckminsterfullerene. *Science*, 258(5087):1474–1476, 1992.

[51] G. Yu, J. Gao, J. C. Hummelen, F. Wudl, and A. J. Heeger. Polymer photovoltaic cells: Enhanced efficiencies via a network of internal donor-acceptor heterojunctions. *Science*, 270(5243):1789–1791, 1995.

[52] JJM Halls, CA Walsh, Neil C Greenham, EA Marseglia, Richard H Friend, SC Moratti, and AB Holmes. Efficient photodiodes from interpenetrating polymer networks. *Nature*, 376(6540):498–500, 1995.

[53] Olle Inganäs. Organic photovoltaics over three decades. *Advanced Materials*, 30(35):1800388, 2018.

[54] Yuze Lin, Jiayu Wang, Zhi-Guo Zhang, Huitao Bai, Yongfang Li, Daoben Zhu, and Xiaowei Zhan. An electron acceptor challenging fullerenes for efficient polymer solar cells. *Advanced Materials*, 27(7):1170–1174, 2015.

[55] Hua Sun, Fei Chen, and Zhi-Kuan Chen. Recent progress on non-fullerene acceptors for organic photovoltaics. *Materials Today*, 24:94–118, 2018.

[56] William Shockley and Hans J Queisser. Detailed balance limit of efficiency of p-n junction solar cells. *Journal of Applied Physics*, 32(3):510–519, 1961.

[57] Jean-Francois Guillemoles, Thomas Kirchartz, David Cahen, and Uwe Rau. Guide for the perplexed to the Shockley–Queisser model for solar cells. *Nature Photonics*, 13(8):501–505, 2019.

[58] Owen D Miller, Eli Yablonovitch, and Sarah R Kurtz. Strong internal and external luminescence as solar cells approach the Shockley–Queisser limit. *IEEE Journal of Photovoltaics*, 2(3):303–311, 2012.

[59] Zhi-Guo Zhang, Boyuan Qi, Zhiwen Jin, Dan Chi, Zhe Qi, Yongfang Li, and Jizheng Wang. Perylene diimides: a thickness-insensitive cathode interlayer for high performance polymer solar cells. *Energy & Environmental Science*, 7(6):1966–1973, 2014.

[60] Kai Wang, Chang Liu, Tianyu Meng, Chao Yi, and Xiong Gong. Inverted organic photovoltaic cells. *Chemical Society Reviews*, 45(10):2937–2975, 2016.

[61] Richard D McCullough, Renae D Lowe, Manikandan Jayaraman, and Deborah L Anderson. Design, synthesis, and control of conducting polymer architectures: structurally homogeneous poly (3-alkylthiophenes). *The Journal of Organic Chemistry*, 58(4):904–912, 1993.

[62] Minh Trung Dang, Lionel Hirsch, and Guillaume Wantz. P3HT:PCBM, best seller in polymer photovoltaic research. *Advanced Materials*, 23(31):3597–3602, 2011.

[63] Guangjin Zhao, Youjun He, and Yongfang Li. 6.5% Efficiency of polymer solar cells based on poly (3-hexylthiophene) and indene-C_{60} bisadduct by device optimization. *Advanced Materials*, 22(39):4355–4358, 2010.

[64] Eva Bundgaard and Frederik C Krebs. Low band gap polymers for organic photovoltaics. *Solar Energy Materials and Solar Cells*, 91(11):954–985, 2007.

[65] Gang Li, Wei-Hsuan Chang, and Yang Yang. Low-bandgap conjugated polymers enabling solution-processable tandem solar cells. *Nature Reviews Materials*, 2(8):17043, 2017.

[66] EE Havinga, W Ten Hoeve, and H Wynberg. A new class of small band gap organic polymer conductors. *Polymer Bulletin*, 29(1-2):119–126, 1992.

[67] Yuhang Liu, Jingbo Zhao, Zhengke Li, Cheng Mu, Wei Ma, Huawei Hu, Kui Jiang, Haoran Lin, Harald Ade, and He Yan. Aggregation and morphology control enables multiple cases of high-efficiency polymer solar cells. *Nature Communications*, 5:5293, 2014.

[68] Huawei Hu, Philip CY Chow, Guangye Zhang, Tingxuan Ma, Jing Liu, Guofang Yang, and He Yan. Design of donor polymers with strong temperature-dependent aggregation property for efficient organic photovoltaics. *Accounts of Chemical Research*, 50(10):2519–2528, 2017.

[69] Sung Heum Park, Anshuman Roy, Serge Beaupré, Shinuk Cho, Nelson Coates, Ji Sun Moon, Daniel Moses, Mario Leclerc, Kwanghee Lee, and Alan J Heeger. Bulk heterojunction solar cells with internal quantum efficiency approaching 100%. *Nature Photonics*, 3(5):297–302, 2009.

[70] Dan Deng, Yajie Zhang, Jianqi Zhang, Zaiyu Wang, Lingyun Zhu, Jin Fang, Benzheng Xia, Zhen Wang, Kun Lu, Wei Ma, et al. Fluorination-enabled optimal morphology leads to over 11% efficiency for inverted small-molecule organic solar cells. *Nature Communications*, 7:13740, 2016.

[71] Jianquan Zhang, Huei Shuan Tan, Xugang Guo, Antonio Facchetti, and He Yan. Material insights and challenges for non-fullerene organic solar cells based on small molecular acceptors. *Nature Energy*, 3(9):720, 2018.

[72] Guangye Zhang, Jingbo Zhao, Philip CY Chow, Kui Jiang, Jianquan Zhang, Zonglong Zhu, Jie Zhang, Fei Huang, and He Yan. Nonfullerene acceptor molecules for bulk heterojunction organic solar cells. *Chemical Reviews*, 118(7):3447–3507, 2018.

[73] Pei Cheng, Gang Li, Xiaowei Zhan, and Yang Yang. Next-generation organic photovoltaics based on non-fullerene acceptors. *Nature Photonics*, 12(3):131–142, 2018.

[74] Cenqi Yan, Stephen Barlow, Zhaohui Wang, He Yan, Alex K-Y Jen, Seth R Marder, and Xiaowei Zhan. Non-fullerene acceptors for organic solar cells. *Nature Reviews Materials*, 3(3):18003, 2018.

[75] Andrew Wadsworth, Maximilian Moser, Adam Marks, Mark S Little, Nicola Gasparini, Christoph J Brabec, Derya Baran, and Iain McCulloch. Critical review of the molecular design progress in non-fullerene electron acceptors towards commercially viable organic solar cells. *Chemical Society Reviews*, 48(6):1596–1625, 2019.

[76] Yuze Lin, Yongfang Li, and Xiaowei Zhan. Small molecule semiconductors for high-efficiency organic photovoltaics. *Chemical Society Reviews*, 41(11):4245–4272, 2012.

[77] Wenchao Zhao, Deping Qian, Shaoqing Zhang, Sunsun Li, Olle Inganäs, Feng Gao, and Jianhui Hou. Fullerene-free polymer solar cells with over 11% efficiency and excellent thermal stability. *Advanced Materials*, 28(23):4734–4739, 2016.

[78] Jing Liu, Shangshang Chen, Deping Qian, Bhoj Gautam, Guofang Yang, Jingbo Zhao, Jonas Bergqvist, Fengling Zhang, Wei Ma, Harald Ade, et al. Fast charge separation in a non-fullerene organic solar cell with a small driving force. *Nature Energy*, 1(7):16089, 2016.

[79] Jun Yuan, Yunqiang Zhang, Liuyang Zhou, Guichuan Zhang, Hin-Lap Yip, Tsz-Ki Lau, Xinhui Lu, Can Zhu, Hongjian Peng, Paul A Johnson, et al. Single-junction organic solar cell with over 15% efficiency using fused-ring acceptor with electron-deficient core. *Joule*, 3(4):1140–1151, 2019.

[80] Yong Cui, Huifeng Yao, Jianqi Zhang, Tao Zhang, Yuming Wang, Ling Hong, Kaihu Xian, Bowei Xu, Shaoqing Zhang, Jing Peng, et al. Over 16% efficiency organic photovoltaic cells enabled by a chlorinated acceptor with increased open-circuit voltages. *Nature Communications*, 10(1):2515, 2019.

[81] Sarah Holliday, Raja Shahid Ashraf, Andrew Wadsworth, Derya Baran, Syeda Amber Yousaf, Christian B Nielsen, Ching-Hong Tan, Stoichko D Dimitrov, Zhengrong Shang, Nicola Gasparini, et al. High-efficiency and air-stable p3ht-based polymer solar cells with a new non-fullerene acceptor. *Nature Communications*, 7:11585, 2016.

[82] Hyojung Cha, Jiaying Wu, Andrew Wadsworth, Jade Nagitta, Saurav Limbu, Sebastian Pont, Zhe Li, Justin Searle, Mark F Wyatt, Derya Baran, et al. An efficient,"burn in" free organic solar cell employing a nonfullerene electron acceptor. *Advanced Materials*, 29(33):1701156, 2017.

[83] Joel Luke, Emily M Speller, Andrew Wadsworth, Mark F Wyatt, Stoichko Dimitrov, Harrison KH Lee, Zhe Li, Wing C Tsoi, Iain McCulloch, Diego Bagnis, et al. Twist and degrade—impact of molecular structure on the photostability of nonfullerene acceptors and their photovoltaic blends. *Advanced Energy Materials*, 9(15):1803755, 2019.

[84] Xiaoyan Du, Thomas Heumueller, Wolfgang Gruber, Andrej Classen, Tobias Unruh, Ning Li, and Christoph J Brabec. Efficient polymer solar cells based on non-fullerene acceptors with potential device lifetime approaching 10 years. *Joule*, 3(1):215–226, 2019.

[85] Quinn Burlingame, Xiaheng Huang, Xiao Liu, Changyeong Jeong, Caleb Coburn, and Stephen R Forrest. Intrinsically stable organic solar cells under high-intensity illumination. *Nature*, 573(7774):394–397, 2019.

[86] Heng Lu, Jicheng Zhang, Jianya Chen, Qian Liu, Xue Gong, Shiyu Feng, Xinjun Xu, Wei Ma, and Zhishan Bo. Ternary-blend polymer solar cells combining fullerene and nonfullerene acceptors to synergistically boost the photovoltaic performance. *Advanced Materials*, 28(43):9559–9566, 2016.

[87] Huifeng Yao, Yong Cui, Runnan Yu, Bowei Gao, Hao Zhang, and Jianhui Hou. Design, synthesis, and photovoltaic characterization of a small molecular acceptor with an ultra-narrow band gap. *Angewandte Chemie International Edition*, 56(11):3045–3049, 2017.

[88] Runnan Yu, Shaoqing Zhang, Huifeng Yao, Bing Guo, Sunsun Li, Hao Zhang, Maojie Zhang, and Jianhui Hou. Two well-miscible acceptors work as one for efficient fullerene-free organic solar cells. *Advanced Materials*, 29(26):1700437, 2017.

[89] Zhen Wang, Xiangwei Zhu, Jianqi Zhang, Kun Lu, Jin Fang, Yajie Zhang, Zaiyu Wang, Lingyun Zhu, Wei Ma, Zhigang Shuai, et al. From alloy-like to cascade blended structure: designing high-performance all-small-molecule ternary solar cells. *Journal of the American Chemical Society*, 140(4):1549–1556, 2018.

[90] Xinjing Huang, Stephen R Forrest, Xiao Liu, and Kan Ding. Is there such a thing as a molecular organic alloy? *Materials Horizons*, 2019.

[91] Derya Baran, Raja Shahid Ashraf, David A Hanifi, Maged Abdelsamie, Nicola Gasparini, Jason A Röhr, Sarah Holliday, Andrew Wadsworth, Sarah Lockett, Marios Neophytou, Christopher JM Emmott, Jenny Nelson, Christoph J Brabec, Aram Amassian, Alberto Salleo, Thomas Kirchartz, James R Durrant, and Iain McCulloch. Reducing the efficiency–stability–cost gap of organic photovoltaics with highly efficient and stable small molecule acceptor ternary solar cells. *Nature Materials*, 16(3):363–369, 2017.

[92] Yaowen Li, Guiying Xu, Chaohua Cui, and Yongfang Li. Flexible and semitransparent organic solar cells. *Advanced Energy Materials*, 8(7):1701791, 2018.

[93] Ruoxi Xia, Christoph J Brabec, Hin-Lap Yip, and Yong Cao. High-throughput optical screening for efficient semitransparent organic solar cells. *Joule*, 3(9):2241–2254, 2019.

[94] Mark A Faist, Thomas Kirchartz, Wei Gong, Raja Shahid Ashraf, Iain McCulloch, John C de Mello, Nicholas J Ekins-Daukes, Donal DC Bradley, and Jenny Nelson. Competition between the charge transfer state and the singlet states of donor or acceptor limiting the efficiency in polymer: fullerene solar cells. *Journal of the American Chemical Society*, 134(1):685–692, 2011.

[95] Johannes Benduhn, Kristofer Tvingstedt, Fortunato Piersimoni, Sascha Ullbrich, Yeli Fan, Manuel Tropiano, Kathryn A McGarry, Olaf Zeika, Moritz K Riede, Christopher J Douglas, et al. Intrinsic non-radiative voltage losses in fullerene-based organic solar cells. *Nature Energy*, 2(6):17053, 2017.

[96] Guitao Feng, Junyu Li, Yakun He, Wenyu Zheng, Jing Wang, Cheng Li, Zheng Tang, Andres Osvet, Ning Li, Christoph J Brabec, et al. Thermal-driven phase separation of double-cable polymers enables efficient single-component organic solar cells. *Joule*, 3(7):1765–1781, 2019.

[97] Stoichko D Dimitrov, Artem A Bakulin, Christian B Nielsen, Bob C Schroeder, Junping Du, Hugo Bronstein, Iain McCulloch, Richard H Friend, and James R Durrant. On the energetic dependence of charge separation in low-band-gap polymer/fullerene blends. *Journal of the American Chemical Society*, 134(44):18189–18192, 2012.

[98] Koen Vandewal, Zaifei Ma, Jonas Bergqvist, Zheng Tang, Ergang Wang, Patrik Henriksson, Kristofer Tvingstedt, Mats R Andersson, Fengling Zhang, and Olle Inganäs. Quantification of quantum efficiency and energy losses in low bandgap polymer: Fullerene solar cells with high open-circuit voltage. *Advanced Functional Materials*, 22(16):3480–3490, 2012.

[99] Weiwei Li, Koen H Hendriks, Alice Furlan, Martijn M Wienk, and Renë AJ Janssen. High quantum efficiencies in polymer solar cells at energy losses below 0.6 ev. *Journal of the American Chemical Society*, 137(6):2231–2234, 2015.

[100] Kazuaki Kawashima, Yasunari Tamai, Hideo Ohkita, Itaru Osaka, and Kazuo Takimiya. High-efficiency polymer solar cells with small photon energy loss. *Nature Communications*, 6:10085, 2015.

[101] Pei Cheng, Mingyu Zhang, Tsz-Ki Lau, Yao Wu, Boyu Jia, Jiayu Wang, Cenqi Yan, Meng Qin, Xinhui Lu, and Xiaowei Zhan. Realizing small energy loss of 0.55 eV, high open-circuit voltage> 1 V and high efficiency> 10% in fullerene-free polymer solar cells via energy driver. *Advanced Materials*, 29(11):1605216, 2017.

[102] Shangshang Chen, Yuhang Liu, Lin Zhang, Philip CY Chow, Zheng Wang, Guangye Zhang, Wei Ma, and He Yan. A wide-bandgap donor polymer for highly efficient non-fullerene organic solar cells with a small voltage loss. *Journal of the American Chemical Society*, 139(18):6298–6301, 2017.

[103] D Baran, T Kirchartz, S Wheeler, S Dimitrov, Maged Abdelsamie, J Gorman, RS Ashraf, S Holliday, A Wadsworth, N Gasparini, et al. Reduced voltage losses yield 10% efficient fullerene free organic solar cells with> 1 V open circuit voltages. *Energy & Environmental Science*, 9(12):3783–3793, 2016.

[104] Yongxi Li, Xiaodong Liu, Fu-Peng Wu, Yi Zhou, Zuo-Quan Jiang, Bo Song, Yuxin Xia, Zhi-Guo Zhang, Feng Gao, Olle Inganäs, et al. Non-fullerene acceptor with low energy loss and high external quantum efficiency: towards high performance polymer solar cells. *Journal of Materials Chemistry A*, 4(16):5890–5897, 2016.

[105] Haijun Bin, Liang Gao, Zhi-Guo Zhang, Yankang Yang, Yindong Zhang, Chunfeng Zhang, Shanshan Chen, Lingwei Xue, Changduk Yang, Min Xiao, et al. 11.4% Efficiency non-fullerene polymer solar cells with trialkylsilyl substituted 2D-conjugated polymer as donor. *Nature Communications*, 7:13651, 2016.

[106] Jun Yuan, Tianyi Huang, Pei Cheng, Yingping Zou, Huotian Zhang, Jonathan Lee Yang, Sheng-Yung Chang, Zhenzhen Zhang, Wenchao Huang, Rui Wang, et al. Enabling low voltage losses and high photocurrent in fullerene-free organic photovoltaics. *Nature Communications*, 10(1):570, 2019.

[107] Heinz Bässler and Anna Köhler. "Hot or cold": how do charge transfer states at the donor–acceptor interface of an organic solar cell dissociate? *Physical Chemistry Chemical Physics*, 17(43):28451–28462, 2015.

[108] Xiaoyang Zhu, Nicholas R Monahan, Zizhou Gong, Haiming Zhu, Kristopher W Williams, and Cory A Nelson. Charge transfer excitons at van der waals interfaces. *Journal of the American Chemical Society*, 137(26):8313–8320, 2015.

[109] Koen Vandewal. Interfacial charge transfer states in condensed phase systems. *Annual Review of Physical Chemistry*, 67:113–133, 2016.

[110] Carsten Deibel, Thomas Strobel, and Vladimir Dyakonov. Role of the charge transfer state in organic donor–acceptor solar cells. *Advanced Materials*, 22(37):4097–4111, 2010.

[111] Sheridan Few, Jarvist M Frost, and Jenny Nelson. Models of charge pair generation in organic solar cells. *Physical Chemistry Chemical Physics*, 17(4):2311–2325, 2015.

[112] Tracey M Clarke and James R Durrant. Charge photogeneration in organic solar cells. *Chemical Reviews*, 110(11):6736–6767, 2010.

[113] Feng Gao and Olle Inganäs. Charge generation in polymer–fullerene bulk-heterojunction solar cells. *Physical Chemistry Chemical Physics*, 16(38):20291–20304, 2014.

[114] Xiao Liu, Barry P Rand, and Stephen R Forrest. Engineering charge-transfer states for efficient, low-energy-loss organic photovoltaics. *Trends in Chemistry*, 2019.

[115] Veaceslav Coropceanu, Xian-Kai Chen, Tonghui Wang, Zilong Zheng, and Jean-Luc Brédas. Charge-transfer electronic states in organic solar cells. *Nature Reviews Materials*, pages 1–19, 2019.

[116] Oleksandr V Mikhnenko, Paul WM Blom, and Thuc-Quyen Nguyen. Exciton diffusion in organic semiconductors. *Energy & Environmental Science*, 8(7):1867–1888, 2015.

[117] S Matthew Menke and Russell J Holmes. Exciton diffusion in organic photovoltaic cells. *Energy & Environmental Science*, 7(2):499–512, 2014.

[118] Ajay Ram Srimath Kandada, Giulia Grancini, Annamaria Petrozza, Stefano Perissinotto, Daniele Fazzi, Sai Santosh Kumar Raavi, and Guglielmo Lanzani. Ultrafast energy transfer in ultrathin organic donor/acceptor blend. *Scientific Reports*, 3:2073, 2013.

[119] Wei Li, Yu Yan, Yanyan Gong, Jinlong Cai, Feilong Cai, Robert S Gurney, Dan Liu, Andrew J Pearson, David G Lidzey, and Tao Wang. Contrasting effects of energy transfer in determining efficiency improvements in ternary polymer solar cells. *Advanced Functional Materials*, 28(5):1704212, 2018.

[120] Aiswarya Abhisek Mohapatra, Vincent Kim, Boregowda Puttaraju, Aditya Sadhanala, Xuechen Jiao, Christopher R McNeill, Richard H Friend, and Satish Patil. Förster resonance energy transfer drives higher efficiency in ternary blend organic solar cells. *ACS Applied Energy Materials*, 1(9):4874–4882, 2018.

[121] Kjell Cnops, Barry P Rand, David Cheyns, Bregt Verreet, Max A Empl, and Paul Heremans. 8.4% Efficient fullerene-free organic solar cells exploiting long-range exciton energy transfer. *Nature Communications*, 5:3406, 2014.

[122] Krishna Feron, James M Cave, Mahir N Thameel, Connor O'Sullivan, Renee Kroon, Mats R Andersson, Xiaojing Zhou, Christopher J Fell, Warwick J Belcher, Alison B Walker, et al. Utilizing energy transfer in binary and ternary bulk heterojunction organic solar cells. *ACS Applied Materials & Interfaces*, 8(32):20928–20937, 2016.

[123] Luyao Lu, Wei Chen, Tao Xu, and Luping Yu. High-performance ternary blend polymer solar cells involving both energy transfer and hole relay processes. *Nature Communications*, 6:7327, 2015.

[124] Domenico Caruso and Alessandro Troisi. Long-range exciton dissociation in organic solar cells. *Proceedings of the National Academy of Sciences*, 109(34):13498–13502, 2012.

[125] Artem A Bakulin, Jan C Hummelen, Maxim S Pshenichnikov, and Paul HM Van Loosdrecht. Ultrafast hole-transfer dynamics in polymer/PCBM bulk heterojunctions. *Advanced Functional Materials*, 20(10):1653–1660, 2010.

[126] Françoise Provencher, Nicolas Bérubé, Anthony W Parker, Gregory M Greetham, Michael Towrie, Christoph Hellmann, Michel Côté, Natalie Stingelin, Carlos Silva, and Sophia C Hayes. Direct observation of ultrafast long-range charge separation at polymer–fullerene heterojunctions. *Nature Communications*, 5:4288, 2014.

[127] Simon Gélinas, Akshay Rao, Abhishek Kumar, Samuel L Smith, Alex W Chin, Jenny Clark, Tom S van der Poll, Guillermo C Bazan, and Richard H Friend. Ultrafast long-range charge separation in organic semiconductor photovoltaic diodes. *Science*, 343(6170):512–516, 2014.

[128] Loren G Kaake, Chengmei Zhong, John A Love, Ikuhiro Nagao, Guillermo C Bazan, Thuc-Quyen Nguyen, Fei Huang, Yong Cao, Daniel Moses, and Alan J Heeger. Ultrafast charge generation in an organic bilayer film. *The Journal of Physical Chemistry Letters*, 5(11):2000–2006, 2014.

[129] Alex J Barker, Kai Chen, and Justin M Hodgkiss. Distance distributions of photogenerated charge pairs in organic photovoltaic cells. *Journal of the American Chemical Society*, 136(34):12018–12026, 2014.

[130] Jonathan D Servaites, Brett M Savoie, Joseph B Brink, Tobin J Marks, and Mark A Ratner. Modeling geminate pair dissociation in organic solar cells: high power conversion efficiencies achieved with moderate optical bandgaps. *Energy & Environmental Science*, 5(8):8343–8350, 2012.

[131] Charles L Braun. Electric field assisted dissociation of charge transfer states as a mechanism of photocarrier production. *The Journal of Chemical Physics*, 80(9):4157–4161, 1984.

[132] Lars Onsager. Initial recombination of ions. *Physical Review*, 54(8):554, 1938.

[133] Safa Shoaee, Tracey M Clarke, Chun Huang, Stephen Barlow, Seth R Marder, Martin Heeney, Iain McCulloch, and James R Durrant. Acceptor energy level control of charge photogeneration in organic donor/acceptor blends. *Journal of the American Chemical Society*, 132(37):12919–12926, 2010.

[134] VD Mihailetchi, LJA Koster, JC Hummelen, and PWM Blom. Photocurrent generation in polymer-fullerene bulk heterojunctions. *Physical Review Letters*, 93(21):216601, 2004.

[135] Artem A Bakulin, Yuxin Xia, Huib J Bakker, Olle Inganäs, and Feng Gao. Morphology, temperature, and field dependence of charge separation in high-efficiency solar cells based on alternating polyquinoxaline copolymer. *The Journal of Physical Chemistry C*, 120(8):4219–4226, 2016.

[136] Steve Albrecht, Koen Vandewal, John R Tumbleston, Florian SU Fischer, Jessica D Douglas, Jean MJ Fréchet, Sabine Ludwigs, Harald Ade, Alberto Salleo, and Dieter Neher. On the efficiency of charge transfer state splitting in polymer: fullerene solar cells. *Advanced Materials*, 26(16):2533–2539, 2014.

[137] Koen Vandewal, Steve Albrecht, Eric T Hoke, Kenneth R Graham, Johannes Widmer, Jessica D Douglas, Marcel Schubert, William R Mateker, Jason T Bloking, George F Burkhard, Alan Sellinger, Jean MJ Fréchet, Aram Amassian, Moritz K Riede, Michael D McGehee, Dieter Neher, and Alberto Salleo. Efficient charge generation by relaxed charge-transfer states at organic interfaces. *Nature Materials*, 13(1):63–68, 2014.

[138] Jiye Lee, Koen Vandewal, Shane R Yost, Matthias E Bahlke, Ludwig Goris, Marc A Baldo, Jean V Manca, and Troy Van Voorhis. Charge transfer state versus hot exciton dissociation in polymer-fullerene blended solar cells. *Journal of the American Chemical Society*, 132(34):11878–11880, 2010.

[139] In-Wook Hwang, Daniel Moses, and Alan J Heeger. Photoinduced carrier generation in P3HT/PCBM bulk heterojunction materials. *The Journal of Physical Chemistry C*, 112(11):4350–4354, 2008.

[140] Bhoj R Gautam, Robert Younts, Wentao Li, Liang Yan, Evgeny Danilov, Erik Klump, Iordania Constantinou, Franky So, Wei You, Harald Ade, et al. Charge photogeneration in organic photovoltaics: Role of hot versus cold charge-transfer excitons. *Advanced Energy Materials*, 6(1):1301032, 2016.

[141] PA Lane, PD Cunningham, JS Melinger, O Esenturk, and EJ Heilweil. Hot photocarrier dynamics in organic solar cells. *Nature Communications*, 6:7558, 2015.

[142] G Grancini, M Maiuri, D Fazzi, A Petrozza, HJ Egelhaaf, D Brida, G Cerullo, and G Lanzani. Hot exciton dissociation in polymer solar cells. *Nature Materials*, 12(1):29–33, 2013.

[143] Hideo Ohkita, Steffan Cook, Yeni Astuti, Warren Duffy, Steve Tierney, Weimin Zhang, Martin Heeney, Iain McCulloch, Jenny Nelson, Donal DC Bradley, et al. Charge carrier formation in polythiophene/fullerene blend films studied by transient absorption spectroscopy. *Journal of the American Chemical Society*, 130(10):3030–3042, 2008.

[144] Askat E Jailaubekov, Adam P Willard, John R Tritsch, Wai-Lun Chan, Na Sai, Raluca Gearba, Loren G Kaake, Kenrick J Williams, Kevin Leung, Peter J Rossky, et al. Hot charge-transfer excitons set the time limit for charge separation at donor/acceptor interfaces in organic photovoltaics. *Nature Materials*, 12(1):66–73, 2013.

[145] Kai Chen, Alex J Barker, Matthew E Reish, Keith C Gordon, and Justin M Hodgkiss. Broadband ultrafast photoluminescence spectroscopy resolves charge photogeneration via delocalized hot excitons in polymer:fullerene photovoltaic blends. *Journal of the American Chemical Society*, 135(49):18502–18512, 2013.

[146] Guangjun Nan, Xu Zhang, and Gang Lu. Do "hot" charge-transfer excitons promote free carrier generation in organic photovoltaics? *The Journal of Physical Chemistry C*, 119(27):15028–15035, 2015.

[147] Yin Song, Scott N Clafton, Ryan D Pensack, Tak W Kee, and Gregory D Scholes. Vibrational coherence probes the mechanism of ultrafast electron transfer in polymer–fullerene blends. *Nature Communications*, 5:4933, 2014.

[148] Ardalan Armin, Yuliang Zhang, Paul L Burn, Paul Meredith, and Almantas Pivrikas. Measuring internal quantum efficiency to demonstrate hot exciton dissociation. *Nature Materials*, 12(7):593, 2013.

[149] G Grancini, Maddalena Binda, L Criante, S Perissinotto, Margherita Maiuri, Daniele Fazzi, Annamaria Petrozza, HJ Egelhaaf, Daniele Brida, Giulio Cerullo, et al. Reply to'Measuring internal quantum efficiency to demonstrate hot exciton dissociation'. *Nature Materials*, 12(7):594–595, 2013.

[150] Jona Kurpiers, Thomas Ferron, Steffen Roland, Marius Jakoby, Tobias Thiede, Frank Jaiser, Steve Albrecht, Silvia Janietz, Brian A Collins, Ian A Howard, et al. Probing the pathways of free charge generation in organic bulk heterojunction solar cells. *Nature Communications*, 9(1):2038, 2018.

[151] Pabitra K Nayak, KL Narasimhan, and David Cahen. Separating charges at organic interfaces: Effects of disorder, hot states, and electric field. *The Journal of Physical Chemistry Letters*, 4(10):1707–1717, 2013.

[152] Hiroyuki Tamura and Irene Burghardt. Ultrafast charge separation in organic photovoltaics enhanced by charge delocalization and vibronically hot exciton dissociation. *Journal of the American Chemical Society*, 135(44):16364–16367, 2013.

[153] Ian A Howard, Ralf Mauer, Michael Meister, and Frédéric Laquai. Effect of morphology on ultrafast free carrier generation in polythiophene: fullerene organic solar cells. *Journal of the American Chemical Society*, 132(42):14866–14876, 2010.

[154] Loren G Kaake, Daniel Moses, and Alan J Heeger. Charge transfer from delocalized excited states in a bulk heterojunction material. *Physical Review B*, 91(7):075436, 2015.

[155] Artem A Bakulin, Stoichko D Dimitrov, Akshay Rao, Philip CY Chow, Christian B Nielsen, Bob C Schroeder, Iain McCulloch, Huib J Bakker, James R Durrant, and Richard H Friend. Charge-transfer state dynamics following hole and electron transfer in organic photovoltaic devices. *The Journal of Physical Chemistry Letters*, 4(1):209–215, 2012.

[156] Gabriele D'Avino, Luca Muccioli, Yoann Olivier, and David Beljonne. Charge separation and recombination at polymer–fullerene heterojunctions: delocalization and hybridization effects. *The Journal of Physical Chemistry Letters*, 7(3):536–540, 2016.

[157] Simon Gélinas, Olivier Paré-Labrosse, Colin-Nadeau Brosseau, Sebastian Albert-Seifried, Christopher R McNeill, Kiril R Kirov, Ian A Howard, Richard Leonelli, Richard H Friend, and Carlos Silva. The binding energy of charge-transfer excitons localized at polymeric semiconductor heterojunctions. *The Journal of Physical Chemistry C*, 115(14):7114–7119, 2011.

[158] B Bernardo, D Cheyns, B Verreet, RD Schaller, BP Rand, and NC Giebink. Delocalization and dielectric screening of charge transfer states in organic photovoltaic cells. *Nature Communications*, 5:3245, 2014.

[159] Safa Shoaee, Selvam Subramaniyan, Hao Xin, Chaz Keiderling, Pabitra Shakya Tuladhar, Fiona Jamieson, Samson A Jenekhe, and James R Durrant. Charge photogeneration for a series of thiazolo-thiazole donor polymers blended with the fullerene electron acceptors PCBM and ICBA. *Advanced Functional Materials*, 23(26):3286–3298, 2013.

[160] Haibo Ma and Alessandro Troisi. Direct optical generation of long-range charge-transfer states in organic photovoltaics. *Advanced Materials*, 26(35):6163–6167, 2014.

[161] Eric R Bittner and Carlos Silva. Noise-induced quantum coherence drives photocarrier generation dynamics at polymeric semiconductor heterojunctions. *Nature Communications*, 5:3119, 2014.

[162] D Amarasinghe Vithanage, A Devižis, V Abramavičius, Yingyot Infahsaeng, D Abramavičius, RCI MacKenzie, PE Keivanidis, Arkady Yartsev, D Hertel, J Nelson, et al. Visualizing charge separation in bulk heterojunction organic solar cells. *Nature Communications*, 4:2334, 2013.

[163] Feng Gao, Wolfgang Tress, Jianpu Wang, and Olle Inganäs. Temperature dependence of charge carrier generation in organic photovoltaics. *Physical Review Letters*, 114(12):128701, 2015.

[164] Brian A Gregg. Entropy of charge separation in organic photovoltaic cells: The benefit of higher dimensionality. *The Journal of Physical Chemistry Letters*, 2(24):3013–3015, 2011.

[165] Nicholas R Monahan, Kristopher W Williams, Bharat Kumar, Colin Nuckolls, and X-Y Zhu. Direct observation of entropy-driven electron-hole pair separation at an organic semiconductor interface. *Physical Review Letters*, 114(24):247003, 2015.

[166] Xian-Kai Chen, Veaceslav Coropceanu, and Jean-Luc Brédas. Assessing the nature of the charge-transfer electronic states in organic solar cells. *Nature Communications*, 9(1):5295, 2018.

[167] Flurin D Eisner, Mohammed Azzouzi, Zhuping Fei, Xueyan Hou, Thomas D Anthopoulos, T John S Dennis, Martin Heeney, and Jenny Nelson. Hybridization of local exciton and charge-transfer states reduces nonradiative voltage losses in organic solar cells. *Journal of the American Chemical Society*, 141(15):6362–6374, 2019.

[168] Guangchao Han and Yuanping Yi. Local excitation/charge-transfer hybridization simultaneously promotes charge generation and reduces nonradiative voltage loss in nonfullerene organic solar cells. *The Journal of Physical Chemistry Letters*, 10:2911–2918, 2019.

[169] Shuixing Li, Lingling Zhan, Chenkai Sun, Haiming Zhu, Guanqing Zhou, Weitao Yang, Minmin Shi, Chang-Zhi Li, Jianhui Hou, Yongfang Li, et al. Highly efficient fullerene-free organic solar cells operate at near zero highest occupied molecular orbital offsets. *Journal of the American Chemical Society*, 141(7):3073–3082, 2019.

[170] Hao Zhang, Sunsun Li, Bowei Xu, Huifeng Yao, Bei Yang, and Jianhui Hou. Fullerene-free polymer solar cell based on a polythiophene derivative with an unprecedented energy loss of less than 0.5 ev. *Journal of Materials Chemistry A*, 4(46):18043–18049, 2016.

[171] Chenyi Yang, Jianqi Zhang, Ningning Liang, Huifeng Yao, Zhixiang Wei, Chang He, Xiaotao Yuan, and Jianhui Hou. Effects of energy-level offset between a donor and acceptor on the photovoltaic performance of non-fullerene organic solar cells. *Journal of Materials Chemistry A*, 7(32):18889–18897, 2019.

[172] Daobin Yang, Yuming Wang, Takeshi Sano, Feng Gao, Hisahiro Sasabe, and Junji Kido. A minimal non-radiative recombination loss for efficient non-fullerene all-small-molecule organic solar cells with a low energy loss of 0.54 ev and high open-circuit voltage of 1.15 v. *Journal of Materials Chemistry A*, 6(28):13918–13924, 2018.

[173] Tracey M Clarke, Amy Ballantyne, Safa Shoaee, Ying W Soon, Warren Duffy, Martin Heeney, Iain McCulloch, Jenny Nelson, and James R Durrant. Analysis of charge photogeneration as a key determinant of photocurrent density in polymer: fullerene solar cells. *Advanced Materials*, 22(46):5287–5291, 2010.

[174] Jiangbin Zhang, Qinying Gu, Thu Trang Do, Kira Rundel, Prashant Sonar, Richard H Friend, Christopher R McNeill, and Artem A Bakulin. Control of geminate recombination by the material composition and processing conditions in novel polymer: Nonfullerene acceptor photovoltaic devices. *The Journal of Physical Chemistry A*, 122(5):1253–1260, 2018.

[175] Safakath Karuthedath, Armantas Melianas, Zhipeng Kan, Vytenis Pranculis, Markus Wohlfahrt, Jafar I Khan, Julien Gorenflot, Yuxin Xia, Olle Inganäs, Vidmantas Gulbinas, et al. Thermal annealing reduces geminate recombination in TQ1:N2200 all-polymer solar cells. *Journal of Materials Chemistry A*, 6(17):7428–7438, 2018.

[176] Sarah R Cowan, Anshuman Roy, and Alan J Heeger. Recombination in polymer-fullerene bulk heterojunction solar cells. *Physical Review B*, 82(24):245207, 2010.

[177] Ching-Hong Tan, Andrew Wadsworth, Nicola Gasparini, Scot Wheeler, Sarah Holliday, Raja Shahid Ashraf, Stoichko D Dimitrov, Derya Baran, Iain McCulloch, and James R Durrant. Excitation wavelength dependent internal quantum efficiencies in a P3HT/non-fullerene acceptor solar cell. *The Journal of Physical Chemistry C*, 2018.

[178] LJA Koster, VD Mihailetchi, and PWM Blom. Bimolecular recombination in polymer/fullerene bulk heterojunction solar cells. *Applied Physics Letters*, 88(5):052104, 2006.

[179] Akshay Rao, Philip CY Chow, Simon Gélinas, Cody W Schlenker, Chang-Zhi Li, Hin-Lap Yip, Alex K-Y Jen, David S Ginger, and Richard H Friend. The role of spin in the kinetic control of recombination in organic photovoltaics. *Nature*, 500(7463):435–439, 2013.

[180] Dan Credgington, Fiona C Jamieson, Bright Walker, Thuc-Quyen Nguyen, and James R Durrant. Quantification of geminate and non-geminate recombination losses within a solution-processed small-molecule bulk heterojunction solar cell. *Advanced Materials*, 24(16):2135–2141, 2012.

[181] Katie D Rosenthal, Michael P Hughes, Benjamin R Luginbuhl, Niva A Ran, Akchheta Karki, Seo-Jin Ko, Huawei Hu, Ming Wang, Harald Ade, and Thuc-Quyen Nguyen. Quantifying and understanding voltage losses due to nonradiative recombination in bulk heterojunction organic solar cells with low energetic offsets. *Advanced Energy Materials*, 9(27):1901077, 2019.

[182] Timothy M Burke, Sean Sweetnam, Koen Vandewal, and Michael D McGehee. Beyond langevin recombination: How equilibrium between free carriers and charge transfer states determines the open-circuit voltage of organic solar cells. *Advanced Energy Materials*, 5(11):1500123, 2015.

[183] S Matthew Menke, Aditya Sadhanala, Mark Nikolka, Niva A Ran, Mahesh Kumar Ravva, Safwat Abdel-Azeim, Hannah L Stern, Ming Wang, Henning Sirringhaus, Thuc-Quyen Nguyen, et al. Limits for recombination in a low energy loss organic heterojunction. *ACS Nano*, 10(12):10736–10744, 2016.

[184] Jiangbin Zhang, Andreas C Jakowetz, Guangru Li, Dawei Di, S Matthew Menke, Akshay Rao, Richard H Friend, and Artem A Bakulin. On the energetics of bound charge-transfer states in organic photovoltaics. *Journal of Materials Chemistry A*, 5(23):11949–11959, 2017.

[185] Cody W Schlenker, Kung-Shih Chen, Hin-Lap Yip, Chang-Zhi Li, Liam R Bradshaw, Stefan T Ochsenbein, Feizhi Ding, Xiaosong S Li, Daniel R Gamelin, Alex K-Y Jen, et al. Polymer triplet energy levels need not limit photocurrent collection in organic solar cells. *Journal of the American Chemical Society*, 134(48):19661–19668, 2012.

[186] Lei Yang, Wenxing Gu, Lei Lv, Yusheng Chen, Yufei Yang, Pan Ye, Jianfei Wu, Ling Hong, Aidong Peng, and Hui Huang. Triplet tellurophene-based acceptors for organic solar cells. *Angewandte Chemie International Edition*, 57(4):1096–1102, 2018.

[187] Xiaowei Zhan and Yongfang Li. A new perspective for organic solar cells: triplet nonfullerene acceptors. *Science China Chemistry*, 61(6):637–638, 2018.

[188] Mark E Ziffer, Sae Byeok Jo, Hongliang Zhong, Long Ye, Hongbin Liu, Francis Lin, Jie Zhang, Xiaosong Li, Harald W Ade, Alex K-Y Jen, et al. Long-lived, non-geminate, radiative recombination of photogenerated charges in a polymer/small-molecule acceptor photovoltaic blend. *Journal of the American Chemical Society*, 140(31):9996–10008, 2018.

[189] Jonathan Mooney and Patanjali Kambhampati. Get the basics right: Jacobian conversion of wavelength and energy scales for quantitative analysis of emission spectra. *The Journal of Physical Chemistry Letters*, 4(19):3316–3318, 2013.

[190] Warren B Jackson, Nabi1 M Amer, AC Boccara, and D Fournier. Photothermal deflection spectroscopy and detection. *Applied Optics*, 20(8):1333–1344, 1981.

[191] Deepak Venkateshvaran, Mark Nikolka, Aditya Sadhanala, Vincent Lemaur, Mateusz Zelazny, Michal Kepa, Michael Hurhangee, Auke Jisk Kronemeijer, Vincenzo Pecunia, Iyad Nasrallah, et al. Approaching disorder-free transport in high-mobility conjugated polymers. *Nature*, 515(7527):384–388, 2014.

[192] G Leahu, R Li Voti, C Sibilia, M Bertolotti, V Golubev, DA Kurdyukov, and S Kaplan. Thermal and optical properties of SiO_2/GaN opals by photo thermal deflection technique. In *The European Conference on Lasers and Electro-Optics*, page CK_27. Optical Society of America, 2007.

[193] Ester Buchaca-Domingo, Koen Vandewal, Zhuping Fei, Scott E Watkins, Fiona H Scholes, James H Bannock, John C de Mello, Lee J Richter, Dean M DeLongchamp, Aram Amassian, et al. Direct correlation of charge transfer absorption with molecular donor: acceptor interfacial area via photothermal deflection spectroscopy. *Journal of the American Chemical Society*, 137(16):5256–5259, 2015.

[194] NC Greenham, IDW Samuel, GR Hayes, RT Phillips, YARR Kessener, SC Moratti, AB Holmes, and RH Friend. Measurement of absolute photoluminescence quantum efficiencies in conjugated polymers. *Chemical Physics Letters*, 241(1-2):89–96, 1995.

[195] John C de Mello, H Felix Wittmann, and Richard H Friend. An improved experimental determination of external photoluminescence quantum efficiency. *Advanced Materials*, 9(3):230–232, 1997.

[196] Anna Köhler and Heinz Bässler. *Electronic processes in organic semiconductors: An introduction*. John Wiley & Sons, 2015.

[197] David A Hanifi, Noah D Bronstein, Brent A Koscher, Zach Nett, Joseph K Swabeck, Kaori Takano, Adam M Schwartzberg, Lorenzo Maserati, Koen Vandewal, Yoeri van de Burgt, et al. Redefining near-unity luminescence in quantum dots with photothermal threshold quantum yield. *Science*, 363(6432):1199–1202, 2019.

[198] Kai Chen, Joseph K Gallaher, Alex J Barker, and Justin M Hodgkiss. Transient grating photoluminescence spectroscopy: an ultrafast method of gating broadband spectra. *The Journal of Physical Chemistry Letters*, 5(10):1732–1737, 2014.

[199] Bhoj R Gautam, Andy Barrette, Cong Mai, Liang Yan, Qianqian Zhang, Evgeny Danilov, Wei You, Harald Ade, and Kenan Gundogdu. Direct optical observation of stimulated emission from hot charge transfer excitons in bulk heterojunction polymer solar cells. *The Journal of Physical Chemistry C*, 119(34):19697–19702, 2015.

[200] Andreas C Jakowetz, Marcus L Böhm, Aditya Sadhanala, Sven Huettner, Akshay Rao, and Richard H Friend. Visualizing excitations at buried heterojunctions in organic semiconductor blends. *Nature Materials*, 16(5):551–557, 2017.

[201] T Wilhelm, J Piel, and E Riedle. Sub-20-fs pulses tunable across the visible from a blue-pumped single-pass noncollinear parametric converter. *Optics Letters*, 22(19):1494–1496, 1997.

[202] Vadim V Lozovoy, Igor Pastirk, and Marcos Dantus. Multiphoton intrapulse interference. iv. ultrashort laser pulse spectral phase characterization and compensation. *Optics Letters*, 29(7):775–777, 2004.

[203] Artem A Bakulin, Carlos Silva, and Eleonora Vella. Ultrafast spectroscopy with photocurrent detection: watching excitonic optoelectronic systems at work. *The Journal of Physical Chemistry Letters*, 7(2):250–258, 2016.

[204] LV Lukin, AV Tolmachev, and BS Yakovlev. The photoexcitation of trapped electrons produced in the photoionization of anthracene in liquid n-hexane. *Chemical Physics Letters*, 81(3):595–598, 1981.

[205] FF Brazgun, VA Nadtochenko, IV Rubtsov, and LV Lukin. Dynamics of geminate charge separation in liquid methylcyclohexane studied by the photoassisted ion pair separation technique. *Chemical Physics*, 211(1-3):469–488, 1996.

[206] Eugene Frankevich, Hisao Ishii, Yasushi Hamanaka, Takahiro Yokoyama, Akihiko Fuji, Sergey Li, Katsumi Yoshino, Arao Nakamura, and Kazuhiko Seki. Formation of polaron pairs and time-resolved photogeneration of free charge carriers in π-conjugated polymers. *Physical Review B*, 62(4):2505, 2000.

[207] JG Müller, U Lemmer, J Feldmann, and U Scherf. Precursor states for charge carrier generation in conjugated polymers probed by ultrafast spectroscopy. *Physical Review Letters*, 88(14):147401, 2002.

[208] Artem A Bakulin, Stefanie Neutzner, Huib J Bakker, Laurent Ottaviani, Damien Barakel, and Zhuoying Chen. Charge trapping dynamics in PbS colloidal quantum dot photovoltaic devices. *ACS Nano*, 7(10):8771–8779, 2013.

[209] Yana Vaynzof, Artem A Bakulin, Simon Gélinas, and Richard H Friend. Direct observation of photoinduced bound charge-pair states at an organic-inorganic semiconductor interface. *Physical Review Letters*, 108(24):246605, 2012.

[210] Olympia Pachoumi, Artem A Bakulin, Aditya Sadhanala, Henning Sirringhaus, Richard H Friend, and Yana Vaynzof. Improved performance of ZnO/polymer hybrid photovoltaic devices by combining metal oxide doping and interfacial modification. *The Journal of Physical Chemistry C*, 118(33):18945–18950, 2014.

[211] Artem A Bakulin, Robert Lovrincic, Xi Yu, Oleg Selig, Huib J Bakker, Yves LA Rezus, Pabitra K Nayak, Alexandr Fonari, Veaceslav Coropceanu, Jean-Luc Brédas, et al. Mode-selective vibrational modulation of charge transport in organic electronic devices. *Nature Communications*, 6:7880, 2015.

[212] Christoph J Brabec, Gerald Zerza, Giulio Cerullo, Sandro De Silvestri, Silvia Luzzati, Jan C Hummelen, and Serdar Sariciftci. Tracing photoinduced electron transfer process in conjugated polymer/fullerene bulk heterojunctions in real time. *Chemical Physics Letters*, 340(3-4):232–236, 2001.

[213] Jean-Luc Brédas, Joseph E Norton, Jérôme Cornil, and Veaceslav Coropceanu. Molecular understanding of organic solar cells: the challenges. *Accounts of Chemical Research*, 42(11):1691–1699, 2009.

[214] Gordon J Hedley, Arvydas Ruseckas, and Ifor DW Samuel. Light harvesting for organic photovoltaics. *Chemical Reviews*, 117(2):796–837, 2016.

[215] Frédéric Laquai, Denis Andrienko, Carsten Deibel, and Dieter Neher. Charge carrier generation, recombination, and extraction in polymer–fullerene bulk heterojunction organic solar cells. In *Elementary Processes in Organic Photovoltaics*, pages 267–291. Springer, 2017.

[216] Maria Antonietta Loi and Alessandro Troisi. Charge generation mechanism in organic solar cells. *Physical Chemistry Chemical Physics*, 16(38):20277–20278, 2014.

[217] Jonathan D Servaites, Mark A Ratner, and Tobin J Marks. Organic solar cells: A new look at traditional models. *Energy & Environmental Science*, 4(11):4410–4422, 2011.

[218] Patrick E Hartnett, Catherine M Mauck, Michelle A Harris, Ryan M Young, Yi-Lin Wu, Tobin J Marks, and Michael R Wasielewski. Influence of anion delocalization on electron transfer in a covalent porphyrin donor–perylenediimide dimer acceptor system. *Journal of the American Chemical Society*, 139(2):749–756, 2017.

[219] Samantha N Hood and Ivan Kassal. Entropy and disorder enable charge separation in organic solar cells. *The Journal of Physical Chemistry Letters*, 7(22):4495–4500, 2016.

[220] Zhiqiang Guan, Ho-Wa Li, Yuanhang Cheng, Qingdan Yang, Ming-Fai Lo, Tsz-Wai Ng, Sai-Wing Tsang, and Chun-Sing Lee. Charge-transfer state energy and its relationship with open-circuit voltage in an organic photovoltaic device. *The Journal of Physical Chemistry C*, 120(26):14059–14068, 2016.

[221] Claudia Piliego and Maria Antonietta Loi. Charge transfer state in highly efficient polymer–fullerene bulk heterojunction solar cells. *Journal of Materials Chemistry*, 22(10):4141–4150, 2012.

[222] Koen Vandewal, Kristofer Tvingstedt, Abay Gadisa, Olle Inganäs, and Jean V Manca. Relating the open-circuit voltage to interface molecular properties of donor:acceptor bulk heterojunction solar cells. *Physical Review B*, 81(12):125204, 2010.

[223] Guangjun Nan, Xu Zhang, and Gang Lu. The lowest-energy charge-transfer state and its role in charge separation in organic photovoltaics. *Physical Chemistry Chemical Physics*, 18(26):17546–17556, 2016.

[224] Ivan G. Scheblykin, Arkady Yartsev, Tonu Pullerits, Vidmantas Gulbinas, and Villy Sundström. Excited state and charge photogeneration dynamics in conjugated polymers. *The Journal of Physical Chemistry B*, 111(23):6303–6321, 2007. PMID: 17521181.

[225] Tracey M Clarke, Jeff Peet, Christoph Lungenschmied, Nicolas Drolet, Xinhui Lu, Benjamin M Ocko, Attila J Mozer, and Maria Antonietta Loi. The role of emissive charge transfer states in two polymer–fullerene organic photovoltaic blends: tuning charge photogeneration through the use of processing additives. *Journal of Materials Chemistry A*, 2(31):12583–12593, 2014.

[226] Marianna Manca, Claudia Piliego, Ergang Wang, Mats R Andersson, Andrea Mura, and Maria A Loi. Tracing charge transfer states in polymer: fullerene bulk-heterojunctions. *Journal of Materials Chemistry A*, 1(25):7321–7325, 2013.

[227] Philip CY Chow, Sebastian Albert-Seifried, Simon Gélinas, and Richard H Friend. Nanosecond intersystem crossing times in fullerene acceptors: Implications for organic photovoltaic diodes. *Advanced Materials*, 26(28):4851–4854, 2014.

[228] Yunlong Zou and Russell J Holmes. Correlation between the open-circuit voltage and charge transfer state energy in organic photovoltaic cells. *ACS Applied Materials & Interfaces*, 7(33):18306–18311, 2015.

[229] Sibel Leblebici, Jiye Lee, Alexander Weber-Bargioni, and Biwu Ma. Dielectric screening to reduce charge transfer state binding energy in organic bulk heterojunction photovoltaics. *The Journal of Physical Chemistry C*, 121(6):3279–3285, 2017.

[230] Julia Kern, Sebastian Schwab, Carsten Deibel, and Vladimir Dyakonov. Binding energy of singlet excitons and charge transfer complexes in MDMO-PPV:PCBM solar cells. *Physica Status Solidi (RRL)–Rapid Research Letters*, 5(10-11):364–366, 2011.

[231] Matthias Muntwiler, Qingxin Yang, William A Tisdale, and X-Y Zhu. Coulomb barrier for charge separation at an organic semiconductor interface. *Physical Review Letters*, 101(19):196403, 2008.

[232] Meng-Ju Sher, Jonathan A Bartelt, Timothy M Burke, Alberto Salleo, Michael D McGehee, and Aaron M Lindenberg. Time-and temperature-independent local carrier mobility and effects of regioregularity in polymer-fullerene organic semiconductors. *Advanced Electronic Materials*, 2(3):1500351, 2016.

[233] Marina Gerhard, Andreas P Arndt, Ian A Howard, Arash Rahimi-Iman, Uli Lemmer, and Martin Koch. Temperature-and energy-dependent separation of charge-transfer states in PTB7-based organic solar cells. *The Journal of Physical Chemistry C*, 119(51):28309–28318, 2015.

[234] Andreas P Arndt, Marina Gerhard, Aina Quintilla, Ian A Howard, Martin Koch, and Uli Lemmer. Time-resolved charge-transfer state emission in organic solar cells: Temperature and blend composition dependences of interfacial traps. *The Journal of Physical Chemistry C*, 119(24):13516–13523, 2015.

[235] Nico Christ, Siegfried W Kettlitz, Sebastian Valouch, Jan Mescher, Mirco Nintz, and Uli Lemmer. Intensity dependent but temperature independent charge carrier generation in organic photodiodes and solar cells. *Organic Electronics*, 14(3):973–978, 2013.

[236] Wojciech J Grzegorczyk, Tom J Savenije, Tieneke E Dykstra, Jorge Piris, Juleon M Schins, and Laurens DA Siebbeles. Temperature-independent charge carrier photogeneration in P3HT-PCBM blends with different morphology. *The Journal of Physical Chemistry C*, 114(11):5182–5186, 2010.

[237] Ryan D Pensack and John B Asbury. Barrierless free carrier formation in an organic photovoltaic material measured with ultrafast vibrational spectroscopy. *Journal of the American Chemical Society*, 131(44):15986–15987, 2009.

[238] Ingo Riedel, Jürgen Parisi, Vladimir Dyakonov, Laurence Lutsen, Dirk Vanderzande, and Jan C Hummelen. Effect of temperature and illumination on the electrical characteristics of polymer–fullerene bulk-heterojunction solar cells. *Advanced Functional Materials*, 14(1):38–44, 2004.

[239] Andreas Petersen, Antti Ojala, Thomas Kirchartz, Thomas A Wagner, Frank Würthner, and Uwe Rau. Field-dependent exciton dissociation in organic heterojunction solar cells. *Physical Review B*, 85(24):245208, 2012.

[240] EA Katz, D Faiman, SM Tuladhar, JM Kroon, MM Wienk, T Fromherz, F Padinger, CJ Brabec, and NS Sariciftci. Temperature dependence for the photovoltaic device parameters of polymer-fullerene solar cells under operating conditions. *Journal of Applied Physics*, 90(10):5343–5350, 2001.

[241] Dorota Jarzab, Fabrizio Cordella, Jio Gao, Markus Scharber, Hans-Joachim Egelhaaf, and Maria Antonietta Loi. Low-temperature behaviour of charge transfer excitons in narrow-bandgap polymer-based bulk heterojunctions. *Advanced Energy Materials*, 1(4):604–609, 2011.

[242] Marina Gerhard, Andreas P Arndt, Mühenad Bilal, Uli Lemmer, Martin Koch, and Ian A Howard. Field-induced exciton dissociation in PTB7-based organic solar cells. *Physical Review B*, 95(19):195301, 2017.

[243] Song Chen, Sai-Wing Tsang, Tzung-Han Lai, John R Reynolds, and Franky So. Dielectric effect on the photovoltage loss in organic photovoltaic cells. *Advanced Materials*, 26(35):6125–6131, 2014.

[244] R Alex Marsh, Justin M Hodgkiss, and Richard H Friend. Direct measurement of electric field-assisted charge separation in polymer:fullerene photovoltaic diodes. *Advanced Materials*, 22(33):3672–3676, 2010.

[245] Harald Hoppe, Michael Niggemann, Christoph Winder, Jürgen Kraut, Renate Hiesgen, Andreas Hinsch, Dieter Meissner, and Niyazi Serdar Sariciftci. Nanoscale morphology of conjugated polymer/fullerene-based bulk-heterojunction solar cells. *Advanced Functional Materials*, 14(10):1005–1011, 2004.

[246] Martina Causa', Jelissa De Jonghe-Risse, Mariateresa Scarongella, Jan C Brauer, Ester Buchaca-Domingo, Jacques-E Moser, Natalie Stingelin, and Natalie Banerji. The fate of electron–hole pairs in polymer: fullerene blends for organic photovoltaics. *Nature Communications*, 7:12556, 2016.

[247] Fernando Fernández-Lázaro, Nathalie Zink-Lorre, and Ángela Sastre-Santos. Perylenediimides as non-fullerene acceptors in bulk-heterojunction solar cells (BHJSCs). *Journal of Materials Chemistry A*, 4(24):9336–9346, 2016.

[248] Christian B Nielsen, Sarah Holliday, Hung-Yang Chen, Samuel J Cryer, and Iain McCulloch. Non-fullerene electron acceptors for use in organic solar cells. *Accounts of Chemical Research*, 48(11):2803–2812, 2015.

[249] Ningning Liang, Wei Jiang, Jianhui Hou, and Zhaohui Wang. New developments in non-fullerene small molecule acceptors for polymer solar cells. *Materials Chemistry Frontiers*, 1(7):1291–1303, 2017.

[250] Bin Kan, Huanran Feng, Xiangjian Wan, Feng Liu, Xin Ke, Yanbo Wang, Yunchuang Wang, Hongtao Zhang, Chenxi Li, Jianhui Hou, et al. Small-molecule acceptor based on the heptacyclic benzodi(cyclopentadithiophene) unit for highly efficient non-fullerene organic solar cells. *Journal of the American Chemical Society*, 139(13):4929–4934, 2017.

[251] Yongxi Li, Minchao Gu, Zhe Pan, Bin Zhang, Xutong Yang, Junwei Gu, and Yu Chen. Indacenodithiophene: a promising building block for high performance polymer solar cells. *Journal of Materials Chemistry A*, 5(22):10798–10814, 2017.

[252] Huifeng Yao, Long Ye, Hao Zhang, Sunsun Li, Shaoqing Zhang, and Jianhui Hou. Molecular design of benzodithiophene-based organic photovoltaic materials. *Chemical Reviews*, 116(12):7397–7457, 2016.

[253] Xueliang Shi, Lijian Zuo, Sae Byeok Jo, Ke Gao, Francis Lin, Feng Liu, and Alex K-Y Jen. Design of a highly crystalline low-band gap fused-ring electron acceptor for high-efficiency solar cells with low energy loss. *Chemistry of Materials*, 29(19):8369–8376, 2017.

[254] Thu Trang Do, Kira Rundel, Qinying Gu, Eliot Gann, Sergei Manzhos, Krishna Feron, John Bell, Christopher R McNeill, and Prashant Sonar. 9-Fluorenone and 9, 10-anthraquinone potential fused aromatic building blocks to synthesize electron acceptors for organic solar cells. *New Journal of Chemistry*, 41(8):2899–2909, 2017.

[255] Wanli Ma, Cuiying Yang, Xiong Gong, Kwanghee Lee, and Alan J Heeger. Thermally stable, efficient polymer solar cells with nanoscale control of the interpenetrating network morphology. *Advanced Functional Materials*, 15(10):1617–1622, 2005.

[256] Muhammad T Sajjad, Alexander J Ward, Christian Kästner, Arvydas Ruseckas, Harald Hoppe, and Ifor DW Samuel. Controlling exciton diffusion and fullerene distribution in photovoltaic blends by side chain modification. *The Journal of Physical Chemistry Letters*, 6(15):3054–3060, 2015.

[257] Wei Ma, John R Tumbleston, Ming Wang, Eliot Gann, Fei Huang, and Harald Ade. Domain purity, miscibility, and molecular orientation at donor/acceptor interfaces in high performance organic solar cells: paths to further improvement. *Advanced Energy Materials*, 3(7):864–872, 2013.

[258] Wenchao Huang, Eliot Gann, Naresh Chandrasekaran, Lars Thomsen, Shyamal KK Prasad, Justin M Hodgkiss, Dinesh Kabra, Yi-Bing Cheng, and Christopher R McNeill. Isolating and quantifying the impact of domain purity on the performance of bulk heterojunction solar cells. *Energy & Environmental Science*, 10(8):1843–1853, 2017.

[259] Justin M Hodgkiss, Andrew R Campbell, R Alex Marsh, Akshay Rao, Sebastian Albert-Seifried, and Richard H Friend. Subnanosecond geminate charge recombination in polymer-polymer photovoltaic devices. *Physical Review Letters*, 104(17):177701, 2010.

[260] Ryota Kabe and Chihaya Adachi. Organic long persistent luminescence. *Nature*, 550(7676):384–387, 2017.

[261] Jiangbin Zhang, Bin Kan, Andrew J Pearson, Andrew J Parnell, Joshaniel FK Cooper, Xiao-Ke Liu, Patrick J Conaghan, Thomas R Hopper, Yutian Wu, Xiangjian Wan, et al. Efficient non-fullerene organic solar cells employing sequentially deposited donor–acceptor layers. *Journal of Materials Chemistry A*, 6(37):18225–18233, 2018.

[262] Alan J Heeger. 25th anniversary article: bulk heterojunction solar cells: understanding the mechanism of operation. *Advanced Materials*, 26(1):10–28, 2014.

[263] Fuwen Zhao, Chunru Wang, and Xiaowei Zhan. Morphology control in organic solar cells. *Advanced Energy Materials*, 8(28):1703147, 2018.

[264] Jarvist M Frost, Fabien Cheynis, Sachetan M Tuladhar, and Jenny Nelson. Influence of polymer-blend morphology on charge transport and photocurrent generation in donor- acceptor polymer blends. *Nano Letters*, 6(8):1674–1681, 2006.

[265] Serap Günes, Helmut Neugebauer, and Niyazi Serdar Sariciftci. Conjugated polymer-based organic solar cells. *Chemical Reviews*, 107(4):1324–1338, 2007.

[266] Jingbo Zhao, Yunke Li, Guofang Yang, Kui Jiang, Haoran Lin, Harald Ade, Wei Ma, and He Yan. Efficient organic solar cells processed from hydrocarbon solvents. *Nature Energy*, 1(2):15027, 2016.

[267] Markus C Scharber, David Mühlbacher, Markus Koppe, Patrick Denk, Christoph Waldauf, Alan J Heeger, and Christoph J Brabec. Design rules for donors in bulk-heterojunction solar cells—towards 10% energy-conversion efficiency. *Advanced Materials*, 18(6):789–794, 2006.

[268] Jean-Luc Brédas, Joseph E Norton, Jérôme Cornil, and Veaceslav Coropceanu. Molecular understanding of organic solar cells: the challenges. *Accounts of Chemical Research*, 42(11):1691–1699, 2009.

[269] Long Ye, Huawei Hu, Masoud Ghasemi, Tonghui Wang, Brian A Collins, Joo-Hyun Kim, Kui Jiang, Joshua H Carpenter, Hong Li, Zhengke Li, Terry McAfee, Jingbo Zhao, Xiankai Chen, Joshua Lin Yuk Lai, Tingxuan Ma, Jean-Luc Brédas, He Yan, and Harald Ade. Quantitative relations between interaction parameter, miscibility and function in organic solar cells. *Nature Materials*, 17(3):253–260, 2018.

[270] Pei Cheng, Cenqi Yan, Yang Wu, Shuixing Dai, Wei Ma, and Xiaowei Zhan. Efficient and stable organic solar cells via a sequential process. *Journal of Materials Chemistry C*, 4(34):8086–8093, 2016.

[271] Jeesoo Seok, Tae Joo Shin, Sungmin Park, Changsoon Cho, Jung-Yong Lee, Du Yeol Ryu, Myung Hwa Kim, and Kyungkon Kim. Efficient organic photovoltaics utilizing nanoscale heterojunctions in sequentially deposited polymer/fullerene bilayer. *Scientific Reports*, 5:8373, 2015.

[272] Dian Chen, Feng Liu, Cheng Wang, Atsuhiro Nakahara, and Thomas P Russell. Bulk heterojunction photovoltaic active layers via bilayer interdiffusion. *Nano Letters*, 11(5):2071–2078, 2011.

[273] Liqiang Huang, Gang Wang, Weihua Zhou, Boyi Fu, Xiaofang Cheng, Lifu Zhang, Zhibo Yuan, Sixing Xiong, Lin Zhang, Yuanpeng Xie, et al. Vertical stratification engineering for organic bulk-heterojunction devices. *ACS Nano*, 12(5):4440–4452, 2018.

[274] Yoonhee Jang, Yun Ju Cho, Minjung Kim, Jeesoo Seok, Hyungju Ahn, and Kyungkon Kim. Formation of thermally stable bulk heterojunction by reducing the polymer and fullerene intermixing. *Scientific Reports*, 7(1):9690, 2017.

[275] Heewon Hwang, Hoyeon Lee, Shafidah Shafian, Wooseop Lee, Jeesoo Seok, Ka Ryu, Yeol Du Ryu, and Kyungkon Kim. Thermally stable bulk heterojunction prepared by sequential deposition of nanostructured polymer and fullerene. *Polymers*, 9(9):456, 2017.

[276] Jacobus J van Franeker, Sandra Kouijzer, Xianwen Lou, Mathieu Turbiez, Martijn M Wienk, and René AJ Janssen. Depositing fullerenes in swollen polymer layers via sequential processing of organic solar cells. *Advanced Energy Materials*, 5(14):1500464, 2015.

[277] Jordan C Aguirre, Steven A Hawks, Amy S Ferreira, Patrick Yee, Selvam Subramaniyan, Samson A Jenekhe, Sarah H Tolbert, and Benjamin J Schwartz. Sequential processing for organic photovoltaics: Design rules for morphology control by tailored semi-orthogonal solvent blends. *Advanced Energy Materials*, 5(11):1402020, 2015.

[278] Pei Cheng, Jianhui Hou, Yongfang Li, and Xiaowei Zhan. Layer-by-layer solution-processed low-bandgap polymer-$PC_{61}BM$ solar cells with high efficiency. *Advanced Energy Materials*, 4(9):1301349, 2014.

[279] Dong Hwan Wang, Ji Sun Moon, Jason Seifter, Jang Jo, Jong Hyeok Park, O Ok Park, and Alan J Heeger. Sequential processing: control of nanomorphology in bulk heterojunction solar cells. *Nano Letters*, 11(8):3163–3168, 2011.

[280] Ji Sun Moon, Christopher J Takacs, Yanming Sun, and Alan J Heeger. Spontaneous formation of bulk heterojunction nanostructures: Multiple routes to equivalent morphologies. *Nano Letters*, 11(3):1036–1039, 2011.

[281] Yu Yan, Xuan Liu, and Tao Wang. Conjugated-polymer blends for organic photovoltaics: Rational control of vertical stratification for high performance. *Advanced Materials*, 29(20):1601674, 2017.

[282] Kyohei Nakano and Keisuke Tajima. Organic planar heterojunctions: From models for interfaces in bulk heterojunctions to high-performance solar cells. *Advanced Materials*, 29(25):1603269, 2017.

[283] Shusei Inaba and Varun Vohra. Fabrication processes to generate concentration gradients in polymer solar cell active layers. *Materials*, 10(5):518, 2017.

[284] Wenchao Zhao, Sunsun Li, Huifeng Yao, Shaoqing Zhang, Yun Zhang, Bei Yang, and Jianhui Hou. Molecular optimization enables over 13% efficiency in organic solar cells. *Journal of the American Chemical Society*, 139(21):7148–7151, 2017.

[285] Guangjun Zhang, Guofang Yang, He Yan, Joo-Hyun Kim, Harald Ade, Wenlin Wu, Xiaopeng Xu, Yuwei Duan, and Qiang Peng. Efficient nonfullerene polymer solar cells enabled by a novel wide bandgap small molecular acceptor. *Advanced Materials*, 29(18):1606054, 2017.

[286] Shaoqing Zhang, Yunpeng Qin, Jie Zhu, and Jianhui Hou. Over 14% efficiency in polymer solar cells enabled by a chlorinated polymer donor. *Advanced Materials*, 30(20):1800868, 2018.

[287] Jia Sun, Xiaoling Ma, Zhuohan Zhang, Jiangsheng Yu, Jie Zhou, Xinxing Yin, Linqiang Yang, Renyong Geng, Rihong Zhu, Fujun Zhang, et al. Dithieno [3,2-b:2',3'-d] pyrrol fused nonfullerene acceptors enabling over 13% efficiency for organic solar cells. *Advanced Materials*, 30(16):1707150, 2018.

[288] Zhuping Fei, Flurin D Eisner, Xuechen Jiao, Mohammed Azzouzi, Jason A Röhr, Yang Han, Munazza Shahid, Anthony SR Chesman, Christopher D Easton, Christopher R McNeill, et al. An alkylated indacenodithieno [3, 2-b] thiophene-based nonfullerene acceptor with high crystallinity exhibiting single junction solar cell efficiencies greater than 13% with low voltage losses. *Advanced Materials*, 30(8):1705209, 2018.

[289] Sunsun Li, Long Ye, Wenchao Zhao, Hongping Yan, Bei Yang, Delong Liu, Wanning Li, Harald Ade, and Jianhui Hou. A wide band gap polymer with a deep highest occupied molecular orbital level enables 14.2% efficiency in polymer solar cells. *Journal of the American Chemical Society*, 140(23):7159–7167, 2018.

[290] Derya Baran, Nicola Gasparini, Andrew Wadsworth, Ching Hong Tan, Nimer Wehbe, Xin Song, Zeinab Hamid, Weimin Zhang, Marios Neophytou, Thomas Kirchartz, et al. Robust nonfullerene solar cells approaching unity external quantum efficiency enabled by suppression of geminate recombination. *Nature Communications*, 9(1):2059, 2018.

[291] Xiaopeng Xu, Zhaozhao Bi, Wei Ma, Zishuai Wang, Wallace CH Choy, Wenlin Wu, Guangjun Zhang, Ying Li, and Qiang Peng. Highly efficient ternary-blend polymer solar cells enabled by a nonfullerene acceptor and two polymer donors with a broad composition tolerance. *Advanced Materials*, 29(46):1704271, 2017.

[292] Guichuan Zhang, Kai Zhang, Qingwu Yin, Xiao-Fang Jiang, Zaiyu Wang, Jingming Xin, Wei Ma, He Yan, Fei Huang, and Yong Cao. High-performance ternary organic solar cell enabled by a thick active layer containing a liquid crystalline small molecule donor. *Journal of the American Chemical Society*, 139(6):2387–2395, 2017.

[293] Lijian Zuo, Jiangsheng Yu, Xueliang Shi, Francis Lin, Weihua Tang, and Alex K-Y Jen. High-efficiency nonfullerene organic solar cells with a parallel tandem configuration. *Advanced Materials*, 29(34):1702547, 2017.

[294] Yamin Zhang, Bin Kan, Yanna Sun, Yanbo Wang, Ruoxi Xia, Xin Ke, Yuan-Qiu-Qiang Yi, Chenxi Li, Hin-Lap Yip, Xiangjian Wan, et al. Nonfullerene tandem organic solar cells with high performance of 14.11%. *Advanced Materials*, 30(18):1707508, 2018.

[295] Yongxi Li, Jiu-Dong Lin, Xiaozhou Che, Yue Qu, Feng Liu, Liang-Sheng Liao, and Stephen R Forrest. High efficiency near-infrared and semitransparent non-fullerene acceptor organic photovoltaic cells. *Journal of the American Chemical Society*, 139(47):17114–17119, 2017.

[296] Yong Cui, Chenyi Yang, Huifeng Yao, Jie Zhu, Yuming Wang, Guoxiao Jia, Feng Gao, and Jianhui Hou. Efficient semitransparent organic solar cells with tunable color enabled by an ultralow-bandgap nonfullerene acceptor. *Advanced Materials*, 29(43):1703080, 2017.

[297] Shuixing Dai and Xiaowei Zhan. Nonfullerene acceptors for semitransparent organic solar cells. *Advanced Energy Materials*, 8(21):1800002, 2018.

[298] Vishal Shrotriya, Gang Li, Yan Yao, Tom Moriarty, Keith Emery, and Yang Yang. Accurate measurement and characterization of organic solar cells. *Advanced Functional Materials*, 16(15):2016–2023, 2006.

[299] Henry J Snaith. How should you measure your excitonic solar cells? *Energy & Environmental Science*, 5(4):6513–6520, 2012.

[300] Greg P Smestad, Frederik C Krebs, Carl M Lampert, Claes G Granqvist, KL Chopra, Xavier Mathew, and Hideyuki Takakura. Reporting solar cell efficiencies in solar energy materials and solar cells, 2008.

[301] Antonio Cravino, Pavel Schilinsky, and Christoph J Brabec. Characterization of organic solar cells: the importance of device layout. *Advanced Functional Materials*, 17(18):3906–3910, 2007.

[302] Deping Qian, Long Ye, Maojie Zhang, Yongri Liang, Liangjie Li, Ye Huang, Xia Guo, Shaoqing Zhang, Zhan'ao Tan, and Jianhui Hou. Design, application, and morphology study of a new photovoltaic polymer with strong aggregation in solution state. *Macromolecules*, 45(24):9611–9617, 2012.

[303] MG Harrison, J Grüner, and GCW Spencer. Analysis of the photocurrent action spectra of MEH-PPV polymer photodiodes. *Physical Review B*, 55(12):7831, 1997.

[304] Jizhong Yao, Thomas Kirchartz, Michelle S Vezie, Mark A Faist, Wei Gong, Zhicai He, Hongbin Wu, Joel Troughton, Trystan Watson, Daniel Bryant, et al. Quantifying losses in open-circuit voltage in solution-processable solar cells. *Physical Review Applied*, 4(1):014020, 2015.

[305] K Vandewal, J Benduhn, and VC Nikolis. How to determine optical gaps and voltage losses in organic photovoltaic materials. *Sustainable Energy & Fuels*, 2(3):538–544, 2018.

[306] Niva A Ran, John A Love, Christopher J Takacs, Aditya Sadhanala, Justin K Beavers, Samuel D Collins, Ye Huang, Ming Wang, Richard H Friend, Guillermo C Bazan, et al. Harvesting the full potential of photons with organic solar cells. *Advanced Materials*, 28(7):1482–1488, 2016.

[307] Huifeng Yao, Deping Qian, Hao Zhang, Yunpeng Qin, Bowei Xu, Yong Cui, Runnan Yu, Feng Gao, and Jianhui Hou. Critical role of molecular electrostatic potential on charge generation in organic solar cells. *Chinese Journal of Chemistry*, 36(6):491–494, 2018.

[308] JJM Halls, K Pichler, RH Friend, SC Moratti, and AB Holmes. Exciton dissociation at a poly (p-phenylenevinylene)/C_{60} heterojunction. *Synthetic Metals*, 77(1-3):277–280, 1996.

[309] Thomas Stübinger and Wolfgang Brütting. Exciton diffusion and optical interference in organic donor–acceptor photovoltaic cells. *Journal of Applied Physics*, 90(7):3632–3641, 2001.

[310] Chang Liu, Kai Wang, Xiong Gong, and Alan J Heeger. Low bandgap semiconducting polymers for polymeric photovoltaics. *Chemical Society Reviews*, 45(17):4825–4846, 2016.

[311] Zichun Zhou, Shengjie Xu, Jingnan Song, Yingzhi Jin, Qihui Yue, Yuhao Qian, Feng Liu, Fengling Zhang, and Xiaozhang Zhu. High-efficiency small-molecule ternary solar cells with a hierarchical morphology enabled by synergizing fullerene and non-fullerene acceptors. *Nature Energy*, 3(11):952, 2018.

[312] Baobing Fan, Xiaoyan Du, Feng Liu, Wenkai Zhong, Lei Ying, Ruihao Xie, Xiaofeng Tang, Kang An, Jingming Xin, Ning Li, et al. Fine-tuning of the chemical structure of photoactive materials for highly efficient organic photovoltaics. *Nature Energy*, 3(12):1051, 2018.

[313] Wei Li, Mengxue Chen, Jinlong Cai, Emma LK Spooner, Huijun Zhang, Robert S Gurney, Dan Liu, Zuo Xiao, David G Lidzey, Liming Ding, et al. Molecular order control of non-fullerene acceptors for high-efficiency polymer solar cells. *Joule*, 3(3):819–833, 2019.

[314] Gilles Dennler, Markus C Scharber, and Christoph J Brabec. Polymer-fullerene bulk-heterojunction solar cells. *Advanced Materials*, 21(13):1323–1338, 2009.

[315] Uttiya Dasgupta and Amlan J Pal. Graded morphology in bulk-heterojunction solar cells based on colloidal semiconductor nanostructures: Directed charge-separation and facile carrier transport. *Journal of Applied Physics*, 120(8):084503, 2016.

[316] Richa Pandey and Russell J Holmes. Graded donor-acceptor heterojunctions for efficient organic photovoltaic cells. *Advanced Materials*, 22(46):5301–5305, 2010.

[317] Yajie Zhang, Dan Deng, Zaiyu Wang, Yuheng Wang, Jianqi Zhang, Jin Fang, Yang Yang, Guanghao Lu, Wei Ma, and Zhixiang Wei. Enhancing the photovoltaic performance via vertical phase distribution optimization in small molecule: $PC_{71}BM$ blends. *Advanced Energy Materials*, 7(22):1701548, 2017.

[318] Zhengguo Xiao, Yongbo Yuan, Bin Yang, Jeremy VanDerslice, Jihua Chen, Ondrej Dyck, Gerd Duscher, and Jinsong Huang. Universal formation of compositionally graded bulk heterojunction for efficiency enhancement in organic photovoltaics. *Advanced Materials*, 26(19):3068–3075, 2014.

[319] Ben Vaughan, Andrew Stapleton, Elisa Sesa, Natalie P Holmes, Xiaojing Zhou, Paul C Dastoor, and Warwick J Belcher. Engineering vertical morphology with nanoparticulate organic photovoltaic devices. *Organic Electronics*, 32:250–257, 2016.

[320] Christian G Bottenfield, Fanan Wei, Hui Joon Park, L Jay Guo, and Guangyong Li. Investigation of printing-based graded bulk-heterojunction organic solar cells. *Energy Technology*, 3(4):414–422, 2015.

[321] Long Ye, Yuan Xiong, Zheng Chen, Qianqian Zhang, Zhuping Fei, Reece Henry, Martin Heeney, Brendan T O'Connor, Wei You, and Harald Ade. Sequential deposition of organic films with eco-compatible solvents improves performance and enables over 12%-efficiency nonfullerene solar cells. *Advanced Materials*, 31(17):1808153, 2019.

[322] Rui Sun, Jie Guo, Qiang Wu, Zhuohan Zhang, Wenyan Yang, Jing Guo, Mumin Shi, Long Ye, Xuechen Jiao, Maria A. Loi, Qing Shen, Harald Ade, Weihua Tang, Christoph J. Brabec, and Jie Min. A multi-objective optimization-based layer-by-layer blade-coating approach for organic solar cells: rational control of vertical stratification for high performance. *Energy & Environmental Science*, 2019.

[323] Yong Cui, Shaoqing Zhang, Ningning Liang, Jingyi Kong, Chenyi Yang, Huifeng Yao, Lijiao Ma, and Jianhui Hou. Toward efficient polymer solar cells processed by a solution-processed layer-by-layer approach. *Advanced Materials*, 30(34):1802499, 2018.

[324] Yifan Dong, Hyojung Cha, Jiangbin Zhang, Ernest Pastor, Pabitra Shakya Tuladhar, Iain McCulloch, James R Durrant, and Artem A Bakulin. The binding energy and dynamics of charge-transfer states in organic photovoltaics with low driving force for charge separation. *The Journal of Chemical Physics*, 150(10):104704, 2019.

[325] Rui Sun, Jing Guo, Chenkai Sun, Tao Wang, Zhenghui Luo, Zhuohan Zhang, Xuechen Jiao, Weihua Tang, Chuluo Yang, Yongfang Li, et al. A universal layer-by-layer solution-processing approach for efficient non-fullerene organic solar cells. *Energy & Environmental Science*, 12(1):384–395, 2019.

[326] Pei Cheng, Rui Wang, Jingshuai Zhu, Wenchao Huang, Sheng-Yung Chang, Lei Meng, Pengyu Sun, Hao-Wen Cheng, Meng Qin, Chenhui Zhu, et al. Ternary system with controlled structure: a new strategy toward efficient organic photovoltaics. *Advanced Materials*, 30(8):1705243, 2018.

[327] Vincent Lami, Andreas Weu, Jiangbin Zhang, Yongsheng Chen, Zhuping Fei, Martin Heeney, Richard H Friend, and Yana Vaynzof. Visualizing the vertical energetic landscape in organic photovoltaics. *Joule*, 2019.

[328] John A Carr and Sumit Chaudhary. The identification, characterization and mitigation of defect states in organic photovoltaic devices: a review and outlook. *Energy & Environmental Science*, 6(12):3414–3438, 2013.

[329] Tobias Eisenbarth, Thomas Unold, Raquel Caballero, Christian A Kaufmann, and Hans-Werner Schock. Interpretation of admittance, capacitance-voltage, and current-voltage signatures in Cu(In, Ga)Se_2 thin film solar cells. *Journal of Applied Physics*, 107(3):034509, 2010.

[330] Pablo P Boix, Germà Garcia-Belmonte, Udane Muñecas, Marios Neophytou, Christoph Waldauf, and Roberto Pacios. Determination of gap defect states in organic bulk heterojunction solar cells from capacitance measurements. *Applied Physics Letters*, 95(23):233302, 2009.

[331] Christopher R McNeill, Inchan Hwang, and Neil C Greenham. Photocurrent transients in all-polymer solar cells: Trapping and detrapping effects. *Journal of Applied Physics*, 106(2):024507, 2009.

[332] Frederik SF Morgenstern, Marcus L Böhm, René JP Kist, Aditya Sadhanala, Simon Gélinas, Akshay Rao, and Neil C Greenham. Charge generation and electron-trapping dynamics in hybrid nanocrystal-polymer solar cells. *The Journal of Physical Chemistry C*, 120(34):19064–19069, 2016.

[333] Warren B Jackson and Nabil M Amer. Direct measurement of gap-state absorption in hydrogenated amorphous silicon by photothermal deflection spectroscopy. *Physical Review B*, 25(8):5559, 1982.

[334] Aditya Sadhanala, Felix Deschler, Tudor H Thomas, Siân E Dutton, Karl C Goedel, Fabian C Hanusch, May L Lai, Ullrich Steiner, Thomas Bein, Pablo Docampo, Cahen David, and Richard H Friend. Preparation of single-phase films of $CH_3NH_3Pb(I_{1-x}Br_x)_3$ with sharp optical band edges. *The Journal of Physical Chemistry Letters*, 5(15):2501–2505, 2014.

[335] Corey V Hoven, Xuan-Dung Dang, Robert C Coffin, Jeff Peet, Thuc-Quyen Nguyen, and Guillermo C Bazan. Improved performance of polymer bulk heterojunction solar cells through the reduction of phase separation via solvent additives. *Advanced Materials*, 22(8):E63–E66, 2010.

[336] Jin Fang, Dan Deng, Zaiyu Wang, Muhammad Abdullah Adil, Tong Xiao, Yuheng Wang, Guanghao Lu, Yajie Zhang, Jianqi Zhang, Wei Ma, and Zhixiang Wei. Critical role of vertical phase separation in small-molecule organic solar cells. *ACS Applied Materials & Interfaces*, 10(15):12913–12920, 2018.

[337] F De la Peña, VT Fauske, P Burdet, E Prestat, P Jokubauskas, M Nord, T Ostasevicius, KE MacArthur, M Sarahan, DN Johnstone, et al. Hyperspy/hyperspy v1. 4.1 (version v1. 4.1). *Zenodo: Meyrin, Switzerland*, 2018.

[338] David B Williams and C Barry Carter. The transmission electron microscope. In *Transmission electron microscopy*, pages 3–17. Springer, 1996.

[339] Yvonne J Hofstetter and Yana Vaynzof. Quantifying the damage induced by X-ray photoelectron spectroscopy depth profiling of organic conjugated polymers. *ACS Applied Polymer Materials*, 1(6):1372–1381, 2019.